MECHANICAL AND CORROSION PROPERTIES OF ULTRAFINE-GRAINED LOW C, N Fe-20%Cr STEEL PRODUCED BY EQUAL CHANNEL ANGULAR PRESSING

A thesis submitted in fulfillment of the requirements

for the award of the degree of

DOCTOR OF ENGINEERING

From

DOSHISHA UNIVERSITY

by

MUHAMMAD RIFAI

B.Sc (Physics Science)

M.Eng (Material Science)

Graduate School of Science and Engineering

November 2014

Thesis Certification

I, Muhammad Rifai, declare that this thesis, submitted in fulfillment of the requirements for the award of Doctor of Engineering, in the Graduate School of Science and Engineering, Doshisha University, is wholly my own work unless otherwise referenced or acknowledged. The document has not been submitted for qualifications at any other academic institution.

Muhammad Rifai

November 21th, 2014

Table of contents

Abstract

In chapter 1, General introduction of material strengthening by severe plastic deformation (SPD) and equal channel angular pressing (ECAP) was described. The majority of papers on SPD materials have been devoted to the face centered cubic (FCC) structure materials such as Al, Cu and Ni. For body centered cubic (BCC) metals, carbon steels have mostly been studied from a practical view point. A non-equilibrium structure of grain boundaries in ECAP processed is an important evidence for investigating the interactions of lattice dislocations with grain boundaries. Annealing, tensile, fatigue, corrosion fatigue and corrosion behavior was described for ultrafine-grained (UFG) structured material.

In Chapter 2, microstructural development of ultralow C, N, Fe-Cr alloy and pure copper processed by ECAP has been examined focusing on the initial stage of the formation of UFG structure. Fe-Cr alloys were pressed at 423 K while pure copper at room temperature for 1 to 3 passes via the route Bc to compare at the equivalent homologous temperature. Microstructural evolutions were characterized by electron backscatter diffraction (EBSD) image and transmission electron microscopy (TEM). It was found that deformation structures were mostly deformation-induced subboundaries in both the materials after one pass, but the fraction of high-angle grain boundary (HAGB) became higher in the Fe-Cr alloys than in pure copper in subsequent passes by increasing misorientation of the boundaries. The more enhanced formation of HAGB in Fe-Cr alloys was discussed in terms of the nature of crystal slip of FCC and BCC structures.

In Chapter 3, the effect of the deformation route on the microstructure, and the mechanical and corrosion properties of this alloy by ECAP have been investigated focusing on the anisotropy of the microstructure. This alloy was pressed at 423 K from one to eight passes via routes A, Bc and C, and the microstructure was observed in three orthogonal planes. As has been acknowledged, overall grain fragmentation proceeded most effectively in route Bc. However, the degree of anisotropy of microstructural

development was different among the three deformation routes. The fractions of HAGB and mean grain boundary misorientation were high and nearly isotropic in route Bc, whereas they were considerably low in one direction and highly anisotropic in routes A and C.

In Chapter 4, the post-ECAP annealing was carried out from 473 until 1373 K for one hour after eight passes of route Bc. The microstructure and hardness were then analyzed by EBSD, TEM, and X-ray diffractometer (XRD), and micro hardness. Hardness tests after post-ECAP annealing showed typical three stages softening comprising the first stage of relatively constant hardness, and the second stage of significant softening and final stage of constant hardness. In the second stage, grains grew uniformly, which differ from typical nucleation-and-growth mode of discontinuous recrystallization. It was found by X-ray line broadening analysis that strain was released in early stage prior to the significant softening stage. It was suggested that the homogeneous grain growth was led by the uniform grain distribution with a HAGB fraction.

In Chapter 5, The ECAP processed and post-ECAP annealed sample was characterized by tensile testing. The initial of this alloy exhibits a longer elongation and lower tensile strength. After one, two, four and eight passes, the tensile strength increases while the elongation decrease drastically. It can be seen that with the increasing number of extrusion passes the tensile strength increases while the elongation decreases. This implies that the improvement in strength accompanies the loss of the ductility in the ECAP processed sample. After the annealing, the tensile strength of the samples extruded by one, two, four and eight passes decreases, while the elongation increases. In general, the ductility of the ECAP processed samples can be improved by annealing at the sacrifice of a little decrease of tensile strength. However, the slight increase of tensile strength after annealing for the samples pressed by two passes is abnormal, which may be attributed to the experimental errors caused by the small sample dimension and the estimation of the tensile strength.

In Chapter 6, an assessment of the mechanical properties, in particular cycle fatigue resistance, compared with microstructural evolution in ECAP processed sample with deformation route was investigated in term of a better understanding of their microstructural evolution and low cycle fatigue (LCF) behavior. The fatigue life of the ECAP processed via route Bc specimens is much shorter than that of route A. This result is not unexpected in view of their lower ductility. LCF behavior after ECAP for up to four passes shows that the deformation microstructure remained fine and stable after cyclic deformation. However, the LCF life decreased along with the limited ductility, as is commonly observed for materials manufactured by ECAP.

In Chapter 7, effect of annealing on pitting corrosion of UFG structure material has been investigated in terms of effect of strain energy and grain size reduction. UFG structures of initial grain size of 140 nm exhibited the typical three stage softening comprising recovery, recrystallization and grain growth. Pitting potential in 1000 $mol \cdot m^{-3}$ NaCl solution was higher in UFG state, but it started to decrease monotonously at lower temperature than hardness. The degradation of corrosion resistance in the early stage of annealing is attributed to stability change of passivation by recovery of dislocations structures inside grains and in non-equilibrium grain boundaries.

In Chapter 8, the corrosion fatigue life of the ECAP processed and post-ECAP annealed sample was analyzed. Under annealing temperature of 773 K, due to the recrystallization stage, there was a little difference in microstructure from the four passes ECAP. This results implies that the improvement in strength accompanies with the loss of the ductility in the ECAPed sample. After the annealing process, the tensile strength of the samples extruded four passes decreases, while the elongation increases. Corrosion fatigue test on ECAPed and post-ECAP annealed sample was clarified that crack initiation started from corrosion pits and propagated.

Acknowledgements

I would like to express deepest gratitude to my supervisors, Professor Hiroyuki Miyamoto and Professor Hiroshi Fujiwara. The successful completion of this thesis is due to their guidance, constant encouragement and stimulating discussions throughout the course of this work. In spite of his busy schedule, Professor Miyamoto always had time to listen to me and responded back at his earliest possible whenever I submitted any draft for corrections.

I am greatly indebted to Professor Miyamoto for ECAP processing of the steel billets and material characterization at Doshisha University. Professor Kaneko of Osaka City University for fatigue testing, Professor Ameyama of Ritsumeikan University for wire cutting and tensile testing. I would also like to acknowledge Mrs. Toda dan Mrs. Morita for carrying out the TEM and SEM experiments.

It was a real pleasure for me having great lab-mates and friends around. I owe a lot to you friends – Mr. Imoto, Mr. Yamada, Mr Shinogi and Mr. Kasazaki and my undergraduate friends – Mr. Satoshi, Mr Nakayama, Mr. Abiko, Mr Yamaguchi and Mr. Tabashi. Especially to Ms. Chen Yanyan, my heartfelt thanks for your good company!

I thank my parents, my sister, my niece and nephew for their loving support and encouragement throughout the progression of this thesis.

Declaration on Publications

This thesis includes the following chapters that have been written as the journal articles:

Chapter 2 :

1. **Rifai, M**., Haga, R., Miyamoto, H., & Fujiwara, H. (2013). Microstructural Development of Fe-20mass% Cr Alloys and Pure Copper Processed by Equal-Channel Angular Pressing. Materials Sciences & Applications, 4(4).
2. **Rifai, M.**, Haga, R., Miyamoto, H., & Fujiwara, H. Microstructure Quantification and Mechanical Properties of Ultrafine Grained Fe‐Cr Alloys and Pure Copper by Equal Channel Angular Pressing. In PRICM: 8 Pacific Rim International Congress on Advanced Materials and Processing (pp. 3329-3335). John Wiley & Sons, Inc.

The result achieved award in :

- **Poster Award** at 6th German-Japan International Symposium on Nanostructures (OZ-13), March 2013, Kyoto, Japan

Chapter 3 :

3. **Rifai, M**., Miyamoto, H., & Fujiwara, H. (2014). Effect of ECAP Deformation Route on the Degree of Anisotropy of Microstructure of Extremely Low CN Fe-20mass% Cr Alloy. Metals, 4(1), 55-63
4. **Rifai, M**., Miyamoto, H., & Fujiwara, H. (2014).The effect of ECAP deformation route on microstructure, mechanical and electrochemical properties of low CN Fe-20%Cr alloy, Materials Sciences & Applications Vol.5 No. 8 (June), 2014.

5. Miyamoto, H., **Rifai, M**, & Fujiwara, H. (2014). Severe plastic deformation as a new processing for enhancing the performance of metallic components. In Construction Materials and Structures: Proceedings of the First International Conference on Construction Materials and Structures (p. 35). IOS Press.

Chapters 4 and 5 :

6. **Rifai, M**., Miyamoto, H., & Fujiwara, H. Effect of deformation route on the development of low CN Fe-20%Cr alloy by Equal Channel Angular Pressing. In NanoSPD 6 IOP Journal Material Science Special Issue 2014.

Chapter 6 :

7. Tomita, R., Kaneko, Y., Vinogradov, A., Miyamoto, H., **Rifai, M**., Processing-Route Dependence of Low Cycle Fatigue Properties in ECAPed Ferritic Stainless Steel. In M & M 2014 Conference

Chapters 7 and 8 :

8. **Rifai, M**., Miyamoto, H., & Fujiwara, H. (2015). Effects of Strain Energy and Grain Size on Corrosion Resistance of Ultrafine Grained Fe-20% Cr Steels with Extremely low C and N Fabricated by ECAP. International Journal of Corrosion, 2015.

Chapter 1. Introduction

1.1. Background on ultrafine-grained (UFG) material

The research in material strengthening is one of the main topics in materials research and development. Hall-Petch relationship predicted an increase of the strength and hardness with small grain achievement **[1,2]**. UFG structured materials have been well produced by several techniques. Research and development in UFG material has greatly grown along with growing scientific paper and articles **[3-5]**. Severe plastic deformation (SPD) is new technique that was developed to produce UFG structured material in polycrystalline materials, especially in face centered cubic (FCC) metal. The present research will discuss about plastic deformation on bulk UFG microstructure material especially of low C, N Fe-20%Cr steel as a pure body centered cubic (BCC) metal.

1.1.1 SPD application

SPD technique was applied to obtain submicrometer grain size of ferritic stainless steel **[6]**. SPD technique fragment polycrystalline into UFG structure with 100 nm to 1 μm grain size. Advantages of SPD technique are to obtain UFG material free of pores, keeping the same specimen dimension and producing non-porous material. SPD technique applied a very large plastic deformation on the material. The three applicable SPD techniques are accumulative roll bonding (ARB), high pressure torsion (HPT) and equal channel angular pressing (ECAP).

1.1.1.1. ARB technique

ARB technique used two sheets of metal for applying a very large plastic deformation. The two sheets of metal are stacked and rolled together to 50% reduction such that the two sheets become bonded together, as shown in **Figure 1.1 [7]**. This technique is carried out repeatedly; cutting into two, degreasing, stacking together and again rolling in the subsequent passes, to get a large plastic deformation on material.

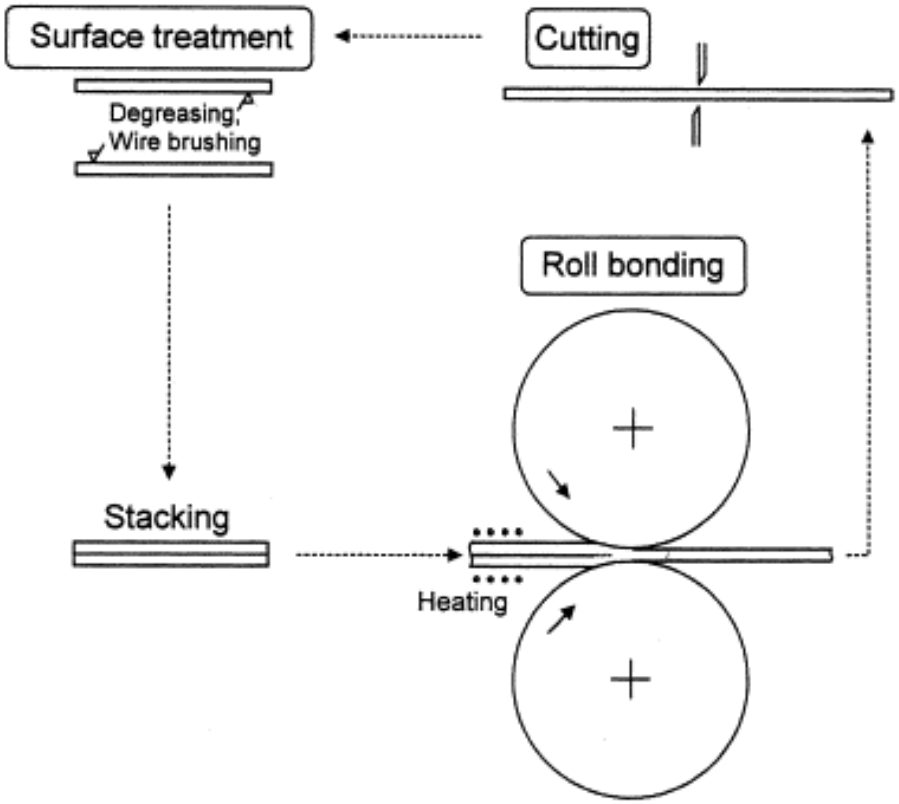

Figure 1.1. Schematic of ARB **[7]**.

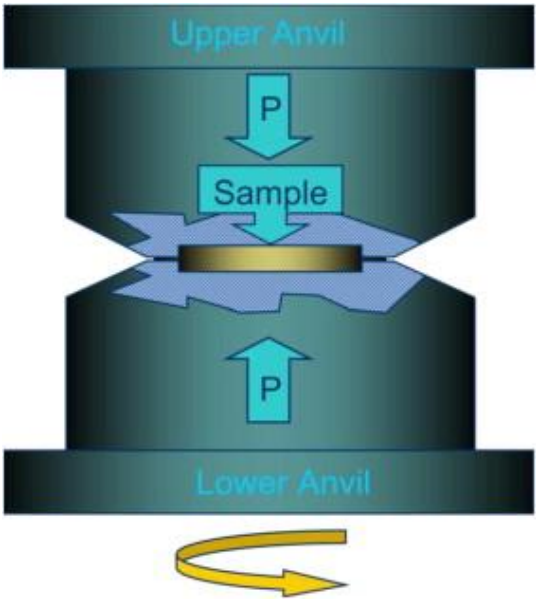

Figure 1.2. Schematic of HPT **[8]**.

1.1.1.2. HPT technique

Grain refinement by HPT technique used directional strain process where the strain direction remains the same path. HPT technique deform a disc shaped specimen which deformed by simple shear between a rotating bottom anvil and a fixed upper anvil, as shown in **Figure 1.2 [8]**. HPT technique has ability to do grain refinement for brittle materials such as intermetallic compound.

1.1.1.3. ECAP technique

ECAP technique is a technique which applies a very large plastic deformation on material without changing dimension of the specimen, and well known as a technique to improve mechanical properties. The ECAP die is a block in which two channels of identical cross sections intersect at an angle Φ, as shown in **Figure 1.3 [9-13]**. ECAP can be carried out repeatedly for same specimen to reach a level of plastic deformation.

The accumulating of equivalent strain can be calculated after *N* cycles, and can be written as **[14]**:

$$\varepsilon_N = \frac{N}{\sqrt{3}}\left[2cot\left(\frac{\Phi}{2}+\frac{\Psi}{2}\right)+\Psi cosec\left(\frac{\Phi}{2}+\frac{\Psi}{2}\right)\right] \quad (1.1)$$

when Φ is angle of intersection of two channels and and Ψ is the angle by the curvature of outer corner. The three deformation routes of ECAP have mainly been proposed as shown in **Figure 1.4**. In Route A, the sample is pressed without rotation. In Route B_C, the sample is rotated 90 degrees counterclockwise between each pass. In Route C, the specimen is rotated by 180 degrees between passes.

Interaction of shear plane of three types of deformation routes can be explained in a cubic element, as shown in **Figure 1.5 [15]**: If a cubic element is taken on the deformed element in plane X as shown, the profile of the deformed element in that plane can be obtained. The shearing patterns show that there are significant differences between the three processing routes. In route A, the samples are introduced to the same shear plane in every pass and led to a progressive compression of the grains in plane X

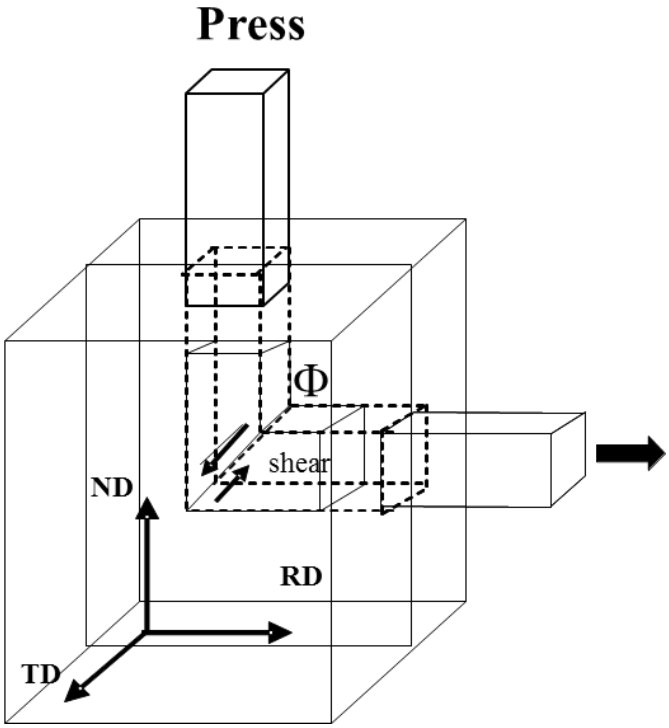

Figure 1.3. Schematic diagram of ECAP process**.**

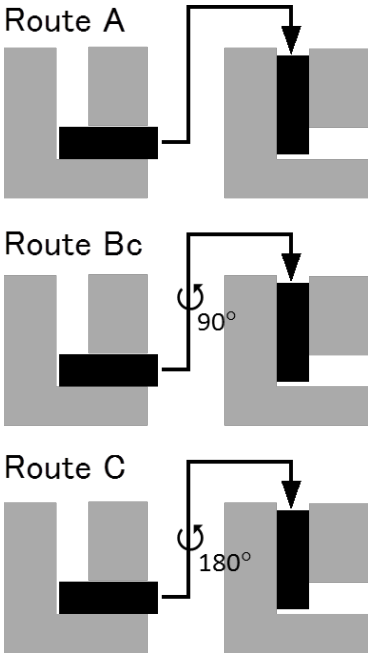

Figure 1.4. ECAP routes A, B_C and C.

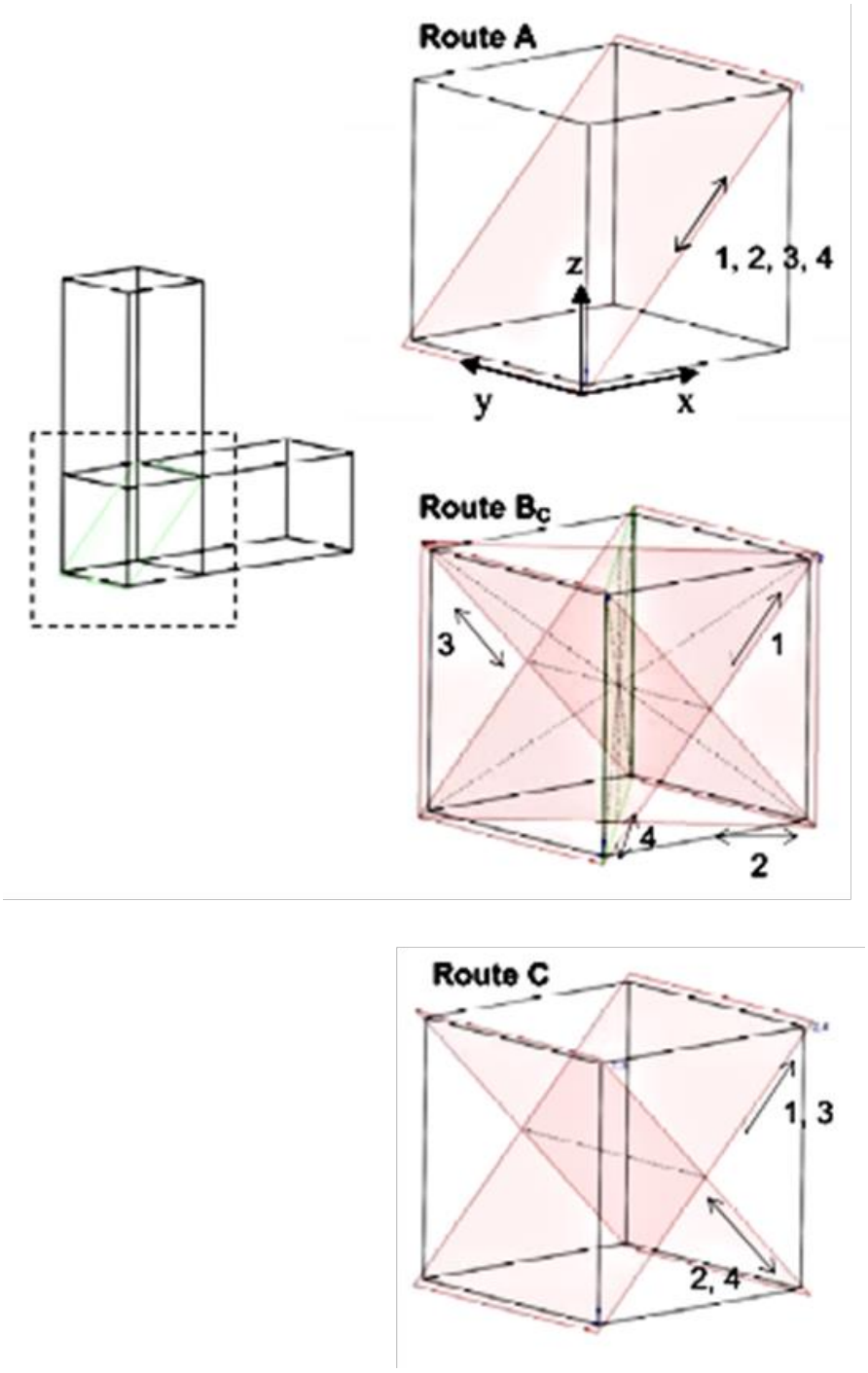

Figure 1.5. Interaction of shear plane for ECAP routes A, Bc and C for the first, second, third and fourth ECAP passes **[15]**.

as illustrated by the shaded rectangles. In plane Y, the deformed element becomes progressively elongated in the X-axis. The important characteristic of processing by route A is the development of distortions on plane X and Y. In route Bc, the element experiences distortion in plane X but the initial profile is restored after every four consecutive passes. In route C, the element's initial profile is restored after every alternate pass on plane X. The significance of rotating billets about the X-axis has been studied by examining the resultant microstructure of the deformed samples processed by the different routes. Based on these explanations, it can be produced most effectively grain refinement by using route Bc while routes A and C are less effective.

1.1.2. Deformation induced UFG material

The process of grain refinement by SPD can be divided into different stages. **Figure 1.8** shows eight different orientation image maps (OIM) of an interstisial free (IF) steel during ECAP, the stages are **[19]**: (1) as the microstructure gradually changes from a cellular structure to a granular structure, the first thing that can be noticed is the build-up of a dislocation structure inside the existing grains, (2) the dislocation structure evolves into a typical deformation microstructure with cells and cell blocks, (3) with further deformation, the grain shape changes to a layered structure that is both crystallographic and morphologically textured, (4) The morphological orientation of the grains tends to align more and more to the shear direction as deformation progresses, (5) In this stage the grain length is much larger than the grain width, which is consistent with the formation of a lamellae structure. In the final stage, both the dimensions of equal the subgrain size and the percentage of high-angle boundaries has greatly augmented, meaning the initial grains in the lamellar structure are subdivided into much smaller grains.

1.1.3. Non-equilibrium grain boundary induced by ECAP

UFG structure materials processed by ECAP methods are characterized by a very high density of grain boundaries. A non-equilibrium structure of grain boundaries in ECAP-processed form as a result of the interactions of lattice dislocations with grain boundaries, as shown in **Figure 1.6 [16,17]**. According to the literature, the formation of

a non-equilibrium grain boundary state is characterized by two main features, namely, excess grain boundary energy and the presence of long range elastic stresses **[17]**. ECAP-processed material show that grain boundaries have a crystallographic ordered structure and discontinuous distortions of such a structure. The sources of elastic stress fields are grain boundary dislocation.

ECAP-processed material have a non-equilibrium grain boundary inside the grain structure, as shown in **Figure 1.6**. The structural change during annealing of nanostructured material is **[18]**: (1) the recovery from non-equilibrium structure of the grain boundaries. Recovery process is connected with the partial annihilation of defects at grain boundaries and inside grains and it is associated with relaxation of internal elastic stresses, (2) The next process is characterized by the onset of migration of non-equilibrium grain boundaries which partially in normal grain growth, (3) The final process is connected with subsequent normal grain growth. This non equilibrium grain boundary by ECAP is expressed by schematic diagram as shown in **Figure 1.7**.

1.1.4. UFG structure of FCC and BCC material

Comparison studies of UFG of FCC and BCC crystal structure are reported in term of UFG formation and final grain size **[20-23]**. These report are carried out by ARB **[7,21,24]** and HPT **[22,23]**. Mechanical properties of UFG material was carried out on pure aluminum as FCC structure and IF steel as BCC structure, as shown in **Figure 1.9**. The microstructure of both material show similar appearance, as shown in **Figure 1.10 and 1.11**. Microstructural change effect to mechanical properties in UFG structured material **[7]**.

The microstructure after post-ARB annealing on pure aluminum and IF steel are quite similar. Recovery process occurred inside the grains at lower temperatures, and the grain size gradually increased with increasing annealing temperature **[7]**. The microstructural evolution of the ARB processed pure aluminum and IF steel during annealing exhibits a normal grain growth accompanied by recovery at grain interior **[7]**.

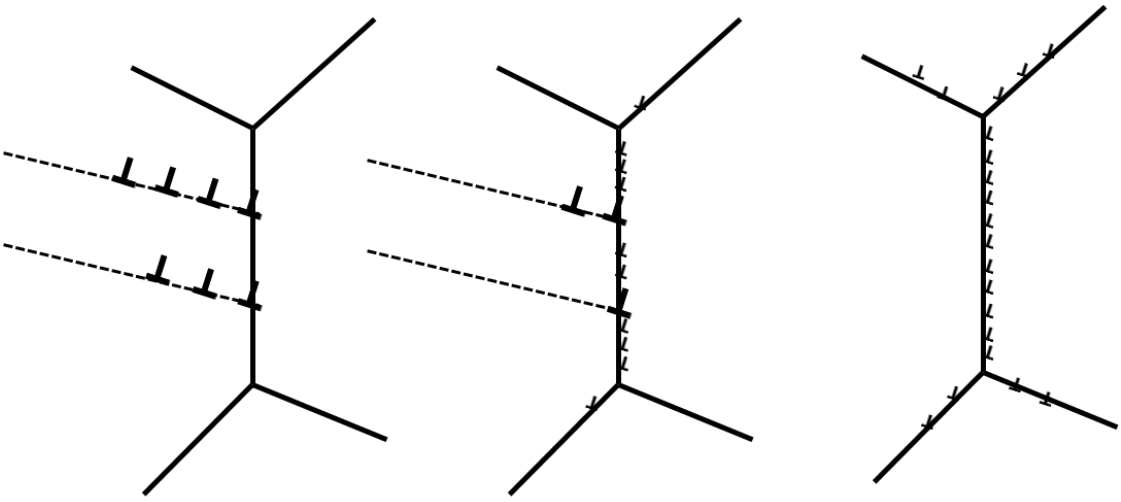

Figure 1.6. Schematic non-equilibrium structure of grain boundary by ECAP.

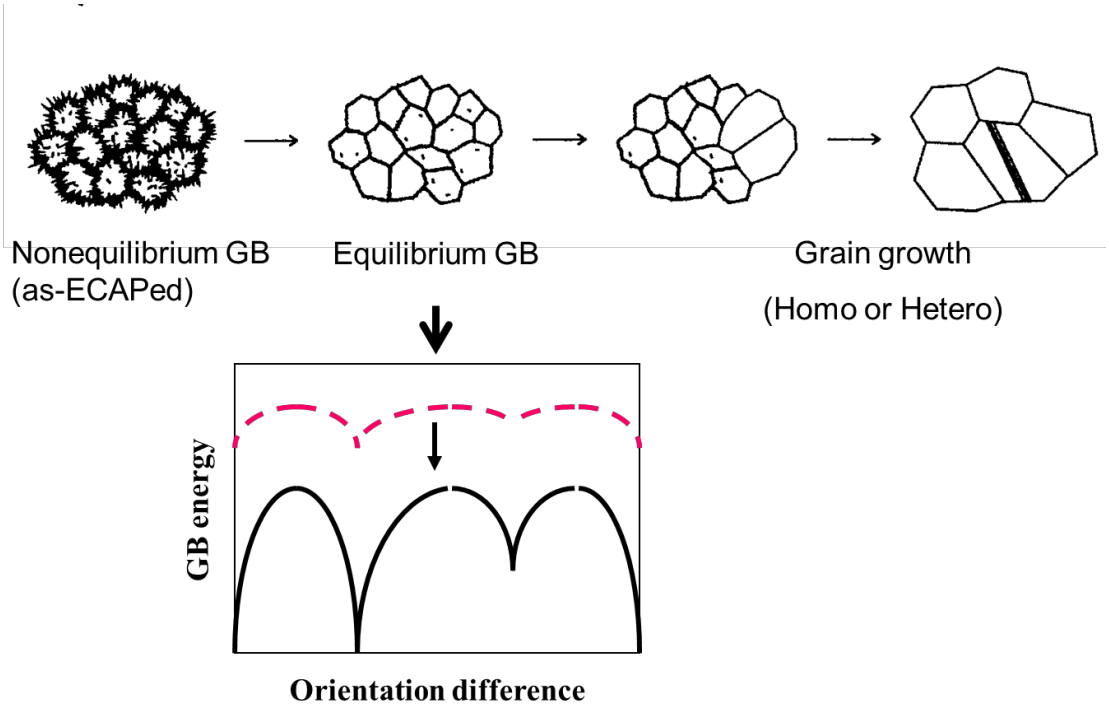

Figure 1.7. Schematic of structure evolution during annealing of nanostructured material **[18]**.

1.1.5 Annealing behavior

When a material is processed by ECAP, its work-hardening capability is limited **[25]**. ECAP increase the grain boundary area and large defect contents. Annealing process is needed to improve mechanical properties and by controlling microstructure. Annealing process includes three main stages, comprising of recovery, recrystallization and grain growth, as shown in **Figure 1.12**.

During annealing process, ECAPed sample shows several microstructure evolution **[26]**: (1) the microstructure and mechanical properties may be restored to their original values by recovery at an elevated temperature. This occurrence exhibit annihilation and rearrangement of the dislocations occurs. (2) The microstructural changes during recovery are relatively homogeneous, and it does not affect to the boundaries between the deformed grains. (3) Similar recovery processes may also occur during deformation, particularly at high temperatures. Recovery stage involves a restoration of mechanical properties due to removal dislocation structure. (4) After recovery stage, recrystallization stage may occur in which new dislocation-free grains are formed within the deformed or recovered structure. The new grain grows and consumes the old grains, resulting in a new grain structure with a low dislocation density. (5) Recrystallization stage takes place during deformation at elevated temperatures. Recrystallization stage removes the dislocations, the material still contains grain boundaries, but thermodynamically unstable. (6) Increasing annealing temperature results in grain growth, in which the smaller grains are eliminated, the larger grains grow, and the grain boundaries assume a lower energy configuration.

1.1.6 Tensile behavior

Material after ECAP processing exhibits poor ductility due to reduced work hardening and an early plastic instability **[27]**. The obtained UFG materials havevery high strength compared with the materials having conventional grain sizes larger than several tens micrometers **[4, 28-32]**. There are few results about mechanical properties of the UFG materials as a function of the grain size. The lack of this topic research is due to the difficulty in obtaining samples test having UFG microstructures.

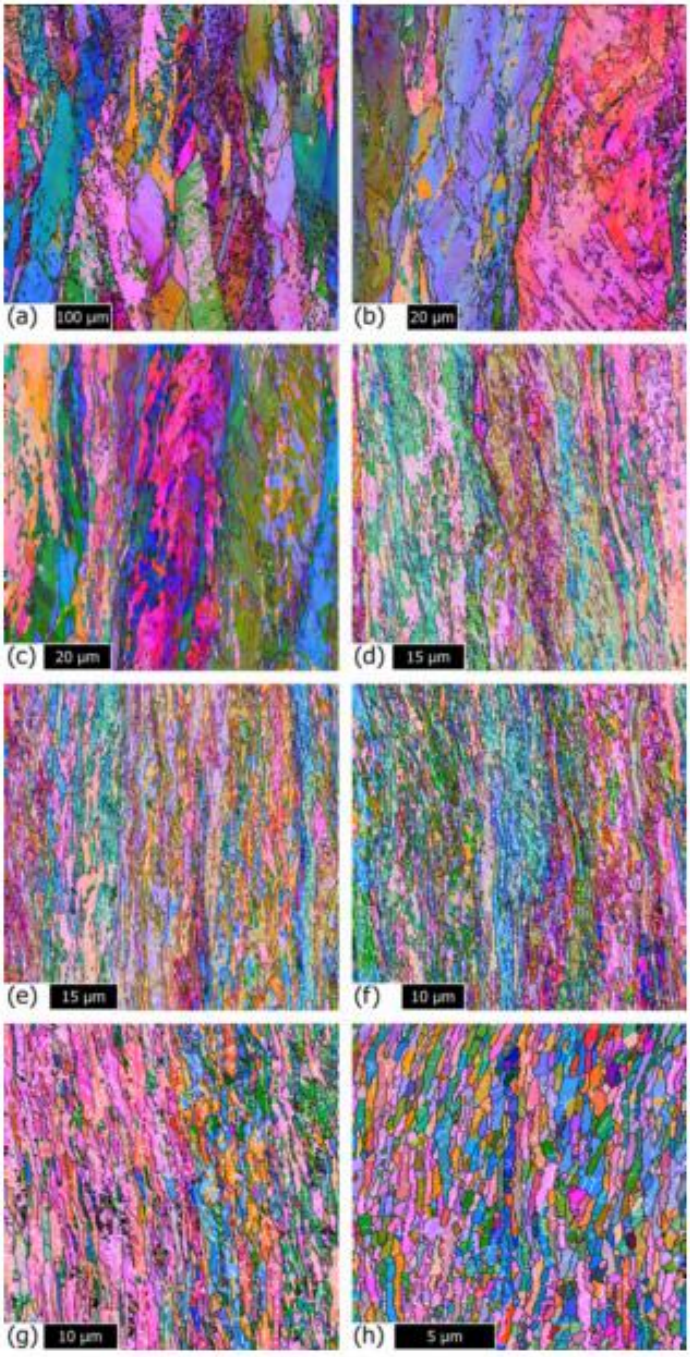

Figure 1.8. OIM of an IF steel deformed by ECAP at temperature 500ºC to (a) two passes, (b) n = 3, (c) n = 4, (d) n = 5, (e) n = 6, (f) n = 7, (g) n = 8 and (h) n = 15. **[19]**

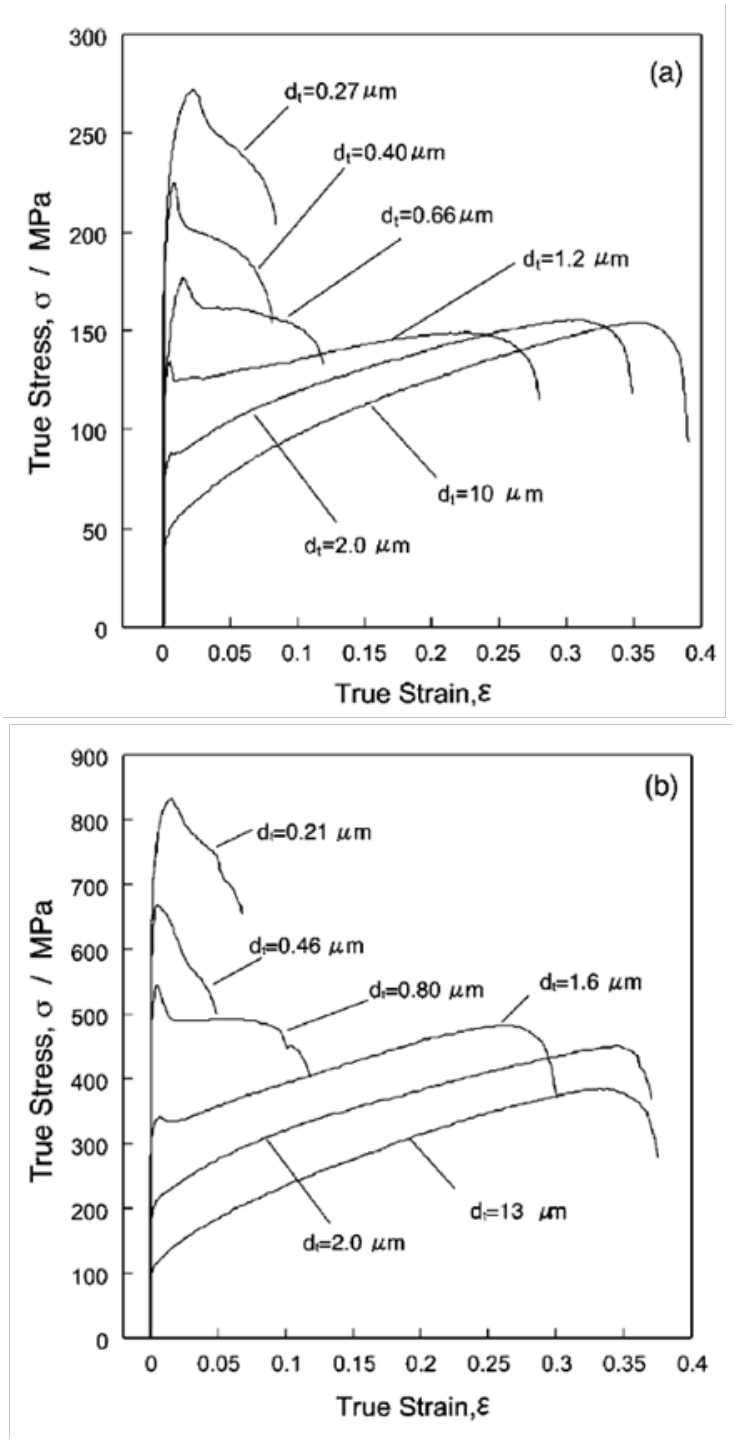

Figure 1.9. True stress and true plastic strain curves of the (a) 1100-Al and (b) IF steel with various grain sizes produced by ARB and subsequent annealing **[7]**.

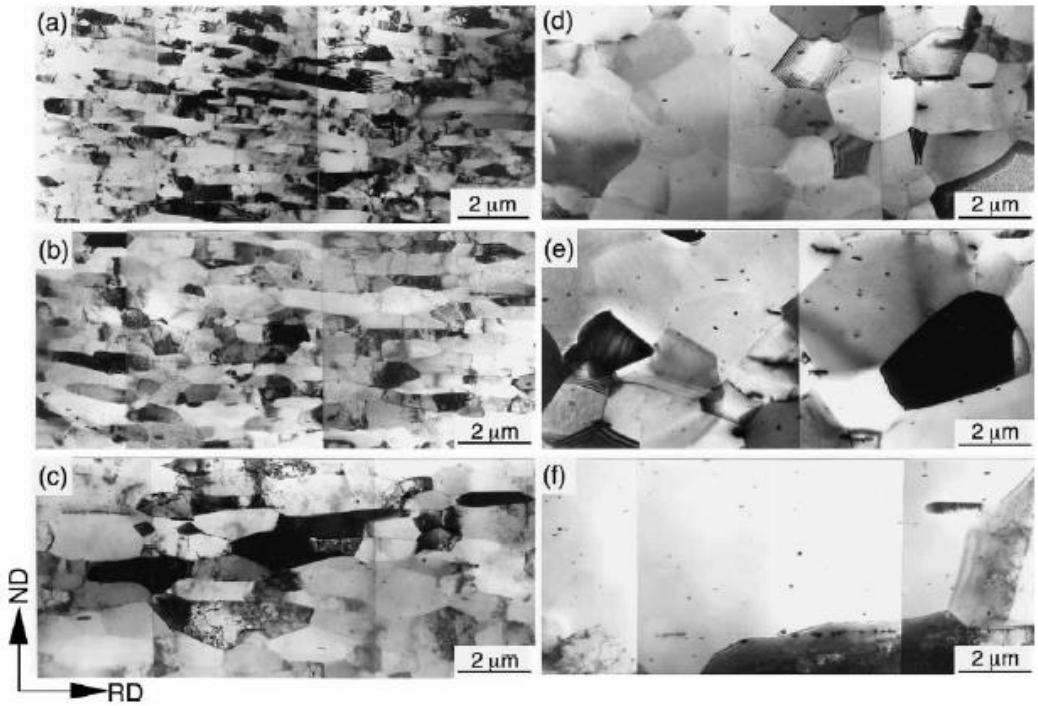

Figure 1.10. TEM microstructures of the 1100 aluminum annealed for 1.8 ks at (a) 373 K, (b) 423 K, (c) 473 K, (d) 498 K, (e) 523 K and (f) 573 K after 6 cycles of ARB at 473 K. Observed from TD **[7]**.

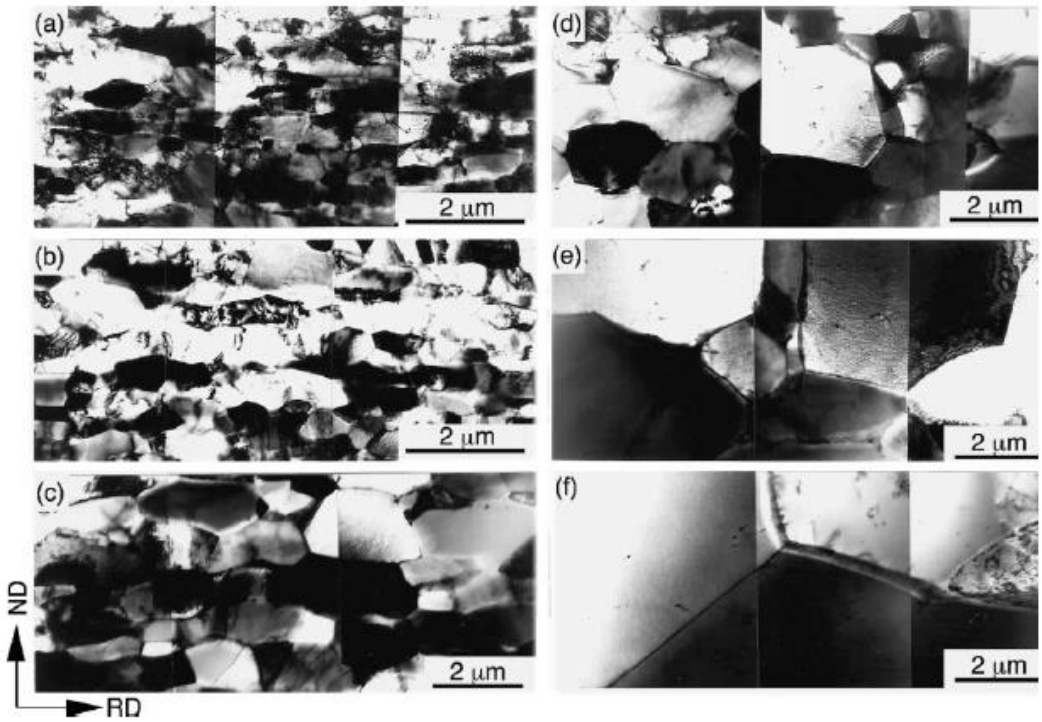

Figure 1.11. TEM microstructures of the IF steel annealed for 1.8 ks at (a) 673 K, (b) 773 K, (c) 873 K, (d) 898 K, (e) 923 K and (f) 973 K after 5 cycles of ARB at 773 K. Observed from TD **[7]**.

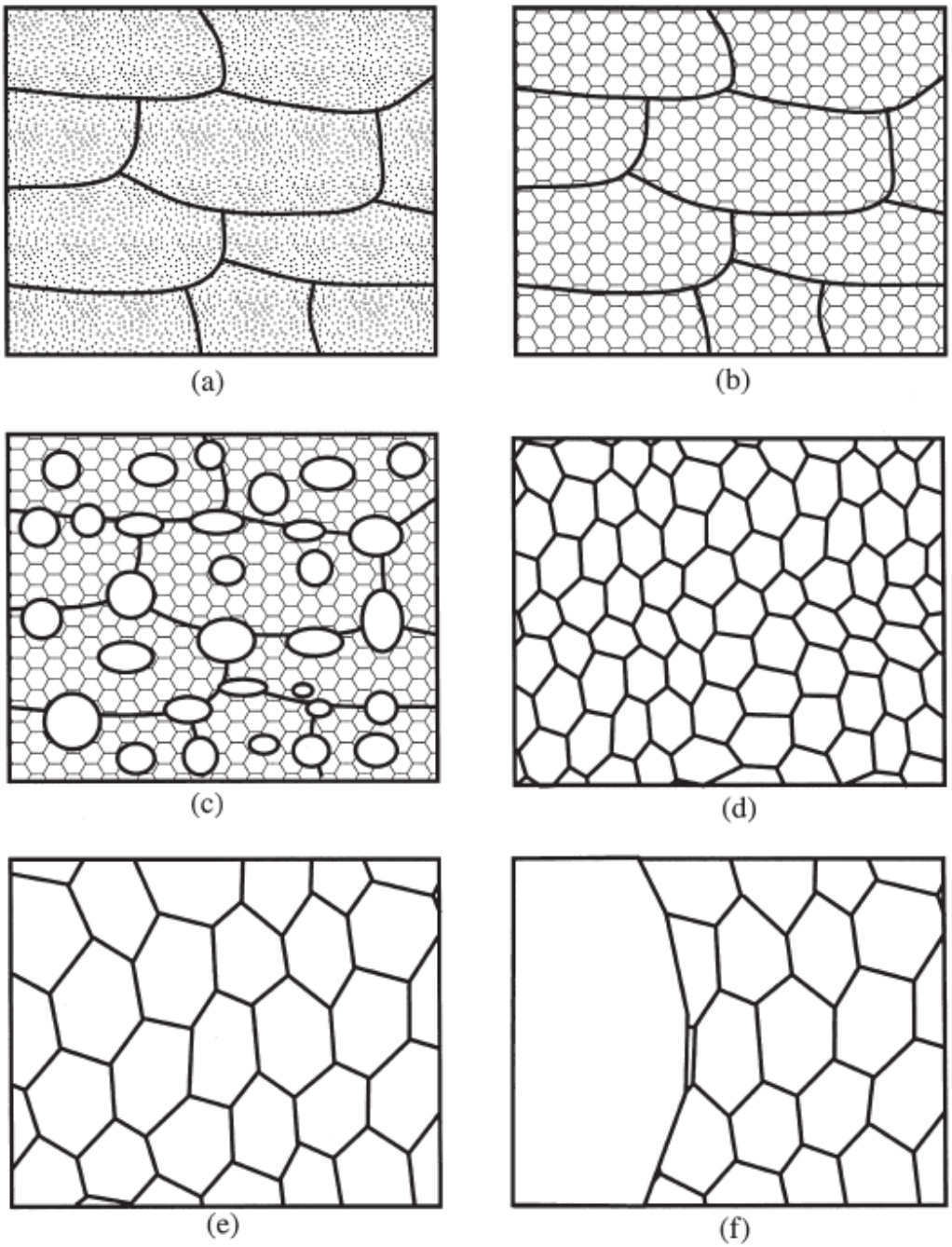

Figure 1.12. Schematic diagram of the main annealing processes; (a) Deformed state, (b) Recovered, (c) Partially recrystallized, (d) Fully recrystallized, (e) Grain growth and (f) Abnormal grain growth **[26]**.

Grain size dependence of strength and ductility suggests that work-hardening is not enhanced but rather suppressed by grain refinement, as shown in **Figure 1.13**. The sudden drop in uniform elongation around the grain size of 1 μm, at which tensile strength becomes nearly equal to yield strength, in other words, at which work-hardening becomes hard to occur, can be explained in terms of plastic instability simply **[7]**. The previous work clarified that work-hardening after yielding becomes rather difficult to occur with decreasing grain size **[7]**. The mechanism of work-hardening reduction by ECAP was needed to be studied in term of effect of deformation route ECAP and subsequent annealing process.

1.1.7 Fatigue behavior

Grain refinement of metal by ECAP results in an increase in strength. Improvement on ultimate tensile strength (UTS) and yield strength does not mean that the UFG structure material exhibit better mechanical properties, due to their resistance against damage by fatigue.

Fatigue properties of UFG structure improve significantly compare to coarse-grained structure. ECAP technique was used in order to achieve a UFG structure, high-strength material with increased ductility **[33]**.

The fatigue properties of ECAP 316L steel and other literature are shown in **Figure 1.14.a** as Wohler S–N curves **[34]**. After one ECAP pass the fatigue life is extended over applied stress amplitudes by three passes, the S-N curve shifts further upward and the fatigue limit reaches approximately 570 MPa, which is far higher than that of conventionally processed steels **[34]**. Literature about the correlation between monotonic and fatigue strength found that the fatigue limit of conventional type 316L coarse grained stainless steel strongly depends on the material strength **[35-37]**. The same trend is seen after grain size reduction into the nanoscale region, as shown in **Figure 1.14.b**. The previous work clarified a significantly higher fatigue endurance limit in nanostructured steel. This is evident in comparison with its conventional counterpart.

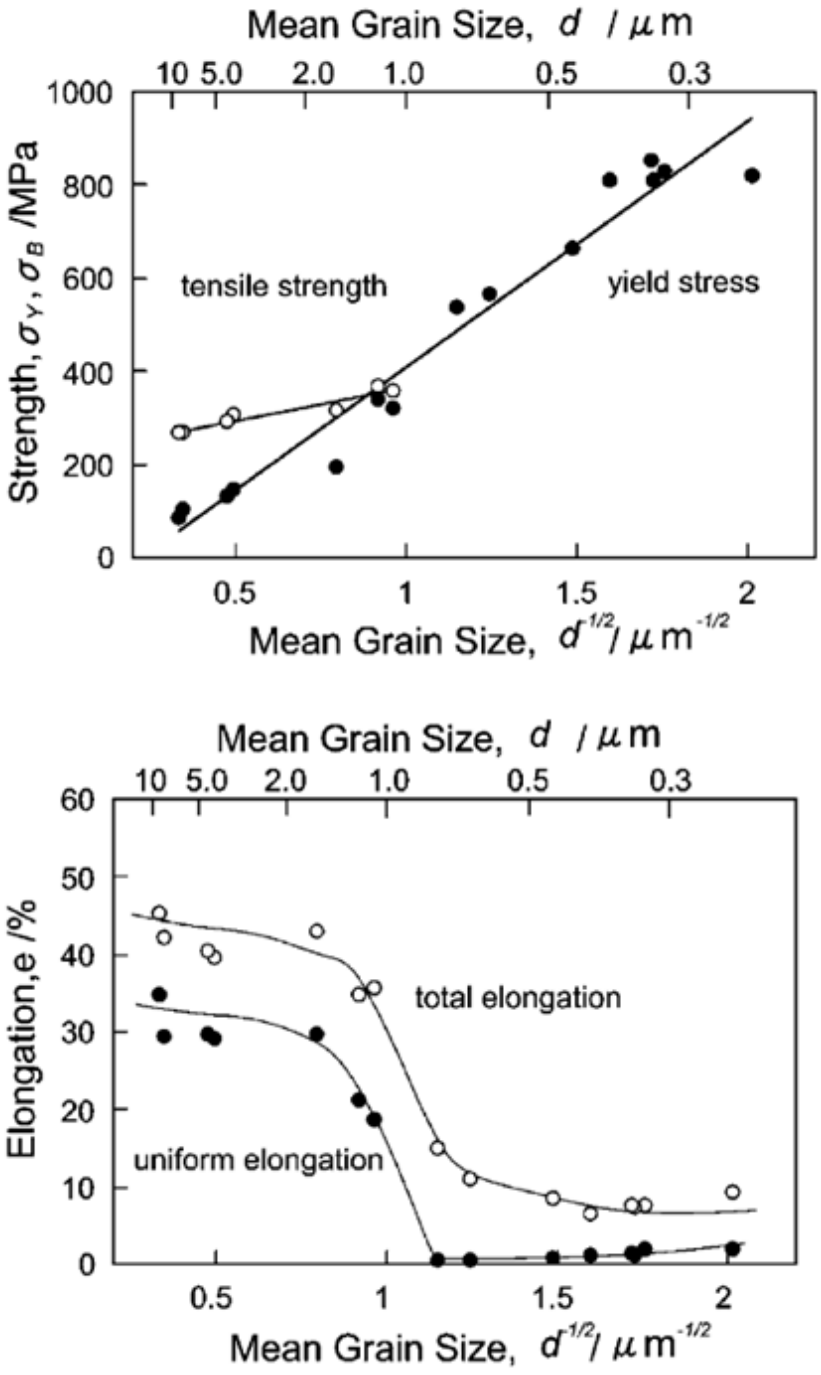

Figure 1.13. Grain size dependence of strength and ductility of the IF-Steel by ARB **[7]**.

The LCF life in the nanostructured state after one and three ECAP passes is considerably shorter than that in the conventional coarse grain material, due to softening effect induced by cyclic loading **[34]**. The purpose of this study is to clarify fatigue properties of ECAP in term of effect of deformation route ECAP.

1.1.8. Corrosion behavior

The corrosion behavior of the UFG structured materials can be investigated by several testing, such as stress corrosion cracking (SCC), corrosion fatigue, tafel testing, pitting testing, etc. Pitting corrosion resistance behaviors of UFG material were discussed in this thesis. The pitting corrosion resistance was also affected by the several factors especially passes number, deformation route and post annealing process **[38]**.

Pitting corrosion is a localized corrosion of a metal surface that resulted in cavities **[39]**. Pitting corrosion is so complicated in nature because of oxide films formed on different metals (passive film) **[40]**. Passive film formed of are thin oxide layers on the metal surface and reduce the rate of corrosion of the alloys. Passive film is often susceptible to localized breakdown, resulting in accelerated dissolution of the underlying metal. Pitting corrosion resistance is affected by several parameters such as environment, metal composition, potential, temperature, and surface condition **[41,42]**. Pitting corrosion show several stages such as passive film breakdown, metastable pitting, pit growth, and pit stifling **[43,44]**. Chromium concentration plays the dominant role on passivity. The pitting potential is found to increase dramatically as the chromium content has increased above the critical 13% which is needed to create stainless steel **[45]**.

The potential at which the passivation starts to break down at localized areas, leading to pitting, is defined as the pitting potential, E_{pit}. Pitting potential can be determined from anodic polarization curve as the potential at which the current with increasing potential, and pitting potential was defined accordingly as shown in **Figure 1.15 [46]**.

The corrosion resistance of the UFG structured material against the formation and growth of corrosion pits is characterized by the pitting potential E_{pit}. The behavior

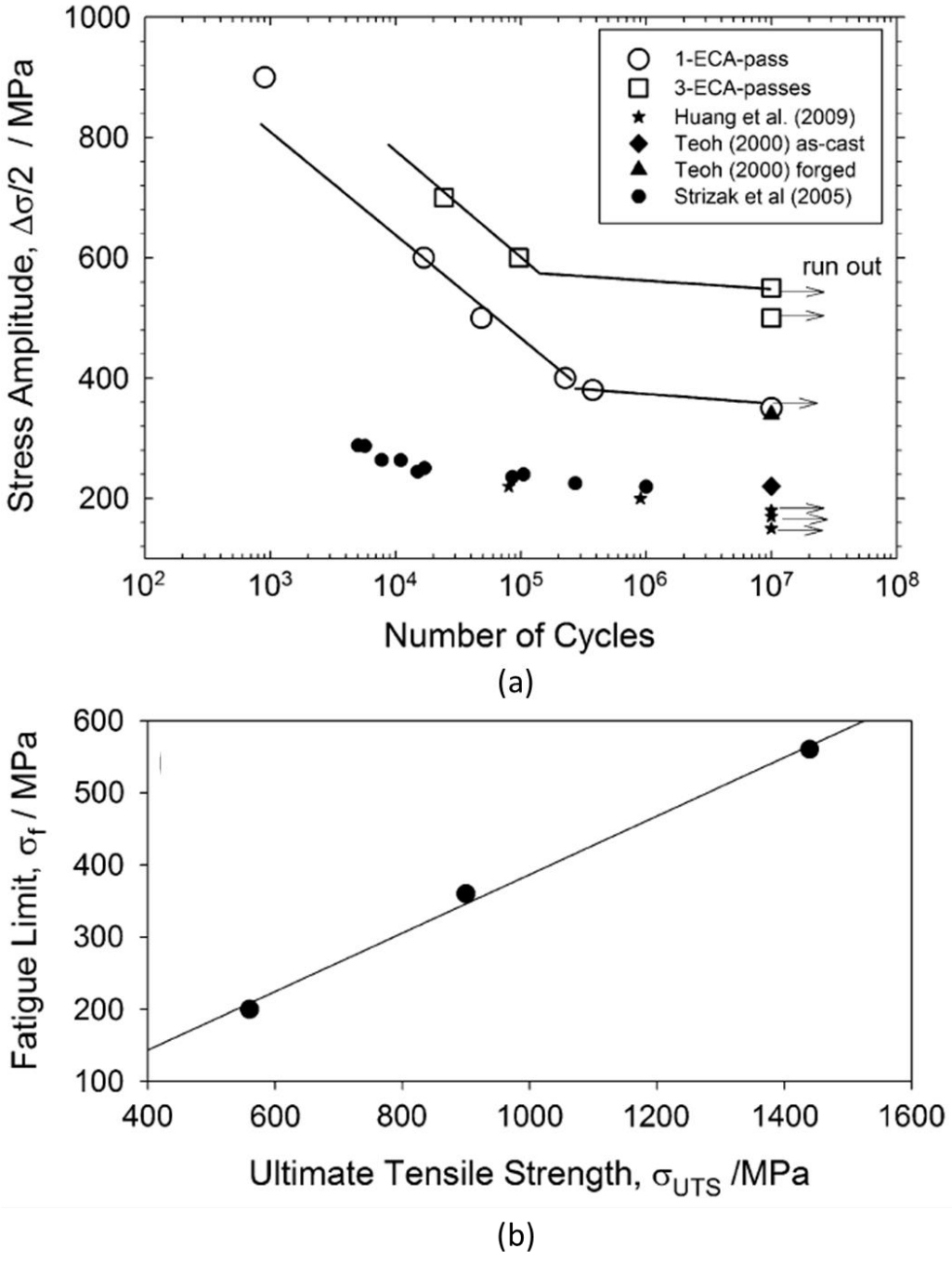

Figure 1.14. (a) S–N curves showing the high cycle fatigue properties of SUS 316L stainless steel after ECAP. (b) Correlation between the tensile strength and fatigue limit **[34]**.

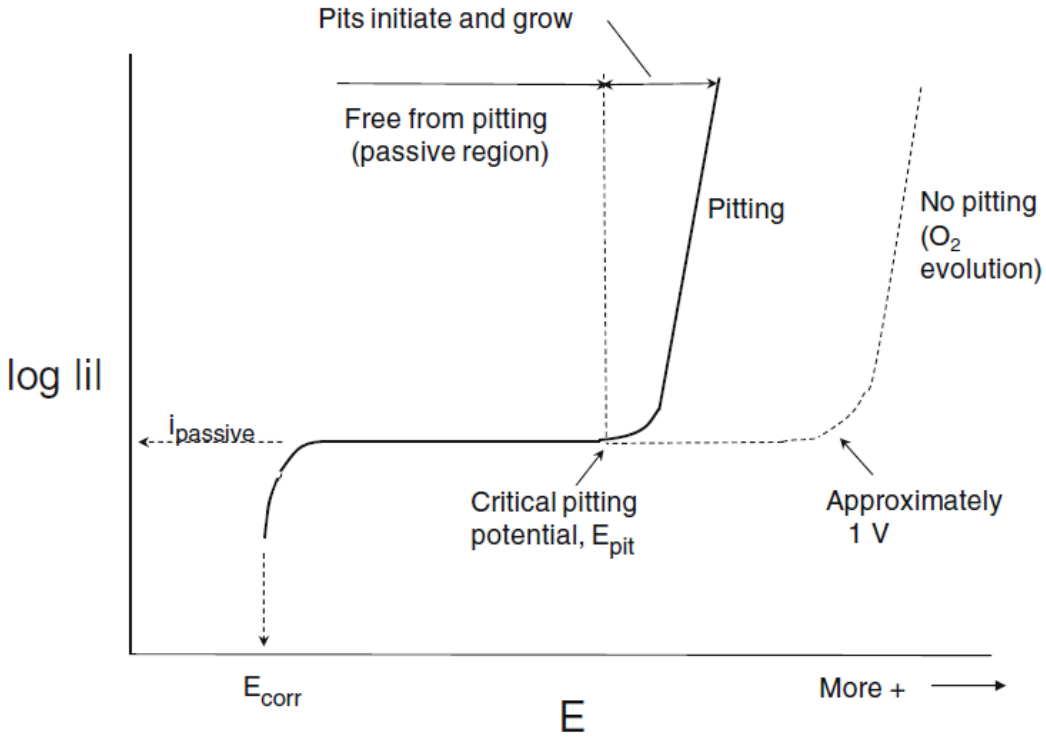

Figure 1.15. Schematic anodic polarization curve showing the critical pitting potential (for a passive metal) **[39]**.

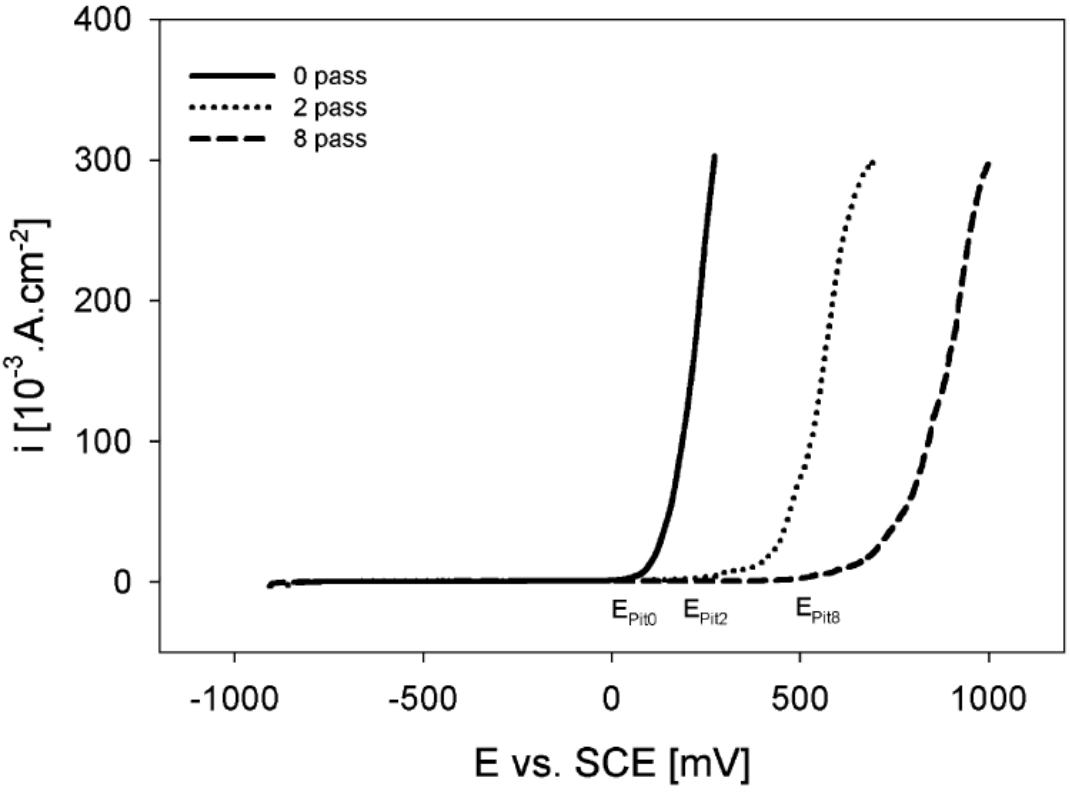

Figure 1.16. The pitting potential of IF steel specimens in 0.9M NaOH + 5% Cl−solution **[47]**.

of the coarse-grained and UFG IF steel specimens in the 0.9M NaOH alkaline medium with 5% Cl^- additions is shown in **Figure 1.16 [47]**. It is clearly seen that the pitting (or passivity breakdown) potential E_{pit} increases with increasing number of ECAP passes **[47]**. The increasing of E_{pit} shifts the boundary between the region of imperfect passivity and the pitting region, indicating that the protective passive layer in the UFG material is more stable than in the coarse grained material **[47]**. The effect of deformation route ECAP and subsequent annealing process on corrosion resistance need to be studied.

1.2. Research objective

The main objective of the present investigation was to examine the microstructural evolution, its mechanical and electrochemical properties during ECAP and subsequent annealing. In this regard, a 423 K route Bc from one until eight passes ECAP Low C, N Fe-20%Cr steel was prepared. Subsequent isothermal annealing was carried out at from 473 K -1373 K.

To accomplish the goal of the thesis the following sub-tasks were defined:

- To observe microstructure evolution during ECAP process in term of deformation route and passes number.
- To investigate annealing behavior of microstructure in term of stored energy by X-Ray line broadening and homogeneous grain growth.
- To study the influence of annealing temperature on subsequent evolution of microstructure and tensile work hardening behavior.
- To study the fatigue properties of UFG structure by ECAP and post-ECAP annealing.
- To investigate the pitting corrosion resistance of post-ECAP annealing.
- To study the corrosion fatigue properties of UFG structure by ECAP and post-ECAP annealing.

Reference

[1] Gleiter, H. (1995). Nanostructured materials: State of the art and perspectives. Nanostructured materials, 6(1), 3-14.

[2] Langdon, T. G. (2013). Twenty-five years of ultrafine-grained materials: achieving exceptional properties through grain refinement. Acta Materialia, 61(19), 7035-7059.

[3] Iwahashi, Y., Furukawa, M., Horita, Z., Nemoto, M., and Langdon, T. G. (1998). Microstructural characteristics of ultrafine-grained aluminum produced using equal-channel angular pressing. Metallurgical and materials transactions A, 29(9), 2245-2252.

[4] Furukawa, M., Horita, Z., Nemoto, M., Valiev, R. Z., and Langdon, T. G. (1996). Microhardness measurements and the Hall-Petch relationship in an Al Mg alloy with submicrometer grain size. Acta Materialia, 44(11), 4619-4629.

[5] Furukawa, M., Horita, Z., and Langdon, T. G. (2002). Factors influencing the shearing patterns in equal-channel angular pressing. Materials Science and Engineering: A, 332(1), 97-109.

[6] Miyamoto, H., Xiao, T., Uenoya, T., & Hatano, M. (2010). Effect of simple shear deformation prior to cold rolling on texture and ridging of 16% Cr ferritic stainless steel sheets. ISIJ international, 50(11), 1653-1659.

[7] Tsuji, N., Ito, Y., Saito, Y., & Minamino, Y. (2002). Strength and ductility of ultrafine grained aluminum and iron produced by ARB and annealing. Scripta Materialia, 47(12), 893-899.

[8] Zhilyaev, A. P., Nurislamova, G. V., Kim, B. K., Baró, M. D., Szpunar, J. A., & Langdon, T. G. (2003). Experimental parameters influencing grain refinement and microstructural evolution during high-pressure torsion. Acta Materialia, 51(3), 753-765.

[9] Segal, V. M. (1995). Materials processing by simple shear. Materials Science and Engineering: A, 197(2), 157-164.

[10] Wang, J., Iwahashi, Y., Horita, Z., Furukawa, M., Nemoto, M., Valiev, R. Z., & Langdon, T. G. (1996). An investigation of microstructural stability in an Al・Mg alloy with submicrometer grain size. Acta materialia, 44(7), 2973-2982.

[11] Mabuchi, M., Iwasaki, H., Yanase, K., & Higashi, K. (1997). Low temperature superplasticity in an AZ91 magnesium alloy processed by ECAE. Scripta Materialia, 36(6), 681-686.

[12] Fukuda, Y., Oh-Ishi, K., Horita, Z., & Langdon, T. G. (2002). Processing of a low-carbon steel by equal-channel angular pressing. Acta Materialia, 50(6), 1359-1368.

[13] Neishi, K., Horita, Z., & Langdon, T. G. (2002). Grain refinement of pure nickel using equal-channel angular pressing. Materials Science and Engineering: A, 325(1), 54-58.

[14] Iwahashi, Y., Wang, J., Horita, Z., Nemoto, M., & Langdon, T. G. (1996). Principle of equal-channel angular pressing for the processing of ultra-fine grained materials. Scripta Materialia, 35(2), 143-146.

[15] Furukawa, M., Horita, Z., & Langdon, T. G. (2002). Factors influencing the shearing patterns in equal-channel angular pressing. Materials Science and Engineering: A, 332(1), 97-109.

[16] Grabski, M. W. (1985). Mechanical properties of internal interfaces. Le Journal de Physique Colloques, 46(C4), C4-567.

[17] Valiev, R. Z., Gertsman, V. Y., & Kaibyshev, O. A. (1986). Grain boundary structure and properties under external influences. Physica status solidi (a), 97(1), 11-56.

[18] Valiev, R. Z., Islamgaliev, R. K., & Alexandrov, I. V. (2000). Bulk nanostructured materials from severe plastic deformation. Progress in materials science, 45(2), 103-189.

[19] Bowen, J.R, The formation of ultra-fine grained model aluminium and steel alloys, PhD. thesis, University of Manchester Institute of Science and Technology, Manchester, Great Britain, 2000.

[20] Gazder, A. A., Torre, F. D., Gu, C. F., Davies, C. H., & Pereloma, E. V. (2006). Microstructure and texture evolution of bcc and fcc metals subjected to equal channel angular extrusion. Materials Science and Engineering: A, 415(1), 126-139.

[21] Li, S., Gazder, A. A., Beyerlein, I. J., Pereloma, E. V., & Davies, C. H. (2006).

Effect of processing route on microstructure and texture development in equal channel angular extrusion of interstitial-free steel. Acta materialia, 54(4), 1087-1100.

[22] Pippan, R., Wetscher, F., Hafok, M., Vorhauer, A., & Sabirov, I. (2006). The limits of refinement by severe plastic deformation. Advanced Engineering Materials, 8(11), 1046-1056.

[23] Wetscher, F., Vorhauer, A., & Pippan, R. (2005). Strain hardening during high pressure torsion deformation. Materials Science and Engineering: A, 410, 213-216.

[24] Shin, D. H., Kim, W. J., & Choo, W. Y. (1999). Grain refinement of a commercial 0.15% C steel by equal-channel angular pressing. Scripta materialia, 41(3), 259-262.

[25] Wang, Y. M., & Ma, E. (2004). Strain hardening, strain rate sensitivity, and ductility of nanostructured metals. Materials Science and Engineering: A, 375, 46-52.

[26] Rollett, A., Humphreys, F. J., Rohrer, G. S., & Hatherly, M. (2004). Recrystallization and related annealing phenomena. Elsevier. [53]

[27] Yu, C. Y., Kao, P. W., & Chang, C. P. (2005). Transition of tensile deformation behaviors in ultrafine-grained aluminum. Acta materialia, 53(15), 4019-4028.

[28] Erbel, S. (1979). Mechanical properties and structure of extremely strainhardened copper. Metals Technology, 6(1), 482-486..

[29] Valiev, R. Z., Korznikov, A. V., & Mulyukov, R. R. (1993). Structure and properties of ultrafine-grained materials produced by severe plastic deformation. Materials Science and Engineering: A, 168(2), 141-148.

[30] Saito Y, Tsuji N, Utsunomiya H, Sakai T, Hong RG. Scripta Mater 1998;39:1221

[31] Tsuji, N., Saito, Y., Utsunomiya, H., & Tanigawa, S. (1999). Ultra-fine grained bulk steel produced by accumulative roll-bonding (ARB) process. Scripta materialia, 40(7), 795-800.

[32] Kimura, Y., Hidaka, H., & Takaki, S. (1999). Work-hardening mechanism during super-heavy plastic deformation in mechanically milled iron powder. Materials Transactions, JIM(Japan), 40(10), 1149-1157.

[33] Mughrabi, H., Höppel, H. W., Kautz, M., & Valiev, R. Z. (2003). Annealing treatments to enhance thermal and mechanical stability of ultrafine-grained metals produced by severe plastic deformation. Zeitschrift für Metallkunde, 94(10), 1079-1083

[34] Ueno, H., Kakihata, K., Kaneko, Y., Hashimoto, S., & Vinogradov, A. (2011). Enhanced fatigue properties of nanostructured austenitic SUS 316L stainless steel. Acta Materialia, 59(18), 7060-7069.

[35] Huang, J. Y., Yeh, J. J., Jeng, S. L., Chen, C. Y., & Kuo, R. C. (2006). High-cycle fatigue behavior of type 316L stainless steel. Materials transactions, 47(02), 409-417..

[36] Estrin, Y., & Vinogradov, A. (2010). Fatigue behaviour of light alloys with ultrafine grain structure produced by severe plastic deformation: an overview. International Journal of Fatigue, 32(6), 898-907.

[37] Vinogradov, A. (2007). Fatigue limit and crack growth in ultra-fine grain metals produced by severe plastic deformation. Journal of materials science, 42(5), 1797-1808.

[38] Song, D., Ma, A., Jiang, J., Lin, P., Yang, D., & Fan, J. (2010). Corrosion behavior of equal-channel-angular-pressed pure magnesium in NaCl aqueous solution. Corrosion Science, 52(2), 481-490.

[39] McAdam, D. J., & Gell, G. W. (1928). Pitting and its effect on the fatigue limit of steels corroded under various conditions. Journal of the Proceedings of the American Society for Testing Materials, 41, 696-732.

[40] Nguyen, T. H., & Foley, R. T. (1979). On the mechanism of pitting of aluminum. Journal of the Electrochemical Society, 126(11), 1855-1860.

[41] Baroux, B. (2002). Further insights on the pitting corrosion of stainless steels. CORROSION TECHNOLOGY-NEW YORK AND BASEL-, 17, 311-348.

[42] Szklarska-Smialowska, Z. (1999). Pitting corrosion of aluminum. Corrosion Science, 41(9), 1743-1767.

[43] Frankel, G. S. (1998). Pitting corrosion of metals a review of the critical factors. Journal of the Electrochemical Society, 145(6), 2186-2198.

[44] From internet on “Pitting Corrosion” http://corrosion.kaist.ac.kr. ch.9, KAIST.

[45] Horvath, J., & Uhlig, H. H. (1968). Critical Potentials for Pitting Corrosion of Ni, Cr‐Ni, Cr‐Fe, and Related Stainless Steels. Journal of the Electrochemical society, 115(8), 791-795. (cited in 73)

[46] McCafferty, E. Introduction to corrosion science. Springer, (2000).

[47] Hadzima, B., Janeček, M., Estrin, Y., & Kim, H. S. (2007). Microstructure and corrosion properties of ultrafine-grained interstitial free steel. Materials Science and Engineering: A, 462(1), 243-247.

Chapter 2. Microstructural development of Fe-20mass%Cr alloys and pure copper processed by ECAP

2.1. Introduction

SPD as a processing for fabricating UFG materials increased in popularity in the field of materials science and engineering. ECAP is one of the SPD to produce UFG material which use a unique deformation processing by incremental shear restricted to the narrow zone parallel to the intersecting plane of the two channels **[1,2]**. The total amount of plastic strain is important as well as the amount of plastic strain imposed in one pass to produce UFG material **[3]**. Large shear deformation can be applied to material in every pressing without changing the billet shape.

UFG structures is generally considered to develop by grain subdivision mechanism, where grains are subdivided by deformation-induced subgrain boundaries or low-angle grain boundaries (LAGB), followed by gradual increase of misorientation forming high-angle grain boundaries (HAGB) **[4]**. The majority of papers on SPD materials have been devoted to the FCC materials such as Al **[5]**, Cu **[6]** and Ni **[7]**. For BCC metals, carbon steels have mostly been studied **[8-16]** from a practical view point.

Despite the recent studies on UFG low-carbon steels **[7-15]**, the underlying mechanism of deformation and UFG formation and their substantial difference from FCC metals in ECAP is not fully understood, largely due to complexities associated with chemical compositions, especially with solute carbon and cementite. As compared to FCC metals, BCC metals show predominant cross-slip by screw dislocation due to the high frictional stress associated with its non-planar core structure. Such difference in nature of crystal slip intrinsic to BCC and FCC may influence the development of UFG, in particular, the density of dislocation boundaries and their rate of transformation to HAGB as a beginning stage of UFG formation. Dislocation glide and deformation microstructures of BCC metals are more sensitive to solute carbon or nitrogen than that of BCC metals. In this respect, pure BCC metals or IF metals should be used in order to clarify the microstructural development intrinsic to BCC structures.

Although the literature on pure BCC or IF steels processed by ECAP has been reported **[16-32]**, there are still very limited papers examining the microstructural evolution quantitatively in particular, the initial stage where dislocation substructure transforms into network of LAGB or HAGB.

There are several comparative studies of BCC and FCC metals, which report the differentiate of UFG formation and final grain size **[22,33-38]**. Comparative stud- ies of UFG formation in BCC/FCC crystals were reported in ARB **[14,33,34]** and HPT **[35,36]**. ARB processed material shows higher fraction of HAGB in IF-Steel, than in OFHC-Cu **[33]**. The large amount of LAGB fraction in OFHC-Cu was attributed to recovery and recrystallization during the ARB process **[33]**. However, in ARB, pure iron or steels as BCC material were mostly rolled at 773 K to obtain good bonding while aluminum as FCC material was rolled at room temperature or 473 K. Namely, the formation of UFG is compared at different homologous temperature **[33]**. Therefore, the influence of thermal activation is different in both the materials on the formation of UFG. In this context, we carried out experiments at the same homologous temperature, focusing on the difference in microstructural evolution of FCC and BCC at the equivalent thermal activation during ECAP. Dislocation structures, and microscopic parameter such as the fraction and spacing of HAGB, distribution of misorientation and dislocation density of pure copper and Fe-Cr with extremely low C,N were carefully examined and compared focusing on the initial stage of UFG formation during ECAP.

2.2. Experimental procedure

The chemical composition of pure copper was 99.99% purity, and that of Fe-Cr alloys where Cr 20.03; C 0.0004; N 0.0013 and Fe balance (in mass percent). Pure copper was machined with dimensions of 20 mm in diameter and 100 mm in length, and Fe-Cr alloys have dimensions of 3.95 mm × 3.95 mm × 40 mm for ECAP pressing. The ECAP procedures were carried out using a split die with two channels intersecting at inner angle of 90° and outer angle of 0°. ECAP of Fe-Cr alloys were carried out at 423 K while pure copper at room temperature in order to examine at the equal temperature ratio to melting temperature for each material. The samples lubricated with high

temperature fluorine lubricating grease were pressed from one to three passes through the so-called Route Bc. The original microstructure of as-received sample was observed using an optical microscope (OM), as is seen in **Figure 2.1**. Original grain size of Fe-Cr alloy is much larger than that of pure copper. A scanning electron microscope of field-emission type (FE-SEM, JSM 7001F), equipped with electron back-scattered diffraction (EBSD, Oxford Instrument Co.) image, and a transmission electron microscope (TEM) were used to examine the microstructures. EBSD orientation maps were processed using INCA^{TM} software. Thin foils for TEM were polished using abrasive papers to about 100 μm thick and then thinned by a twin-jet polishing facility using a solution of nitric acid 33% and 67% methanol for pure copper and acetic acid 40%, phosphoric acid 30%, nitric acid 20% and distilled water 10% for Fe-Cr alloys. Hardness experiments were performed on a Vickers hardness testing machine at room temperature.

2.3. Result

Three-dimensional OIM were obtained by EBSD after ECAP are shown in **Figure 2.2**. It is apparent that grains are more finely subdivided in Fe-Cr alloys than pure copper after the first pressing in spite that the former material has larger grain size before ECAP. Furthermore, arrays of planar and extended grain boundaries are developed parallel to the macroscopic shear plane of ECAP in Fe-Cr alloys whereas grain boundaries are rather curved in copper. After three passes, both materials were finely fragmented, but boundary spacing was still smaller in Fe-Cr alloys.

Misorientation maps showing LAGB ($2° \leq \theta < 15°$) and HAGB ($\theta \geq 15°$) with green and red lines, respectively, are shown in **Figure 2.3**. Because of low orientation resolution, boundaries with misorientation smaller than 2° were omited. As was mentioned in **Figure 2.2**, planar array of grain boundaries was noticeable in Fe-Cr alloys after one or two passes. In Fe-Cr alloy, higher density of LAGB with spacing smaller than 1 μm were formed after one pressing, and then the HAGB fraction becomes higher by increasing misorientation angle with increasing strain. On the other hand, density of LAGB increased after two and three passes while HAGB were very

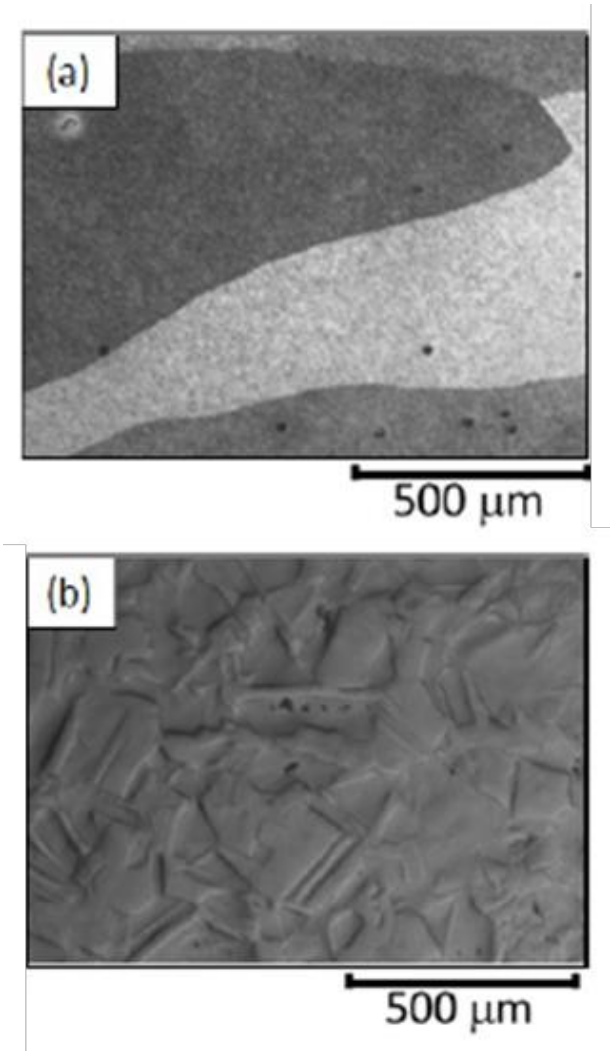

Figure 2.1. Microstructure using OM for (a) Fe-Cr alloys; (b) Pure copper.

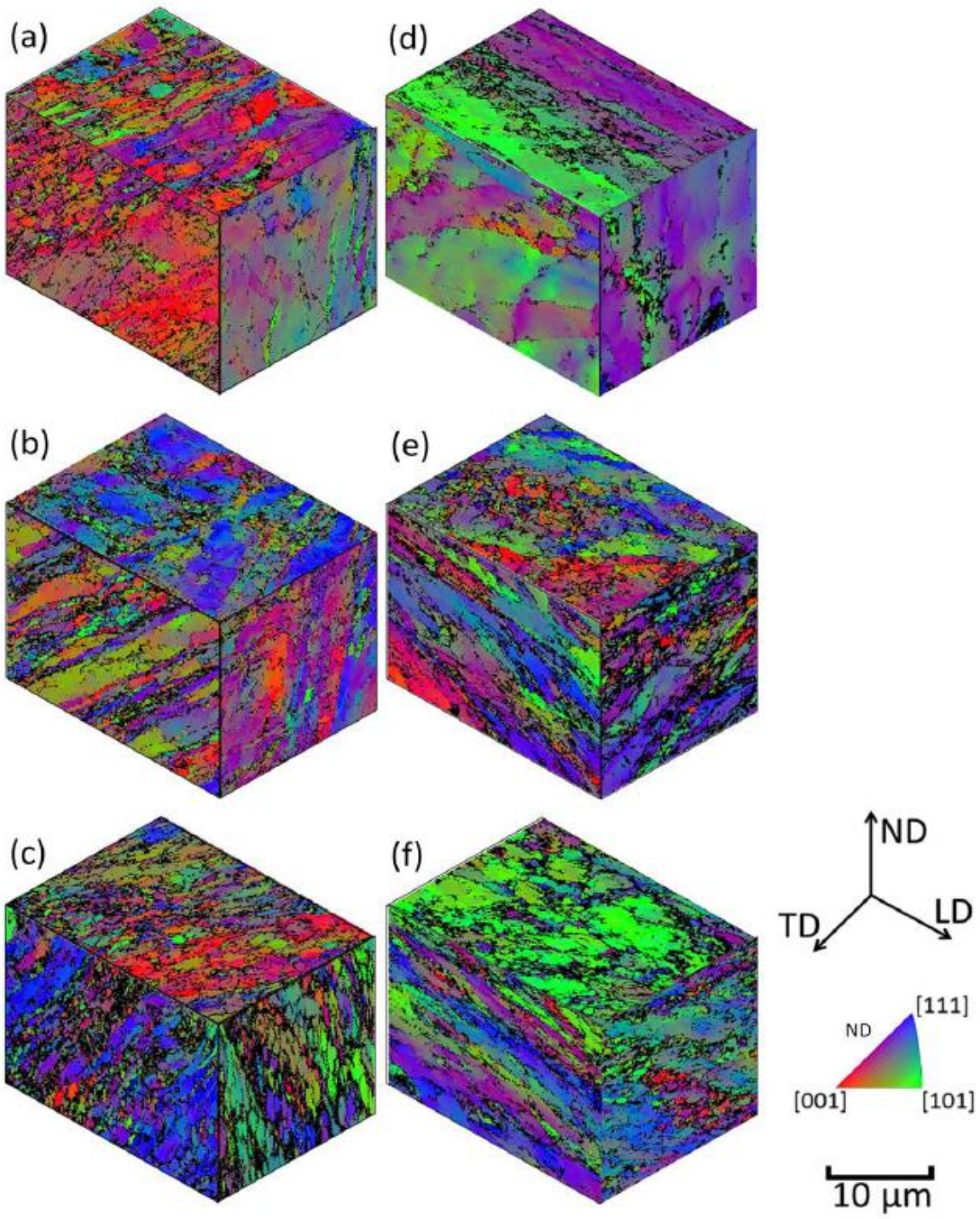

Figure 2.2. 3D representation EBSD orientation color map of Fe-Cr alloys after ECAP (a) one pass; (b) two passes; (c) three passes, and pure copper after ECAP (d) one pass; (e) two passes; and (f) three passes.

scarce in pure copper, and they are still scarcer after three passes. It seems that lines defined as LAGB in the misorientation map are diffuse, and mostly still dislocation cell boundaries in pure copper.

Distribution of misorientation angle was obtained from EBSD observation after one to three passes of ECAP as shown in **Figure 2.4.** Result of single pass for both the materials shows boundary misorientation with a peak in the range of 2° - 4° with low HAGB misorientation distribution. After two and three passes, the difference became noticeable between both the materials. Misorientation distribution of Fe-Cr alloys shows two small peaks at low and high angle misorientation with relatively flat distribution while pure copper shows peaks only at misorientation smaller than 5°, and it shows average apparently increased with the number of ECAP passes in **Figure 2.4**. Quantitative analysis of microstructures by EBSD is shown in **Figure 2.5**. As shown in **Figure 2.5(a)** and **(b)**, fraction of HAGB and average misorientation is higher in Fe-Cr alloys and increased until three passes. The equivalent strain imposed on a sample as it passes through an ECAP die was given in the reference [39]. However, while, boundary spacing decreased considerably after two passes in both the materials, there were smaller changes after three passes, as seen in **Figure 2.5(c)**.

Microstructure was observed using TEM in **Figure 2.6**. Dislocation cells structures were predominant after one pass in both the materials. However, elongated sub grains can be found out at Fe-Cr alloys and they became finely divided by sharper boundaries after three passes. On the other hand, subboundaries in pure copper after three passes are still diffused, and seem to be still mainly dislocation cell structures. Dislocation density inside grains was estimated from TEM images by Ham's interception method **[40]**. The thickness of specimen was estimated 245 nm for calculating dislocation density with Ham's interception method. Fe-Cr alloys and pure copper show that similar trend of dislocation density as shown in **Figure 2.7** with increasing number of passes, but the density of Fe-Cr alloys is higher than pure copper.

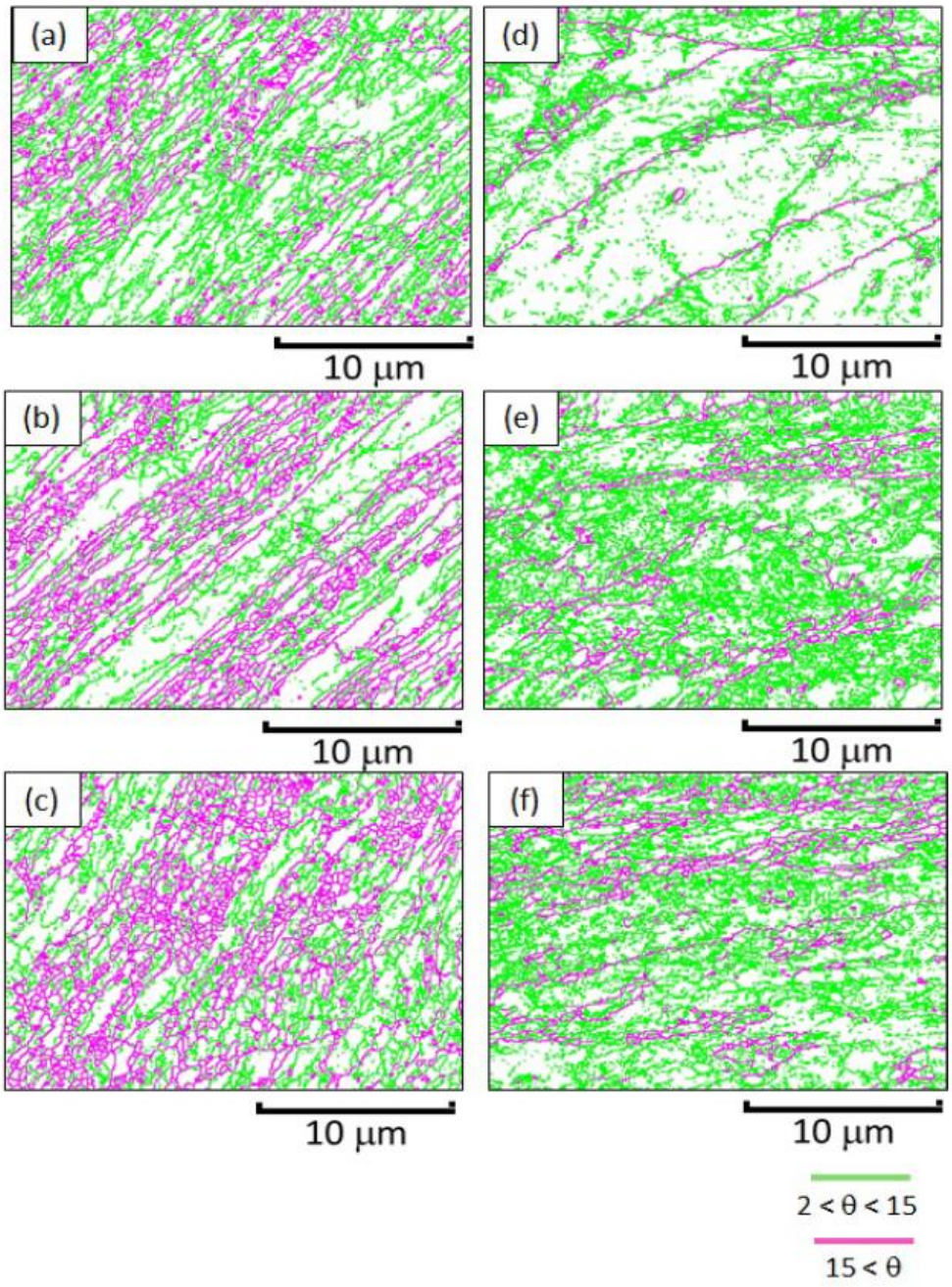

Figure 2.3. Misorientation map of Fe-Cr alloys after ECAP (a) one pass; (b) two passes; (c) three passes, and pure copper after ECAP (d) one pass; (e) two passes; and (f) three passes.

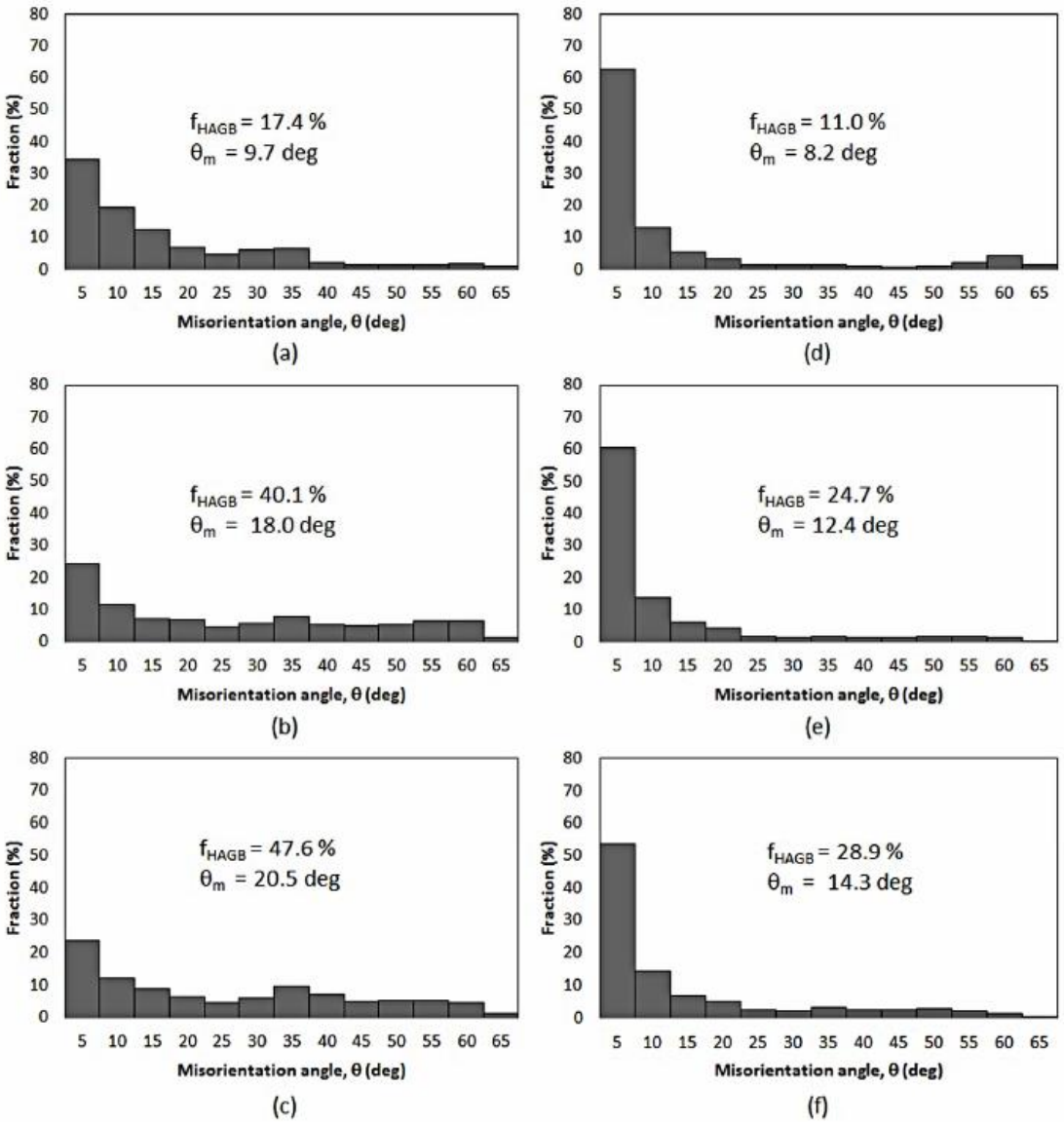

Figure 2.4. Distribution of misorientation of Fe-Cr alloys after ECAP (a) one pass; (b) two passes; (c) three passes, and pure copper after ECAP (d) one pass; (e) two passes; and (f) three passes.

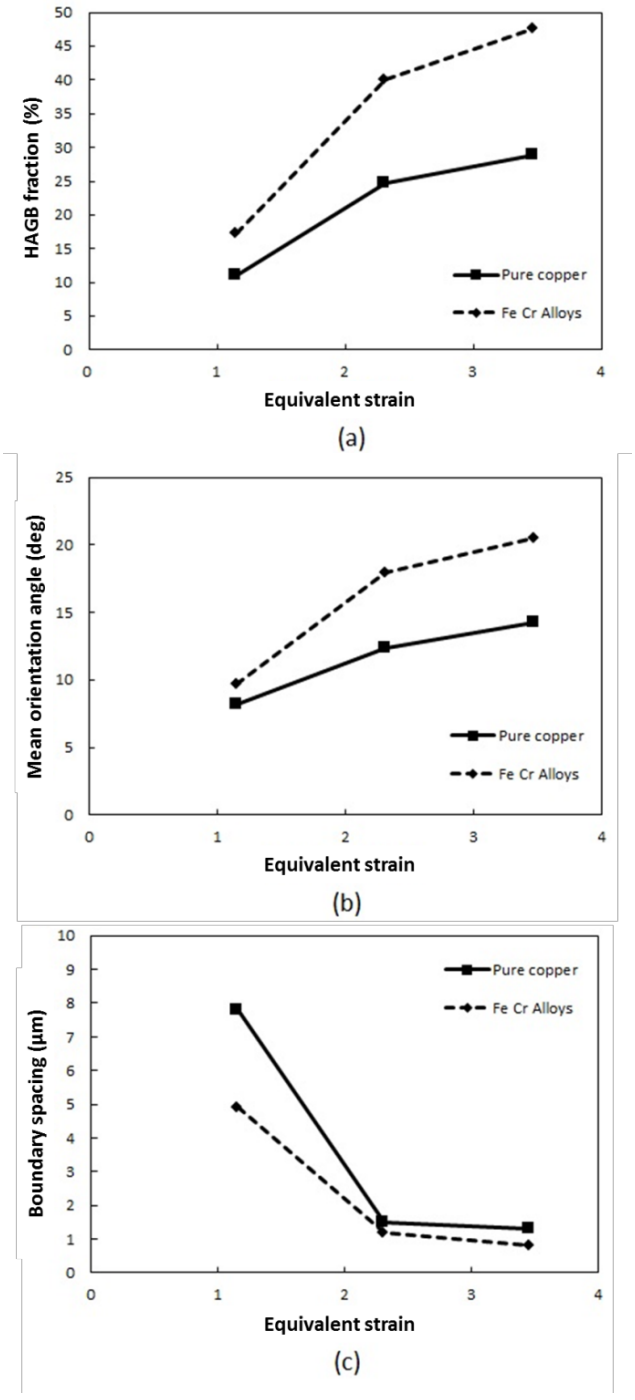

Figure 2.5. Microstructural parameters as a function of equivalent strain, (a) fraction of HAGB; (b) average misorientation angle; and (c) average boundary spacing.

Hardness change after ECAP is shown in **Figure 2.8**. Hardness after a single pass increase significantly in both the materials, but the rate of becoming harder is higher in Fe-Cr alloys. It is probably because of higher HAGB density with comparable dislocation density.

2.4. Discussion

Finer grain subdivision with higher fraction of HAGB in Fe-Cr alloys in the initial stage during one to three passes ECAP of the formation of UFG structures is now apparent as compared with pure copper. Since both materials have high purity, we can discuss the microstructural difference in terms of nature of crystal slip intrinsic to FCC/BCC structures. Since Peierls potential of screw dislocations is higher than that of edge dislocation in BCC crystals, the plastic deformation is rate-controlled by screw dislocations [41], and glided area swept by screw dislocation is higher than that by edge dislocation **[42]**. Thus, the nature of slip intrinsic to screw dislocation such as cross slip, or pensile glide become pronounced and influential on the macroscopic behavior of plastic deformation. According to the grain subdivision mechanism **[4]**, grains are subdivided by deformation-induced subboundaries in the initial state. These subboundaries are generally planar and extended, which is typical features of geometrically necessary boundaries (GNBs) **[4]**. In general, these boundaries are parallel to the trace of active slip planes, and are parallel to {110} trace in the present study **[43]**. The dislocations on various {110}, and possibly {211}, with the common slip direction form the dislocation boundaries. With increasing plastic strain, subboundaries increase their misorientation by absorbing lattice dislocations from the adjoining grains **[4,42]**. In BCC, high frictional stress of screw dislocations and resultant frequent cross slip promote dislocation multiplications and the formation of subgrain boundaries **[41]**. This is the reason why the finer subgrains were formed in earlier stage after one pressing.

In FCC, the dislocations tend to form pile-up rather than cross slip, then they are accumulated as plastic strain rather than absorbed in the grain boundaries and they are

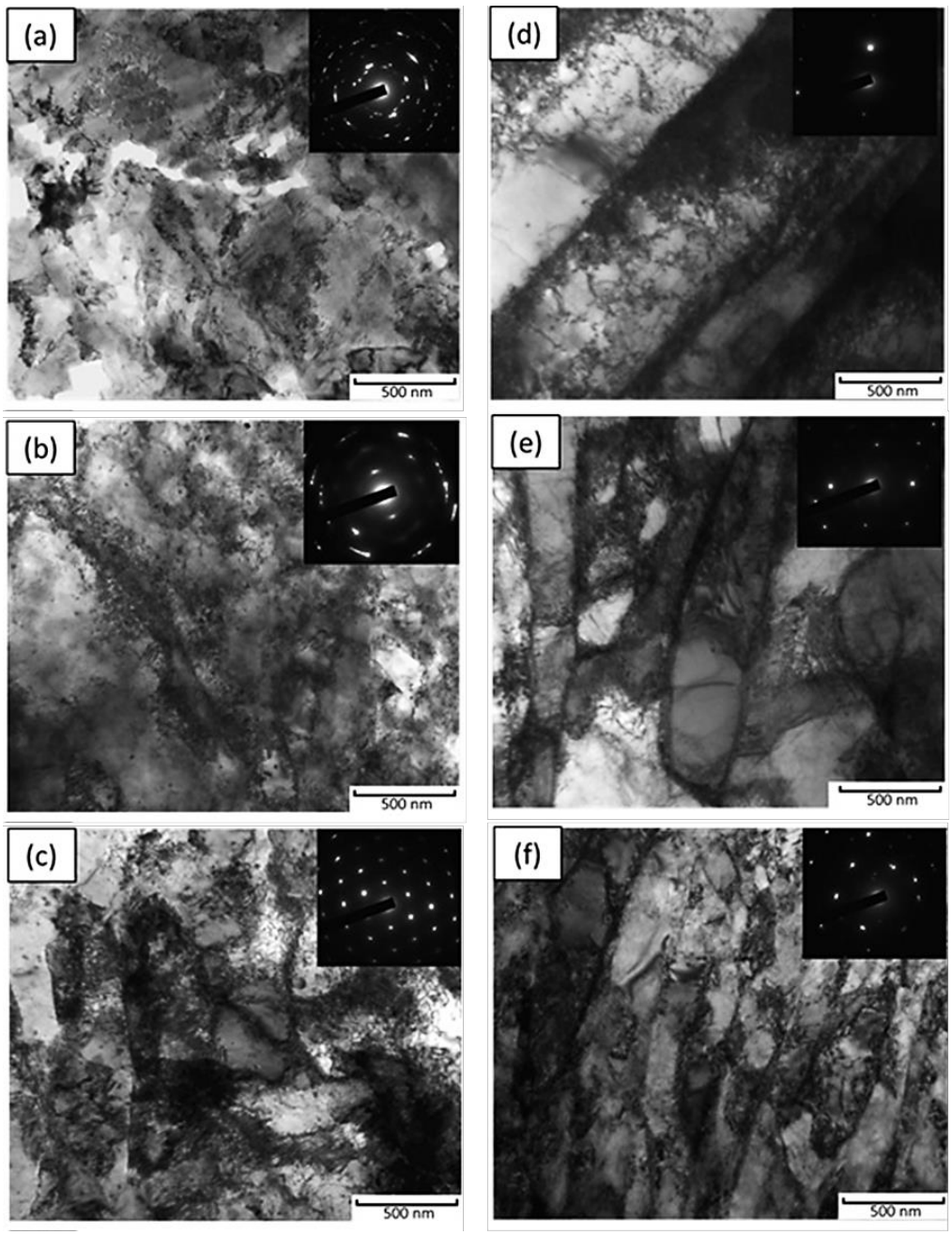

Figure 2.6. Microstructure using TEM of pure copper after ECAP (a) one pass; (b) two passes; (c) three passes, and Fe-Cr alloys after ECAP (d) one pass; (e) two passes; and (f) three passes.

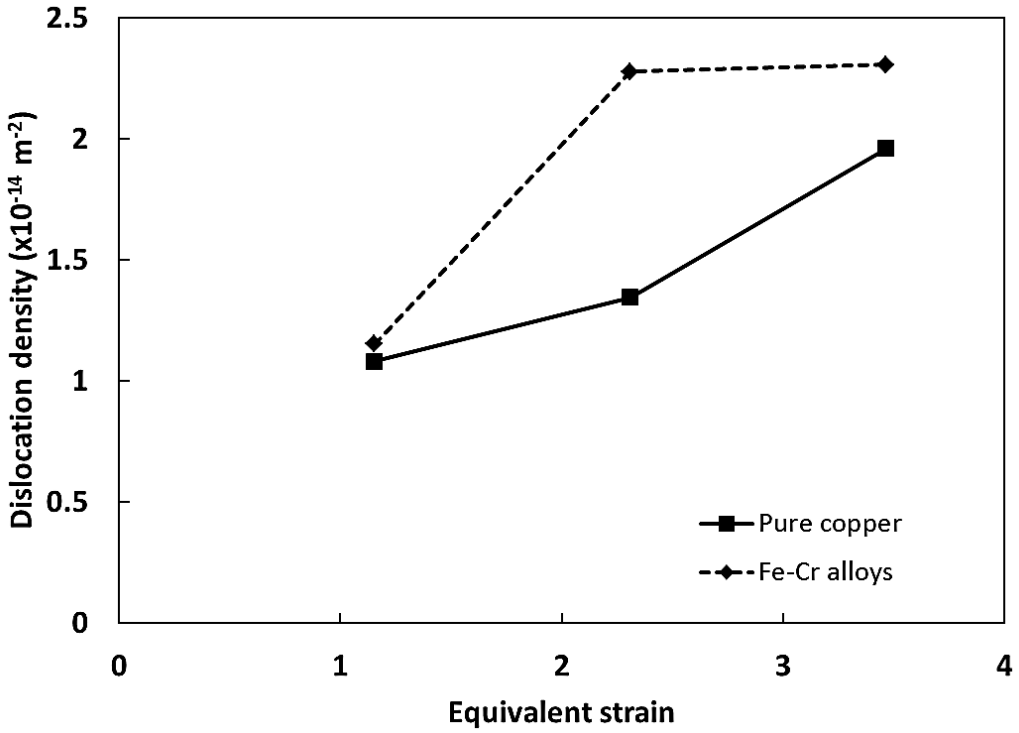

Figure 2.7. Dislocation density after ECAP for Fe-Cr alloys and pure copper.

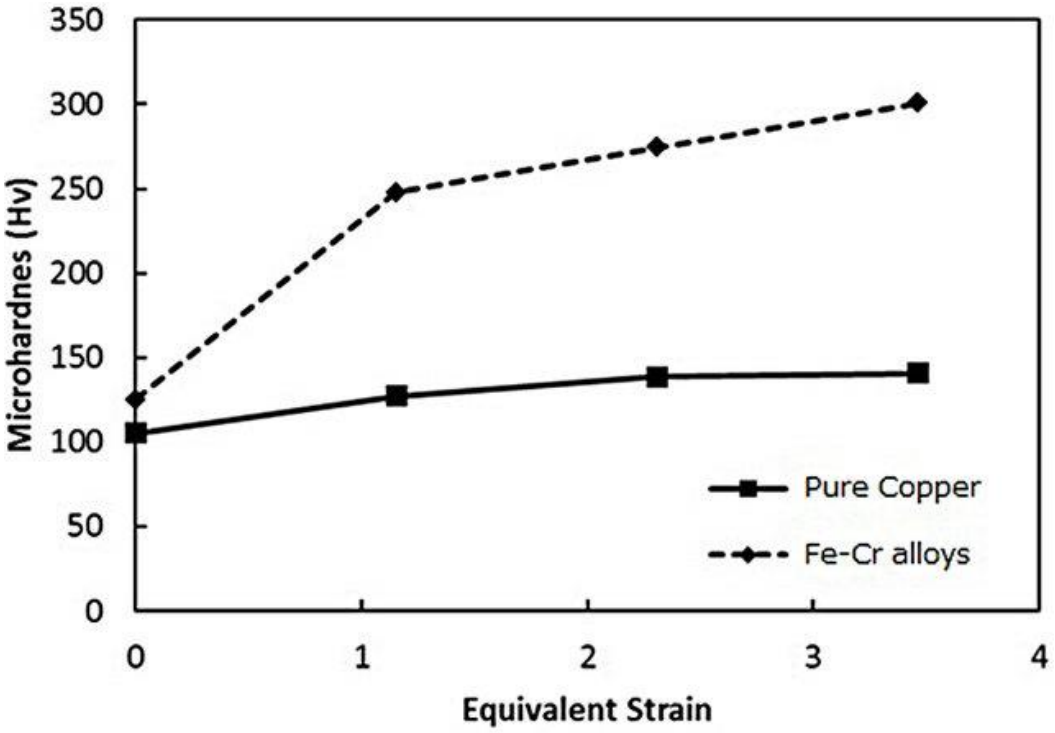

Figure 2.8. Microhardness after ECAP for Fe-Cr alloys and pure copper.

hard to be restructured as grain boundary dislocation. This may explain the reason why the fraction HAGB is lower after three passes in pure copper in spite of comparable low-angle sub grain/cell size with Fe-Cr alloy.

In this case, dislocation density should be higher in pure copper than Fe-Cr alloy at the same strain level. Dislocation density of Cu is lower than Fe-Cr alloys as shown in the **Figure 2.8**, and it seems inconsistent with the explanation mentioned above. Possible explanation of lower dislocation of pure copper is dynamic recrystallization, which may occur during ECAP. Inhomogeneous microstructures observed in **Figure 2.3** with large and small grains may be originated from the dynamic recrystallization. ARB Cu was carried out at ambient temperature with six cycles ($\varepsilon = 4.8$). The large fraction of LAGB in copper was attributed to partial re- crystallization during the ARB process due to high purity of the material and adiabatic heating. The possibility of dynamic recrystallization in copper during SPD is also reported in ARB **[33]**.

2.5. Conclusion

The microstructural evolution of Fe-Cr alloys and pure copper processed by ECAP for up to three passes was quantitatively analyzed by EBSD focusing on the initial stage of UFG formation. The deformation microstructure after one pass consist of deformation-induced extended subgrain boundaries typical to the geometrically necessary boundaries. The density of the boundaries is higher in Fe-Cr alloys than pure copper.

With increasing ECAP passes, the fraction of HAGB and mean misorientation angle increase, and HAGB spacing decreases. This phenomenon is noticeable in Fe-Cr steels, and can be explained in terms of slip behavior intrinsic to BCC structure.

Reference

[1] Valiev, R. Z., Islamgaliev, R. K., & Alexandrov, I. V. (2000). Bulk nanostructured materials from severe plastic deformation. Progress in materials science, 45(2), 103-189.

[2] Valiev, R. Z., & Langdon, T. G. (2006). Principles of equal-channel angular pressing as a processing tool for grain refinement. Progress in Materials Science, 51(7), 881-981.

[3] Nakashima, K., Horita, Z., Nemoto, M., & Langdon, T. G. (1998). Influence of channel angle on the development of ultrafine grains in equal-channel angular pressing. Acta materialia, 46(5), 1589-1599.

[4] Hansen, N., & Jensen, D. J. (1999). Development of microstructure in FCC metals during cold work. Philosophical Transactions of the Royal Society of London. Series A: Mathematical, Physical and Engineering Sciences, 357(1756), 1447-1469.

[5] Fukuda, Y., Oh-Ishi, K., Horita, Z., & Langdon, T. G. (2002). Processing of a low-carbon steel by equal-channel angular pressing. Acta Materialia, 50(6), 1359-1368.

[6] Huang, C. X., Yang, H. J., Wu, S. D., & Zhang, Z. F. (2008, August). Microstructural characterizations of Cu processed by ECAP from 4 to 24 passes. In Materials Science Forum (Vol. 584, pp. 333-337).

[7] Shin, D. H., & Park, K. T. (2005). Ultrafine grained steels processed by equal channel angular pressing. Materials Science and Engineering: A, 410, 299-302.

[8] Shin, D. H., Kim, I., Kim, J., & Park, K. T. (2001). Grain refinement mechanism during equal-channel angular pressing of a low-carbon steel. Acta Materialia, 49(7), 1285-1292.

[9] Shin, D. H., Kim, B. C., Park, K. T., & Choo, W. Y. (2000). Microstructural changes in equal channel angular pressed low carbon steel by static annealing. Acta Materialia, 48(12), 3245-3252.

[10] Huang, C. X., Gao, Y. L., Yang, G., Wu, S. D., Li, G. Y., & Li, S. X. (2006). Bulk nanocrystalline stainless steel fabricated by equal channel angular pressing. Journal of materials research, 21(07), 1687-1692.

[11] Kim, J., Kim, I., & Shin, D. H. (2001). Development of deformation structures in low carbon steel by equal channel angular pressing. Scripta materialia, 45(4), 421-426.

[12] Pang, J. C., Yang, M. X., Yang, G., Wu, S. D., Li, S. X., & Zhang, Z. F. (2012). Tensile and fatigue properties of ultrafine-grained low-carbon steel processed by equal channel angular pressing. Materials Science and Engineering: A, 553, 157-163.

[13] Shin, D. H., Kim, W. J., & Choo, W. Y. (1999). Grain refinement of a commercial 0.15% C steel by equal-channel angular pressing. Scripta materialia, 41(3), 259-262.

[14] Shin, D. H., Seo, C. W., Kim, J., Park, K. T., & Choo, W. Y. (2000). Microstructures and mechanical properties of equal-channel angular pressed low carbon steel. Scripta Materialia, 42(7), 695-699.

[15] Son, Y. I., Lee, Y. K., Park, K. T., Lee, C. S., & Shin, D. H. (2005). Ultrafine grained ferrite–martensite dual phase steels fabricated via equal channel angular pressing: microstructure and tensile properties. Acta materialia, 53(11), 3125-3134.

[16] Yang, G., Yang, M. X., Liu, Z. D., Wang, C., & Huang, C. X. (2010, February). Investigation on Three-Dimensional Microstructures and Tensile Properties of Pure Iron during Equal-Channel Angular Pressing. In Materials Science Forum (Vol. 667, pp. 791-796).

[17] Gibbs, M. A., Hartwig, K. T., Cornwell, L. R., Goforth, R. E., & Payzant, E. A. (1998). Texture formation in bulk iron processed by simple shear. Scripta materialia, 39(12), 1699-1704.

[18] Suś-Ryszkowska, M., Wejrzanowski, T., Pakieła, Z., & Kurzydłowski, K. J. (2004). Microstructure of ECAP severely deformed iron and its mechanical properties. Materials Science and Engineering: A, 369(1), 151-156.

[19] Han, B. Q., Mohamed, F. A., & Lavernia, E. J. (2003). Mechanical properties of iron processed by severe plastic deformation. Metallurgical and Materials Transactions A, 34(1), 71-83.

[20] Han, B. Q., Lavernia, E. J., & Mohamed, F. A. (2004). Dislocation structure and

deformation in iron processed by equal-channel-angular pressing. Metallurgical and Materials Transactions A, 35(4), 1343-1350.

[21] Gazder, A. A., Cao, W., Davies, C. H., & Pereloma, E. V. (2008). An EBSD investigation of interstitial-free steel subjected to equal channel angular extrusion. Materials Science and Engineering: A, 497(1), 341-352.

[22] Gazder, A. A., Torre, F. D., Gu, C. F., Davies, C. H., & Pereloma, E. V. (2006). Microstructure and texture evolution of bcc and fcc metals subjected to equal channel angular extrusion. Materials Science and Engineering: A, 415(1), 126-139.

[23] Hazra, S. S., Pereloma, E. V., & Gazder, A. A. (2011). Microstructure and mechanical properties after annealing of equal-channel angular pressed interstitial-free steel. Acta Materialia, 59(10), 4015-4029.

[24] Li, S., Gazder, A. A., Beyerlein, I. J., Davies, C. H., & Pereloma, E. V. (2007). Microstructure and texture evolution during equal channel angular extrusion of interstitial-free steel: Effects of die angle and processing route. Acta materialia, 55(3), 1017-1032.

[25] Mathaudhu, S. N., & Ted Hartwig, K. (2006). Grain refinement and recrystallization of heavily worked tantalum. Materials Science and Engineering: A, 426(1), 128-142.

[26] Máthis, K., Krajňák, T., Kužel, R., & Gubicza, J. (2011). Structure and mechanical behaviour of interstitial-free steel processed by equal-channel angular pressing. Journal of Alloys and Compounds, 509(8), 3522-3525.

[27] Saray, O., Purcek, G., & Karaman, I. (2010). Principles of equal-channel angular sheet extrusion (ECASE): application to IF-steel sheets. Rev. Adv. Mater. Sci, 25, 42-51.

[28] Saray, O., Purcek, G., Karaman, I., Neindorf, T., & Maier, H. J. (2011). Equal-channel angular sheet extrusion of interstitial-free (IF) steel: Microstructural evolution and mechanical properties. Materials Science and Engineering: A, 528(21), 6573-6583.

[29] Wei, Q., Jiao, T., Mathaudhu, S. N., Ma, E., Hartwig, K. T., & Ramesh, K. T. (2003). Microstructure and mechanical properties of tantalum after equal channel

angular extrusion (ECAE). Materials Science and Engineering: A, 358(1), 266-272.

[30] Wei, Q., Kecskes, L., Jiao, T., Hartwig, K. T., Ramesh, K. T., & Ma, E. (2004). Adiabatic shear banding in ultrafine-grained Fe processed by severe plastic deformation. Acta materialia, 52(7), 1859-1869.

[31] Yang, G., Yang, M. X., Liu, Z. D., & Wang, C. (2011). Three-Dimensional Microstructures and Tensile Properties of Pure Iron During Equal Channel Angular Pressing. Journal of Iron and Steel Research, International, 18(12), 40-44.

[32] Sandim, H. R. Z., Bernardi, H. H., Verlinden, B., & Raabe, D. (2007). Equal channel angular extrusion of niobium single crystals. Materials Science and Engineering: A, 467(1), 44-52.

[33] Li, B. L., Tsuji, N., & Kamikawa, N. (2006). Microstructure homogeneity in various metallic materials heavily deformed by accumulative roll-bonding. Materials Science and Engineering: A, 423(1), 331-342.

[34] Tsuji, N., Ito, Y., Saito, Y., & Minamino, Y. (2002). Strength and ductility of ultrafine grained aluminum and iron produced by ARB and annealing. Scripta Materialia, 47(12), 893-899.

[35] Wetscher, F., & Pippan, R. (2009). Hardening and softening behavior by cyclic high-pressure torsion. Metallurgical and Materials Transactions A, 40(13), 3258-3263.

[36] Wetscher, F., Vorhauer, A., & Pippan, R. (2005). Strain hardening during high pressure torsion deformation. Materials Science and Engineering: A, 410, 213-216.

[37] Huang, X., Kamikawa, N., & Hansen, N. (2008). Increasing the ductility of nanostructured Al and Fe by deformation. Materials Science and Engineering: A, 493(1), 184-189.

[38] Huang, X., Kamikawa, N., Tsuji, N., & Hansen, N. (2008). Nanostructured aluminum and IF steel produced by rolling-a comparative study. ISIJ international, 48(8), 1080-1087.

[39] Iwahashi, Y., Wang, J., Horita, Z., Nemoto, M., & Langdon, T. G. (1996). Principle of equal-channel angular pressing for the processing of ultra-fine grained

materials. Scripta Materialia, 35(2), 143-146.

[40] Ham, R. K. (1961). The determination of dislocation densities in thin films. Philosophical Magazine, 6(69), 1183-1184.

[41] Argon, A. S., & Maloof, S. R. (1966). Plastic deformation of tungsten single crystals at low temperatures. Acta metallurgica, 14(11), 1449-1462.

[42] Mughrabi, H., Herz, K., & Stark, X. (1976). The effect of strain-rate on the cyclic deformation properties of α-iron single crystals. Acta Metallurgica, 24(7), 659-668.

[43] Wert, J. A., Huang, X., Winther, G., Pantleon, W., & Poulsen, H. F. (2007). Revealing deformation microstructures. Materials Today, 10(9), 24-32.

Chapter 3. Effect of deformation route of ECAP on development of UFG structure and mechanical properties of low C, N Fe-20%Cr Steel

3.1. Introduction

Low carbon ferritic stainless steel is widely used for corrosive environments as it satisfies the material requirements for high resistance to SCC, intergranular corrosion, as well as high ductility and formability **[1-2]**. However, this class of material is of low-strength and this restricts its application to the limited field; hence, grain refinement is often regarded as a useful method for improving its mechanical properties. The method of ECAP is one of the SPD techniques that produces UFG materials.

Several ECAP parameters that have an influence on microstructural development and mechanical properties are the die angle, the pressing speed, the die temperature, and the deformation route. The four deformation routes of ECAP have mainly been proposed as follows. In Route A, the sample is pressed without rotation. In Route B_A, the sample is rotated by 90 degrees in an alternate direction between consecutive passes. In Route B_C, the sample is rotated 90 degrees counterclockwise between each pass. In Route C, the specimen is rotated by 180 degrees between passes **[3]**. There are many studies concerning the effective deformation routes for grain refinement in FCC structure metals such as pure aluminum **[2]**, nickel **[5]**, copper **[6]**, and titanium **[7]**; however, there are few studies on BCC.

Previous studies have attempted to explain the effect of deformation routes on microstructure and mechanical properties, especially in FCC materials **[8-10]**. They have found that Route Bc is the most efficient for producing isotropic microstructures, due to the crossing of the shear planes in every pass **[8-10]**. However, the degree of anisotropy on microstructural development has not been carefully evaluated so far, especially in BCC metals **[8, 11-13]**. Therefore, the effect of deformation routes on the microstructure in the ECAP process as well as the mechanical and electrochemical properties will be further discussed.

3.2. Experimental procedure

The material used in this experiment had a chemical composition of low carbon

nitrogen (CN) Fe-20%Cr alloy with Cr 19.97, C 0.0020, N 0.0015 and Fe balance (in mass percent). This material was machined with dimensions of 8 mm × 8 mm × 120 mm for ECAP pressing. ECAP was carried out using a split die with two channels intersecting at an inner angle of 90° and an outer angle of 0° at 423 K. Parts of ECAP die and three dimensional appearance of ECAP die are shown in **Figure 3.1.a and b**. The samples were lubricated with high temperature fluorine lubricating grease and pressed from one pass until eight passes via routes A, Bc and C.

ECAP experiment was carried out using an Autograph Shimadzu 500 kN testing machine, as shown in **Figure 3.1.c.** The plunger of ECAP was fixed at the testing machine, which can move up and down precisely to ECAP die. A heating equipment was attached at outer of ECAP die which the temperature can be controlled up to 773K.

A TEM (JEM 2100F) was used to examine the microstructures. Thin foils for TEM were polished using abrasive papers to about 100 μm thick and then thinned by a twin-jet polishing Tenupol 5 facility using a solution of 40% acetic acid, 30% phosphoric acid, 20% nitric acid and 10% distilled water.

Mechanical and electrochemical properties were measured by micro hardness and pitting corrosion. The micro hardness experiments were performed on a Vickers hardness testing machine at room temperature. Corrosion testing was carried out at ambient temperature in a flat polarization cell, using platinum counter electrodes and Ag/AgCl reference electrodes to measure the corrosion current and corrosion potential. The pitting corrosion characteristic was obtained in neutral solutions 1 M NaCl.

3.3 Result

3.3.1. Microstructure

A TEM micrograph including a selected area diffraction pattern (SADP) was observed on one pass as shown in **Figure 3.2**. In the ECAP process, after the first pass, deformation bands of the width of 500 nm can be observed clearly on the Y-plane. Therefore, SADP appeared as a network with little dispersion. It indicated small misorientations on the deformation bands. In addition, after one pass, the elongated sub-grain structure was displayed through a TEM. Consequently, the grains were revealed as

(a)

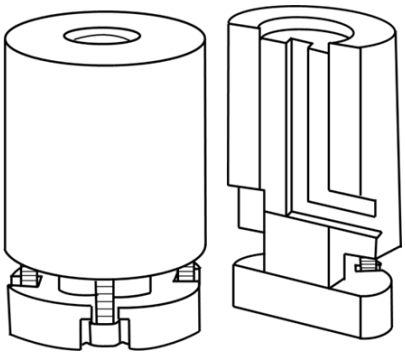

(b)

Figure 3.1. (a) parts of ECAP die, (b) 3D view of ECAP die arrangement **(c)** ECAP system.

being finely subdivided after one pass, though the initial structure had larger grain sizes. Several boundaries could then be observed as LAGB misorientations.

The microstructure of material processed by ECAP from two to eight passes via routes A, Bc, and C was observed by TEM on the Y-plane as shown in **Figure 3.3**. After two passes of ECAP, the microstructure became finer and consisted of elongated grains with rather planar boundaries. Larger grains were also observed within UFG structures. Since the SADP exhibited a rather regular pattern, this microstructure consisted of dislocation cell structures with a similar orientation. After four passes, more homogenous equiaxed UFG structures were observed with sharper boundaries. Due to grain refinement, the SADP of eight passes of the ECAPed sample displayed a ring diffraction pattern.

The increase in the number of ECAP passes resulted in a decreased boundary spacing on the Y-plane as shown in **Figure 3.4**. The boundary spacing of the material processed by routes A and Bc decreased more significantly than those processed by Route C, while the boundary spacing of Route C saturated after four passes. These results corresponded with the mechanical properties. As a result, boundary spacing achieved 150 nm on materials processed by Route A.

Grain boundary misorientation can be observed in three orthogonal planes by EBSD, as shown in **Figure 3.5**. After one and two passes of ECAP, microstructure appeared mostly as elongated grains with LAGB. These grains were limited in Y and X planes. Grain and sub grain with LAGB were mostly oriented into same direction with shear direction. These orientations can be seen after two passes especially at material processed by route Bc. After four passes of ECAP, HAGB appearance can be seen clearly along shear direction at Y-plane. It also appeared in others plane. At these planes, fragmented grain was surround by HAGB. After eight passes by material processed by route Bc, microstructure appeared more equiaxed than others route especially at Y-plane. However, after eight passes, microstructure of route Bc showed more HAGB than routes A and C. Structure of route A and C anisotropic than route Bc.

Material processed by route Bc showed more fragmented structure than others routes. It also corresponded with the number of passes. After two passes, all routes of

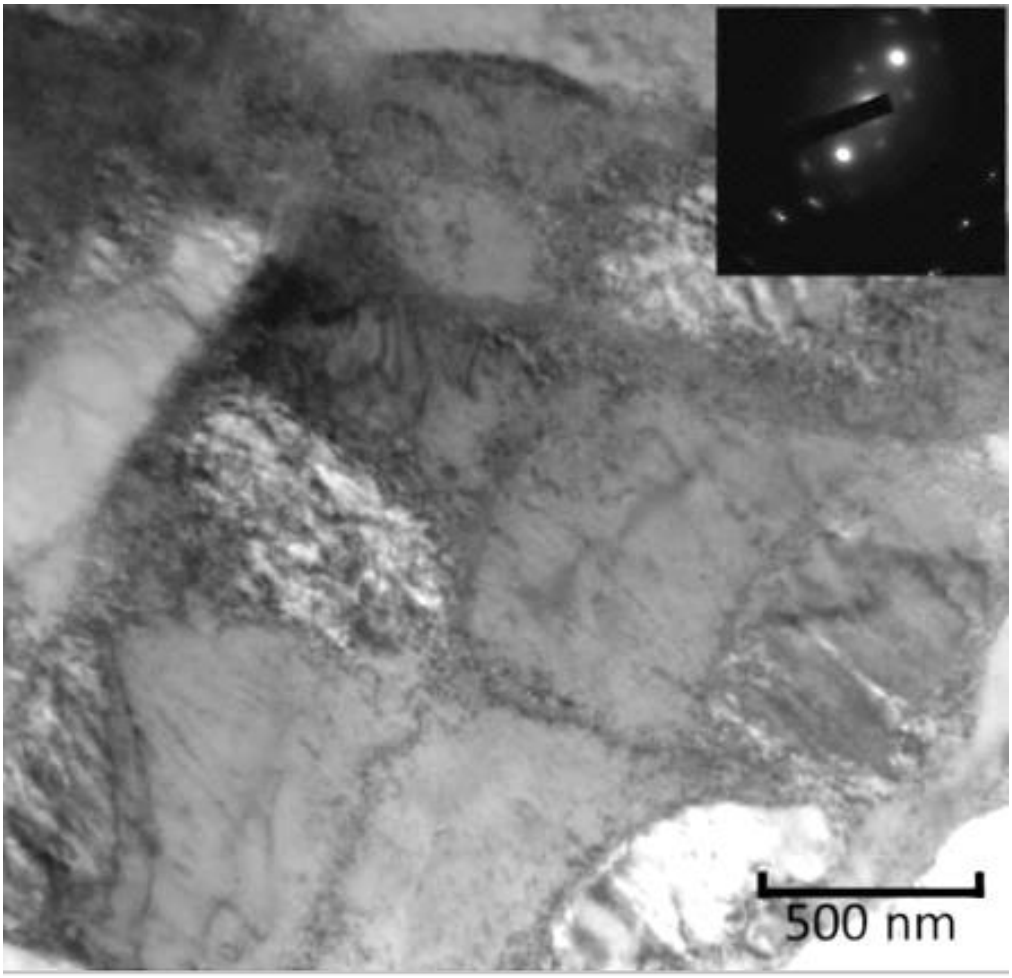

Figure 3.2. TEM micrograph of one pass ECAP (Y-plane).

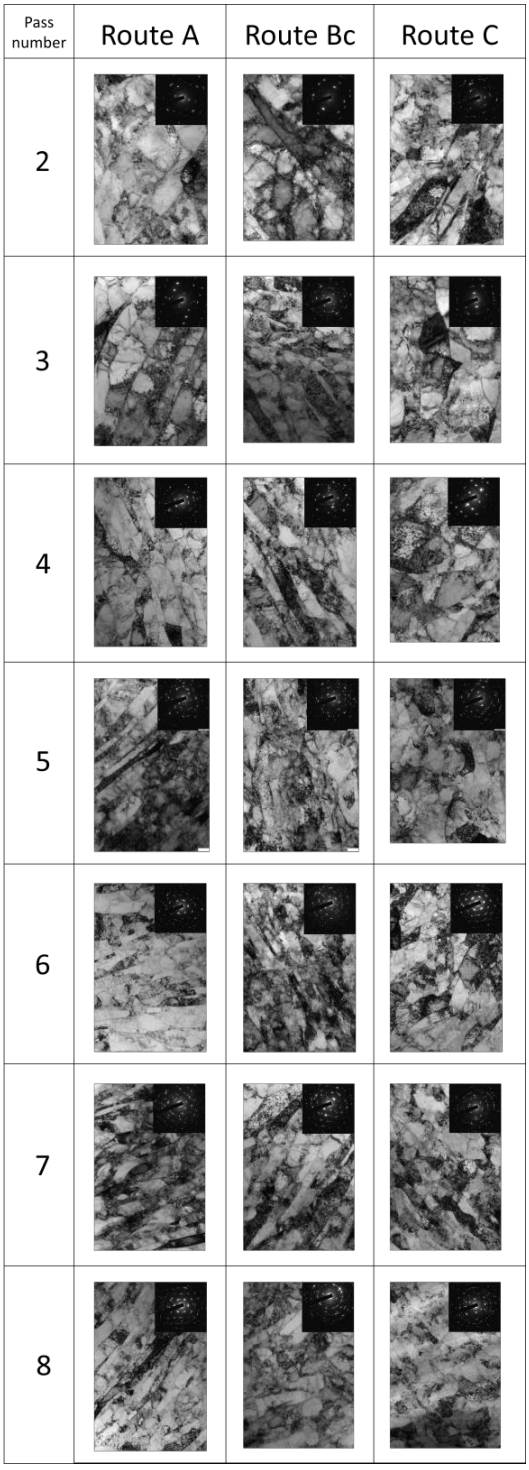

Figure 3.3. TEM micrograph after ECAP from two passes until eight passes by route A, Bc and C (Y-plane).

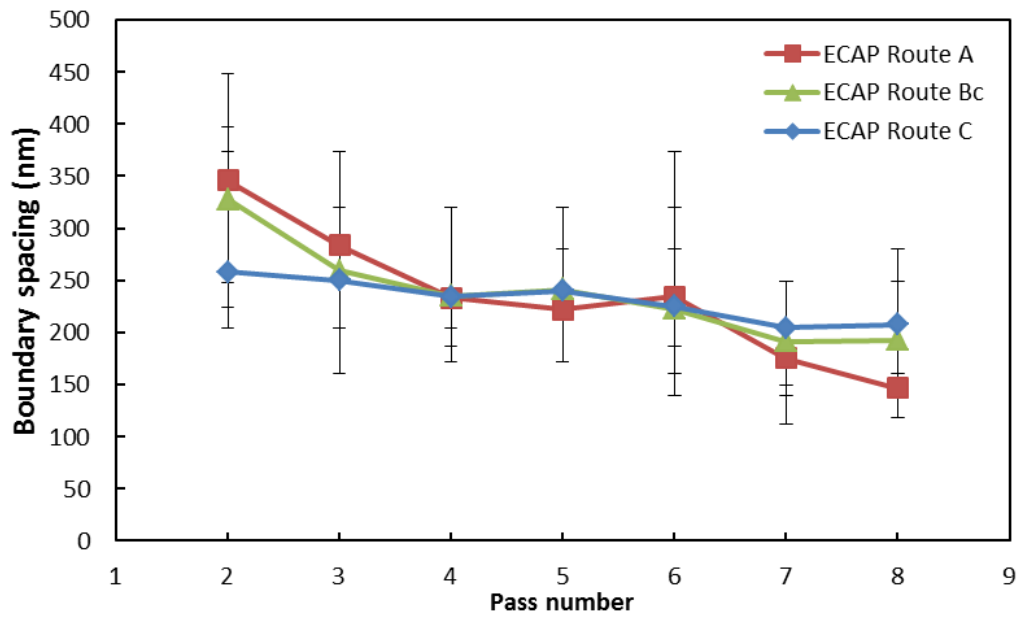

Figure 3.4. Boundary spacing of ECAP passes number on different deformation routes (Y-plane)

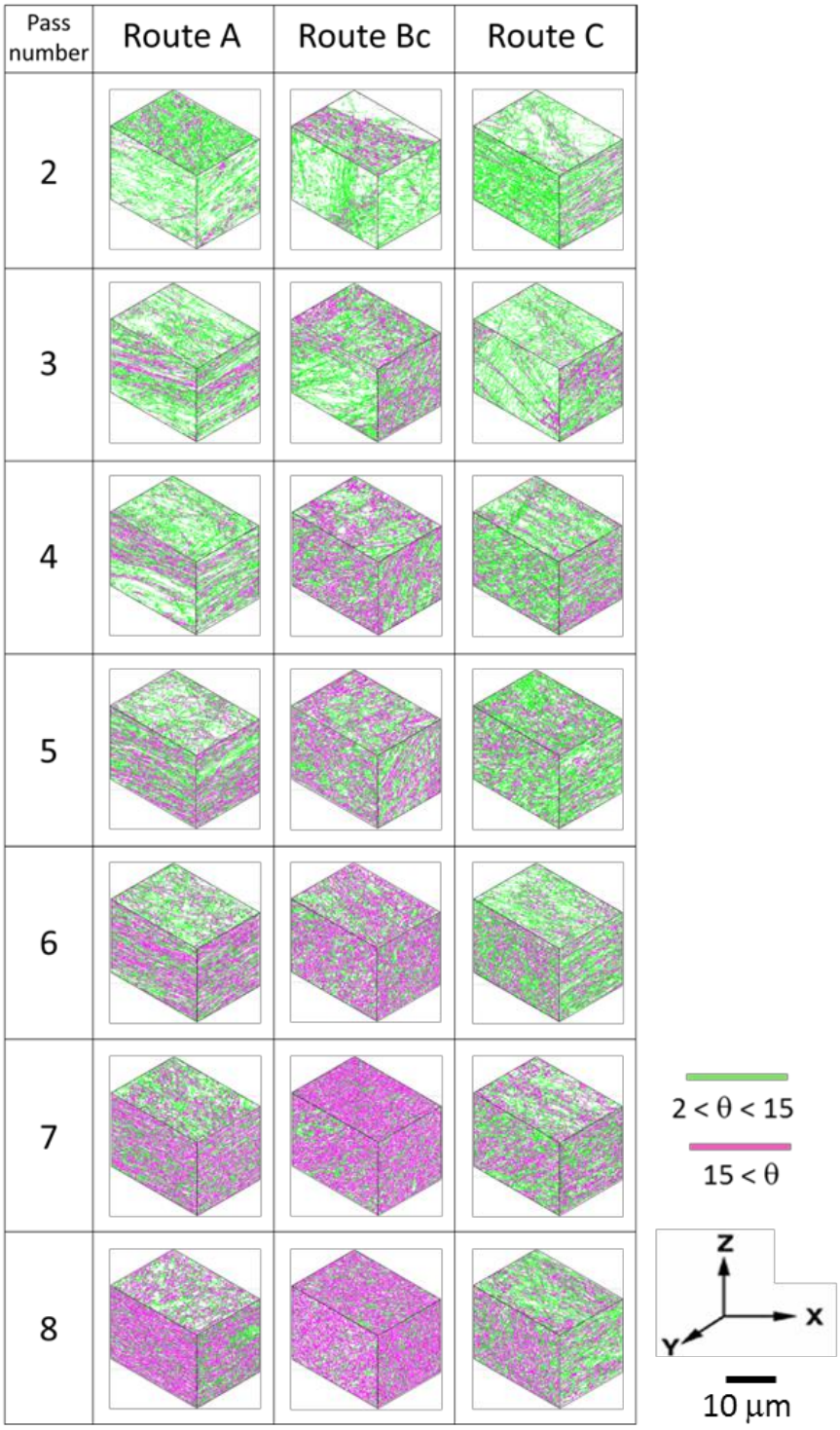

Figure 3.5. 3D misorientation map after ECAP on different plane and passes number.

ECAP showed significant improvement on HAGB fraction and mean grain boundary misorientation angle. Microstructure appearance at Z-plane of ECAPed sample has not changed with increasing passes number in routes A and C. After five passes of ECAP, X and Y-planes showed homogeneous structure especially in LAGB and HAGB distribution. Therefore, with increasing passes, microstructure resulted in homogeneous structure by increasing density of HAGB. Y-plane of ECAPed sample exhibited mostly HAGB with corresponding to passes number.

HAGB fraction and mean grain boundary misorientation can be observed in three orthogonal planes, as shown in **Figure 3.6**. This microstructural parameter increased with increase in passes number of ECAP. HAGB fraction of routes A and Bc increased quite similar with about 70 percent difference between one and eight passes. But material processed by route C showed 50 percent difference. However, Y-plane of route Bc showed significantly increasing after four passes. These results appeared in three orthogonal planes. Average HAGB fraction increment was 10 percent every passes until eight passes for route A and Bc. The different of HAGB fraction on three orthogonal planes is high in routes A and C. However, material processed by route Bc exhibited equal HAGB fraction in three orthogonal planes. The difference of HAGB fraction in three routes could be explained by in-homogeneous microstructure by ECAP.

Pole figures obtained from EBSD, is shown in **Figure 3.7**. Texture analysis by the pole figures demonstrated a complex shear after ECAP process. The evolution of texture development can be seen from two until four passes via routes A, Bc and C, as shown in **Figure 3.7**.

From **Figure 3.7**, schematic diagram showing simplified spatial configuration of HAGB is constructed and shown in **Figure 3.8**. In route A and C, the preferred texture is modeled as a collection of orientations rotated around the Y-axes bounded by HAGB with tilt character. However, there is a difference; there is one and two sets of HAGB on Y-plane eight four passes in routes A and C, respectively.

3.3.2 Mechanical properties

The micro hardness in the pre extrusion area before shear zone shows a range

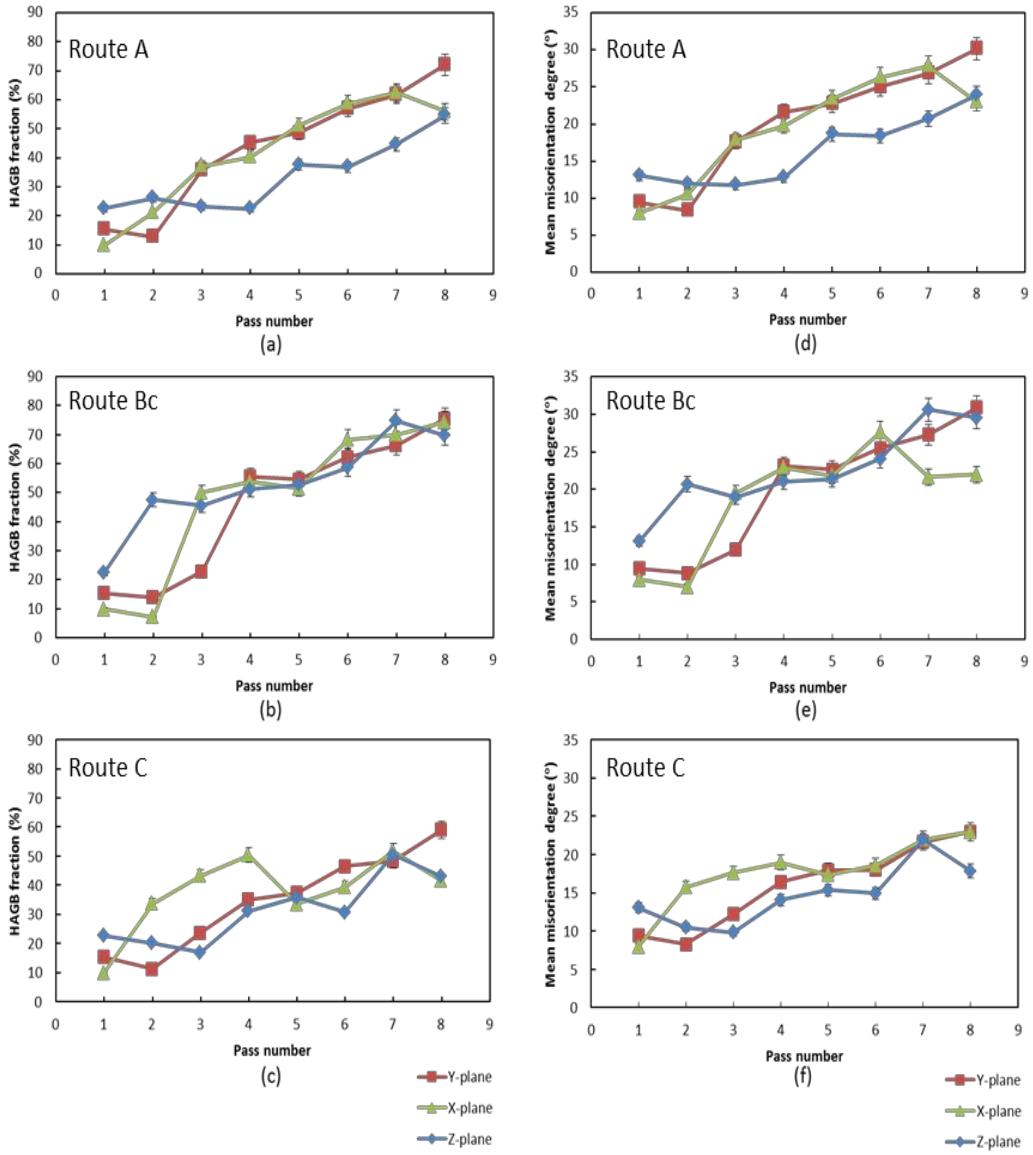

Figure 3.6. HAGB fraction and mean misorientation angle of ECAP processed with respect three orthogonal plane.

	Y-plane			X-plane			Z-plane		
Pass number	Route A	Route Bc	Route C	Route A	Route Bc	Route C	Route A	Route Bc	Route C
2	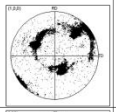	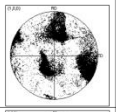	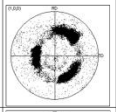	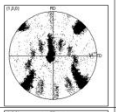	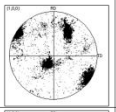	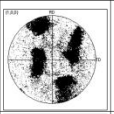	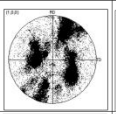	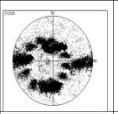	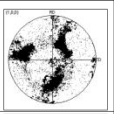
4	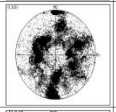	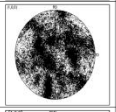	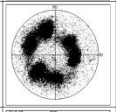	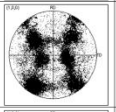	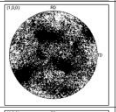	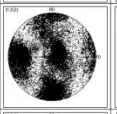	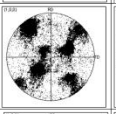	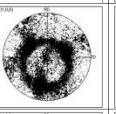	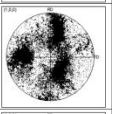
6	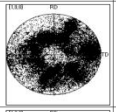	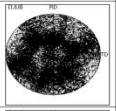	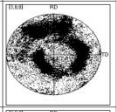	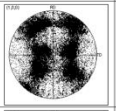	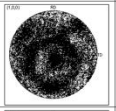	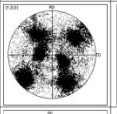	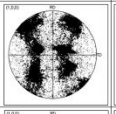	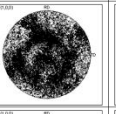	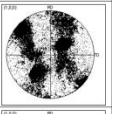
8	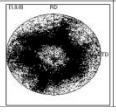	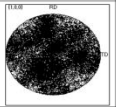	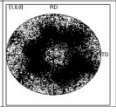	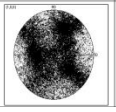	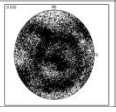	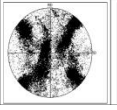	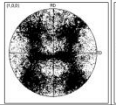	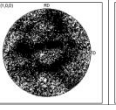	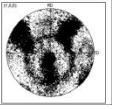

Figure 3.7. {100}-Pole figure of ECAPed sample on different plane, deformation route and passes number.

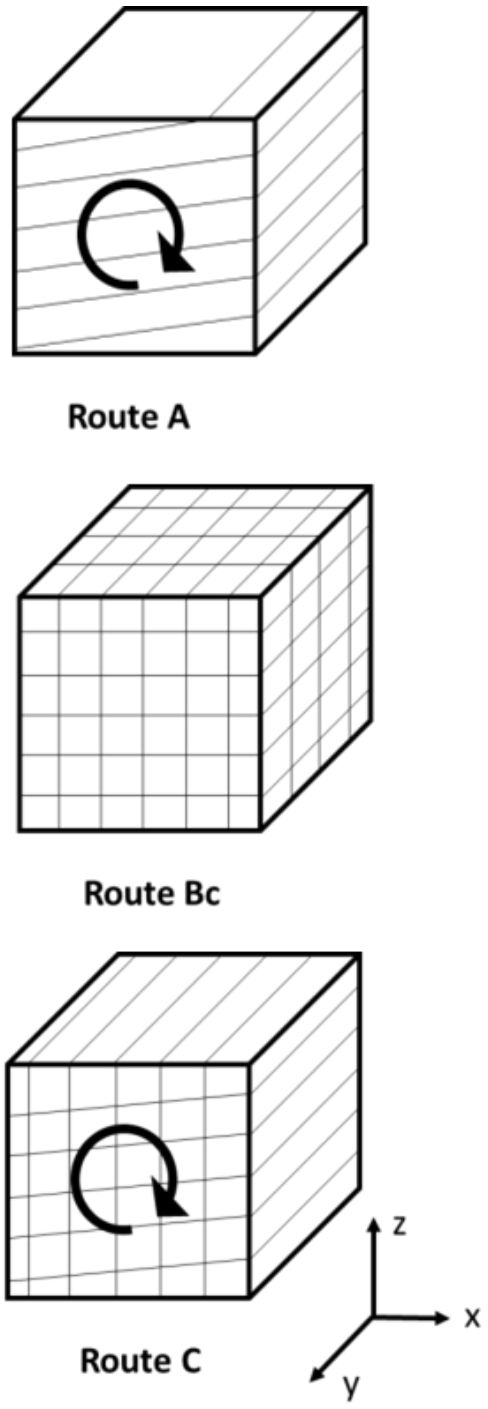

Figure 3.8. Schematic diagram showing spatial configuration of HAGB in three orthogonal planes in routes A, Bc and C

of hardness from 160-260 Hv. After shear zone, the micro hardness increased significantly due to a very large plastic deformation to the corner of specimen, as shown in **Figure 3.9**.

Micro hardness from one to eight passes of ECAP was measured in three orthogonal planes, as shown in **Figure 3.10**. Hardness testing was carried out on the transverse plane (Y-plane), rolling plane (X-plane) and normal plane (Z-plane). Micro hardness at three routes was comparable. This testing was carried out more than ten points every sample and experimental error was around five percent of the average value. The hardness of as-received material was 125 Hv. A significant increment of micro hardness can be observed with the increasing passes number. After eight passes, material processed routes A and Bc increased three times higher than route C. Therefore, material processed by route Bc exhibited comparable micro hardness value in three orthogonal planes than routes A and C. On the other hand, micro hardness of route C saturated after four passes.

3.3.3. Electrochemical properties

Electrochemical properties can be defined by pitting corrosion resistance and tafel extrapolation method. Tafel interpolation determined the corrosion potential for characterizing the material surface in corrosion atmosphere and the corrosion current density for characterizing the corrosion speed. This testing were determined using potentiodynamic tests. The corrosion behavior of ECAPed specimens in the 1 M NaCl is shown in **Figure 3.11**. Pitting potential decreased after one pass, and then increase after two passes, as shown in **Figure 3.12**. SEM micrograph of pitting corrosion testing can be seen in **Figure 3.13**. Tafel extrapolation method characteristics were evaluated from the potentiodynamic curves to determine the corrosion potential and the corrosion current density. **Figure 3.14** shows typical potentiodynamic polarization curves for the several number ECAP passes and deformation route specimens measured in 1M NaCl solutions. Four passes of route C shows higher stabilization than route A and Bc, it is because this route perform higher hardness than other routes. With increasing number of ECAP, the curves are shifted to higher values of the current density. The corrosion potential *Ecorr* ECAPed specimens increase while the corrosion current density *icorr*

decreases

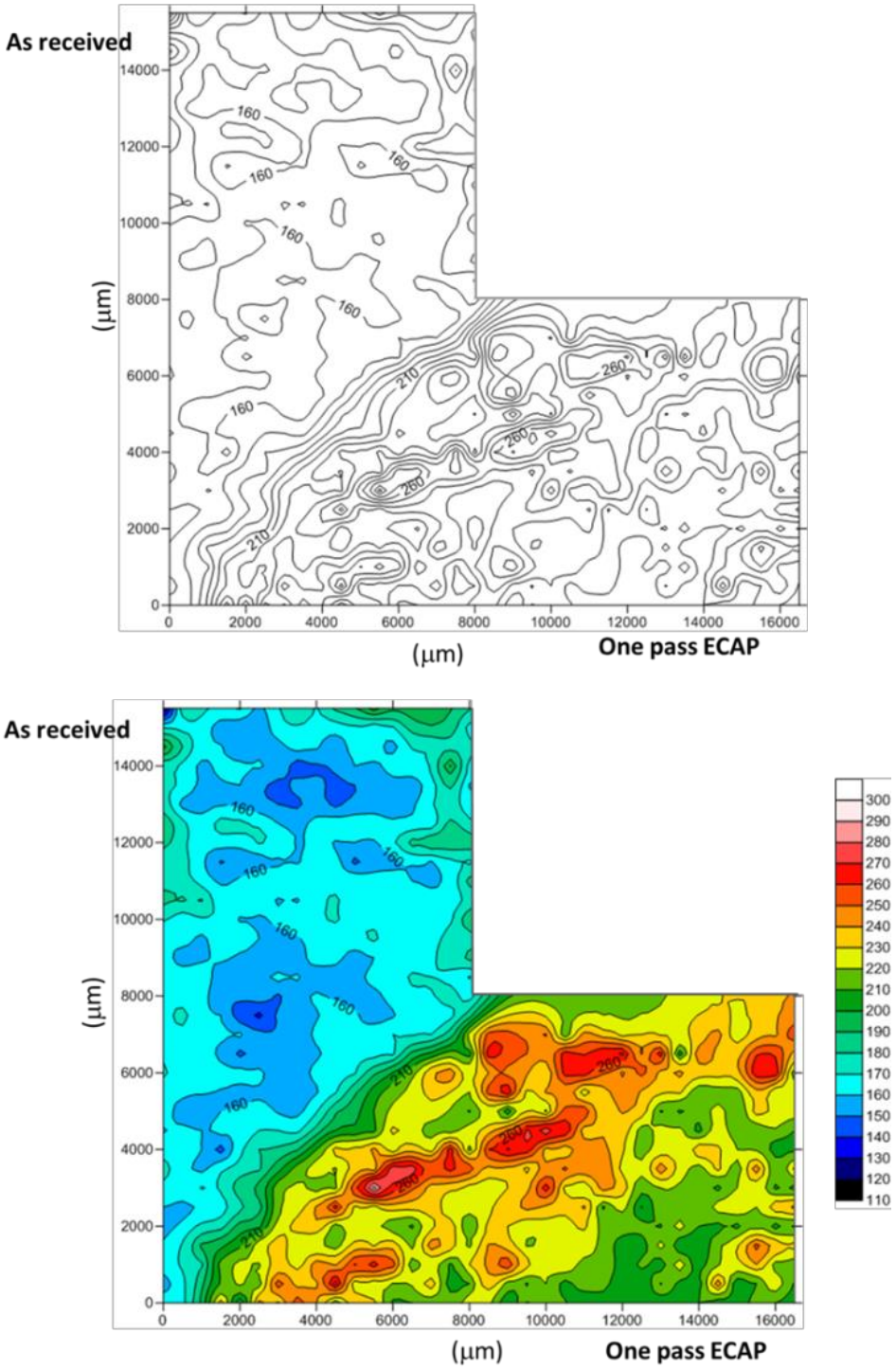

Figure 3.9. Hardness distribution in first pass ECAP of low C, N Fe-20%Cr

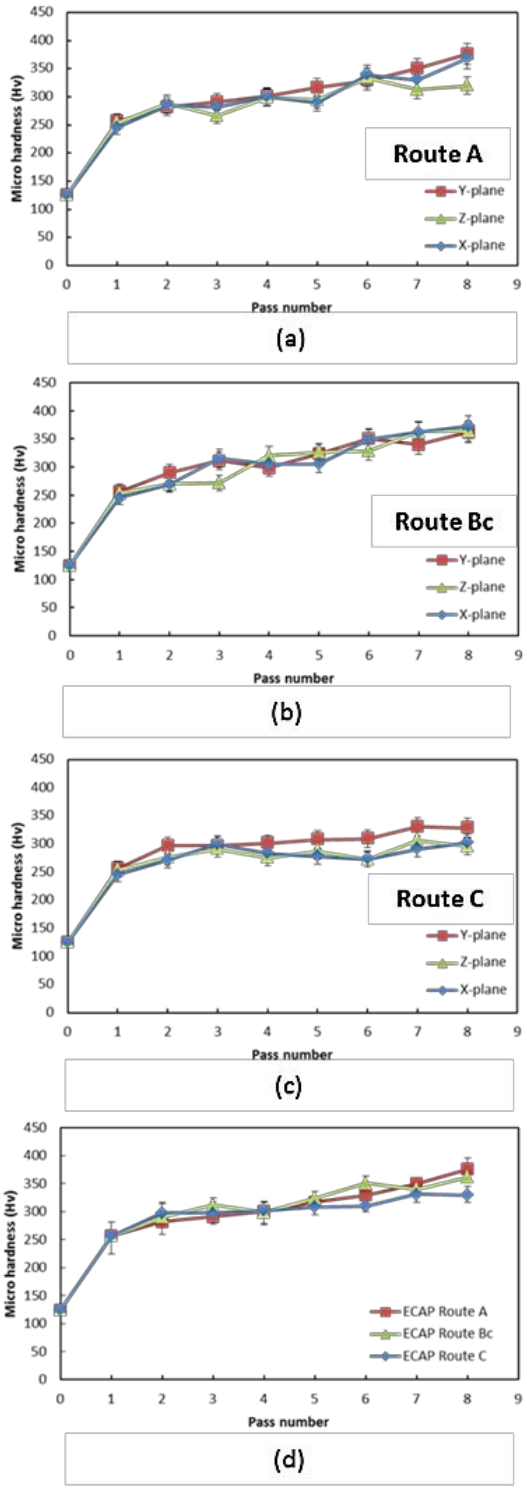

Figure 3.10. Microhardness after ECAP with different plane and deformation route.

with increasing number ECAP passes.

3.4. Discussion

The microstructural evolution of extremely low CN Fe-20%Cr alloy as low carbon steel can be examined in terms of crystal slips that are intrinsic to BCC structures. The Peierls barrier of screw dislocations is higher than that of edge dislocation in BCC crystals; thus, slip by screw character is more predominant than by edge dislocation. When plastic straining increases by the formation and extension of dislocation loops, edge dislocations characters with high mobility slip faster than screw dislocation characters with lower mobility, resulting in extended lines of screw dislocations. Therefore, the nature of the slip, which is intrinsic to screw dislocation, has an influence on the macroscopic behavior of plastic deformation. The micro hardness exhibited an increase by ECAP as was reported before in many metals and alloys. However, the degree of hardening of the ECAPed sample was different among three orthogonal planes in different routes. This anisotropic strain hardening seems to be a characteristic of BCC metals. The isotropic hardening in the material processed by route Bc was reflected in the isotropic configuration of HAGB. Namely, this isotropic hardening tendency was observed due to high dislocation density in route Bc. This hardening was suggested that the 45°rotation of billets in route Bc, which resulted in cross hardening. Since screw dislocations are predominant in BCC metals, positive and negative screw dislocation pairs tend to meet by cross-slip and disappear in both the forward-forward and forward-reverse shear in successive passes.

Electrochemical properties can be determined by pitting corrosion testing. The pitting potential increased as the number of ECAP passes increased. An increase in the pitting potential can be explained by a shift in the boundary between imperfect passivity and the pitting region **[14]**. It indicated that the protective passive layer in the ECAPed sample is more stable than the as-received sample **[14]**. In the percolation model for passivation in stainless steels, high Cr concentration on the surface is required to for passivation **[15,16]**. Preferential dissolution of less noble Fe elements accelerate the passivity **[15,16]**. In UFG structures by SPD, there are high density of grain boundaries and dislocations on the surface, and they should enhance the diffusion of Cr elements

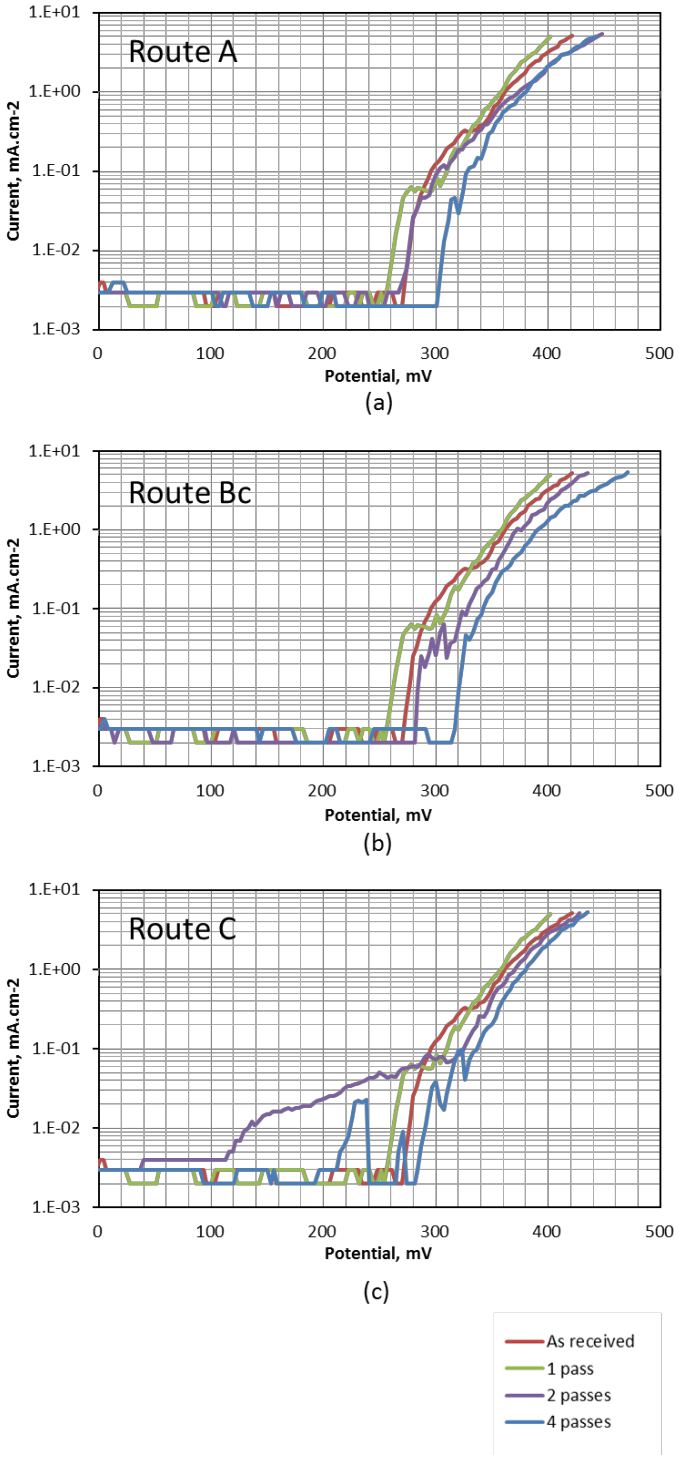

Figure 3.11. Pitting corrosion testing curve of low C,N Fe-20%Cr alloy ECAPed on Y-plane: (a) route A, (b) route Bc and (c) route C specimen in 1 M NaCl.

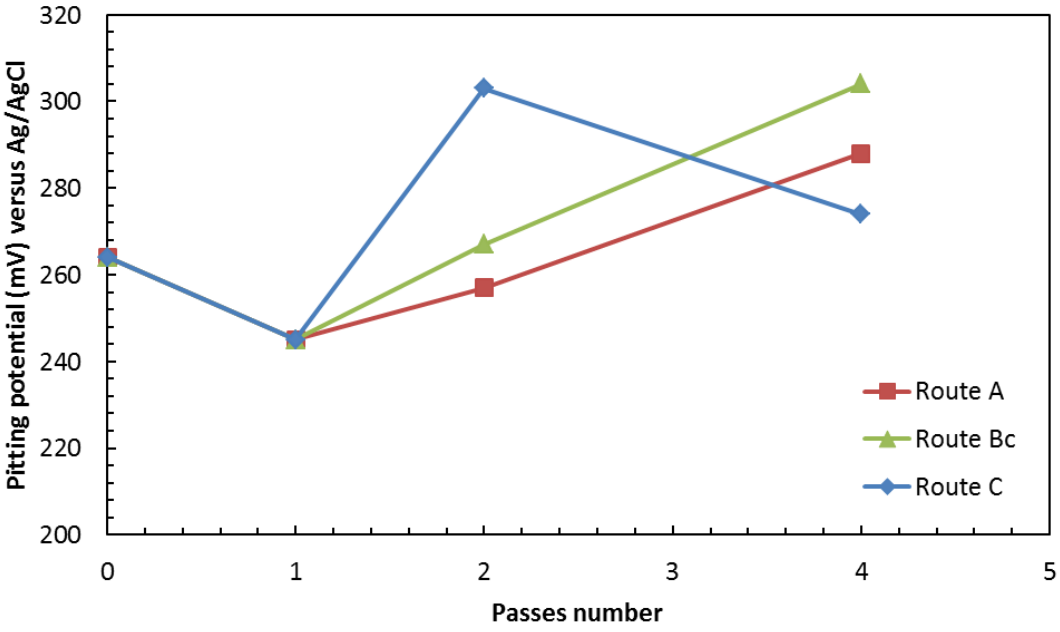

Figure 3.12. Effect of deformation route on pitting potential versus Ag/AgCl.

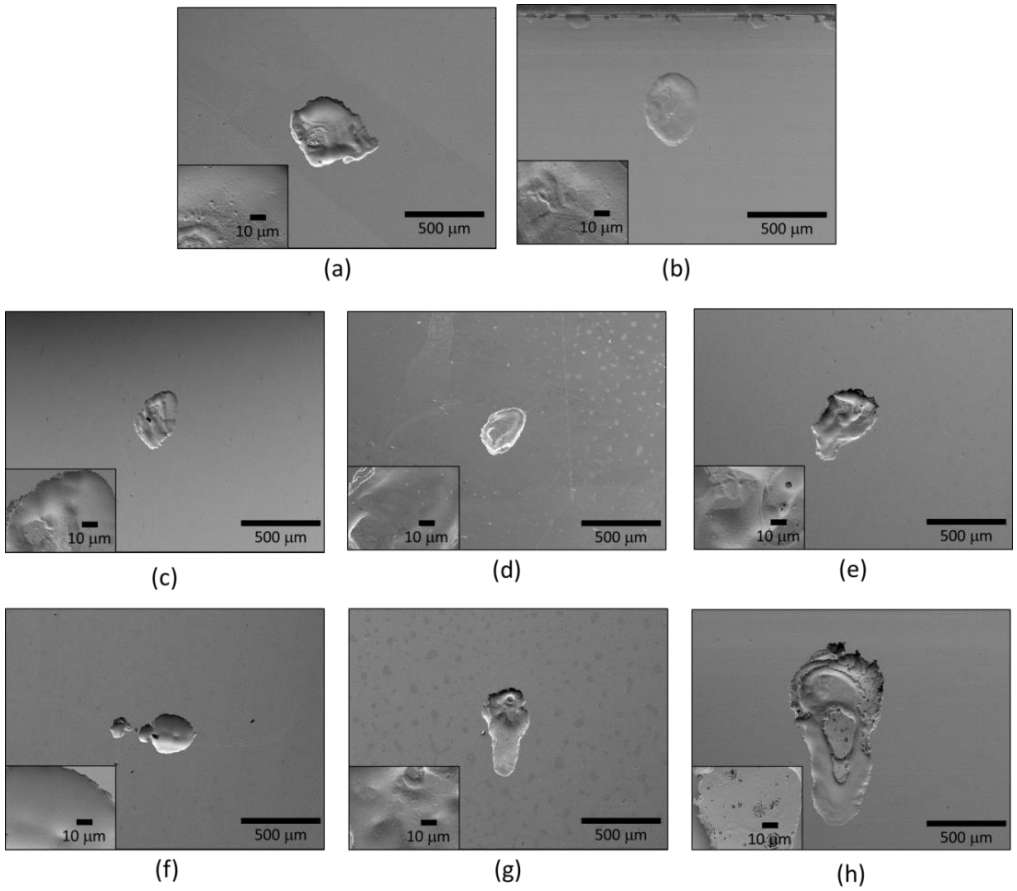

Figure 3.13. SEM micrographs showing corroded surfaces on Y-plane after pitting corrosion testing (a) as received, (b) one pass, (c) two passes route A, (d) two passes route Bc, (e) two passes route C, (f) four passes route A, (g) four passes route Bc, (h) four passes route C.

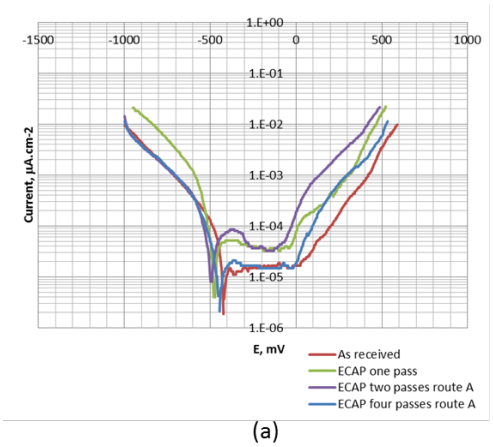

(a)

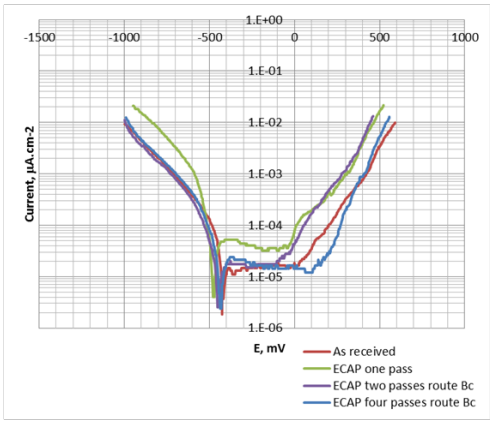

(b)

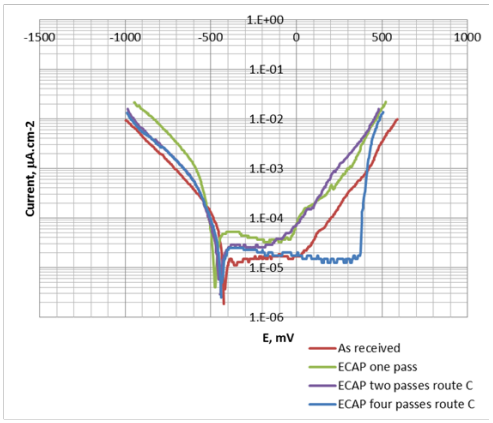

(c)

Figure 3.14. Tafel plots for as-ECAPed specimen on Y-plane for (a) route A, (b) route Bc and (c) route C in 1 M NaCl and 1 M CH_3COOH solution.

from the interior to the surface. Therefore, when the passivated surface is locally attacked by aggressive species such as Cl^-, then the passivation can be recovered by faster supply of Cr elements from the interior part through enhanced diffusion. In summary, the increased pitting resistance may also be attributed to the enhanced diffusion of Cr elements due to the high density of grain boundaries and dislocations.

3.5. Conclusion

The microstructural evolution of extremely low CN Fe-20%Cr alloy processed by ECAP from one to eight passes via routes A, Bc, and C were quantitatively analyzed by focusing on the degree of their anisotropy. The degree of anisotropy of microstructures was different among the three deformation routes. They were generally isotropic in route Bc, namely the grains were equiaxial, and the hardness was comparable in the three orthogonal planes.

References

[1] Shin, D. H., and Park, K. T. (2005). Ultrafine grained steels processed by equal channel angular pressing. Materials Science and Engineering: A, 410, 299-302.

[2] Pang, J. C., Yang, M. X., Yang, G., Wu, S. D., Li, S. X., and Zhang, Z. F. (2012). Tensile and fatigue properties of ultrafine-grained low-carbon steel processed by equal channel angular pressing. Materials Science and Engineering: A, 553, 157-163.

[3] Furukawa, M., Iwahashi, Y., Horita, Z., Nemoto, M., and Langdon, T. G. (1998). The shearing characteristics associated with equal-channel angular pressing. Materials Science and Engineering: A, 257(2), 328-332.

[4] Cabibbo, M. (2010). A TEM Kikuchi pattern study of ECAP AA1200 via routes A, C, Bc. Materials characterization, 61(6), 613-625.

[5] Segal, V. M. (1995). Materials processing by simple shear. Materials Science and Engineering: A, 197(2), 157-164.

[6] Salimyanfard, F., Reza Toroghinejad, M., Ashrafizadeh, F., and Jafari, M. (2011). EBSD analysis of nano-structured copper processed by ECAP. Materials Science and Engineering: A, 528(16), 5348-5355.

[7] Kang, D. H., and Kim, T. W. (2010). Mechanical behavior and microstructural evolution of commercially pure titanium in enhanced multi-pass equal channel angular pressing and cold extrusion. Materials and Design, 31, S54-S60.

[8] Iwahashi, Y., Furukawa, M., Horita, Z., Nemoto, M., and Langdon, T. G. (1998). Microstructural characteristics of ultrafine-grained aluminum produced using equal-channel angular pressing. Metallurgical and materials transactions A, 29(9), 2245-2252.

[9] Furukawa, M., Horita, Z., Nemoto, M., Valiev, R. Z., and Langdon, T. G. (1996). Microhardness measurements and the Hall-Petch relationship in an Al Mg alloy with submicrometer grain size. Acta Materialia, 44(11), 4619-4629.

[10] Furukawa, M., Horita, Z., and Langdon, T. G. (2002). Factors influencing the shearing patterns in equal-channel angular pressing. Materials Science and Engineering: A, 332(1), 97-109.

[11] Iwahashi, Y., Horita, Z., Nemoto, M., and Langdon, T. G. (1998). The process of grain refinement in equal-channel angular pressing. Acta Materialia, 46(9), 3317-3331.

[12] Langdon, T. G. (2007). The principles of grain refinement in equal-channel angular pressing. Materials Science and Engineering: A, 462(1), 3-11.

[13] Li, S., Gazder, A. A., Beyerlein, I. J., Davies, C. H., and Pereloma, E. V. (2007). Microstructure and texture evolution during equal channel angular extrusion of interstitial-free steel: Effects of die angle and processing route. Acta materialia, 55(3), 1017-1032.

[14] Hadzima, B., Janeček, M., Estrin, Y., and Kim, H. S. (2007). Microstructure and corrosion properties of ultrafine-grained interstitial free steel. Materials Science and Engineering: A, 462(1), 243-247.

[15] Sieradzki, K., and Newman, R. C. (1986). A percolation model for passivation in stainless steels. J. Electrochem. Soc.;(United States), 133(9).

[16] Qian, S., Newman, R. C., Cottis, R. A., and Sieradzki, K. (1990). Validation of a Percolation Model for Passivation of Fe-Cr Alloys: Two-Dimensional Computer Simulations. Journal of The Electrochemical Society, 137(2), 435-439.

Chapter 4. Homogeneous grain growth of UFG low C, N Fe-20%Cr steel by ECAP

4.1. Introduction

UFG structures by SPD have been regarded as partially deformation structure as well as UFG structure. Namely, UFG structures by ECAP are considered to have stored residual dislocations in grain or at grain boundaries. Such grain boundaries with extrinsic grain boundary dislocations are called non-equilibrium grain boundaries, and they are considered to be origin of unique mechanical, physical and chemical properties **[1]**.

Thermal stability of UFG materials is important properties along with mechanical properties. The annealing behavior of the UFG material has been investigated, such as copper **[2-5]**, aluminum, and its alloy **[6-12]**, titanium **[13]**, iron **[14]**, and low carbon steel **[15,16]**. It was reported that the thermal stability of the microstructure of the ECAPed FCC metals is low, and in general they grow apparently by the mode of so-called abnormal grain growth **[20.21]**, where a small fraction of grains grow preferentially replacing other grains. However, it can be regarded as the so-called discontinuous recrystallization with nucleation and its growth process since ECAPed UFG structure is partially deformation structure. In other words, such small fraction of growing grains can be regarded as nucleus. In this context, it is effective to create the dislocation-free UFG with equilibrium grain boundaries and examine annealing behavior focusing on the early stage of grain growth in order to clarify the origin of low thermal stability and abnormal grain growth. Such knowledge can contribute to create the UFG materials with high thermal stability.

Pure metals of BCC is intrinsically fast to be recovered, and may exhibit different annealing behavior from FCC counterparts. Namely, one can expect to obtain dislocation-free UFG by appropriate annealing avoiding grain growth. However, annealing behavior of UFG of pure BCC alloy has not been investigated focusing on the early stage of restoration of strain. The stored dislocation can be analyzed through TEM or X-ray line broadening analysis. The X-ray line broadening analysis corresponded to grain refinement and dislocation density **[22]**. In this study, annealing behavior on UFG

structure of extremely low C,N Fe-20%Cr steel is investigated in order to examine the origin of low thermal stability and ECAPed materials in terms of residual strain.

4.2. Experimental procedure

The present material had a chemical composition of low C, N Fe-20%Cr steel with Cr 20.03; C 0.0004; N 0.0013 and Fe balance (in mass percent). This alloy was machined with dimensions of 8 mm × 8 mm × 120 mm for ECAP pressing. ECAP procedures were carried out using a split die with two channels intersecting at an inner angle of 90 degrees and an outer angle of 0 degrees at 423 K. Before the ECAP process, the samples were lubricated with a high temperature fluorine lubricating grease, and then pressed for eight passes via routes Bc. A die ECAP set with an internal angle, Φ of 90 degrees and outer angle, Ψ of 0 degrees was assembled. After ECAP, billets were annealed using infrared furnace (ULVAC MILA5000) from 473 to 1373 K in a vacuum for one hour. A corrosion testing specimen was prepared from an ECAPed sample using a spark-erosion machine. Mechanical properties were measured by hardness. The micro hardness experiments were performed on a Vickers hardness testing machine under a load, for 15 s dwell time for each annealing temperature. Hardness testing was carried out for ten times per each sample. And then, microstructure observation was carried out by a FE-SEM (JSM 7001F), equipped with EBSD (Oxford Instrument Co.) image, and a TEM (JEM 2100F). Therefore, EBSD orientation maps were processed using INCA^{TM} software. TEM sample preparation was needed. Thin foils for TEM were polished using abrasive papers to about 100 μm in thickness and then thinned by a twin-jet polishing Tenupol 5 facility using a solution of 40% acetic acid, 30% phosphoric acid, 20% nitric acid, and 10% distilled water. An X-ray diffraction (XRD) on ECAPed and post annealing sample was carried out by SmartLab, Rigaku. XRD samples surface was polished by an automatic polisher. The SmartLab x-ray diffractometer used CuKα, 40kV, 200mA from 30 deg until 120 deg with a continuous scanning type. Full width half maximum (FWHM) and integral breadth was determined after fitting the scattered XRD data.

4.3. Result

4.3.1 Micro hardness

Vickers hardness of the ECAPed and post-ECAP annealing sample was shown in **Figure 4.1**. The micro hardness results exhibited three stages of softening with increasing annealing temperature. The hardness was constant up to the annealing temperature of 698 K and then decreased gradually until the annealing temperature of 973 K. Finally, hardness became constant again.

4.3.2. Microstructure

The color orientation map by EBSD after ECAP and the post-ECAP annealing process can be seen in **Figure 4.2**. UFG structure can be seen in the ECAPed sample, and grain size remained constant until 698 K. It corresponds with in first stage of softening of the material. Appreciable grain growth was observed to occur homogeneously at a temperature higher than 698 K. It corresponded with the second stage of appreciable softening during the second stages.

Grain boundary misorientation maps on ECAP and after post-ECAP annealing from 473 – 1373 K are represented in **Figure 4.3**. HAGB fraction on ECAPed microstructure are predominant with little fraction of LAGB. Because of low orientation resolution, boundaries with misorientation smaller than 2° was omitted. Homogeneous microstructure evolution with small equiaxed grains and high HAGB fraction was exhibited on post-ECAP annealing sample until 698 K. However, grain size increased gradually until the annealing temperature of 1373 K, but HAGB fraction almost remained constant.

Distribution of misorientation angle was obtained from EBSD observation after ECAP and post-ECAP annealing as shown in **Figure 4.4**. Result of as-ECAPed materials shows boundary misorientation with a peak in the range of 2° - 5° with low HAGB misorientation distribution. After 773 K annealing temperature, the difference of

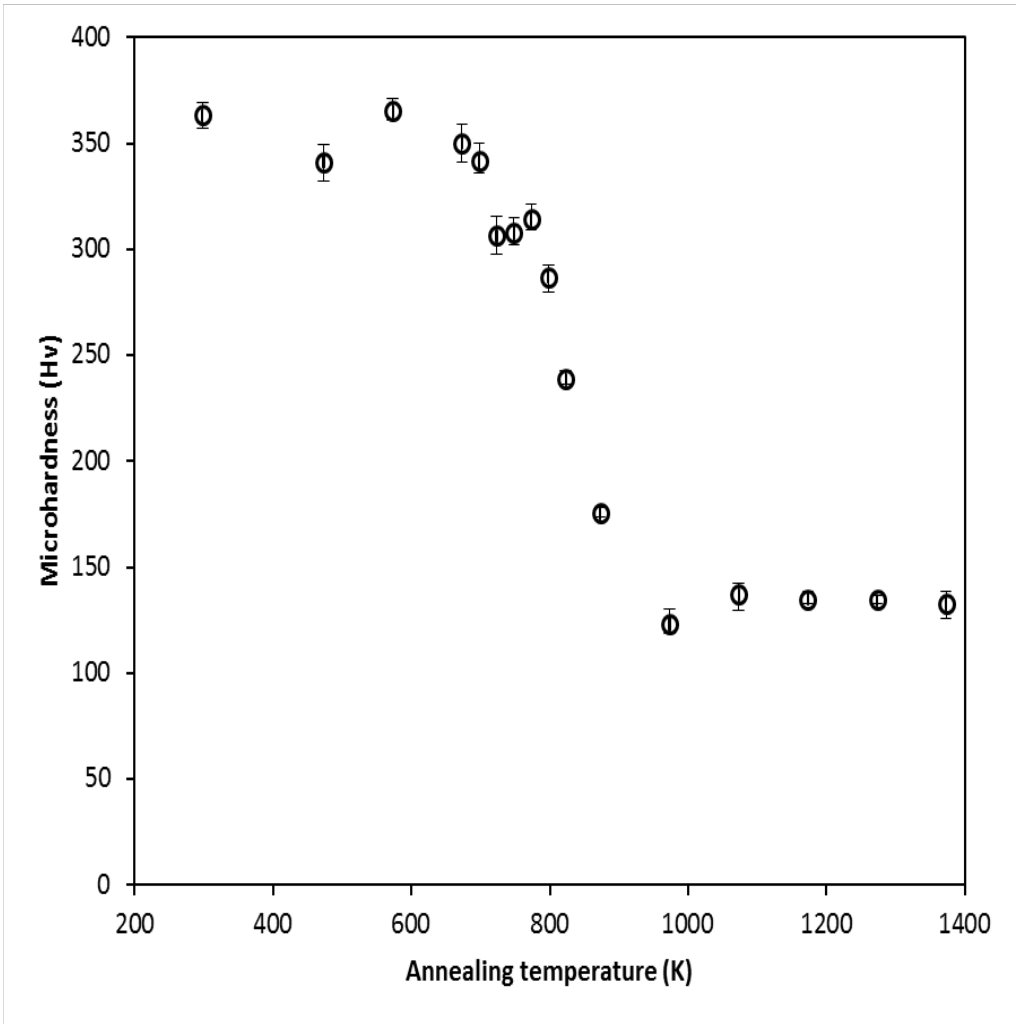

Figure 4.1. Vickers hardness of ECAPed and post-ECAP annealing sample.

misorientation distribution became noticeable. Misorientation distribution of this alloy shows one small peaks at low and high angle misorientation.

The microstructure of TEM was also observed on ECAP and after post-ECAP annealing up to 823 K, as shown in **Figure 4.5**. Under annealing temperature of 698 K, due to the recovery stage, there was not much difference in microstructure from the eight passes ECAP. The microstructure of ECAPed sample exhibited a dark contrast as compared to that of the post-ECAP annealing; it indicates that the dislocation was kept inside the UFG structure. The light contrast appeared at the TEM micrograph of the post-ECAP annealing due to the releasing of dislocation in grains. The boundary spacing remained constant up to the annealing temperature of 698 K, and then gradually increased as the annealing temperature increased, as shown in **Figure 4.6.**

4.3.3 XRD analysis

One of the methods for estimating dislocation density is X-ray line broadening by XRD. X-ray {110} broadening can be seen in **Figure 4.7**. X-ray line broadening of the ECAPed sample can be observed significantly. The line broadening became smaller with the increasing annealing temperature.

The broadening in XRD data line consists of contributions due to coherent domain size, D and micro strain, ε **[24]**. The relationship at equation 4.1 can be used to separate the contributions from each of them for dislocation density, ρ **[24]**:

$$(\beta \cos\theta/\lambda)^2 = (1/D)^2 + (4\varepsilon \sin\theta/\lambda)^2 \quad (4.1)$$

Where β is the integral breadth (in radians), θ is Bragg`s diffraction angle, D is coherent domain size (Å), ε is micro strain and λ is wave length of X-ray (Å). The peak data is obtained using XRD. Several peaks of high intensity between 2θ = 30 – 130 degrees were taken and it constructs a plot between $(\beta \cos\theta/\lambda)^2$ versus$(\sin\theta/\lambda)^2$. The plots D and ε were calculated using $\text{intercept} = 1/D^2$ and$\text{slope} = 16\varepsilon^2$. Then, dislocation density can be calculated from D and ε using formula **[24]**:

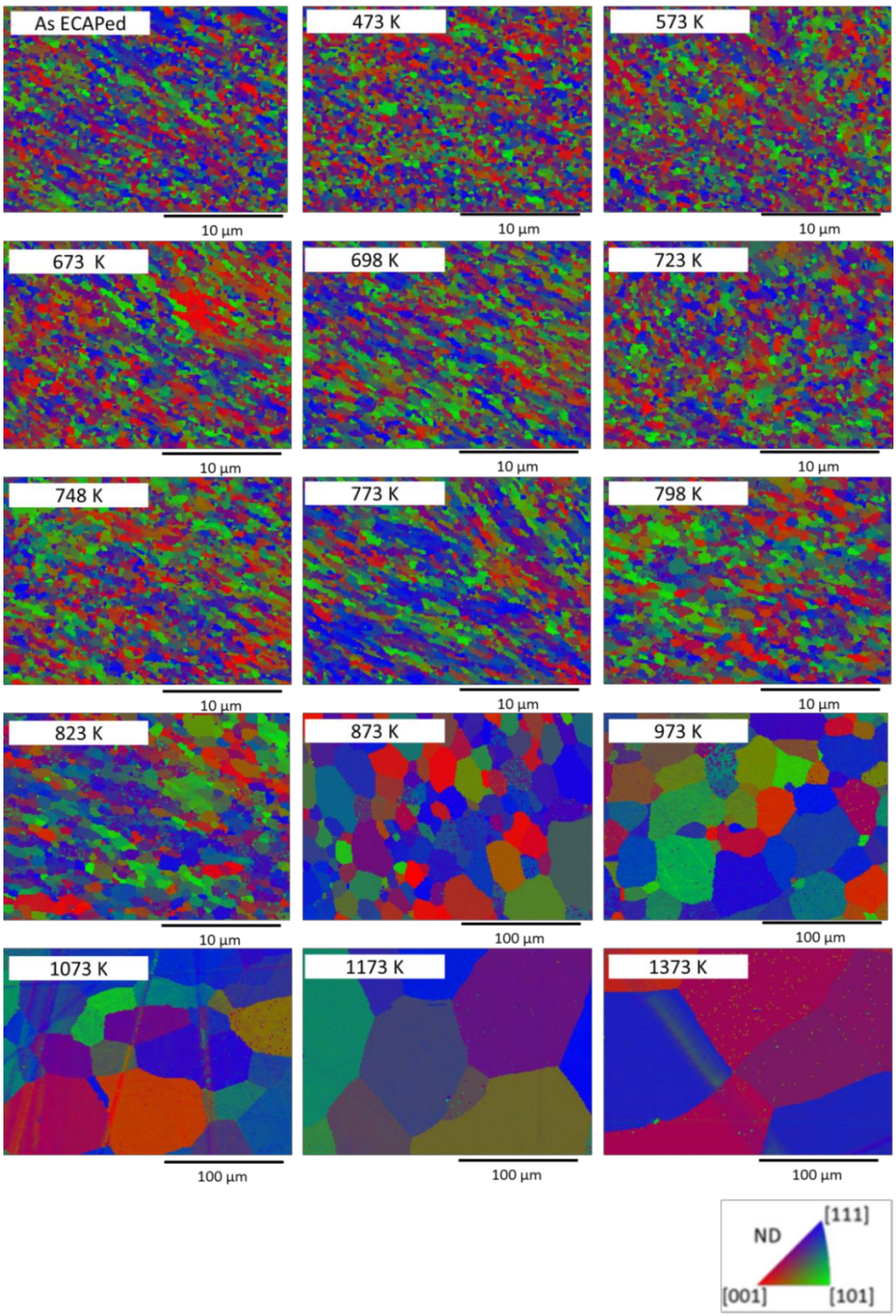

Figure 4.2. Color OIM by EBSD after the post-ECAP annealing.

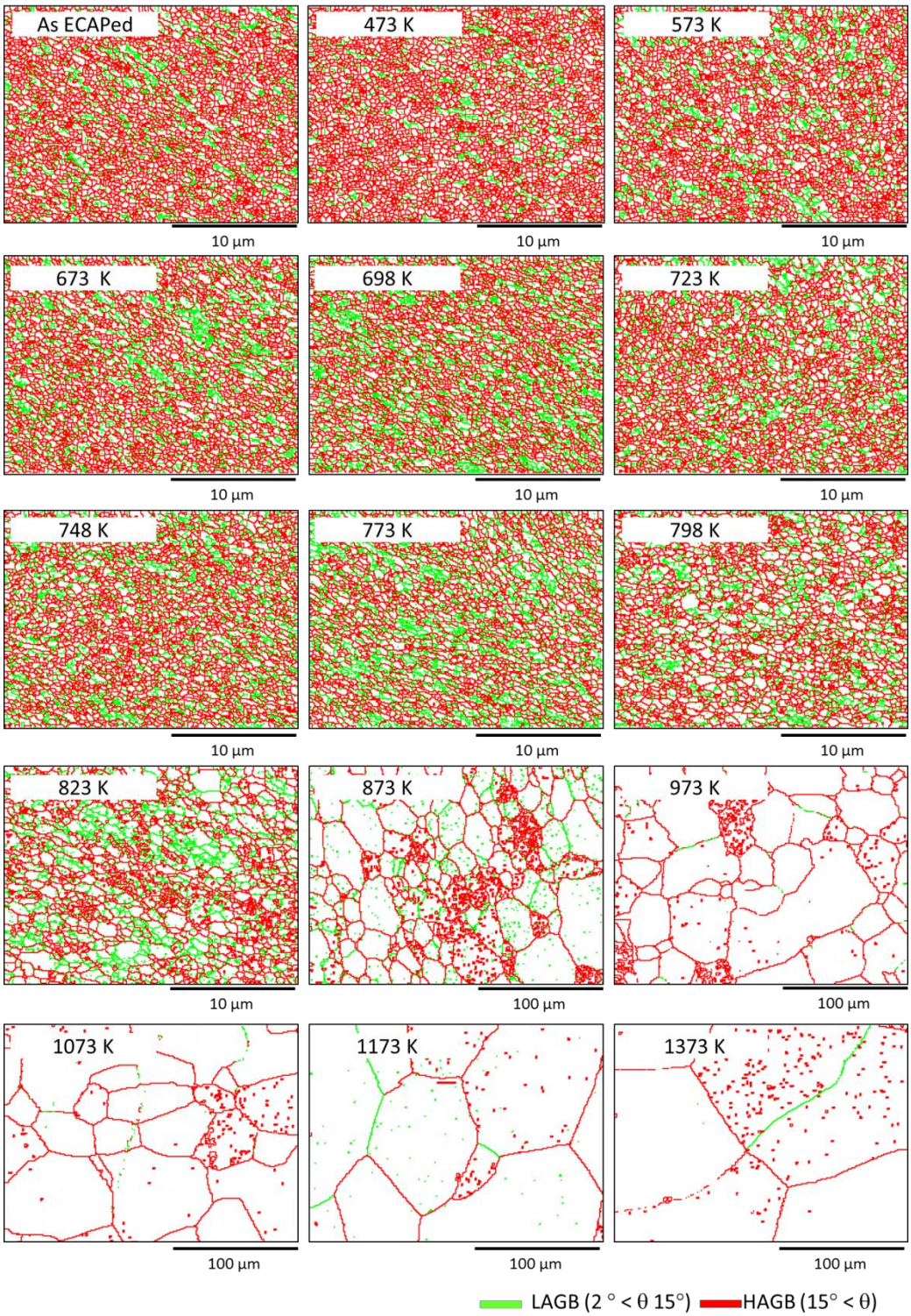

Figure 4.3. Misorientation image map by EBSD after the post-ECAP annealing.

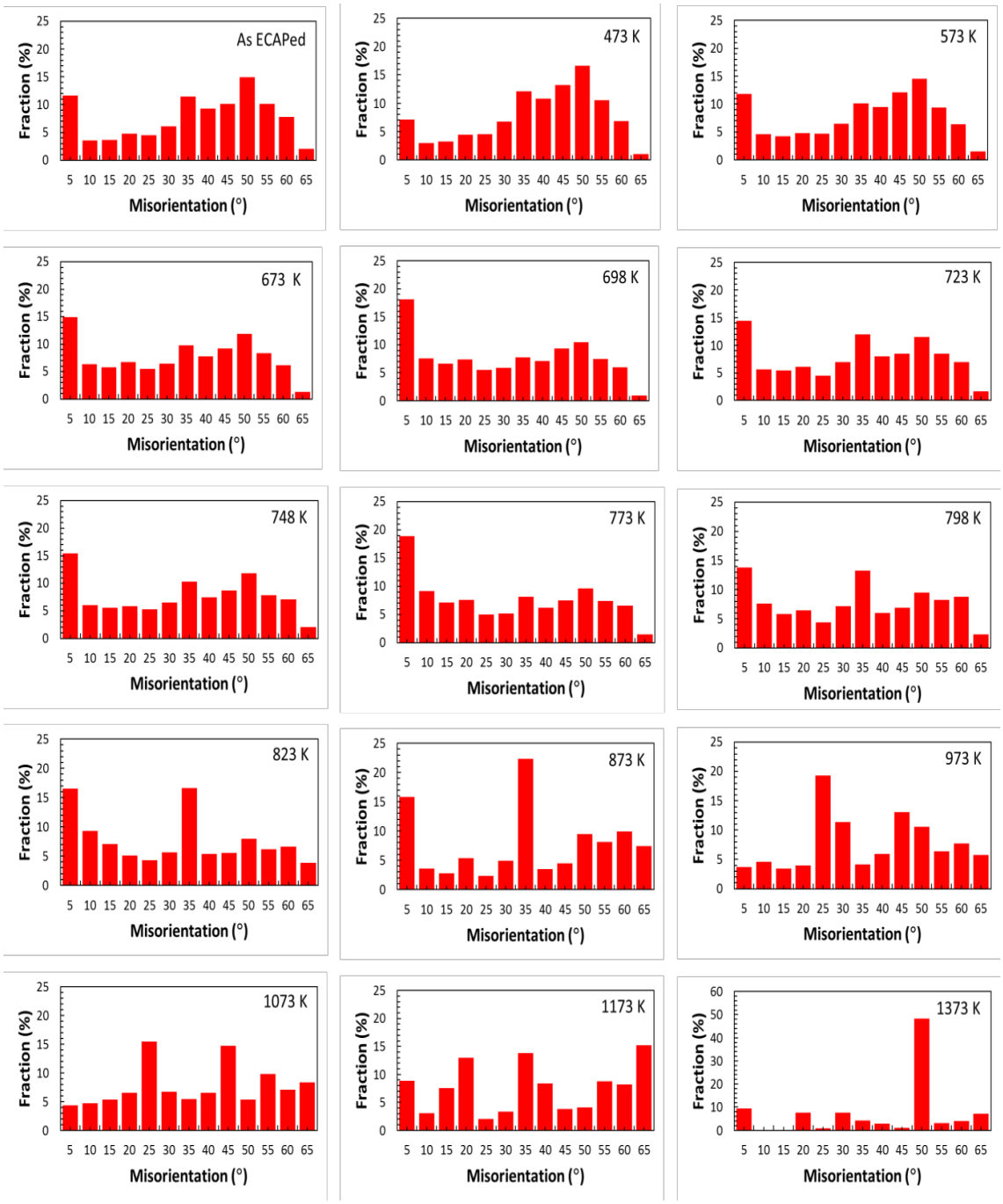

Figure 4.4. Distribution misorientation by EBSD after the post-ECAP annealing.

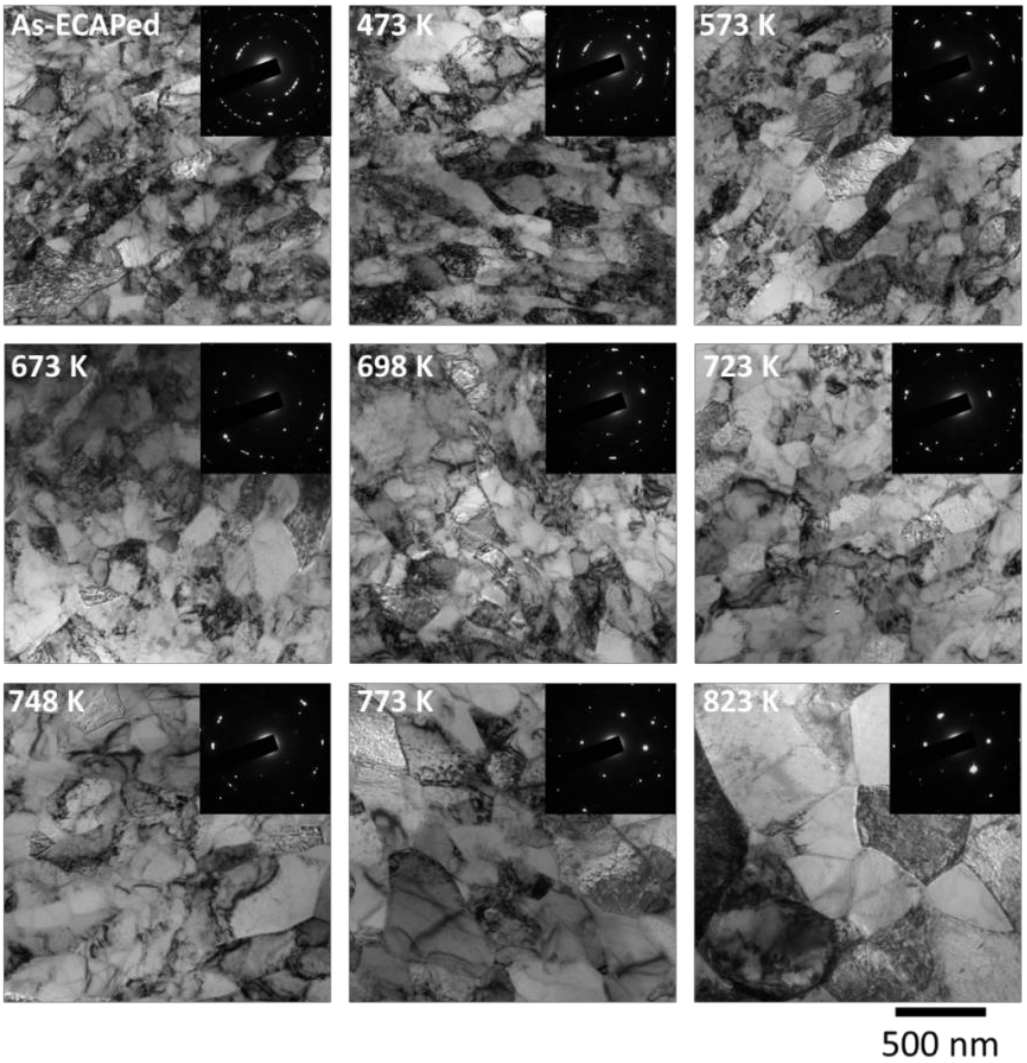

Figure 4.5. TEM micrograph after the post-ECAP annealing.

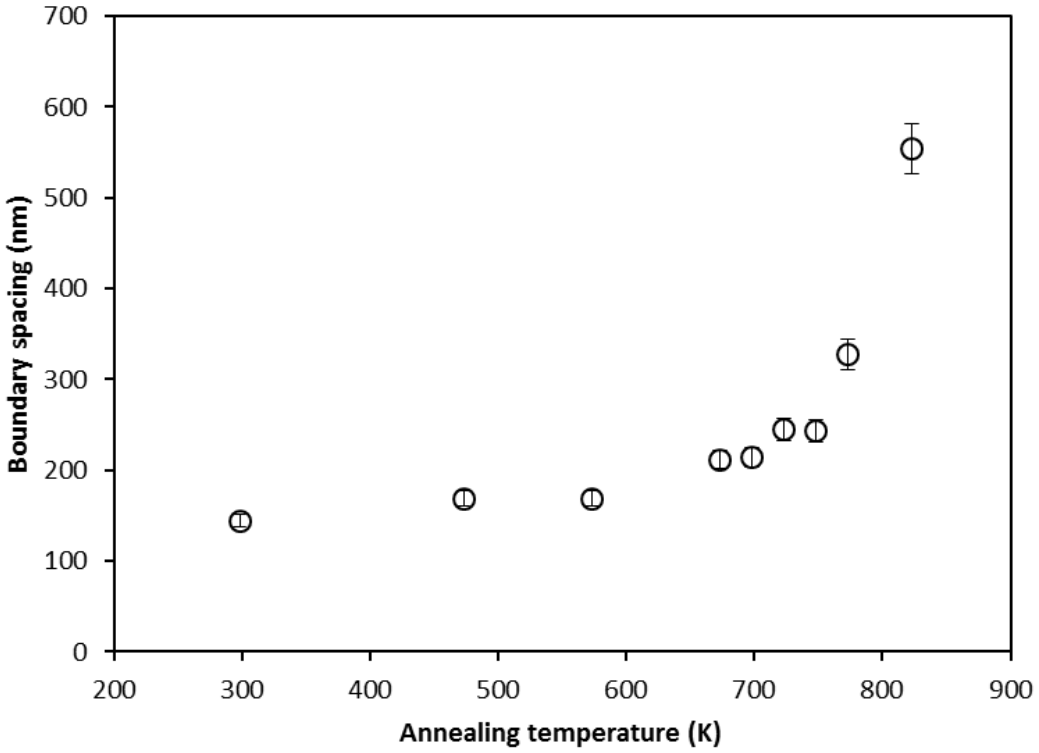

Figure 4.6. Boundary spacing of the post-ECAP annealing.

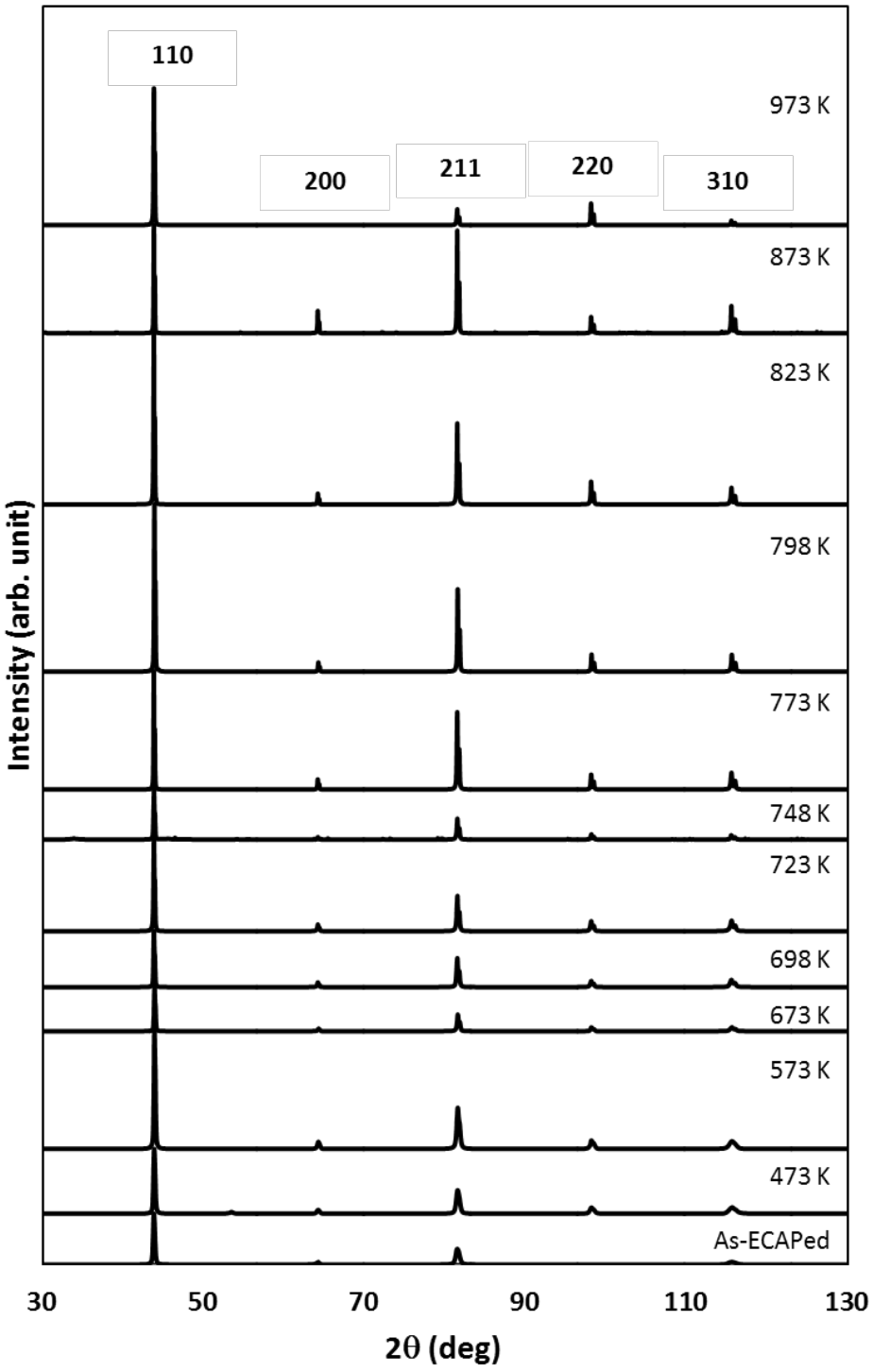

Figure 4.7. XRD after ECAP and annealing process

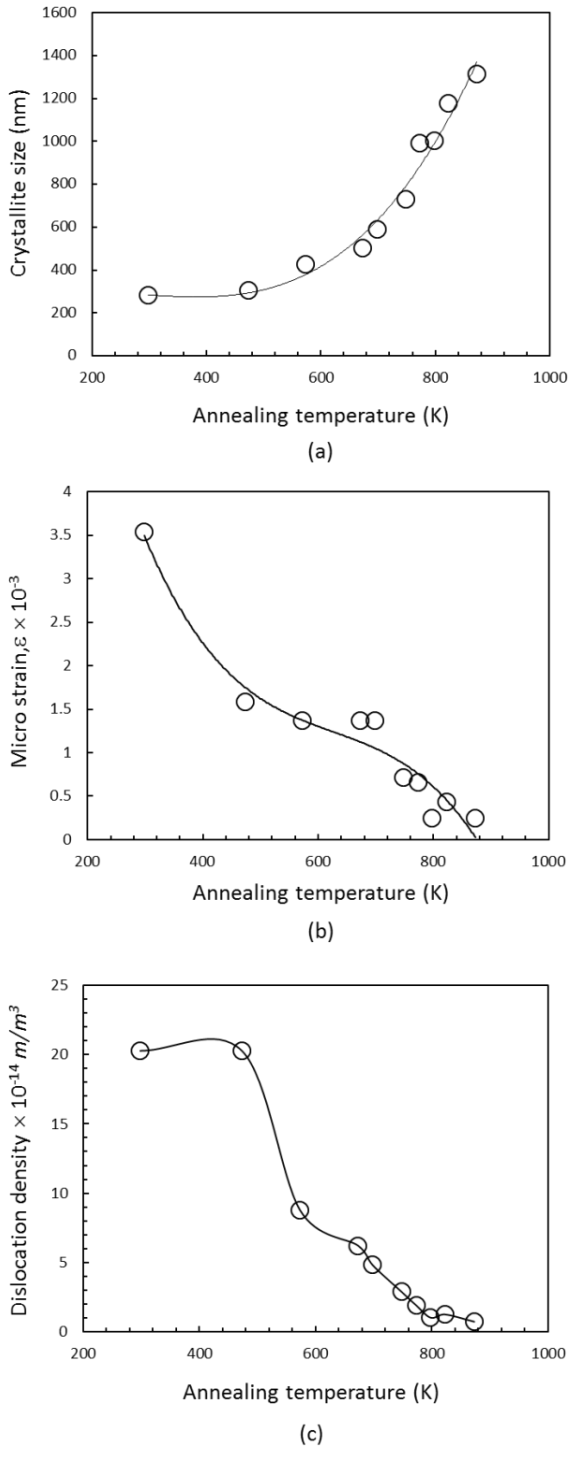

Figure 4.8. Effect of annealing temperature on (a) crystallite size, (b) micro strain and (c) dislocation density.

$$\rho_D = 3\eta/D^2 \text{ with } \eta = 1 \quad (4.2)$$

$$\rho_\varepsilon = 2k\varepsilon^2/b^2 \text{ with } k = 10 \text{ and } b = \text{Burges vector} \quad (4.3)$$

Dislocation density (ρ) is obtained from dislocation density that is related with D (ρ_D) and ε (ρ_ε) as follow **[24]**:

$$\rho = (\rho_D . \rho_\varepsilon)^{1/2} \quad (4.4)$$

The D, ε and ρ values of different annealing temperature can be seen in **Figure 4.8**.

Several parameters, such as crystallite size, micro strain, and dislocation density obtained by X-ray line broadening analysis, shown in **Figure 4.7**. The crystallite size increased with the increasing annealing temperature. On the other hand, micro strain and dislocation density decreased with the increasing annealing temperature.

4.4. Discussion

Grain growth stage on the annealing process may be divided into two types, normal grain growth and abnormal grain growth or secondary recrystallization **[18]**. Normal grain growth, in which the microstructure coarsens uniformly, is classified as a continuous process and result in a relatively narrow range of grain sizes and shapes **[18]**. On other hand, in abnormal grain growth, which is a discontinuous process, a few grains in the microstructure grow and consume the matrix of other smaller grains and a bimodal grain size distribution develops **[18]**.

In this study, low C, N Fe-20%Cr steel was deformed in 423K by ECAP until eight passes via route Bc and was annealed from 473-1373K. During the annealing temperature, material softening occurred gradually and uniformly in a fixed time. This behavior was different from the softening behavior of aluminum alloys which inhibits discontinuous recrystallization by extended recovery stage **[18]**. Strain energy stored as

dislocations can be released in recovery process easily prior to recrystallization. Therefore, strain energy stored in UFG structures in as-ECAP state may be released prior to the next stage, resulting in the formation of UFG structure with less stored strain energy. Homogeneous grain size distribution with high fraction of HAGB (81%) may lead to homogeneous and normal grain growth whose driving force is solely grain boundary energy **[18]**, rather than recrystallization which requires strain energy as driving force.

This grain growth process is different from the common material in the FCC material such as aluminum alloys **[7]**, copper **[3,4,25,26]**, nickel **[27]** and austenitic stainless steels **[28]**. The abnormal grain growth in FCC material shows small fractions of grain grow that replaced the other smaller grains due to discontinuous recrystallization **[15]**. Material processed by ECAP is characterized by high internal stresses, which are associated with both high dislocation densities and non-equilibrium grain boundaries **[1,29-31]**. Materials with high HAGB fraction have been suggested as being essentially resistant to discontinuous recrystallization regardless of an apparently high stored energy, and only the grain growth can operate frequently in such structures **[32,33]**.

The BCC material showed the releasing of strain energy as dislocation density in recovery process easier than the recrystallization process. The strain energy that was stored in UFG structure was released earlier and this early recovery of strain affected the grain formation of the UFG structure. Humphreys et al. **[18]** explained that annealing phenomena may occur in two ways. The annealing phenomena occur heterogeneously throughout the material and formally described in terms of nucleation and growth stages, and in this case they are described as discontinuous processes. On the other hand, the annealing phenomena may occur homogeneously and evolve gradually with no identifiable nucleation and growth stages in the microstructure and this case they are described as continuous processes. The continuous annealing phenomena include recovery by sub-grain growth, continuous recrystallization and normal grain growth and the discontinuous annealing phenomena include discontinuous sub-grain growth, primary recrystallization and abnormal grain growth.

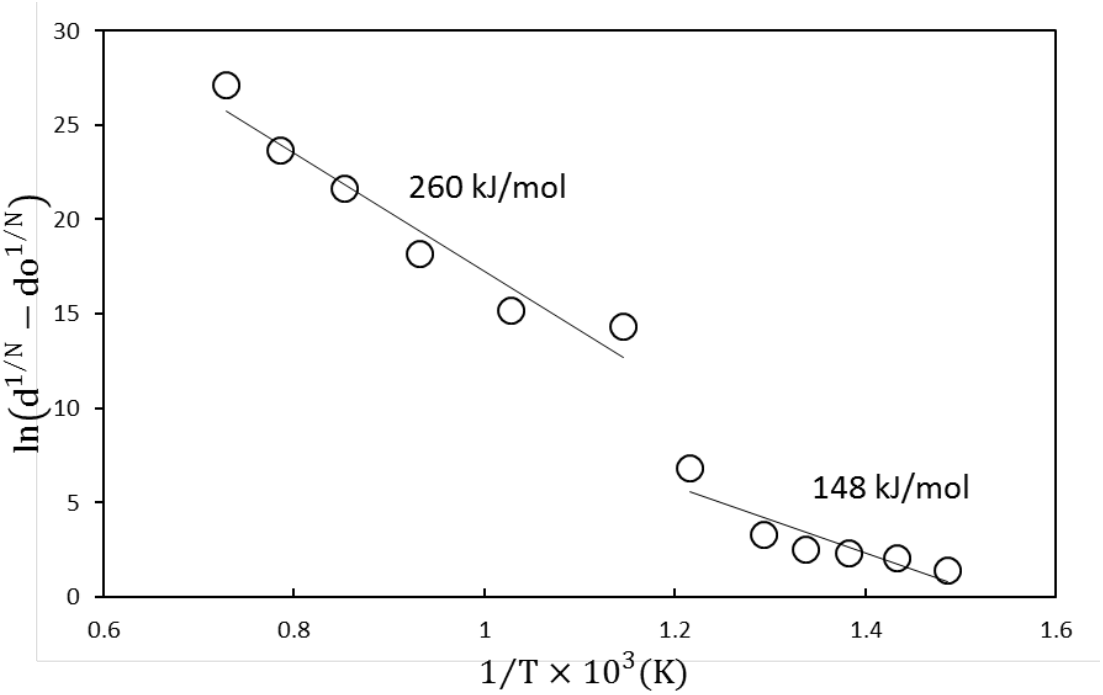

Figure 4.9. Graph of $\ln(d^{1/N} - d_o^{1/N})$ versus 1/T for determining the activation grain growth.

The homogeneous and normal grain growth behavior in terms of activation energy during annealing process can be determined using the following equation **[10, 14, 15]**:

$$d^{1/N} - d_o^{1/N} = K_o t \, exp\left(-\frac{Q}{RT}\right) \quad (4.6)$$

where d_o is the initial grain size ; d is the grain size after annealing; N is a constant usually taken as unity; K_o is a temperature-dependent constant; t is the annealing time; Q is the activation energy for grain growth; R is the gas constant ; and T is the annealing temperature. The activation energy for grain growth was obtained by constructing a semi-logarithmic plot $\left(d^{1/N} - d_o^{1/N}\right)$ versus $1/T$ as shown in **Figure 4.9**. The graph of activation energies shows two different slopes at low and high temperature regime. At low temperature regime, the low activation of 148 kJ/mol that close to activation energy of grain boundary diffusion, may correspond to the energy for the reordering of grain boundaries in the UFG material **[34]**.The activation energy of 260 kJ/mol estimated for temperatures higher than 698K is close to self-diffusion of Fe, and can be correlated lattice diffusion. It should be pointed out that the value Q obtained in the current study at high temperatures regime is significantly higher than nano crystalline pure iron alpha, **[15]**.

The decrease of dislocation density in low annealing temperatures was reported in pure iron **[35]**. It happened due to the partial annihilation of stored dislocation by recovery process and the change from non-equilibrium grain boundaries to equilibrium grain boundaries and the relaxation of internal elastic stress **[35]**. Because of the character and mobility of the boundaries, the recovery stage is the main point in the annealing process **[18]**. The extended recovery stage relates to the softening of the material **[36]**. After the annealing temperature reached 698K, the microstructure showed homogeneous grain coarsening with grain appearance comparable with the ECAP processed structure. It can be summarized that the annealing process of an UFG iron-chromium alloy can be regarded as two-stage homogeneous normal grain growth with two levels of activation energy.

4.5. Conclusion

The effect of the annealing behavior on a UFG low C, N Fe-20%Cr steel by ECAP was studied focusing on the residual dislocation-related strain on early stage of grain growth. The softening of a material occurred in the typical three stages, comprised of recovery with constant hardness, and subsequent significant softening accompanying homogeneous grain-growth, and the final slow grain growth with little change of hardness. The extended recovery stage was confirmed by XRD prior to the appreciable grain-growth. The microstructure of the recovery stage shows homogeneous coarsened grain with grain appearance comparable with the ECAP

References

[1] Valiev, R. Z., Islamgaliev, R. K., & Alexandrov, I. V. (2000). Bulk nanostructured materials from severe plastic deformation. Progress in materials science, 45(2), 103-189.

[2] Haouaoui, M., Hartwig, K. T., & Andrew Payzant, E. (2005). Effect of strain path on texture and annealing microstructure development in bulk pure copper processed by simple shear. Acta materialia, 53(3), 801-810.

[3] Komura, S., Horita, Z., Nemoto, M., & Langdon, T. G. (1999). Influence of stacking fault energy on microstructural development in equal-channel angular pressing. Journal of Materials Research, 14(10), 4044-4050.

[4] Molodova, X., Gottstein, G., Winning, M., & Hellmig, R. J. (2007). Thermal stability of ECAP processed pure copper. Materials Science and Engineering: A, 460, 204-213.

[5] Zi, A. (2010). Pure copper processed by extrusion preceded equal channel angular pressing. Materials Characterization, 61(2), 141-144.

[6] Hasegawa, H., Komura, S., Utsunomiya, A., Horita, Z., Furukawa, M., Nemoto, M., & Langdon, T. G. (1999). Thermal stability of ultrafine-grained aluminum in the presence of Mg and Zr additions. Materials Science and Engineering: A, 265(1), 188-196.

[7] Wang, J., Furukawa, M., Horita, Z., Nemoto, M., Valiev, R. Z., & Langdon, T. G. (1996). Enhanced grain growth in an Al-Mg alloy with ultrafine grain size. Materials Science and Engineering: A, 216(1), 41-46.

[8] Cao, W. Q., Godfrey, A., Liu, W., & Liu, Q. (2003). EBSP study of the annealing behavior of aluminum deformed by equal channel angular processing. Materials Science and Engineering: A, 360(1), 420-425.

[9] Cao, W. Q., Godfrey, A., Liu, W., & Liu, Q. (2003). Annealing behavior of aluminium deformed by equal channel angular pressing. Materials Letters, 57(24), 3767-3774.

[10] Ferry, M., Hamilton, N. E., & Humphreys, F. J. (2005). Continuous and discontinuous grain coarsening in a fine-grained particle-containing Al–Sc alloy. Acta materialia, 53(4), 1097-1109.

[11] Sitdikov, O., Sakai, T., Avtokratova, E., Kaibyshev, R., Tsuzaki, K., & Watanabe, Y. (2008). Microstructure behavior of Al–Mg–Sc alloy processed by ECAP at elevated temperature. Acta Materialia, 56(4), 821-834.

[12] Zhao, Y. H., Liao, X. Z., Jin, Z., Valiev, R. Z., & Zhu, Y. T. (2004). Microstructures and mechanical properties of ultrafine grained 7075 Al alloy processed by ECAP and their evolutions during annealing. Acta Materialia, 52(15), 4589-4599.

[13] Xirong, Y., Xicheng, Z., & Wenjie, F. (2009). Deformed Microstructures and Mechanical Properties of CP-Ti Processed by Multi-Pass ECAP at Room Temperature. Rare Metal Materials and Engineering, 38(6), 955-957.

[14] Moelle, C. H., & Fecht, H. J. (1995). Thermal stability of nanocrystalline iron prepared by mechanical attrition. Nanostructured Materials, 6(1), 421-424.

[15] Maier, G. G., Astafurova, E. G., Maier, H. J., Naydenkin, E. V., Raab, G. I., Odessky, P. D., & Dobatkin, S. V. (2013). Annealing behavior of ultrafine grained structure in low-carbon steel produced by equal channel angular pressing. Materials Science and Engineering: A, 581, 104-107.

[16] Stolyarov, V. V., Zhu, Y. T., Lowe, T. C., Islamgaliev, R. K., & Valiev, R. Z. (1999). A two step SPD processing of ultrafine-grained titanium. Nanostructured Materials, 11(7), 947-954.

[17] Koch, C. C., Ovid'ko, I. A., Seal, S., & Veprek, S. Structural nanocrystalline materials: fundamentals and applications, 2007.

[18] Rollett, A., Humphreys, F. J., Rohrer, G. S., & Hatherly, M. (2004). Recrystallization and related annealing phenomena. Elsevier.

[19] Lowe, T. C.; Valiev, R. Z. Proceedings of the NATO Advanced Research Workshop on Investigations and Applications of Severe Plastic Deformation, Russia, 2-7 August 1999

[20] Kumar, N., & Mishra, R. S. (2012). Thermal stability of friction stir processed ultrafine grained AlMgSc alloy. Materials Characterization, 74, 1-10.

[21] Amouyal, Y., & Rabkin, E. (2007). A scanning force microscopy study of grain boundary energy in copper subjected to equal channel angular pressing. Acta Materialia, 55(20), 6681-6689.

[22] Korchef, A., Njah, N., Masmoudi, J., Kolsi, A., Champion, Y., Guérin, S., & Leroux, C. (2004). Evolution of the mechanical properties of aluminum containing Al8Fe2Si precipitates during equal channel angular pressing. Advanced Engineering Materials, 6(8), 639-643.

[23] Iwahashi, Y., Wang, J., Horita, Z., Nemoto, M., & Langdon, T. G. (1996). Principle of equal-channel angular pressing for the processing of ultra-fine grained materials. Scripta Materialia, 35(2), 143-146.

[24] Sharp, J. V., Makin, M. J., & Christian, J. W. (1965). Dislocation structure in deformed single crystals of magnesium. physica status solidi (b), 11(2), 845-864.

[25] Čížek, J., Melikhova, O., Janeček, M., Srba, O., Barnovská, Z., Procházka, I., & Dobatkin, S. (2011). Homogeneity of ultrafine-grained copper deformed by high-pressure torsion characterized by positron annihilation and microhardness. Scripta Materialia, 65(2), 171-174.

[26] Gertsman, V. Y., & Birringer, R. (1994). On the room-temperature grain growth in nanocrystalline copper. Scripta metallurgica et materialia, 30(5), 577-581.

[27] Neishi, K., Horita, Z., & Langdon, T. G. (2002). Grain refinement of pure nickel using equal-channel angular pressing. Materials Science and Engineering: A, 325(1), 54-58.

[28] Sun, C., Yang, Y., Liu, Y., Hartwig, K. T., Wang, H., Maloy, S. A., ... & Zhang, X.

(2012). Thermal stability of ultrafine grained Fe–Cr–Ni alloy. Materials Science and Engineering: A, 542, 64-70.

[29] Suryanarayana, C. (1996). Recent advances in the synthesis of alloy phases by mechanical alloying/milling. Metals and Materials, 2(4), 195-209.

[30] Belyakov, A., Sakai, Y., Hara, T., Kimura, Y., & Tsuzaki, K. (2001). Thermal stability of ultra fine-grained steel containing dispersed oxides. Scripta materialia, 45(10), 1213-1219.

[31] Belyakov, A., Sakai, T., Miura, H., & Kaibshev, R. (1999). Iron Steel Inst. Japan Int., 39, 593; 2000. Scripta mater, 42, 319.

[32] Humphreys, F. J., Prangnell, P. B., Bowen, J. R., Gholinia, A., & Harris, C. (1999). Developing stable fine–grain microstructures by large strain deformation. Philosophical Transactions of the Royal Society of London. Series A: Mathematical, Physical and Engineering Sciences, 357(1756), 1663-1681.

[33] Humphreys, F. J. (1999). A new analysis of recovery, recrystallisation, and grain growth. Materials science and technology, 15(1), 37-44.

[34] Roy, I., Chauhan, M., Mohamed, F. A., & Lavernia, E. J. (2006). Thermal stability in bulk cryomilled ultrafine-grained 5083 Al alloy. Metallurgical and Materials Transactions A, 37(3), 721-730.

[35] Moelle, C. H., & Fecht, H. J. (1995). Thermal stability of nanocrystalline iron prepared by mechanical attrition. Nanostructured Materials, 6(1), 421-424.

[36] Doherty, R. D., Hughes, D. A., Humphreys, F. J., Jonas, J. J., Jensen, D. J., Kassner, M. E., & Rollett, A. D. (1997). Current issues in recrystallization: a review. Materials Science and Engineering: A, 238(2), 219-274.

Chapter 5. Effect of annealing temperature on tensile properties of UFG low C, N Fe-20%Cr steel by ECAP

5.1. Introduction

SPD technique by ECAP is an effective grain refinement method for polycrystalline materials **[1-3]**. The majority of papers on SPD materials have been devoted to FCC materials such as Al **[4-9]**, Cu **[10-19]** and Ni **[20-27]**. For BCC metals, carbon steels have mostly been studied **[28-36]** from a practical view point.

UFG materials processed by ECAP methods are characterized by a very high density of grain boundaries. A non-equilibrium structure of grain boundaries in ECAP-processed is an important evidence for investigating the interactions of lattice dislocations with grain boundaries. ECAP-processed materials have a non-equilibrium grain boundary inside the grain structure. Transformation from non-equilibrium into equilibrium grain boundary state can be occurred by annealing process. The annealing temperature becomes an important parameter that influences the microstructure and related mechanical properties of the ECAPed material. The tensile behavior of ECAP materials on pure BCC metal has not been investigated yet in term grain boundary state. The purpose of this study is to clarify the effect of grain boundary state such as equilibrium and non-equilibrium) on tensile behavior as yield stress.

5.2. Experimental procedure

The material used in this experiment had a chemical composition of low C,N Fe-20%Cr alloy with Cr 19.97, C 0.0020, N 0.0015 and Fe balance (in mass percent). This material was machined with dimensions of 8 mm × 8 mm × 120 mm for ECAP pressing. ECAP was carried out using a split die with two channels intersecting at an inner angle of 90° and an outer angle of 0° at 423 K. The samples were lubricated with high temperature fluorine lubricating grease and pressed from one, two, four and eight passes via routes Bc. Annealing process was carried out at 773 K for one hour. A TEM (JEM 2100F) was used to examine the microstructures. Thin foils for TEM were polished using abrasive papers to about 100 μm thick and then thinned by a twin-jet

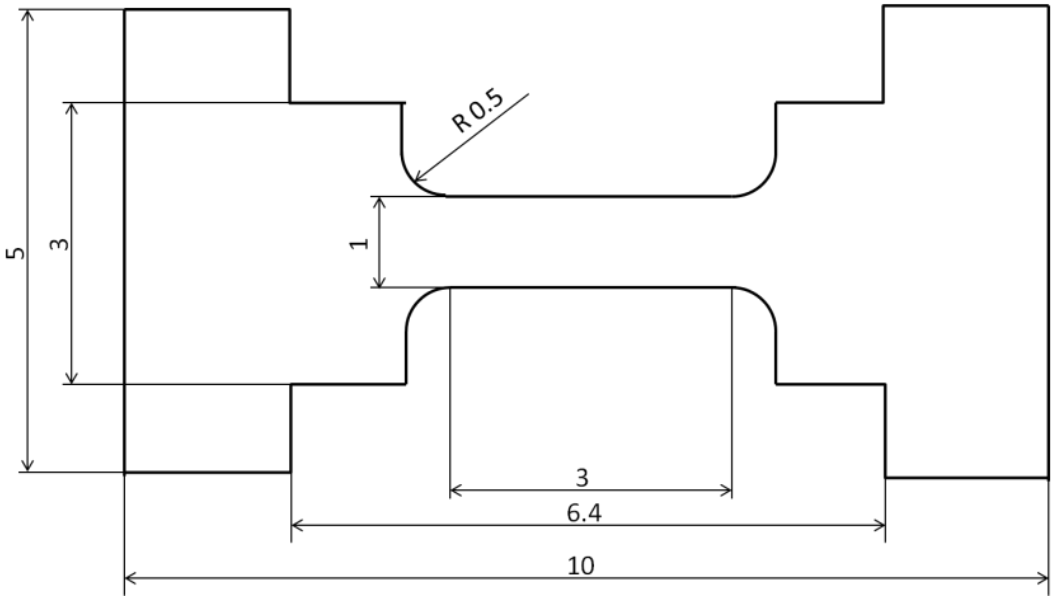

Figure 5.1. Schema of tensile testing specimen.

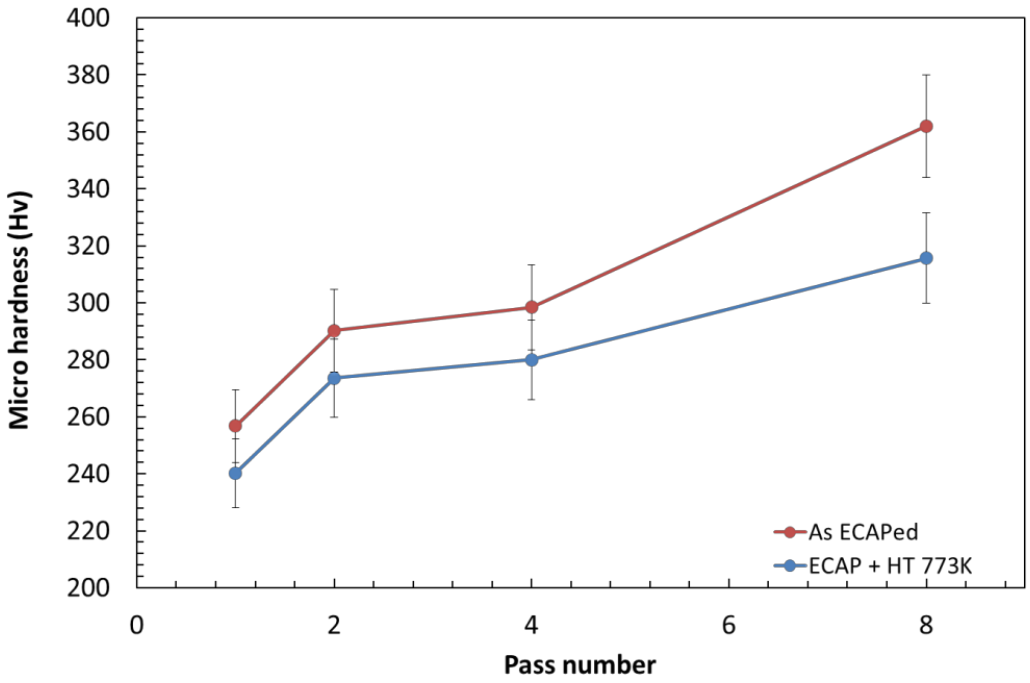

Figure 5.2. Micro hardness of as ECAPed and post-ECAP annealed sample for one, two, four and eight passes.

polishing Tenupol 5 facility using a solution of 40% acetic acid, 30% phosphoric acid, 20% nitric acid and 10% distilled water. Mechanical and electrochemical properties were measured by micro hardness and pitting corrosion. The micro hardness experiments were performed on a Vickers hardness testing machine at room temperature. Tensile experiments were conducted in a Universal testing machine (Autograph AGS-10k ND, SHIMAZU), under displacement control. The specimen for tensile test was 3 mm in gage length and 1mm in gage width. The thickness is less than 1mm. The dimensions and appearance of specimen is indicated in **Figure 5.1**.

5.3. Result and Discussion

The effect of heat treatment on UFG low C, N Fe-20%Cr alloy refined by ECAP processing, was examined after by annealing process at at 773 K. As seen in **Figure 5.2**, Hardness increased with an increasing number of ECAP cycles. Hardness after a single pass increased significantly, but the rate of become higher. Hardness measurements are taken on transverse direction. This material is different with other observed materials such as aluminum **[37-42]**, copper **[43-45]** and steel **[46-50]** that can be saturated in hardness. Another experiment found that the hardening appearance at the ferrite phase was larger than pearlite at low carbon steel **[32]**. The hardening of two phase steel (ferrite and pearlite) is controlled by the soft ferrite having a large volume fraction **[32]**. The hardness of three directions did not have any big difference in value.

A representative on microstructure observation by TEM can be seen in **Figure 5.3**. First pass shows a formation of a small grain. This area consists of parallel bands of elongated grains. Dislocation cells structures are predominant after one pass. However, elongated sub grains can be found out and they became finely divided by sharper boundaries after four passes. After eight passes, a homogeneous microstructure can be seen clearly with a pronounced grain pattern. It is included by large regions with more equiaxed grain than an elongated grain. Two passes result in several well developed grain within the elongated grain, but after eight passes it almost shows an elongated grain with a smaller grain size than the two and four passes. The post-ECAP annealed sample exhibit larger grain than as-ECAPed sample.

Dislocation density and crystallite size also can be identified by X-ray line

broadening by XRD, as shown in **Figure 5.4**. The line broadening became smaller with the increasing annealing temperature. Several parameters, such as crystallite size, micro strain, and dislocation density obtained by X-ray line broadening analysis, shown in **Figure 5.5**. The crystallite size increased with the increasing annealing temperature. On the other hand, micro strain and dislocation density decreased with the increasing annealing temperature, as shown in **Figure 5.5**.

OIM that are observed in transverse direction of the ECAP sample which are shown in **Figure 5.6**. It is apparent that grains are finely subdivided in the first pressing. ECAPed sample by one, two, four and eight passes via routes Bc was observed by EBSD on the transverse direction. Furthermore, arrays of planar and extended grain boundaries are developed parallel to the macroscopic shear plane of ECAP. After annealing at 773 K, the band structure becomes well-developed subgrains. They are formed, especially at eight passes ECAP. The formation of subgrains also can be confirmed by the corresponding by TEM micrograph, as shown in **Figure 5.3**. The formation of equiaxed sub-grains at high temperature was associated with dynamic and also static recovery.

Figure 5.7 shows engineering stress strain curve of as ECAPed and post- ECAP annealed samples from one, two, four and eight passes via routes Bc. It can be seen that tensile strength increases with the number of passes. For ECAP-processed samples, tensile strengths and strain hardening rates are almost indistinguishable. UTS improved with increasing the number of passes are shown in **Figure 5.7**. The improvement of UTS can be assigned to grain refinement. It can be seen in **Figure 5.7** that with increasing strength of ECAPed samples, elongation decreases. These phenomena that related to strength and elongation is dependable with many studies using ECAP process for metal and alloys **[51-56]**.

Figure 5.8 show schematic diagram of relationship between stress-strain curves with grain boundary state (non-equilibrium and equilibrium grain boundary). The phenomenon of yield stress on equilibrium grain boundary can be explained in dislocation-source hardening. The dislocations that can easily glide are annealed out, which means a higher yield stress is required to activate new dislocation sources during loading **[6]**. When dislocations are reintroduced, the yield stress is decreased

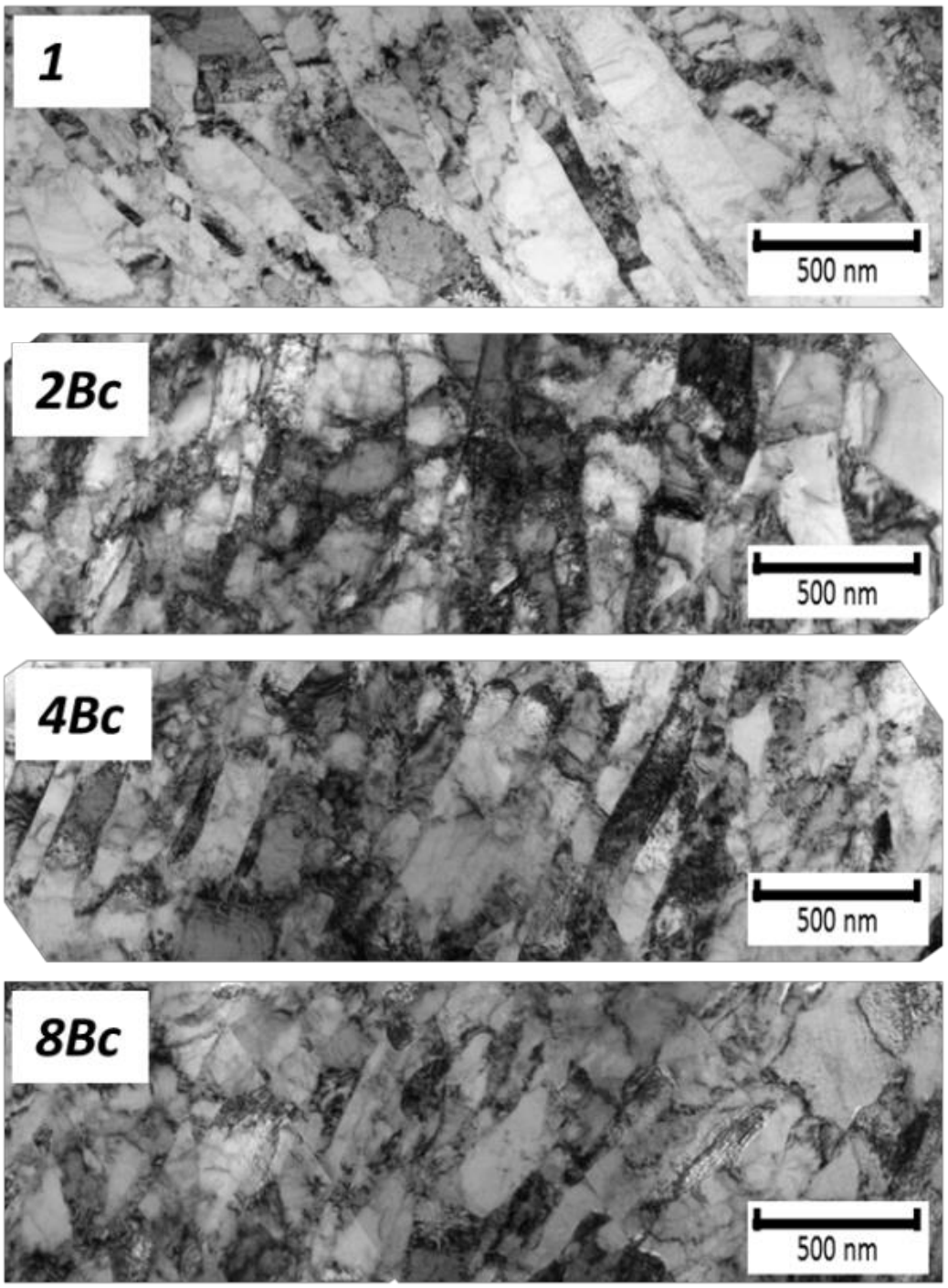

(a)

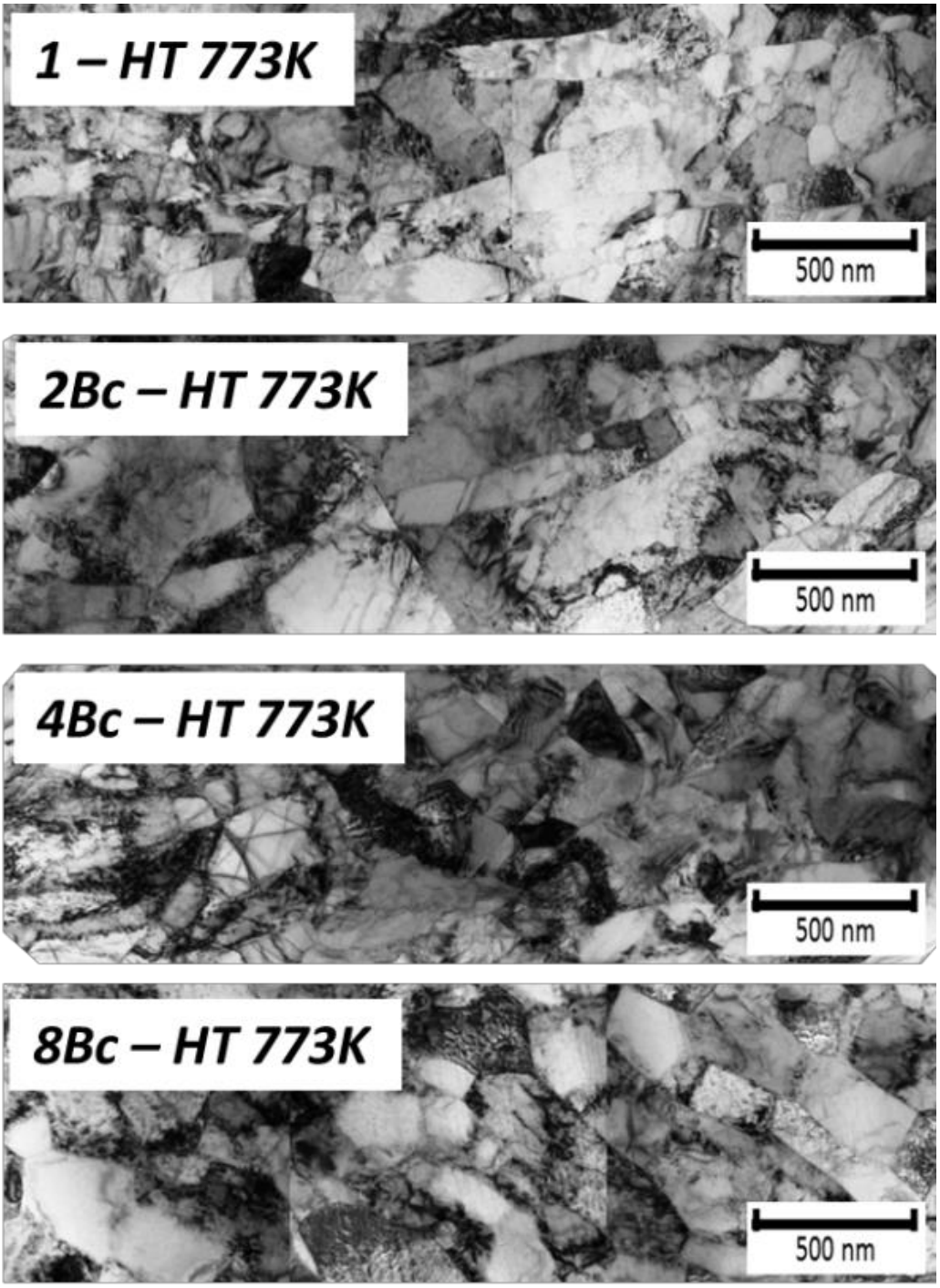

(b)

Figure 5.3. TEM micrograph of (a) as ECAPed and (b) post-ECAP annealed sample for one, two, four and eight passes.

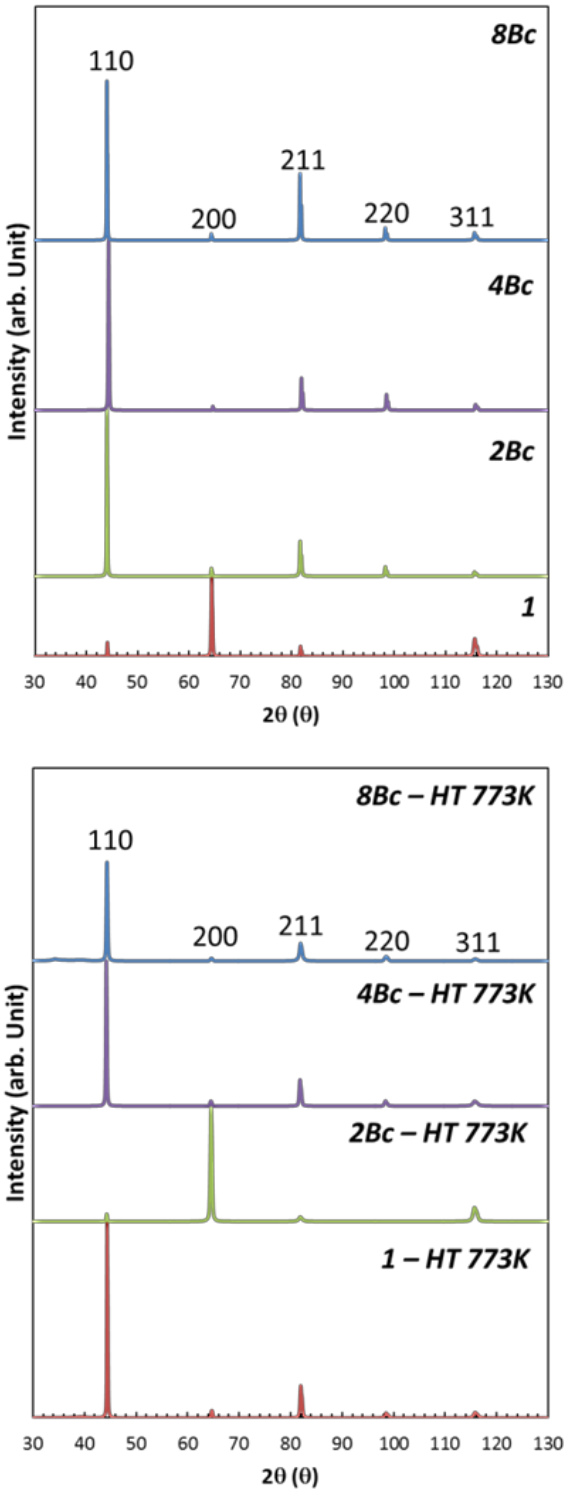

Figure 5.4. XRD of as ECAPed and post-ECAP annealed sample.

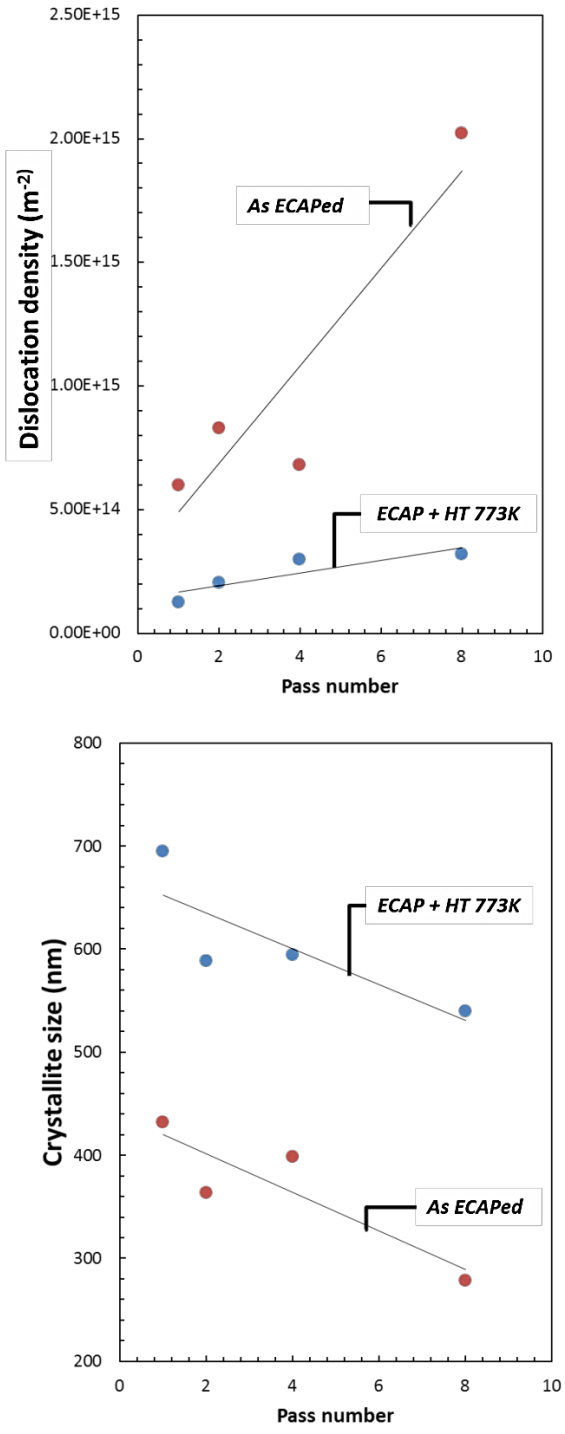

Figure 5.5. Dislocation density and crystal size of as-ECAPed and post-ECAP annealed.

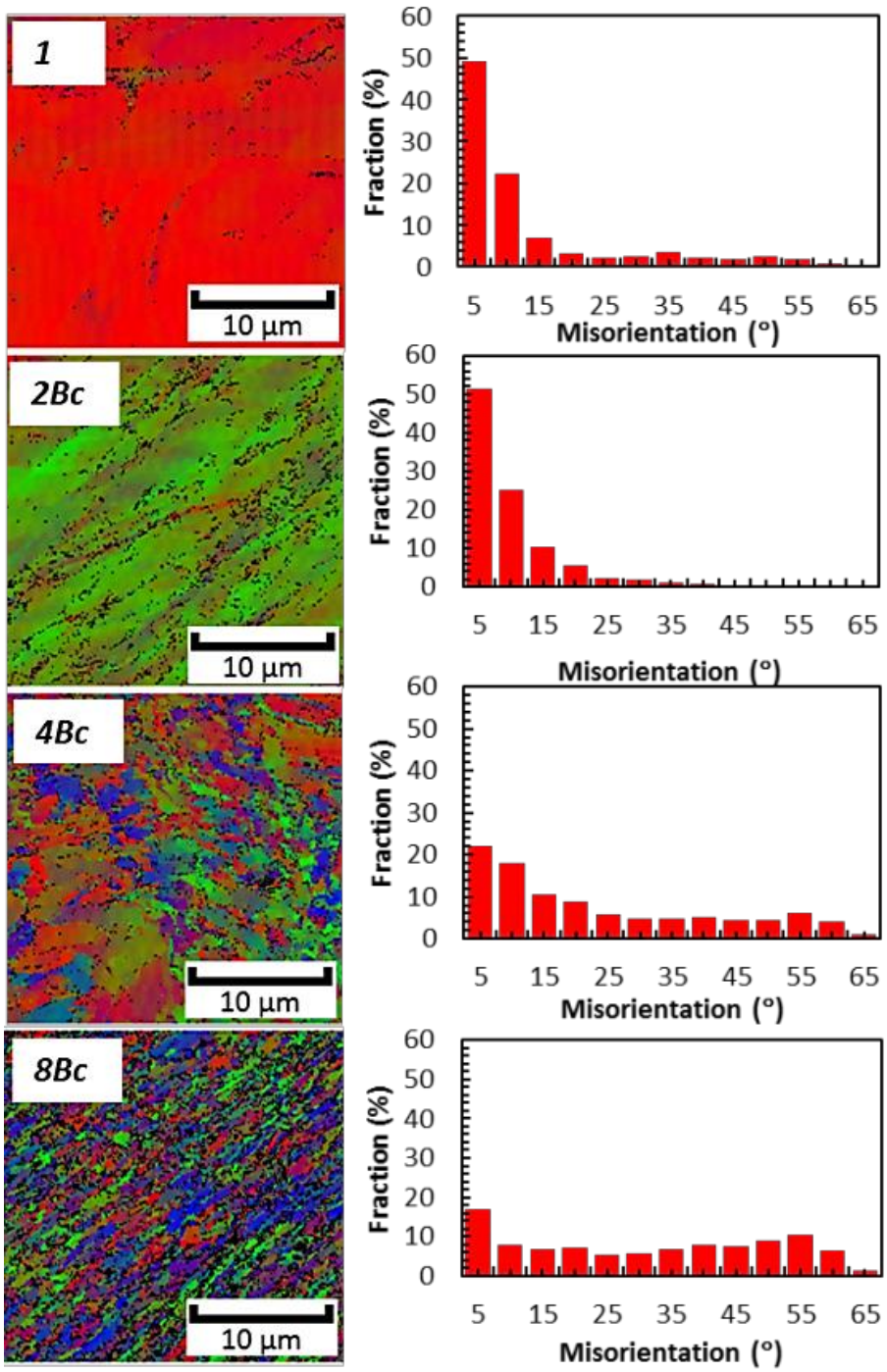
1
10 µm
2Bc
10 µm
4Bc
10 µm
8Bc
10 µm
Fraction (%)
Misorientation (°)
0
10
20
30
40
50
60
5
15
25
35
45
55
65

(a)

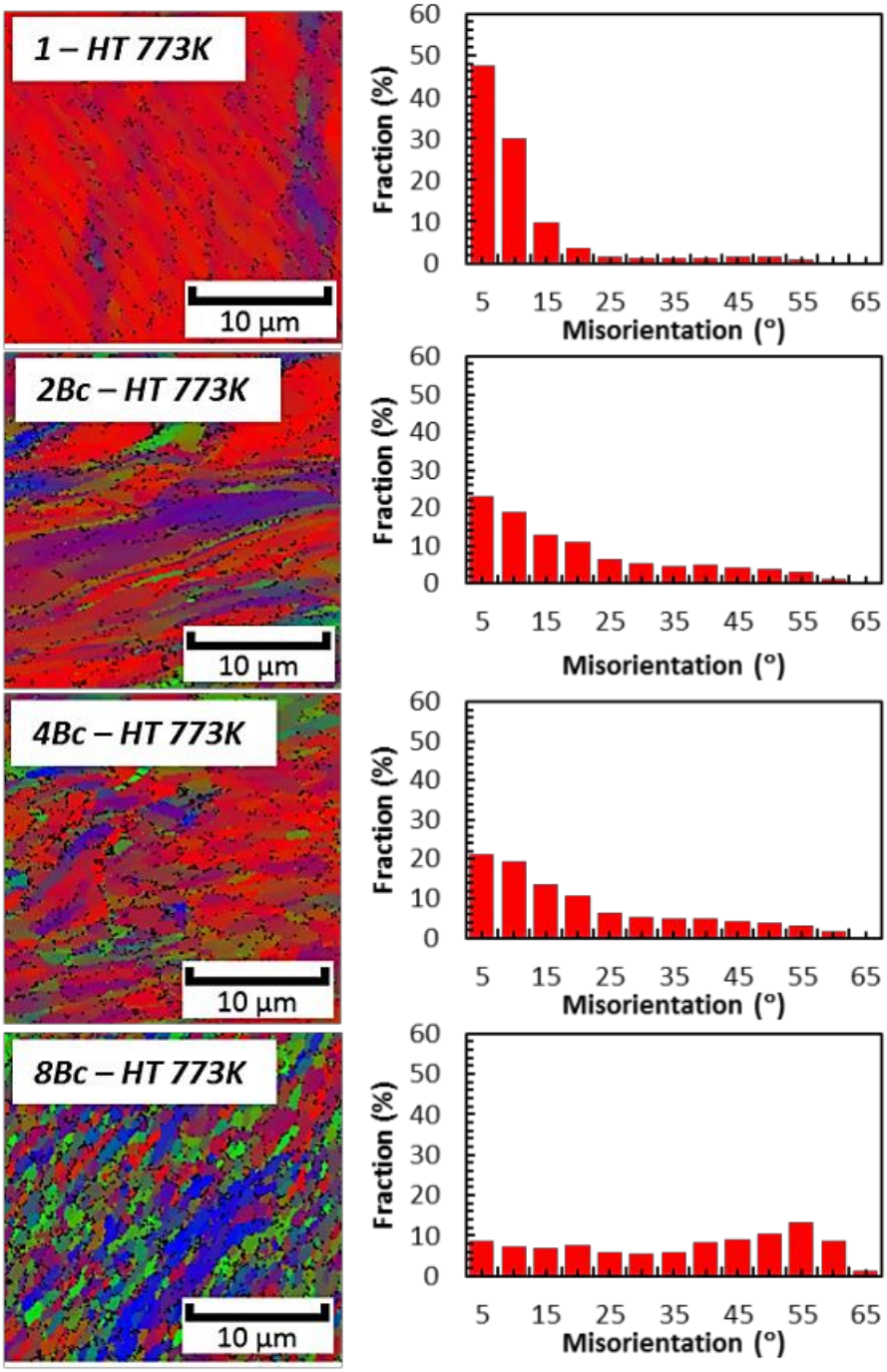

(b)

Figure 5.6. OIM and distribution misorientation of (a) as-ECAPed and (b) post-ECAP annealed sample.

as new dislocation sources are now available **[6]**. The dislocation source hardening observed in nanoscale structures can also be found in large-scale structure **[57]**. This explanation was compared with Frank-Read dislocation source theory (coarse grain material).

It is significant to highlight the ECAP processing through eight passes for giving higher strength and lower ductility. Annealing process would be applied to the ECAPed sample to improve total elongation of the ECAPed sample. This observation found post necking elongation at Fe-Cr alloys ECAPed sample. Post necking elongation can be improved from the equiaxial grain structure. This appearance can be seen at route Bc especially at eight passes. A plot of the experimental data on Hall-Petch in annealed samples and ECAPed can be seen in **Figure 5.9**. This plot to different strength–structure relationships correspond to previous discussion. Hall-Petch relationship can be described in terms of dislocation and boundary strengthening contribution. This description was related to grain boundary stated such as non-equilibrium and equilibrium, as shown in **Figure 5.10**.

Constraint of total elongation and uniform elongation can be explained by plastic instability. Plastic instability corresponds to necking propagations. The increase of yield strength with strengthening mechanism such as grain refinement can be affected by the strain hardening rate. Plastic instability can be accomplished at early stages of tensile deformation as the yield strength increase. The UTS and yield strength increased by grain refinement.

The fracture mechanism is identified in several stages. First, after necking begins, small cavities or microvoids form in the interior of the cross section. And then, as deformation continues, these microvoids come together and coalesce to form an elliptical crack, which has its long axis perpendicular to the stress direction. The crack continues to grow in a direction parallel to its major axis by this microvoid coalescence process. Finally, fracture ensues by the rapid propagation of a crack around the outer perimeter of the neck. Fracture appearance by laser microscope can be seen in **Figure 5.11**.

Figure 5.12 shows the SEM micrograph of the distributed homogeneously dimple appearance on as ECAPed and post-ECAP annealed samples after tensile

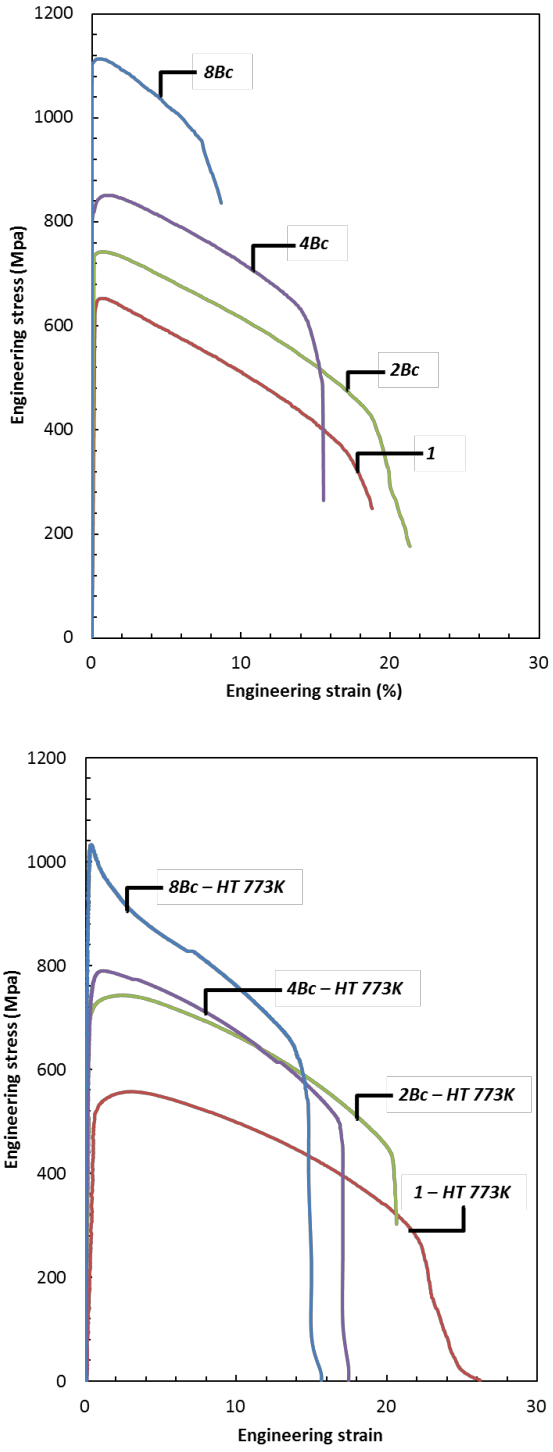

Figure 5.7. Stress-strain curve of as-ECAPed and post-ECAP annealed sample.

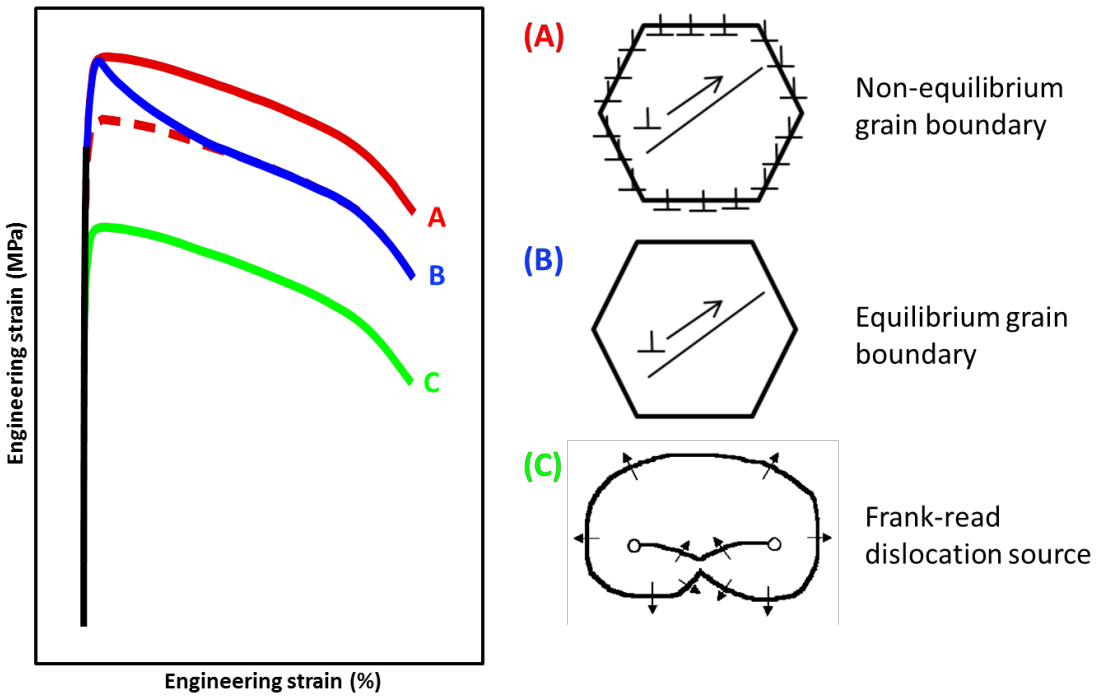

Figure 5.8. Schematic of relationship between stress-strain curves with grain boundary state. This explanation was inspired by Dislocation-Source Hardening. **[57]**

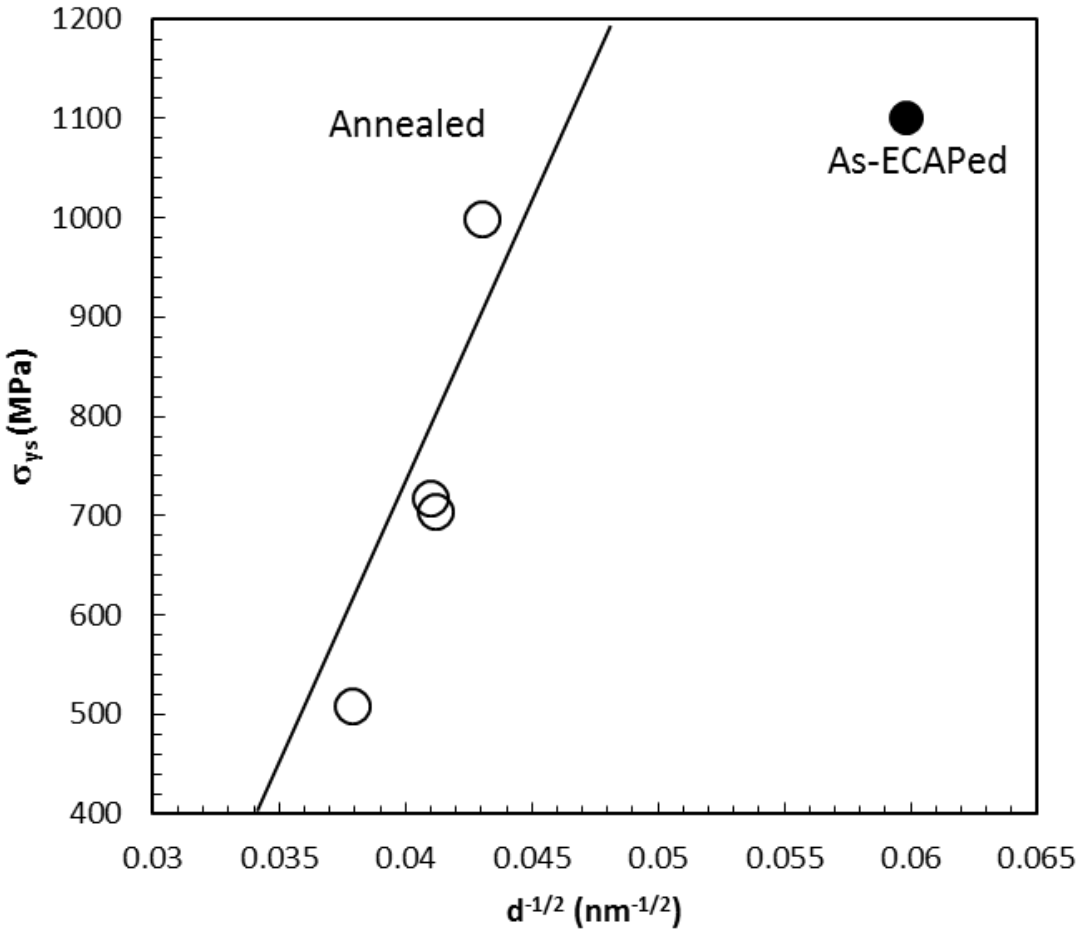

Figure 5.9. Hall-Petch plot for yield stress of as-ECAPed and post-ECAP annealed.

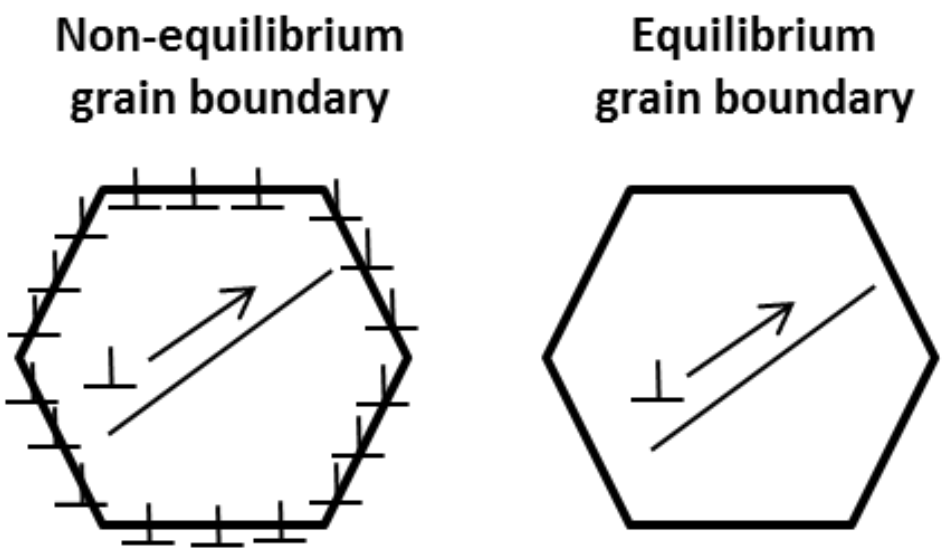

Figure 5.10. Dislocation and boundary strengthening for equilibrium and non-equilibrium grain boundary.

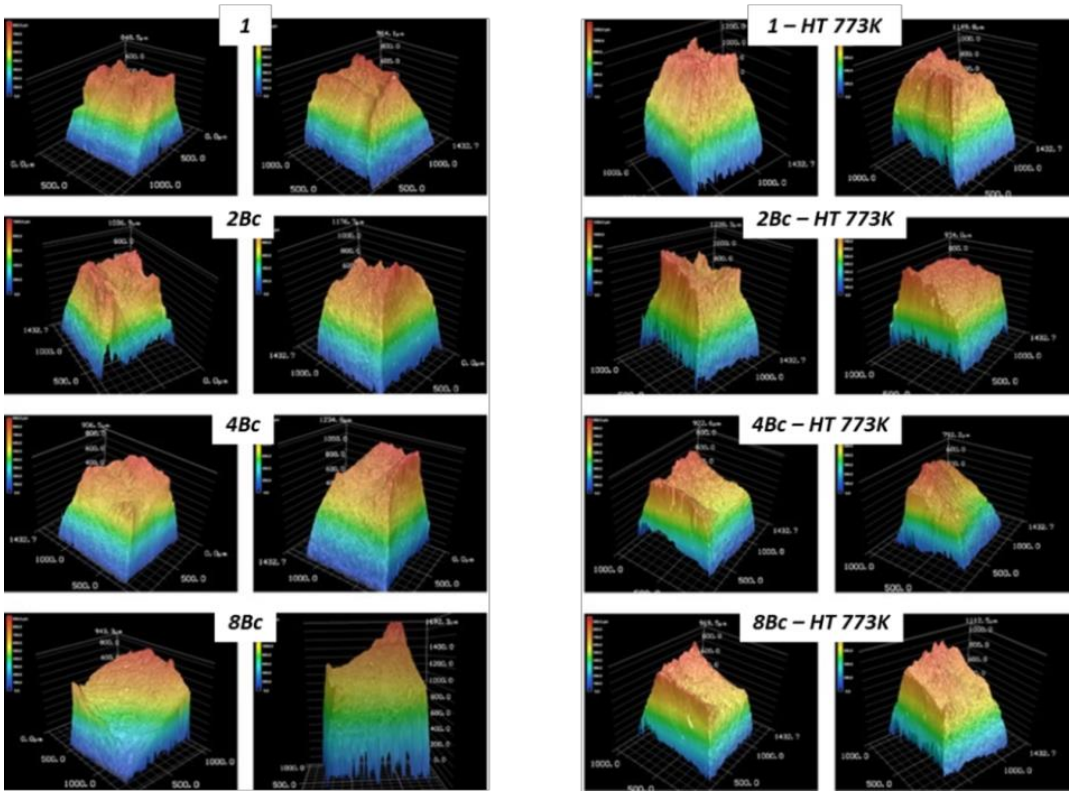

Figure 5.11. Fracture appearance of as-ECAPed and post-ECAP annealed sample by laser microscope observation.

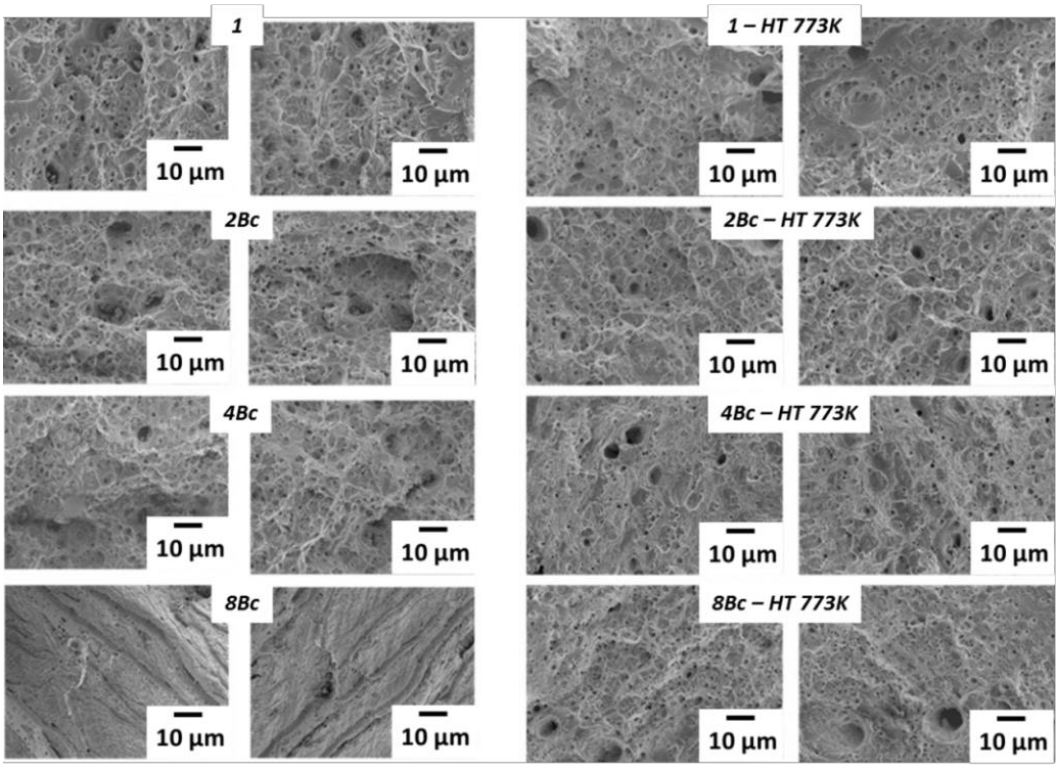

Figure 5.12. Dimple appearance as-ECAPed and post-ECAP annealed sample by SEM.

testing. After two passes, dimple appearance became smaller. Small dimples appear at local area and distributed on the fracture surface of four passes ECAP-processed sample. From the observation above, it can be explained that as received sample has good elongation with ductile fracture appearance. But with the increasing the number of passes, fracture mode is transformed from ductile to brittle. It can be confirmed with the decreasing elongation of ECAP-processed sample.

5.4. Conclusion

The ECAP method was used to refine the grain size of Low C, N Fe-20%Cr alloy. With the increasing number of passes, the average grain size was gradually refined and the minimum average grain size is about 100 nm when the sample was extruded after eight passes at room temperature. The micro hardness and the tensile strength increase with the number of passes, while the corresponding elongation decreases. The annealing at 773K for 1 h can increase the average grain size to 200 nm at eight passes ECAPed sample and improve the ductility of the ECAPed samples at the sacrifice of a little decrease in tensile strength. It also was found that yield stress became higher after ECAP and annealing, if it was compared with ECAPed sample with the same grain size.

References

[1] Langdon, T. G. (2013). Twenty-five years of ultrafine-grained materials: achieving exceptional properties through grain refinement. Acta Materialia, 61(19), 7035-7059.

[2] Valiev, R. Z., Islamgaliev, R. K., & Alexandrov, I. V. (2000). Bulk nanostructured materials from severe plastic deformation. Progress in materials science, 45(2), 103-189.

[3] Valiev, R. Z., & Langdon, T. G. (2006). Principles of equal-channel angular pressing as a processing tool for grain refinement. Progress in Materials Science, 51(7), 881-981..

[4] Nakayama, Y., Hayakawa, Y, Keikinzoku. (2012). Yielding behavior of 1050 aluminum fabricated by equal channel angular pressing and annealing. 軽金属,

62(11), 429-436.

[5] Cepeda-Jiménez, C. M., García-Infanta, J. M., Rauch, E. F., Blandin, J. J., Ruano, O. A., & Carreño, F. (2012). Influence of Processing Severity During Equal-Channel Angular Pressing on the Microstructure of an Al-Zn-Mg-Cu Alloy. Metallurgical and Materials Transactions A, 43(11), 4224-4236. .

[6] Huang, C. X., Hu, W., Yang, G., Zhang, Z. F., Wu, S. D., Wang, Q. Y., & Gottstein, G. (2012). The effect of stacking fault energy on equilibrium grain size and tensile properties of nanostructured copper and copper–aluminum alloys processed by equal channel angular pressing. Materials Science and Engineering: A, 556, 638-647..

[7] Gu, C. F., & Tóth, L. S. (2012). Texture development and grain refinement in non-equal-channel angular-pressed Al. Scripta Materialia, 67(1), 33-36..

[8] Zhilyaev, A. P., McNelley, T. R., & Ruano, O. A. (2012, April). Microstructure and Texture Evolution in Metals and Alloys during Intense Plastic Deformation. In Materials Science Forum (Vol. 715, pp. 51-60)..

[9] Tolaminejad, B., Brisset, F., & Baudin, T. (2012, March). EBSD study of the microstructure evolution in a commercially pure aluminium severely deformed by ECAP. In IOP Conference Series: Materials Science and Engineering (Vol. 32, No. 1, p. 012025). IOP Publishing.

[10] Wadamori, Y., Hirayama, K., Fujiwara, H., Uenoya, T., & Miyamoto, H. (2012). Misorientation Change of the Grain Boundary in Pure Copper Bicrystals Subjected to One-Pass Equal-Channel Angular Pressing. Materials Transactions, 53(11), 1858-1862..

[11] Wang, Q. J., Zhang, P. P., Du, Z. Z., & Wang, J. Y. (2012). Thermal stability of ultra-fine grained copper processed by equal channel angular pressing. Transactions of Materials and Heat Treatment, 33(8), 105-109.

[12] Orlov, D., & Vinogradov, A. (2011). The control of texture to improve high-cyclic fatigue performance in copper after equal channel angular pressing. Materials Science and Engineering: A, 530, 174-182.

[13] Wang, Q., Wang, Q., & Du, Z. (2011). Mechanical Properties of Ultra-fine Grain Copper Produced by Equal Channel Angular Pressing(ECAP). Tezhong Zuzao Ji

Youse Hejin(Special Casting & Nonferrous Alloys), 31(10), 887-890.

[14] Král, P., Dvořák, J., Kvapilová, M., Svoboda, M., Beneš, V., Ponížil, P. & Sklenička, V. (2010, February). Quantitative Characterization of Microstructure in Copper Processed by Equal-Channel Angular Pressing. In Materials Science Forum (Vol. 667, pp. 235-240).

[15] Głuchowski, W., Stobrawa, J. P., & Rdzawski, Z. M. (2011). Microstructure refinement of selected copper alloys strips processed by SPD method. Archives of Materials Science and engineering, 47(2), 103-109.

[16] Lugo, N., Llorca, N., Sunol, J. J., & Cabrera, J. M. (2010). Thermal stability of ultrafine grains size of pure copper obtained by equal-channel angular pressing. Journal of materials science, 45(9), 2264-2273.

[17] Zi, A. (2010). Pure copper processed by extrusion preceded equal channel angular pressing. Materials Characterization, 61(2), 141-144.

[18] Zhao, Y. H., Zhu, Y. T., Liao, X. Z., Horita, Z., & Langdon, T. G. (2006). Tailoring stacking fault energy for high ductility and high strength in ultrafine grained Cu and its alloy. Applied physics letters, 89(12), 121906.

[19] Han, W. Z., Wu, S. D., Li, S. X., & Wang, Y. D. (2008). Intermediate annealing of pure copper during cyclic equal channel angular pressing. Materials Science and Engineering: A, 483, 430-432.

[20] Zhilyaev, A. P., Kim, B. K., Szpunar, J. A., Baró, M. D., & Langdon, T. G. (2005). The microstructural characteristics of ultrafine-grained nickel. Materials Science and Engineering: A, 391(1), 377-389.

[21] Neishi, K., Horita, Z., & Langdon, T. G. (2002). Grain refinement of pure nickel using equal-channel angular pressing. Materials Science and Engineering: A, 325(1), 54-58.

[22] Zhilyaev, A. P., Baró, M. D., Langdon, T. G., & McNelley, T. R. (2004). An examination of microtexture and microstructure in ultrafine-grained nickel. Reviews on Advanced Materials Science, 7(1), 41-49.

[23] Akiyama, E., Zhang, Z., Watanabe, Y., & Tsuzaki, K. (2009). Effects of severe plastic deformation on the corrosion behavior of aluminum alloys. Journal of Solid State Electrochemistry, 13(2), 277-282.

[24] Nurislamova, G. V., Islamgaliev, R. K., & Valiev, R. (2006, January). Microstructure and Mechanical Properties of Pure Nickel Processed by Severe Plastic Deformation. In Materials Science Forum (Vol. 503, pp. 579-584).

[25] Zhilyaev, A. P., Gubicza, J., Nurislamova, G., Révész, Á., Suriñach, S., Baró, M. D., & Ungár, T. (2003). Microstructural characterization of ultrafine‐grained nickel. physica status solidi (a), 198(2), 263-271.

[26] Zhang, Y., Liu, J. Q., Wang, J. T., Wu, Z. B., & Liu, F. (2011, May). Microstructures and Mechanical Properties of Fcc Pure Metals with Different Stacking Fault Energies by Equal Channel Angular Pressing. In Materials Science Forum (Vol. 682, pp. 193-203).

[27] Liu, F., Zhang, Y., & Wang, J. T. (2010, February). Microstructure Evolution of Pure Nickel up to a High Strain Level during Equal-Channel Angular Pressing. In Materials Science Forum (Vol. 667, pp. 319-324).

[28] Shin, D. H., & Park, K. T. (2005). Ultrafine grained steels processed by equal channel angular pressing. Materials Science and Engineering: A, 410, 299-302.

[29] Shin, D. H., Kim, I., Kim, J., & Park, K. T. (2001). Grain refinement mechanism during equal-channel angular pressing of a low-carbon steel. Acta Materialia, 49(7), 1285-1292.

[30] Shin, D. H., Kim, B. C., Park, K. T., & Choo, W. Y. (2000). Microstructural changes in equal channel angular pressed low carbon steel by static annealing. Acta Materialia, 48(12), 3245-3252.

[31] Huang, C. X., Gao, Y. L., Yang, G., Wu, S. D., Li, G. Y., & Li, S. X. (2006). Bulk nanocrystalline stainless steel fabricated by equal channel angular pressing. Journal of materials research, 21(07), 1687-1692.

[32] Kim, J., Kim, I., & Shin, D. H. (2001). Development of deformation structures in low carbon steel by equal channel angular pressing. Scripta materialia, 45(4), 421-426.

[33] Pang, J. C., Yang, M. X., Yang, G., Wu, S. D., Li, S. X., & Zhang, Z. F. (2012). Tensile and fatigue properties of ultrafine-grained low-carbon steel processed by equal channel angular pressing. Materials Science and Engineering: A, 553, 157-163.

[34] Shin, D. H., Kim, W. J., & Choo, W. Y. (1999). Grain refinement of a commercial 0.15% C steel by equal-channel angular pressing. Scripta materialia, 41(3), 259-262.

[35] Shin, D. H., Seo, C. W., Kim, J., Park, K. T., & Choo, W. Y. (2000). Microstructures and mechanical properties of equal-channel angular pressed low carbon steel. Scripta Materialia, 42(7), 695-699.

[36] Son, Y. I., Lee, Y. K., Park, K. T., Lee, C. S., & Shin, D. H. (2005). Ultrafine grained ferrite–martensite dual phase steels fabricated via equal channel angular pressing: microstructure and tensile properties. Acta materialia, 53(11), 3125-3134.

[37] Xu, C., Furukawa, M., Horita, Z., & Langdon, T. G. (2005). The evolution of homogeneity and grain refinement during equal-channel angular pressing: A model for grain refinement in ECAP. Materials Science and Engineering: A, 398(1), 66-76.

[38] Xu, C., & Langdon, T. G. (2007). The development of hardness homogeneity in aluminum and an aluminum alloy processed by ECAP. Journal of materials science, 42(5), 1542-1550.

[39] Reihanian, M., Ebrahimi, R., Tsuji, N., & Moshksar, M. M. (2008). Analysis of the mechanical properties and deformation behavior of nanostructured commercially pure Al processed by equal channel angular pressing (ECAP). Materials Science and Engineering: A, 473(1), 189-194.

[40] Dvorak, J., Sklenicka, V., & Horita, Z. (2008). Microstructural evolution and mechanical properties of high purity aluminium processed by equal-channel angular pressing. Materials transactions, 49(1), 15-19.

[41] Saravanan, M., Pillai, R. M., Pai, B. C., Brahmakumar, M., & Ravi, K. R. (2006). Equal channel angular pressing of pure aluminium-an analysis. Bulletin of Materials Science, 29(7), 679.

[42] El-Danaf, E. A., Soliman, M. S., Almajid, A. A., & El-Rayes, M. M. (2007). Enhancement of mechanical properties and grain size refinement of commercial purity aluminum 1050 processed by ECAP. Materials Science and Engineering: A, 458(1), 226-234.

[43] Molodova, X., Gottstein, G., Winning, M., & Hellmig, R. J. (2007). Thermal stability of ECAP processed pure copper. Materials Science and Engineering: A, 460, 204-213.

[44] Wu, S. D., Wang, Z. G., Jiang, C. B., Li, G. Y., Alexandrov, I. V., & Valiev, R. Z. (2004). Shear bands in cyclically deformed ultrafine grained copper processed by ECAP. Materials Science and Engineering: A, 387, 560-564.

[45] Goto, M., Han, S. Z., Kim, S. S., Kawagoishi, N., & Lim, C. Y. (2007). Tensile Properties and Fatigue Strength of Ultrafine Grained Pure Copper. Key Engineering Materials, 353, 1649-1652.

[46] Qu, S., Huang, C. X., Gao, Y. L., Yang, G., Wu, S. D., Zang, Q. S., & Zhang, Z. F. (2008). Tensile and compressive properties of AISI 304L stainless steel subjected to equal channel angular pressing. Materials Science and Engineering: A, 475(1), 207-216..

[47] Zheng, Z. J., Gao, Y., Gui, Y., & Zhu, M. (2012). Corrosion behaviour of nanocrystalline 304 stainless steel prepared by equal channel angular pressing. Corrosion Science, 54, 60-67.

[48] Yang, M. X., Yang, G., Liu, Z. D., Wang, C. Y., & Huang, C. X. (2010, February). Microstructures and Tensile Properties of Maraging Steel Processed by Equal-Channel Angular Pressing. In Materials Science Forum (Vol. 667, pp. 421-426).

[49] Yang, G., & Yin, F. S. (2010, February). Effect of ECAP on the Microstructure and Mechanical Properties of 17-4PH Stainless Steel. In Materials Science Forum (Vol. 667, pp. 879-884).

[50] Akita, T., Gotoh, M., Dobatkin, S. V., Kitagawa, K., & Hirose, Y. (2010, April). Influence of annealing on strength of ultrafine grained low carbon steels by ECAP. In Materials Science Forum (Vol. 638, pp. 1899-1904).

[51] Han, B. Q., Mohamed, F. A., & Lavernia, E. J. (2003). Mechanical properties of iron processed by severe plastic deformation. Metallurgical and Materials Transactions A, 34(1), 71-83.

[52] Sabirov, I., Estrin, Y., Barnett, M. R., Timokhina, I., & Hodgson, P. D. (2008). Enhanced tensile ductility of an ultra-fine-grained aluminum alloy. Scripta materialia, 58(3), 163-166.

[53] Yang, G., Yang, M. X., Liu, Z. D., & Wang, C. (2011). Three-Dimensional Microstructures and Tensile Properties of Pure Iron During Equal Channel Angular Pressing. Journal of Iron and Steel Research, International, 18(12), 40-44.

[54] Luis, C. J., Puertas, I., Luri, R., León, J., Salcedo, D., & Pérez, I. (2012). Development of nanostructured Armco-Fe by equal channel angular extrusion (ECAE). Materials and Manufacturing Processes, 27(12), 1276-1284..

[55] Yang, G., Yang, M. X., Liu, Z. D., Wang, C., & Huang, C. X. (2010, February). Investigation on Three-Dimensional Microstructures and Tensile Properties of Pure Iron during Equal-Channel Angular Pressing. In Materials Science Forum (Vol. 667, pp. 791-796).

[56] Salimyanfard, F., Toroghinejad, M. R., Ashrafizadeh, F., Hoseini, M., & Szpunar, J. A. (2010). Textural evaluation of copper produced by equal channel angular pressing with routes A and B< sub> 30</sub>. Materials Science and Engineering: A, 527(23), 6260-6269.

[57] Kamikawa, N., Huang, X., Tsuji, N., & Hansen, N. (2009). Strengthening mechanisms in nanostructured high-purity aluminium deformed to high strain and annealed. Acta Materialia, 57(14), 4198-4208.

Chapter 6. Fatigue properties of UFG low C, N, Fe-20%Cr steel by ECAP

6.1. Introduction

Grain refinement in metals and alloys has been studied to improve the material strength by ECAP **[1,2]**. Nanostructured and UFG structure metals that subjected to cyclic loads became a significantly concern on their application **[3]**. There are many studies concerning the effective deformation routes ECAP for grain refinement in FCC structure metals such as pure aluminum **[4-6]**, nickel **[7-9]**, copper **[10-12]**, and titanium **[13-15]**. There are only a few report available on the relationship between the fatigue properties and microstructure evolution of UFG low C, N Fe-20%Cr steels by various ECAP deformation routes. These studies commonly focused on cyclic load for copper and aluminum alloy **[16-19]**.

UFG materials are to exhibit a lower resistance of fatigue crack growth. This phenomena is explained in view of intrinsic factors such as reverse plastic zone size and extrinsic factors such as roughness induced crack closure **[16,20].** Since the plastic deformation zone in the UFG materials is larger than grain size, a reverse slip of the dislocations during unloading is often impossible so that the accumulation of damage is large during cycling **[21]**. UFG materials are well known to have higher crack resistance, which leads to an increase in high-cycle fatigue life **[18]**. There have only a limited number of studies on the low cycle fatigue (LCF) behavior of UFG material

Cycle fatigue resistance and microstructural evolution of UFG materials will be discussed in term of microstructural evolution and LCF behavior.

6.2. Experimental procedure

The material used in this experiment had a chemical composition of low C,N Fe-20%Cr alloy with Cr 19.97, C 0.0020, N 0.0015 and Fe balance (in mass percent). This material was machined with dimensions of 8 mm × 8 mm × 120 mm for ECAP pressing. ECAP was carried out using a split die with two channels intersecting at an inner angle of 90° and an outer angle of 0° at 423 K. The samples were lubricated with high temperature fluorine lubricating grease and pressed four passes via routes A and

Bc. A TEM (JEM 2100F) was used to examine the microstructures. Thin foils for TEM were polished using abrasive papers to about 100 μm thick and then thinned by a twin-jet polishing Tenupol 5 facility using a solution of 40% acetic acid, 30% phosphoric acid, 20% nitric acid and 10% distilled water. Tensile experiments were conducted in a universal testing machine with $\varepsilon_{pl} = 5\times10^{-4}$ and 0.2 Hz frequency. Fatigue sample dimension is 1.5 × 1.5 mm^2 area and 2 mm gage length, as shown in **Figure 6.1**. This specimen was grinded with grinding paper from #200 - #1500, and then polished by electro polishing technique.

6.3. Result and discussion

The microstructure after four ECAP pass is homogeneous with several amounts of HAGB fraction, as is commonly observed in BCC metals at this equivalent strain. **Figure 6.2** show shows a representative large area of the sample by TEM observation. With four passes the structure becomes much more uniform, as confirmed by the large area TEM observations shown in **Figure 6.2**. An elongated grain structure can be seen in the deformed sample after four passes. SADP analysis shows a ring diffraction that related UFG structure. It is concluded that while a UFG structure forms in many materials during SPD, UFG can be produced in iron chromium alloys. High density dislocation configurations are seen in TEM images. These dislocations are supposed to be responsible for the high elastic strains which accumulate in the lattice during ECAP by X-ray line broadening **[22]**.

The process of grain refinement by SPD can be seen in **Figure 6.3** for several kinds of deformation route. **Figure 6.3** was obtained by EBSD on transverse planes by ECAP for four passes ECAP via routes A and Bc. Due to the low orientation resolution, boundaries with misorientation smaller than 2° were omitted. It is apparent that grains are finely subdivided after four pass of ECAP. After four passes via route A, grain boundaries, mostly HAGB, are set in the planar parallel boundaries whereas via route Bc, microstructures are equiaxed grain substructure can be recognized.

Stress strain curves can be seen in figure for the samples manufactured at 423 K with up to four ECAP passes via routes A and Bc, as shown in **Figure 6.4**. Work

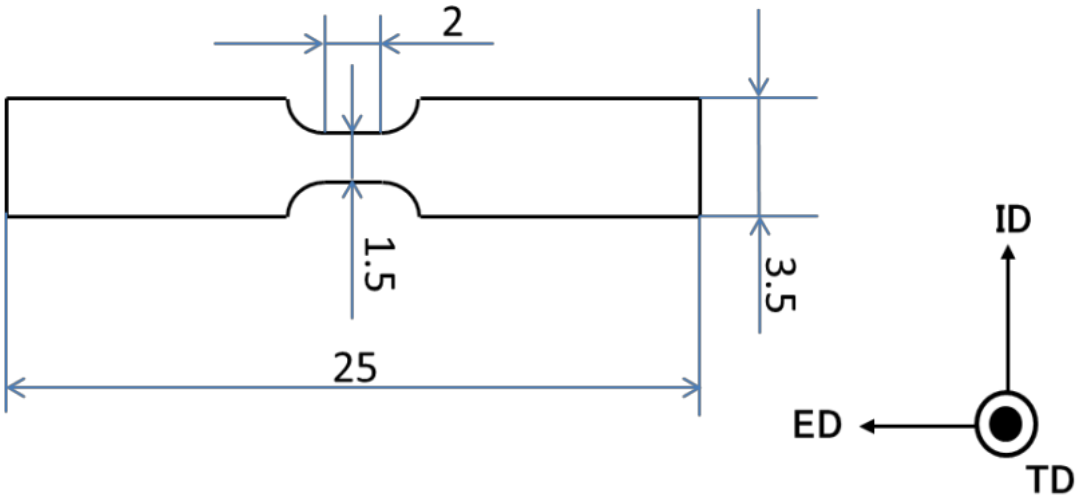

Figure 6.1. Schematic of fatigue specimen.

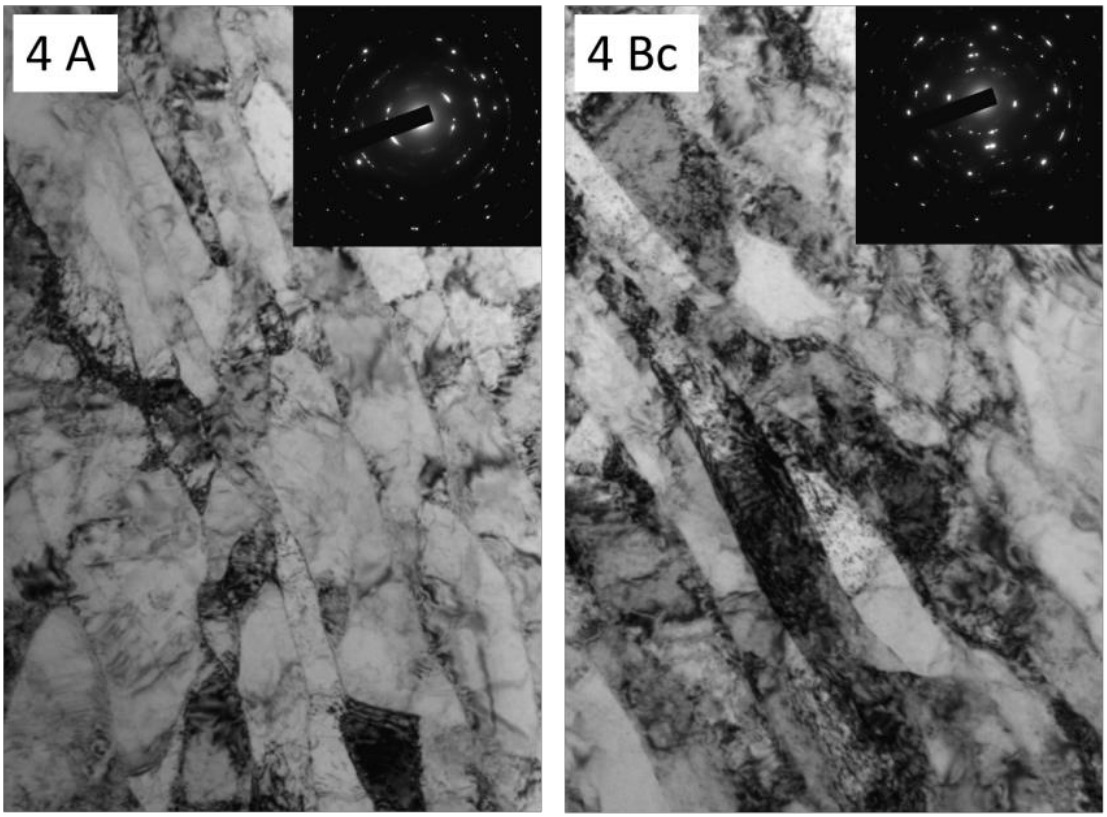

Figure 6.2. TEM micrograph of four passes ECAP via routes A and Bc (transverse plane).

hardening is observed after ECAP, although the ductility is limited, as is commonly observed in SPD metals **[23-28]**. After four passes, the tensile strength increases while the elongation drastically. The ECAPed sample via routes A and Bc exhibited comparable. Cyclic softening is common for most cold worked and ECAPed sample. The cyclic softening is associated with dislocation density in fatigue of ECAPed sample in general.

The fatigue life of the ECAPed via route Bc specimens is much shorter than that of route A, as shown in **Figure 6.5**. This results is not unexpected in view of their lower ductility, as has been discussed in the literature **[29-34]**. LCF behavior of iron chromium steel after ECAP for up to four passes shows that the deformation microstructure remained fine and stable after cyclic deformation. However, the LCF life decreased along with the limited ductility, as is commonly observed for materials manufactured by ECAP, as shown in **Table 6.1**.

Table 6.1. Effect of ECAP deformation route on stress amplitude and fatigue life.

No	Route	Stress amplitude	Fatigue life
1	A	Large	Short
2	Bc	Medium	Long

Fatigue fracture image by SEM of iron chromium alloy manufactured by four passes ECAP via routes A and Bc can be seen in **Figure 6.6**. Fatigue appearance can be seen less pronounced and micro cracks. According to literature, It can be showed that at low stress amplitudes in the high cycle fatigue (HCF) regime, where plastic incompatibilities between neighboring grains are small and can be neglected, micro cracks tend to initiate preferentially **[35]**.

Grain refinement by ECAP improved resistance to fatigue crack nucleation, which is controlled by strength. However, the grain refinement has a harmful effect on LCF properties associated with subcritical crack growth, which is controlled by ductility **[36, 37]**. Fatigue fracture of routes A occurred along shear band in 45 degree, but route Bc showed longer propagation than route A.

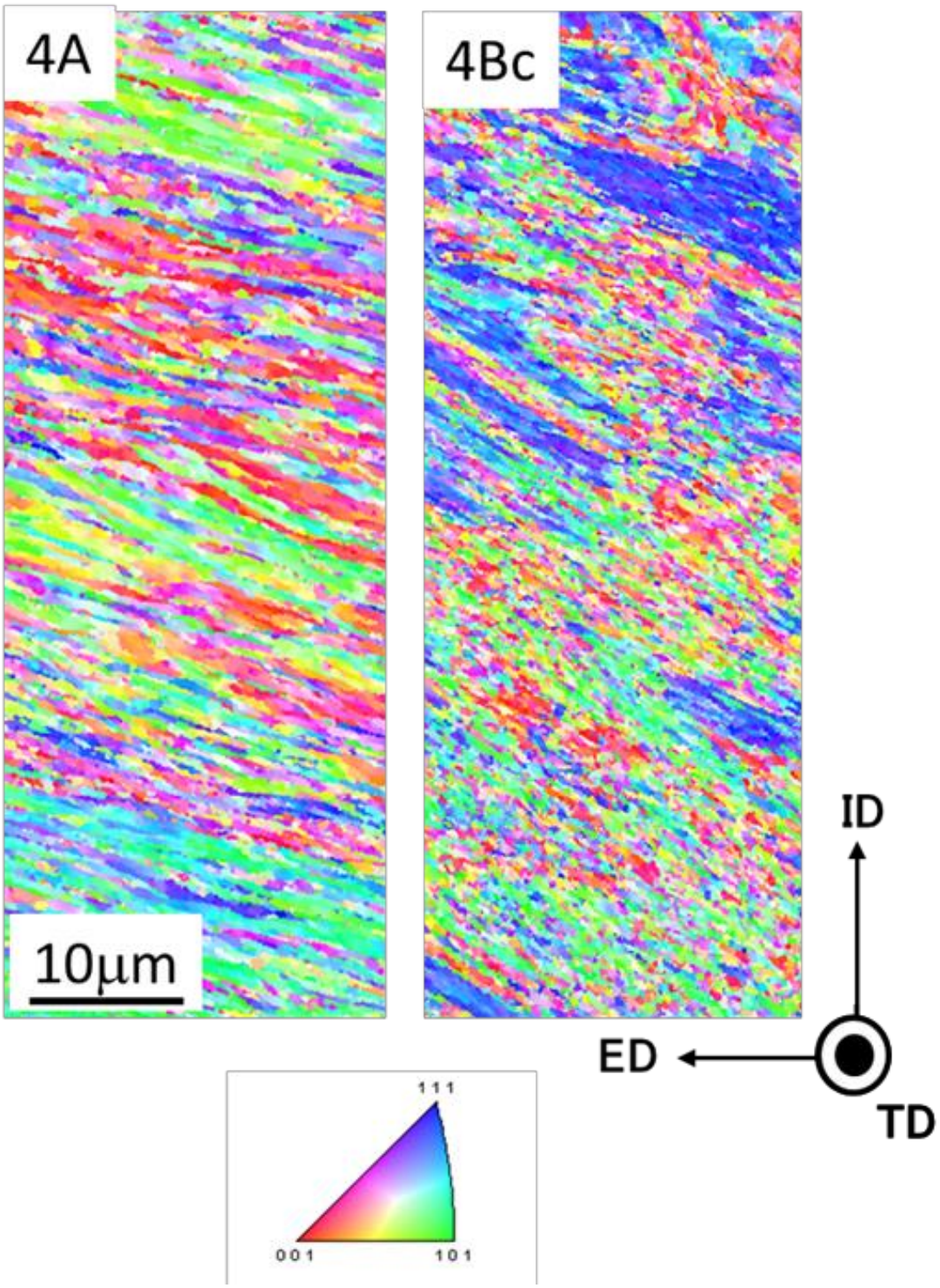

Figure 6.3. Misorientation image map of four passes ECAPed by route A and Bc.

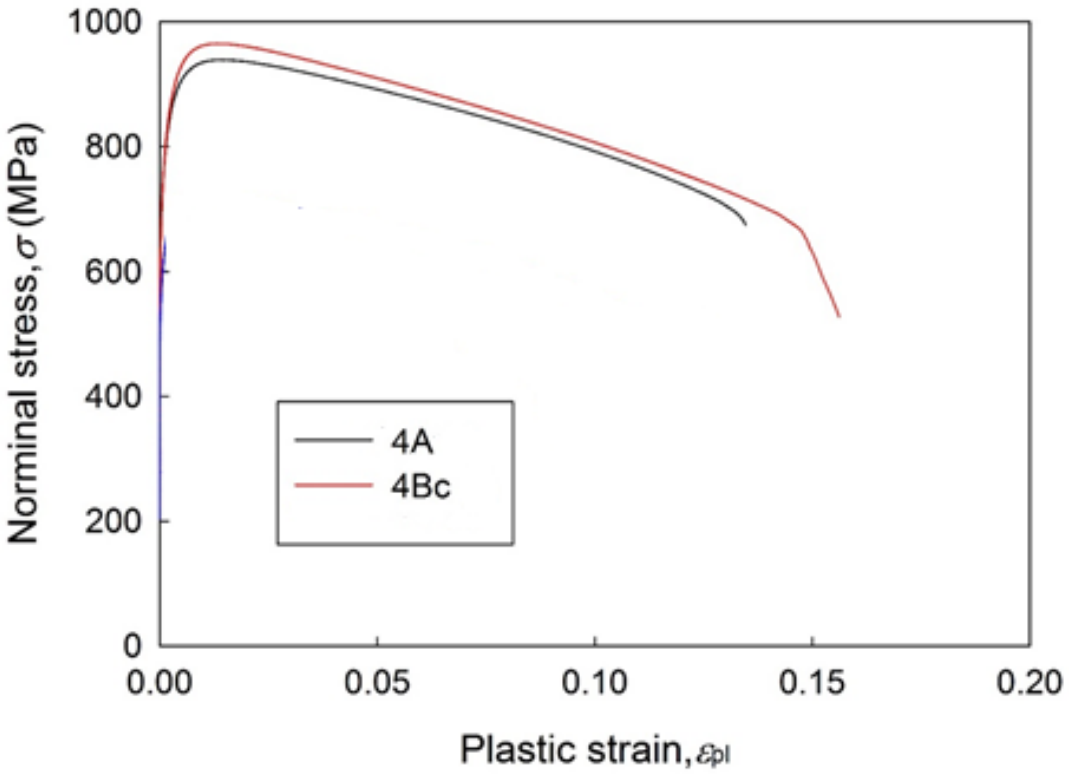

Figure 6.4. Stress and strain curve of four passes ECAPed by routes A and Bc.

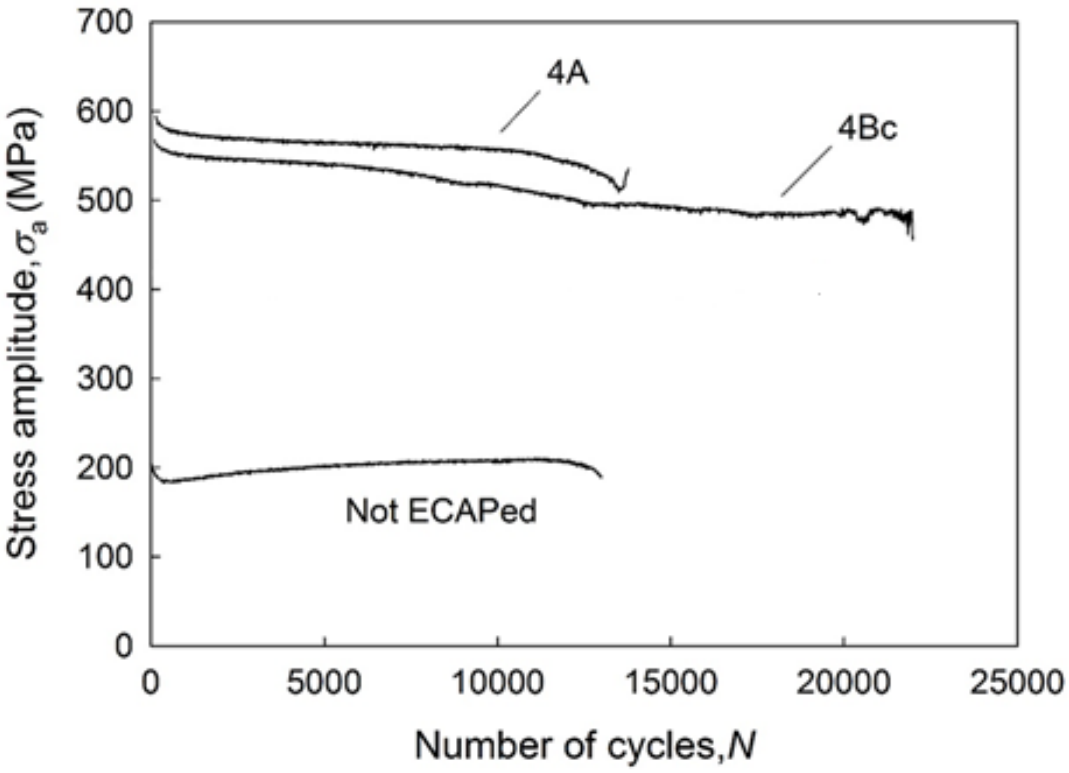

Figure 6.5. Stress amplitude and number of cycles graph of as received and as-ECAPed.

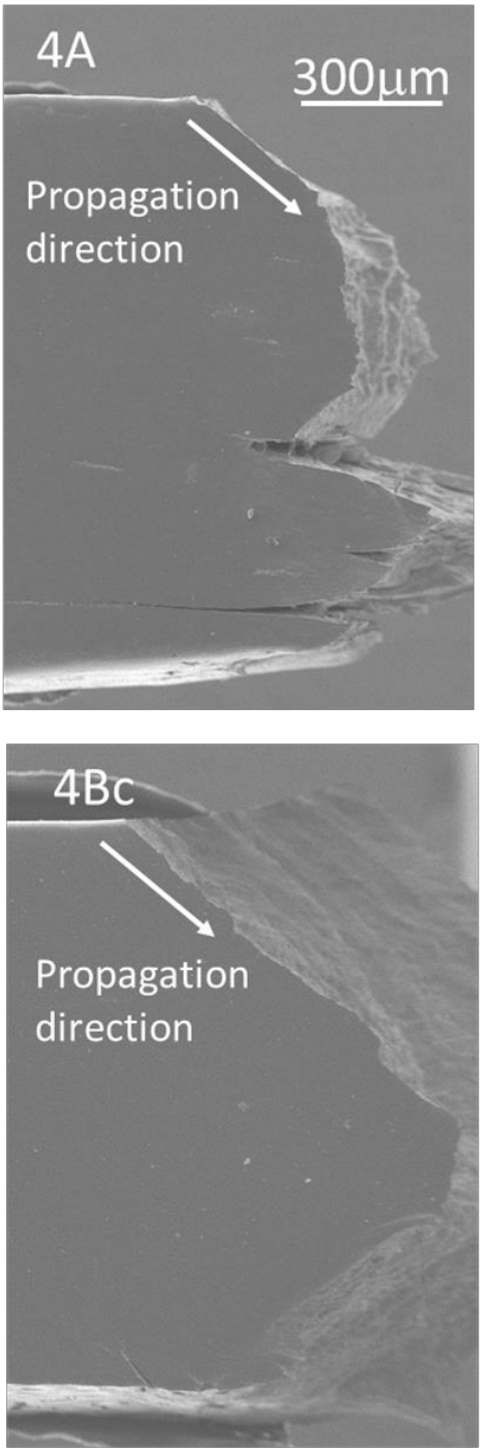

Figure 6.6. Fatigue fracture side appearance of as-ECAPed sample by routes A and Bc.

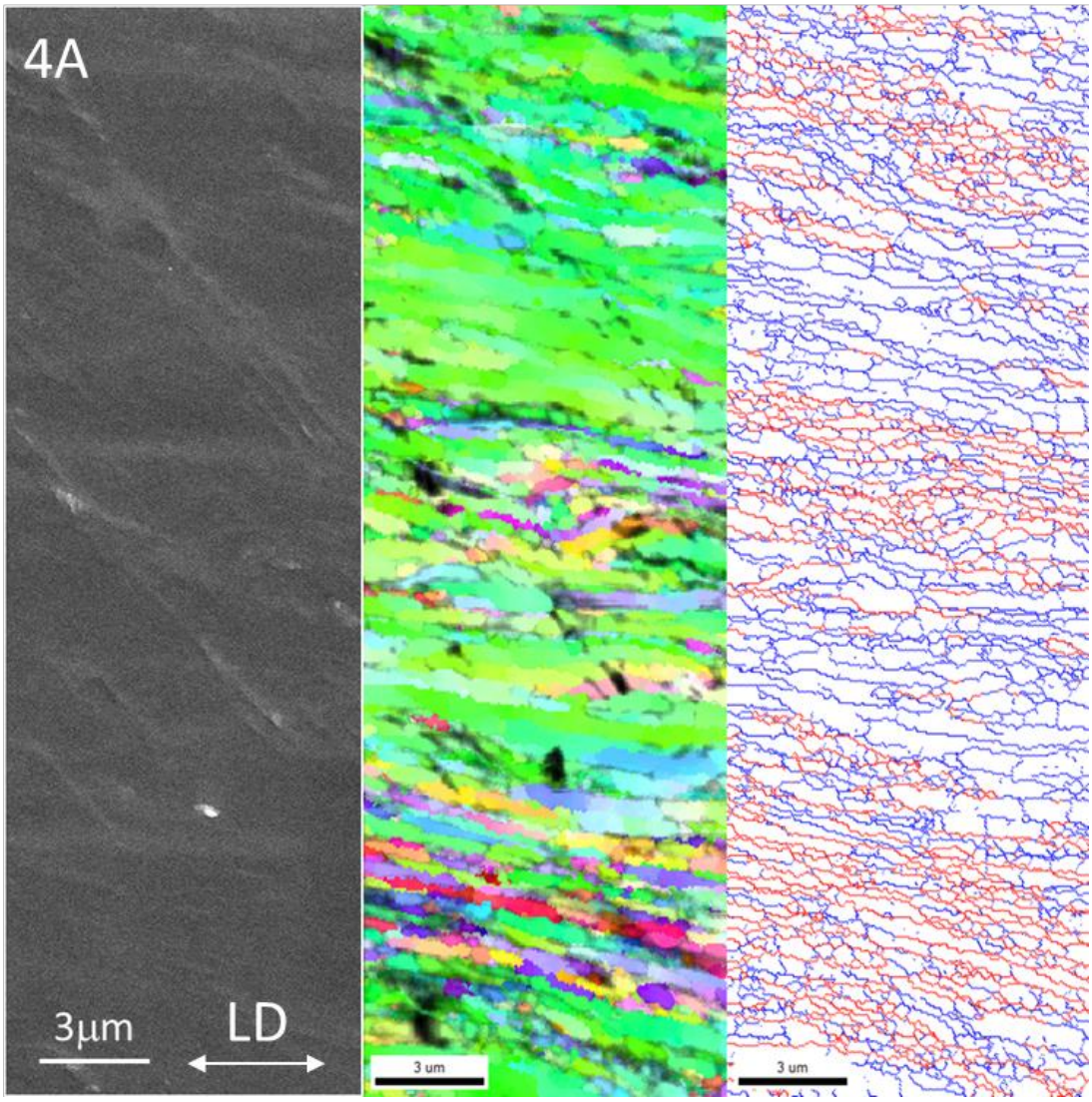

Figure 6.7. Misorientation image map of fatigue fracture side on four passes ECAP by route A.

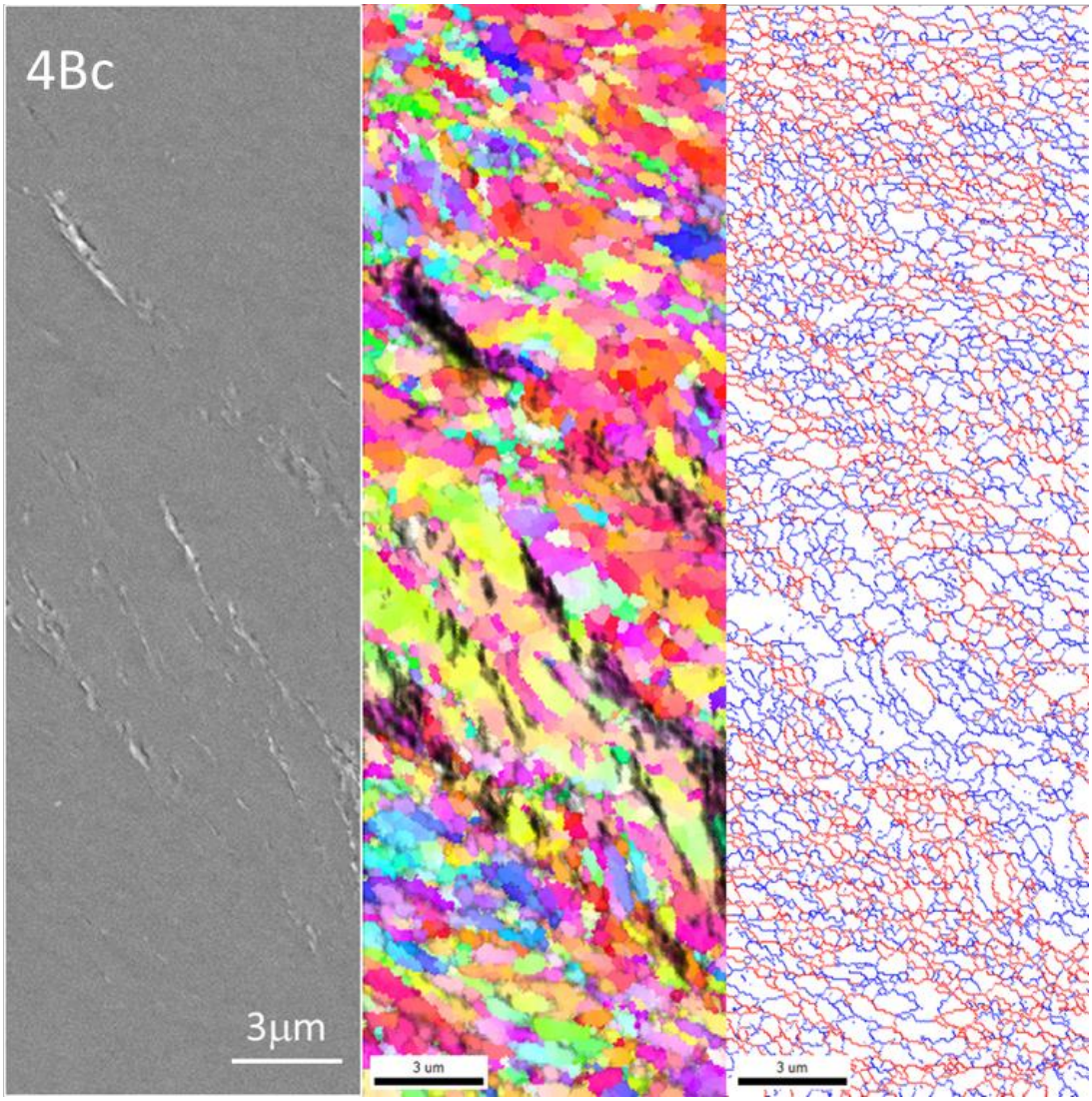

Figure 6.8. Misorientation image map of fatigue fracture side on four passes ECAP by route Bc.

EBSD analysis of fatigue fracture on route A exhibited several information, such as linear crack propagation, initiation of crack in coarse grain area and layered grain growth, as shown in **Figure 6.7**. And then, route Bc exhibited multiple crack propagation, initiation crack in coarse grain and equiaxed grain growth, as shown in **Figure 6.8**.

6.4. Conclusion

The low C, N Fe-20%Cr alloy has been subjected to SPD by ECAP at 423 K up to four passes via route Bc. A relatively uniform nanostructure had formed after four ECAP passes. Microstructural observations showed that the UFG structure formed by ECAP. Following a common trend for SPD metals the yield strength increased significantly after the first ECAP processing and kept increasing gradually with increasing accumulated strain during further pressing.

References

[1] Valiev, R. Z., Estrin, Y., Horita, Z., Langdon, T. G., Zechetbauer, M. J., & Zhu, Y. T. (2006). Producing bulk ultrafine-grained materials by severe plastic deformation. Jom, 58(4), 33-39.

[2] Valiev, R. Z., Korznikov, A. V., & Mulyukov, R. R. (1993). Structure and properties of ultrafine-grained materials produced by severe plastic deformation. Materials Science and Engineering: A, 168(2), 141-148.

[3] Mishnaevsky Jr, L., Levashov, E., Valiev, R. Z., Segurado, J., Sabirov, I., Enikeev, N., ... & Smolin, A. (2014). Nanostructured titanium-based materials for medical implants: Modeling and development. Materials Science and Engineering: R: Reports, 81, 1-19.

[4] Tsuji, N., Ito, Y., Saito, Y., & Minamino, Y. (2002). Strength and ductility of ultrafine grained aluminum and iron produced by ARB and annealing. Scripta Materialia, 47(12), 893-899.

[5] Tsuji, N., Toyoda, T., Minamino, Y., Koizumi, Y., Yamane, T., Komatsu, M., & Kiritani, M. (2003). Microstructural change of ultrafine-grained aluminum during high-speed plastic deformation. Materials Science and Engineering: A, 350(1),

108-116.

[6] Höppel, H. W., May, J., & Göken, M. (2004). Enhanced Strength and Ductility in Ultrafine‐Grained Aluminium Produced by Accumulative Roll Bonding. Advanced engineering materials, 6(9), 781-784.

[7] Zhilyaev, A. P., Kim, B. K., Szpunar, J. A., Baró, M. D., & Langdon, T. G. (2005). The microstructural characteristics of ultrafine-grained nickel. Materials Science and Engineering: A, 391(1), 377-389.

[8] Zhilyaev, A. P., Gubicza, J., Nurislamova, G., Révész, Á., Suriñach, S., Baró, M. D., & Ungár, T. (2003). Microstructural characterization of ultrafine‐grained nickel. physica status solidi (a), 198(2), 263-271.

[9] Krasilnikov, N., Lojkowski, W., Pakiela, Z., & Valiev, R. (2005). Tensile strength and ductility of ultra-fine-grained nickel processed by severe plastic deformation. Materials Science and Engineering: A, 397(1), 330-337.

[10] Zhao, Y. H., Zhu, Y. T., Liao, X. Z., Horita, Z., & Langdon, T. G. (2006). Tailoring stacking fault energy for high ductility and high strength in ultrafine grained Cu and its alloy. Applied physics letters, 89(12), 121906.

[11] Takata, N., Lee, S. H., & Tsuji, N. (2009). Ultrafine grained copper alloy sheets having both high strength and high electric conductivity. Materials Letters, 63(21), 1757-1760.

[12] Li, Y. S., Zhang, Y., Tao, N. R., & Lu, K. (2008). Effect of thermal annealing on mechanical properties of a nanostructured copper prepared by means of dynamic plastic deformation. Scripta Materialia, 59(4), 475-478.

[13] Stolyarov, V. V., Zhu, Y. T., Lowe, T. C., Islamgaliev, R. K., & Valiev, R. Z. (1999). A two step SPD processing of ultrafine-grained titanium. Nanostructured Materials, 11(7), 947-954.

[14] Shankar, M. R., Rao, B. C., Lee, S., Chandrasekar, S., King, A. H., & Compton, W. D. (2006). Severe plastic deformation (SPD) of titanium at near-ambient temperature. Acta Materialia, 54(14), 3691-3700.

[15] Sergueeva, A. V., Stolyarov, V. V., Valiev, R. Z., & Mukherjee, A. K. (2001). Advanced mechanical properties of pure titanium with ultrafine grained structure. Scripta Materialia, 45(7), 747-752.

[16] Rabinovich, M. K., & Markushev, M. V. (1995). Influence of fine grained structure and superplastic deformation on the strength of aluminium alloys. Journal of materials science, 30(18), 4692-4702.

[17] Agnew, S. R., & Weertman, J. R. (1998). Cyclic softening of ultrafine grain copper. Materials Science and Engineering: A, 244(2), 145-153.

[18] Patlan, V., Vinogradov, A., Higashi, K., & Kitagawa, K. (2001). Overview of fatigue properties of fine grain 5056 Al-Mg alloy processed by equal-channel angular pressing. Materials Science and Engineering: A, 300(1), 171-182..

[19] Agnew, S. R., Vinogradov, A. Y., Hashimoto, S., & Weertman, J. R. (1999). Overview of fatigue performance of Cu processed by severe plastic deformation. Journal of Electronic Materials, 28(9), 1038-1044..

[20] Vinogradov, A., Nagasaki, S., Patlan, V., Kitagawa, K., & Kawazoe, M. (1999). Fatigue properties of 5056 Al-Mg alloy produced by equal-channel angular pressing. Nanostructured materials, 11(7), 925-934.

[21] Kim, H. K., Choi, M. I., Chung, C. S., & Shin, D. H. (2003). Fatigue properties of ultrafine grained low carbon steel produced by equal channel angular pressing. Materials Science and Engineering: A, 340(1), 243-250.

[22] Ueno, H., Kakihata, K., Kaneko, Y., Hashimoto, S., & Vinogradov, A. (2011). Enhanced fatigue properties of nanostructured austenitic SUS 316L stainless steel. Acta Materialia, 59(18), 7060-7069.

[23] Han, B. Q., Mohamed, F. A., & Lavernia, E. J. (2003). Mechanical properties of iron processed by severe plastic deformation. Metallurgical and Materials Transactions A, 34(1), 71-83.

[24] Sabirov, I., Estrin, Y., Barnett, M. R., Timokhina, I., & Hodgson, P. D. (2008). Enhanced tensile ductility of an ultra-fine-grained aluminum alloy. Scripta materialia, 58(3), 163-166.

[25] Yang, G., Yang, M. X., Liu, Z. D., & Wang, C. (2011). Three-Dimensional Microstructures and Tensile Properties of Pure Iron During Equal Channel Angular Pressing. Journal of Iron and Steel Research, International, 18(12), 40-44.

[26] Luis, C. J., Puertas, I., Luri, R., León, J., Salcedo, D., & Pérez, I. (2012). Development of nanostructured Armco-Fe by equal channel angular extrusion

(ECAE). Materials and Manufacturing Processes, 27(12), 1276-1284..

[27] Yang, G., Yang, M. X., Liu, Z. D., Wang, C., & Huang, C. X. (2010, February). Investigation on Three-Dimensional Microstructures and Tensile Properties of Pure Iron during Equal-Channel Angular Pressing. In Materials Science Forum (Vol. 667, pp. 791-796).

[28] Salimyanfard, F., Toroghinejad, M. R., Ashrafizadeh, F., Hoseini, M., & Szpunar, J. A. (2010). Textural evaluation of copper produced by equal channel angular pressing with routes A and B< sub> 30</sub>. Materials Science and Engineering: A, 527(23), 6260-6269.

[29] Mughrabi, H., Höppel, H. W., & Kautz, M. (2004). Fatigue and microstructure of ultrafine-grained metals produced by severe plastic deformation. Scripta Materialia, 51(8), 807-812.

[30] Mughrabi, H., Höppel, H. W., Kautz, M., & Valiev, R. Z. (2003). Annealing treatments to enhance thermal and mechanical stability of ultrafine-grained metals produced by severe plastic deformation. Zeitschrift für Metallkunde, 94(10), 1079-1083.

[31] Vinogradov, A., & Hashimoto, S. (2001). Multiscale phenomena in fatigue of ultra-fine grain materials--an overview. Materials Transactions(Japan), 42(1), 74-84.

[32] Vinogradov, A., & Hashimoto, S. (2003). Fatigue of severely deformed metals. Advanced Engineering Materials, 5(5), 351-358.

[33] Vinogradov, A., Hashimoto, S., & Kopylov, V. I. (2003). Enhanced strength and fatigue life of ultra-fine grain Fe–36Ni Invar alloy. Materials Science and Engineering: A, 355(1), 277-285.

[34] Vinogradov, A. (2007). Fatigue limit and crack growth in ultra-fine grain metals produced by severe plastic deformation. Journal of materials science, 42(5), 1797-1808.

[35] Heinz, A., & Neumann, P. (1990). Crack initiation during high cycle fatigue of an austenitic steel. Acta metallurgica et materialia, 38(10), 1933-1940.

[36] Kim, H. K., Choi, M. I., Chung, C. S., & Shin, D. H. (2003). Fatigue properties of ultrafine grained low carbon steel produced by equal channel angular pressing.

Materials Science and Engineering: A, 340(1), 243-250.

[37] Sawai, T., Matsuoka, S., & Tsuzaki, K. (2003). Low- and High-cycle Fatigue Properties of Ultrafine-grained Low Carbon Steels. Tetsu-to-Hagane(Journal of the Iron and Steel Institute of Japan), 89(6), 726-733.

Chapter 7. Effect of annealing on pitting corrosion of UFG low C, N Fe-20%Cr steels fabricated by ECAP

7.1. Introduction

SPD is now recognized as a process to fabricate nanocrystalline or UFG metallic materials in a bulk form **[1]**. Deformation-induced nanocrystalline or UFG materials by SPD exhibit high strength with smaller sacrifice of ductility **[1,2]**. Since SPD does not require alloying element for strengthening, it is also expected to become an important processing for structural application. Microstructural development and resultant deformation-induced grain subdivision during SPD has been of interest from scientific and practical standpoints, and have extensively been studied with mechanical and physical properties in the last 20 years **[1,3-5]**. Corrosion properties are also important properties for structural application. The beneficial effect of grain size reduction to the nano-scale was first demonstrated for intergranular corrosion in electrodeposited nanocrystalline nickel by the pioneering work of Rofagha et al. **[6]**, and followed by Kim et al **[7,8]**. They observed a rather smooth surface with a smaller penetration rate at grain boundaries and thus considerable improvement in intergranular corrosion. For SPD materials, corrosion behavior such as general corrosion **[9-19]**, intergranular corrosion **[20-22]** and pitting corrosion **[20,23-31]** of UFG aluminum and aluminum alloy **[16,20,21,23,24,28-31]**, copper and copper alloy **[10,14,18,27]** as well as stainless steels **[9,11,17,22,26]** and magnesium **[12,13,15,19]** processed by SPD, and corrosive environment dependence **[32-34]** have been reported. For example, corrosion resistance of aluminum alloys has mostly been reported to improve by UFG formation by SPD **[16,20,24,28,29]** and is attributed to (1) fragmentation of precipitation or second phase which tend to be pitting sites **[16,20,24,28,29]**, and (2) dissolution of precipitation forming supersaturation. When the precipitation becomes smaller than critical size, it does not work as cathode site for pitting formation **[29]**. For Fe-Cr steels in which passivation occurs by Cr elements, pitting corrosion resistance is enhanced by UFG formation by SPD because Cr diffusion to the surface is enhanced by high density of dislocations and grain boundaries, and promotes the passivation **[11,26,35,36]**.

Corrosion resistance is expected to be enhanced by UFG structure by the following two reasons. First, the increase of grain boundary area may reduce the impurity segregation at grain boundaries. It is, in general, called “dilution effect”. If one suppose that all impurity atoms are segregated at grain boundaries, impurity concentration at grain boundaries become 1000 times higher than that bulk concentration. However, it become 100 times higher than that of bulk concentration if the grain size become 500 nm, and it becomes further reduced to 10 times in a grain size of 20 nm, as shown in **Figure 7.1.a.** Reduced segregation may reduce grain boundary energy and chemical reaction in a corrosive media so that the resistance to intergranular corrosion, intergranular SCC, corrosion fatigue can be enhanced.

Second effect is mechanical rather than chemical. When materials are under stress state, plastic deformation is inhomogeneous. Namely, dislocation piled up at grain boundaries forming the local stress concentration in the vicinity of grain boundaries, as shown in **Figure 7.1.b.** According to the classical dislocation theory, stress concentration becomes n times higher than applied stress when the number of pile-up dislocations is n. Stress concentration at grain boundaries in a corrosive environment may facilitate crack formation along grain boundaries under static and cyclic load. When grain size is reduced to submicron scale, dislocation can no more remain inside the grains. Therefore, stress becomes more homogeneous. Such a homogeneous stress state may enhance the resistance to crack formation at grain boundaries. In addition, inhomogeneity of dislocation structures such as slip bands, deformation bands, persistant slip bands (PSB) can be suppressed, which may also enhance the resistance to crack formation.

UFG metals by SPD exhibits unique mechanical and physical properties. Deformation-induced nanocrystalline or UFG structure with stored dislocations and non-equilibrium grain boundaries are believed to cause these unique properties. For example, Huang reported that UFG aluminum fabricated by ARB become harder by post-ARB annealing, and becomes softer by the subsequent deformation. The present author reported that corrosion resistance of UFG copper was inferior to coarse grain counterparts, but was improved by short-time post-ECAP annealing without

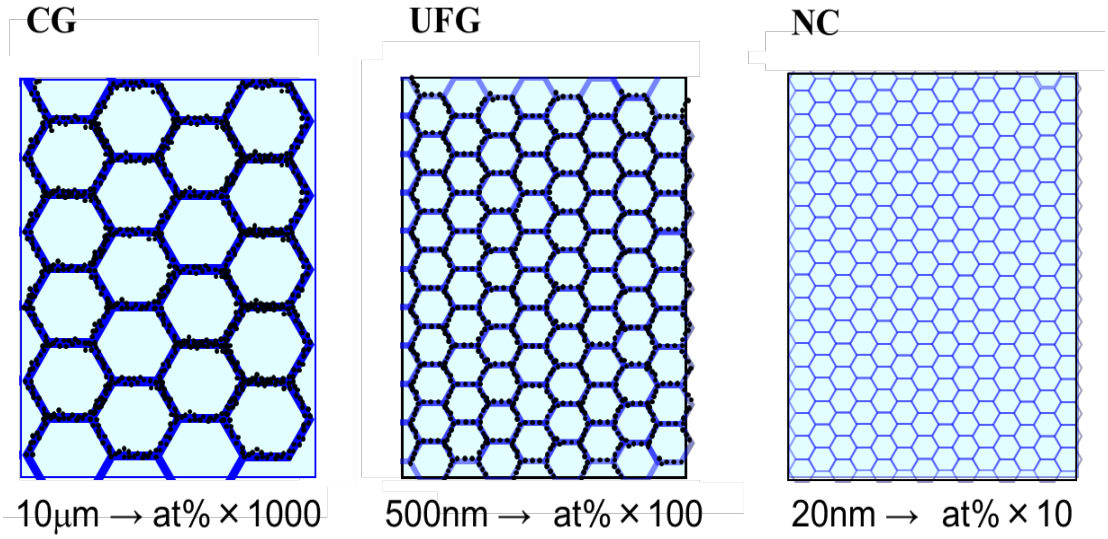

(a)

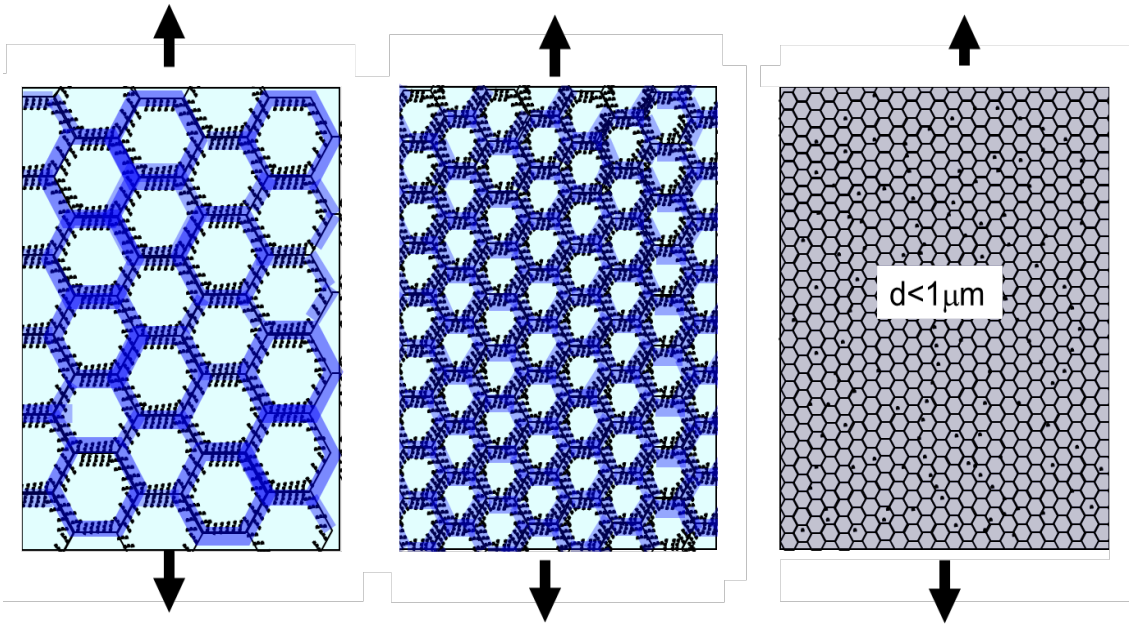

(b)

Figure 7.1. (a) Schematic of dilution effect on UFG structure material, (b) Schematic of local stress concentration in the vicinity of grain boundaries.

accompanying grain size change. This improvement is attributed to the grain boundary structural change from non-equilibrium to equilibrium state. Since non-equilibrium grain boundaries comprise the extrinsic grain boundary dislocations **[1]**, mechanical, physical and chemical properties should be affected **[1]**. However, corrosion properties have not been well studied from this view point as compared with mechanical properties. In this study, effect of post-ECAP annealing on pitting corrosion of low-C,N Fe-20%Cr steels is investigated focusing on the structural transition which may occur during annealing process.

7.2. Experimental Procedure

7.2.1 Material

The material used in this experiment has a chemical composition of low-C,N Fe-20%Cr with Cr; 20.03, C; 0.0004, N; 0.0013 and Fe balance (in mass percent). Measurement of chemical composition of the material was carried by Nitetsu Sumikin Technology Co.Ltd. A chemical analysis of C, Cr and N contents were measured by infrared absorption spectroscopy, inductively coupled plasma emission spectrometry and inert gas fusion method, respectively.

7.2.2 Sample Processing

This material was machined with dimensions of 8 × 8 × 100 mm^3 for ECAP pressing. ECAP procedures are carried out up to 8 passes at 423 K via the so-called route Bc using a split die with two channels intersecting at an inner angle of 90°. The samples are lubricated with high temperature fluorine lubricating grease. After ECAP, billets were annealed using infrared furnace (ULVAC MILA5000) from 473 to 1373 K in a vacuum for one hour. A corrosion testing specimen was prepared from an ECAPed sample using a spark-erosion machine. The specimen was in the shape of a square with an area of 8 mm x 6 mm and a thickness of 2 mm. This specimen was soldered with a connection cable on the backside of the surface of the corrosion and then coated with

epoxy molding to cover the connection. The edge area was sealed with tape to prevent any corrosion due to edge effect of pitting corrosion. The mounted specimen was ground with grind paper from #240 until #2000 and then polished with buff paper with alumina suspension (PRESI^{TM}) 9 μm, 3 μm, and 1 μm. For the last step of the polishing process, an OP-S suspension (Struers^{TM}) was used.

7.2.3 Micro hardness

The micro hardness experiments were performed on a Vickers hardness testing machine under a load, for 15 s dwell time after each annealing. Hardness testing was carried out for ten times per each sample.

7.2.4. Microstructural characterization

A FE-SEM (JSM 7001F), equipped with EBSD (Oxford Instrument Co.) image was used to observe orientation map of grains. EBSD orientation maps were processed using INCA^{TM} software.

A FE-TEM (JEM 2100F) was used to examine the microstructures. Thin foils for TEM were polished using abrasive papers to about 100 μm thick and then thinned by a twin-jet polishing Tenupol 5 facility (Struers Co.Ltd) using a solution of 40% acetic acid, 30% phosphoric acid, 20% nitric acid and 10% distilled water.

7.2.5. XRD

XRD on ECAPed and post-annealed sample was carried out by SmartLab, Rigaku. XRD samples surface was polished by automatic polisher. The SmartLab x-ray diffractometer used CuKα, 40 kV, 0.2 A from 30 until 120 deg with continuous scanning type. FWHM was determined after fitting the scattered XRD data.

7.2.6. Electrochemical testing

The specimen for pitting corrosion testing is shown in **Figure 7.2.a**. Pitting corrosion testing was carried out in neutral solutions of 1000 mol·m^{-3} NaCl at room temperature by dynamic anodic polarization, using a potentiostat (HOKUTO H100) at a scan rate of 20 mV/min, a corrosion current, and an Ag/AgCl reference electrode were recorded by a data logger. Ag/AgCl electrode reference was put in 3000 mol·m^{-3} KCl (potassium chloride solution saturated) for three times. This pitting testing arrangement is shown in **Figure 7.2.b**. Before pitting corrosion testing was carried out, argon gas was used to remove dissolved oxygen. The testing process was initialized after the open circuit potential (OCP) of the specimen was stabilized. The polarization was started from 50mV lower than the OCP after immersion in the test solution for 5 minutes.

The potential at which the passivation starts to break down at localized areas, leading to pitting, is defined as the pitting potential. Pitting potential can be determined from anodic polarization curve as the potential at which the current starts to sharply rise with increasing potential **[37]** and pitting potential was defined accordingly as shown in **Fig. 1.13.** The pitting potential of as received specimen was -0.033 V versus Ag/AgCl.

7.3. Results

7.3.1. Micro hardness

Vickers hardness of after the post-ECAP annealing at temperature ranging from 473-1373K was shown in **Figure 7.3**. The hardness exhibited the typical three-stages softening. Namely, the hardness remained relatively constant after the annealing at temperature up to 698 K and then declined considerably until the temperature of 973 K. The hardness remained again constant at higher temperature. In the general interpretation for this softening behavior, recovery process might proceeds accompanying dislocation rearrangement and annihilation in the first stage where the hardness relatively remains constant, followed by the recrystallization which

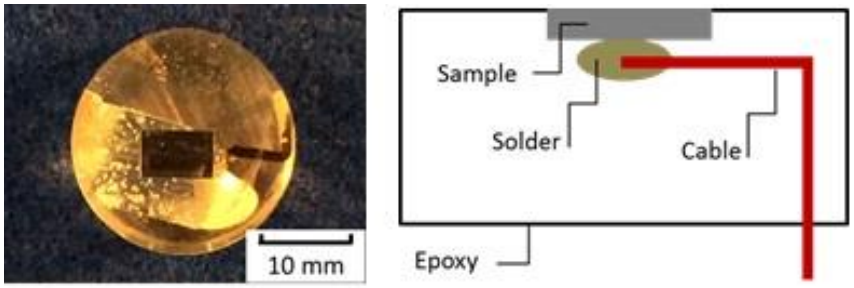

(a) (b)

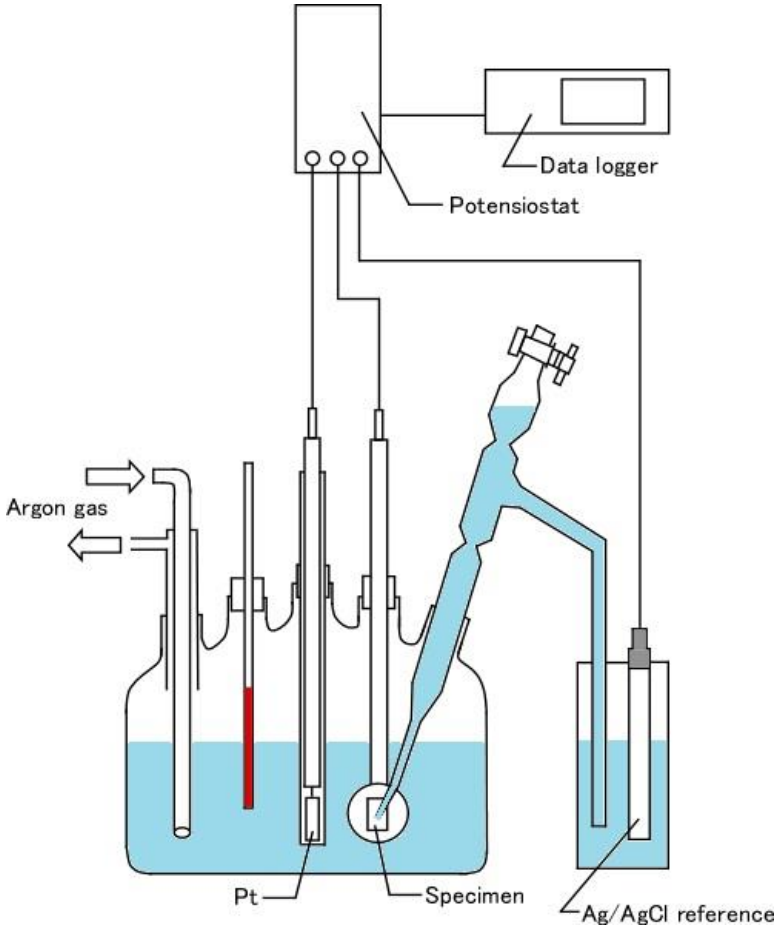

(c)

Figure 7.2. (a) Pitting testing specimen, (b) schema of specimen (electric conduction), (c) Schematic of pitting testing equipment arrangement.

accompany the noticeable softening in the second stage and grain growth of constant hardness again as the third stage.

7.3.2. Microstructural characterization

OIM by EBSD after the post-ECAP annealing is shown in **Figure 7.4**. UFG structure of grain size less than 200 nm can be recognized in as-ECAPed state, and the grain size remained constant in the first stage at temperature up to 698 K. In the second stage from 698 to 973 K where significant softening occurred, uniform grain growth was observed. This uniform grain growth during post-ECAP annealing is contrasted with those observed in FCC structure metals such as copper **[38-41]**, nickel **[41, 32]** and austenitic stainless steels **[43]** where a small fraction of grains grow preferentially, replacing the other smaller grains. This inhomogeneous microstructure coarsening observed in FCC metals is similar to abnormal grain growth, and can be viewed also as nucleation and the grain growth process in the discontinuous recrystallization **[38]**. In BCC structure metals, on the other hand, strain energy stored as dislocations can be released in recovery process easily prior to recrystallization. Therefore, strain energy stored in UFG structures in as-ECAP state was possibly released prior to the next stage, resulting in the formation of UFG with less stored strain energy. Uniform grain size distribution with high fraction of HAGB may lead to uniform grain growth whose driving force is solely grain boundary energy **[44]**, rather than the nucleation-growth mode of restoration which requires strain energy as driving force.

The micro hardness indenter appearance and Hall-Petch relation for annealed UFG specimens can be seen in **Figure 7.5**. The linear fit was applied only to data corresponding to annealing temperatures from 298 – 823 K. In high temperature range, only the grain size affects material hardness as the dislocation density is high. At low temperatures, both grain size and dislocation density contribute to strengthening and the linear fit of microhardness data. **Figure 7.6** shows TEM micrographs of as-ECAPed and after post-ECAP annealing at 698 K. If one compares two micrographs, the grain sizes are essentially the same, and little difference is recognized. However, detail observation

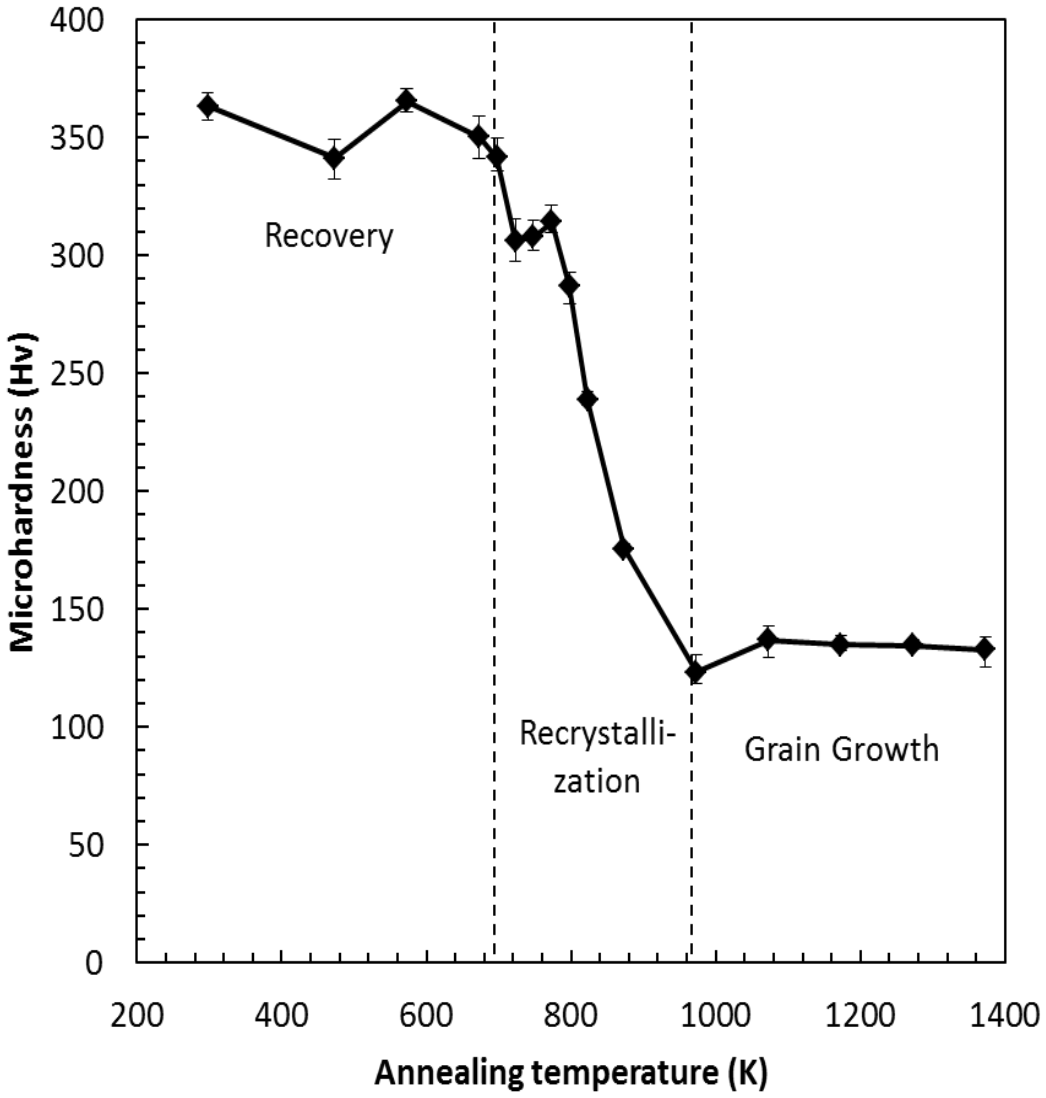

Figure 7.3. Effect of the post-ECAP annealing temperature on Vickers hardness

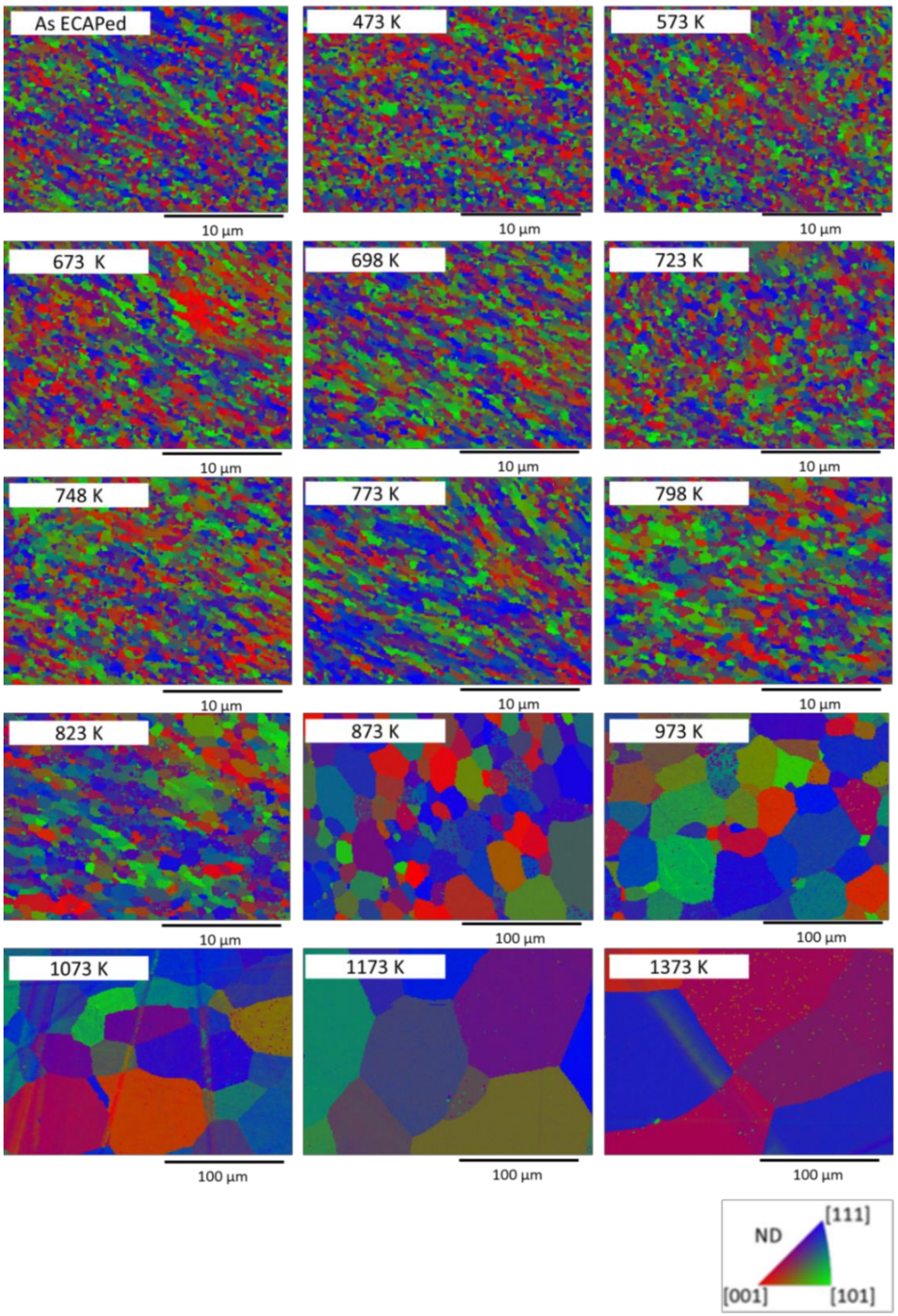

Figure 7.4. Color OIM obtained by EBSD after the post-ECAP annealing

can notice that there are some grains with darker contrast in as-ECAPed state, which indicate dislocation was stored inside grains.

This suggests that some fraction of dislocations stored by SPD was released by the post-ECAP annealing. **Figure 7.7** shows XRD after ECAP and the annealing. In as-ECAP state, significant line broadening can be observed, and this line broadening is a result of non-equilibrium grain boundaries having a high density of extrinsic defects in their structure and resultant long range elastic stresses **[45,46]**. After the annealing this line broadening becomes sharper with increasing temperature. Thus, the parameter *X* is defined as a measure of the structural change during the annealing as follows:

$$X = \frac{(W_i - W_r)}{(W_d - W_r)} \tag{7.1}$$

where W_i is width of the peak at half height at temperature T_i, W_r and W_d are those in recrystallized and deformed state, respectively. **Figure 7.8** shows the variation of *X* parameter of {110} as a function of annealing temperature. Note that the parameter *X* started to decrease at lower temperature than that hardness decreased as shown in **Figure 7.3**. This early reduction of *X* was reported in pure iron **[47]**, and can be interpreted as follows, (1) the partial annihilation of stored dislocations by recovery process. Recovery process is fast in BCC as compared with FCC metals because of easy cross-slip of screw dislocations, and (2) change from non-equilibrium grain boundaries to equilibrium grain boundaries and relaxation of internal elastic stress. Since non-equilibrium grain boundaries have extrinsic grain boundaries dislocations, they exert stress field in grain interior. The annihilation and rearrangement of extrinsic dislocations result in the relaxation of internal elastic stress **[45, 46]**.

7.3.3. Electrochemical properties

The **Figure 7.9** shows the time-dependence of the anodic current density of

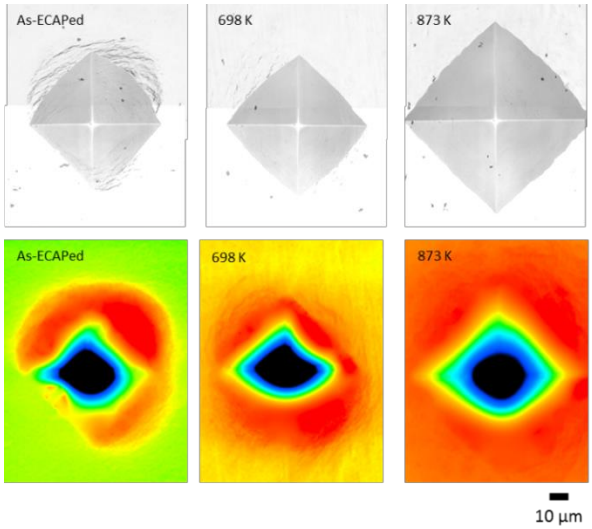

(a)

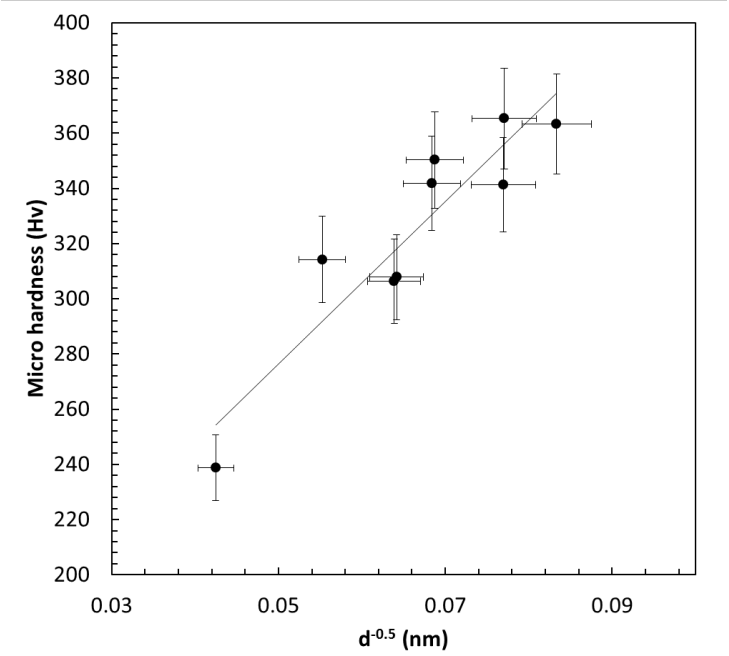

(b)

Figure 7.5. (a) Indenter appearance of Vickers hardness, (b) relationship between hardness and grain size.

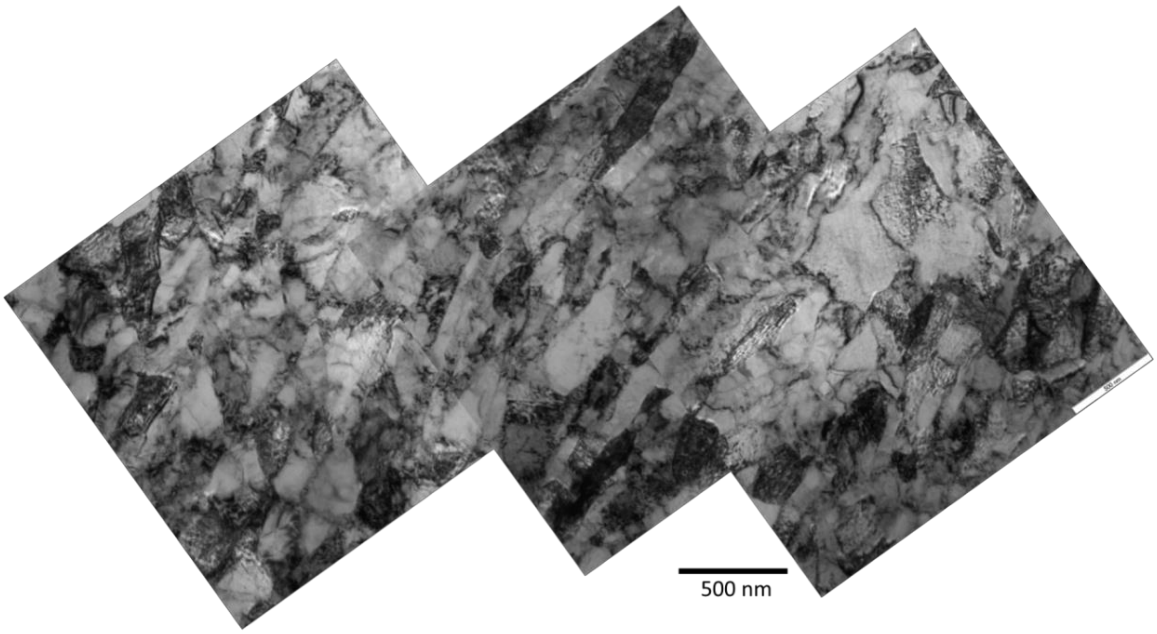

(a)

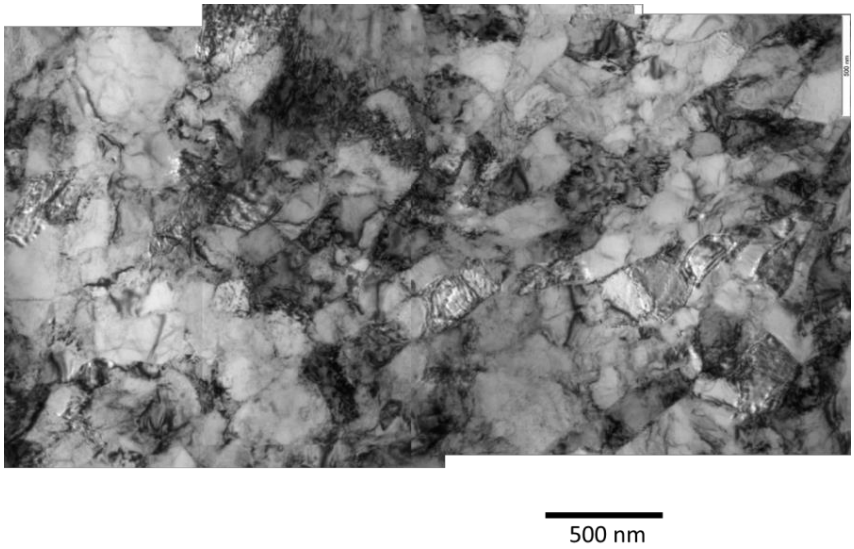

(b)

Figure 7.6. TEM micrographs (a)after eight passes ECAP, and (b) after post-ECAP annealing at 698K

passes number variation at 1,2,4 and 8 passes via route Bc, while kept at constant potential. The anode current density of ECAPed sample increased sharply after a certain period of time due to the initiation of pitting corrosion.

The time required before the initiation of pitting corrosion for sample was longer with high pass number ECAP than without. It could be seen in **Figure 7.9**, Sample of 8 pass ECAP shows the slowest corrosion occurrence. The degree of increase in time of sample with high pass number ECAP was smaller than that without. The anodic current density after initiating pitting corrosion, or the growth rate of pitting corrosion, was also smaller with ECAP than without ECAP. Resistance to pitting corrosion is investigated by dynamic anodic polarization tests as shown in **Figure 7.10**. As typical anodic behavior, anodic current stayed at relatively constant level and increased abruptly at a nobler potential than a critical value where pitting start to form. Only as-ECAPed state exhibited anomalous two-stage development prior to pitting. This high anodic current at passive region in as-ECAPed state may be associated with defective passive film formed on the surface with high grain boundaries and dislocation density. Pitting potential, E_p versus Ag/AgCl, increased with annealing temperature as shown in **Figure 7.11. (a)**. If E_p versus Ag/AgCl is plotted as a function of the parameter X, then these two has linear relation, as shown in **Figure 7.11(b).** Pitting corrosion was confirmed from laser microscope observations, which shows that larger and more pitting corrosion occurred after annealing process as shown in **Figure 7.12**.

7.4. Discussion

Pitting corrosion of stainless steel is a form of corrosion in which the chromium in the passive layer is dissolved removing iron. Pitting is localized attack that can produce penetration of a stainless steel with weight loss to the total structure. Pitting is associated with a local discontinuity of the passive film. It can be a mechanical imperfection, such as an inclusion or surface damage, or it can be a local chemical breakdown of the film **[48]**. Once a pit is formed, it in effect becomes a crevice; the

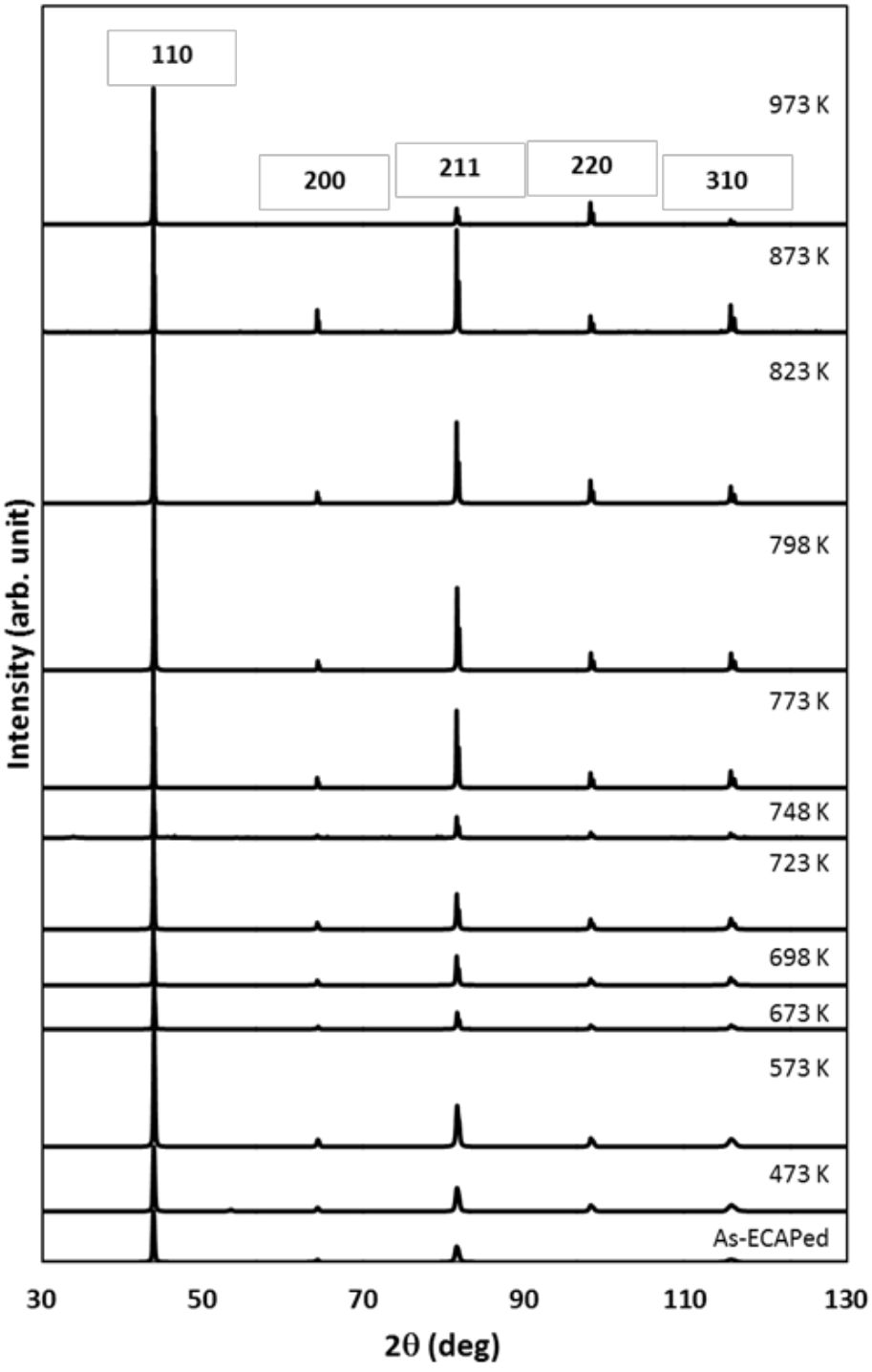

Figure 7.7. X-ray {110} diffractions after ECAP and annealing.

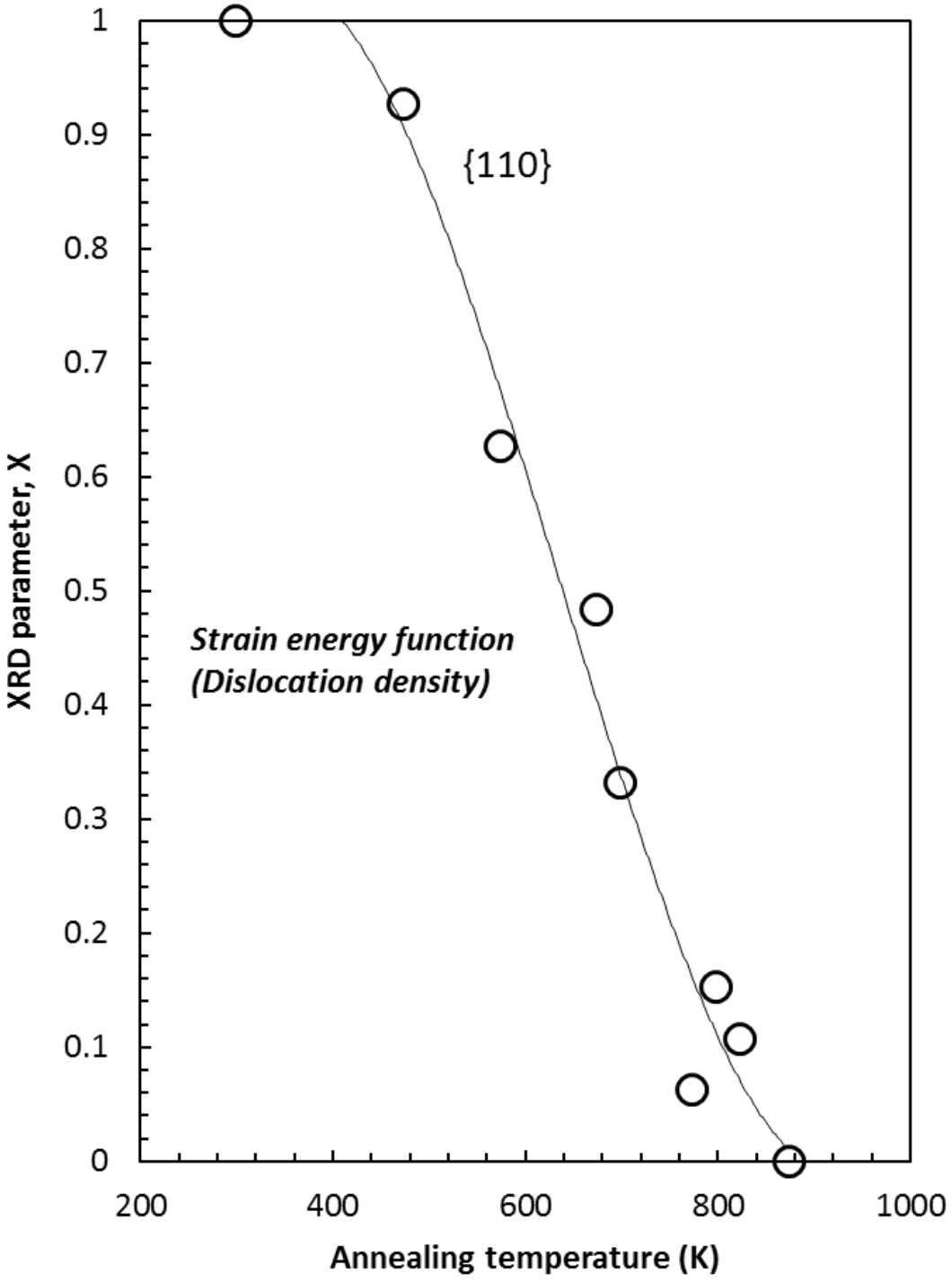

Figure 7.8. X-ray parameter as a function of the post-ECAP annealing temperature

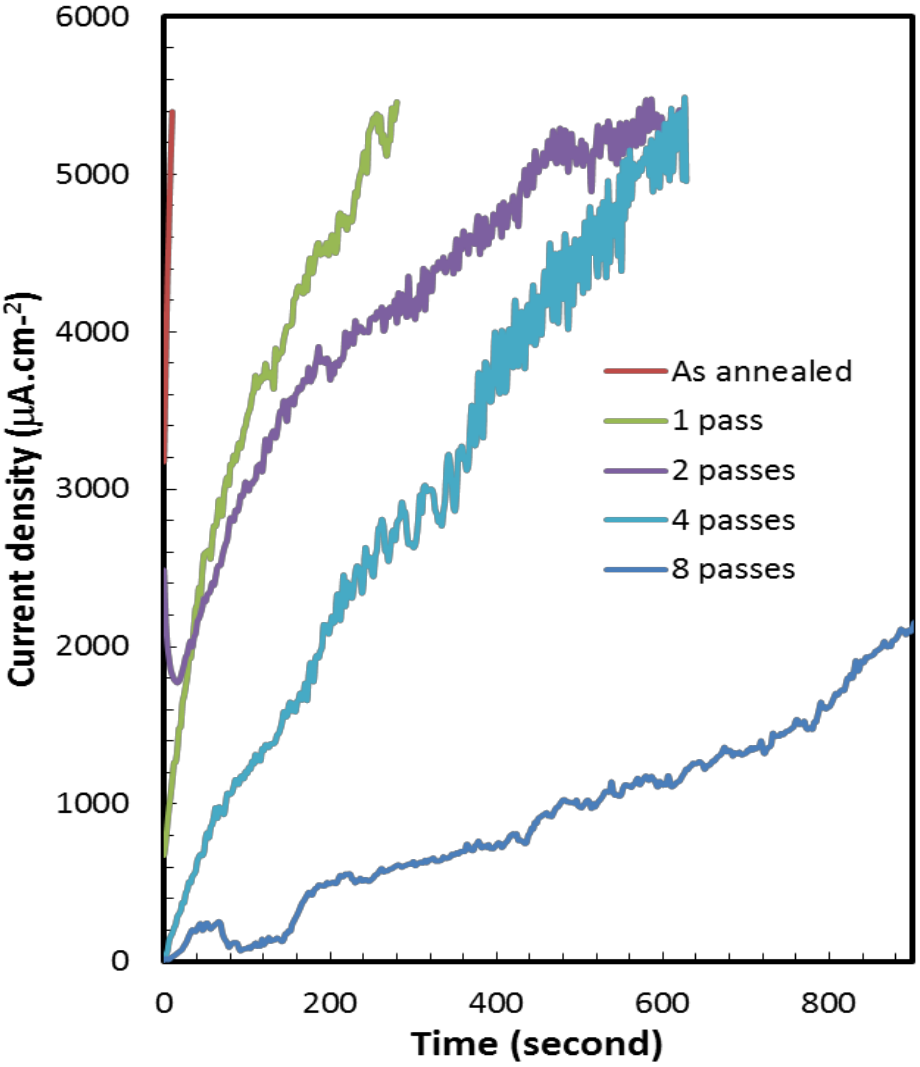

Figure 7.9. the time-dependence of the anodic current density of passes number variation at 1,2,4 and 8 passes via route B in 1000 mol·m-3 NaCl solution.

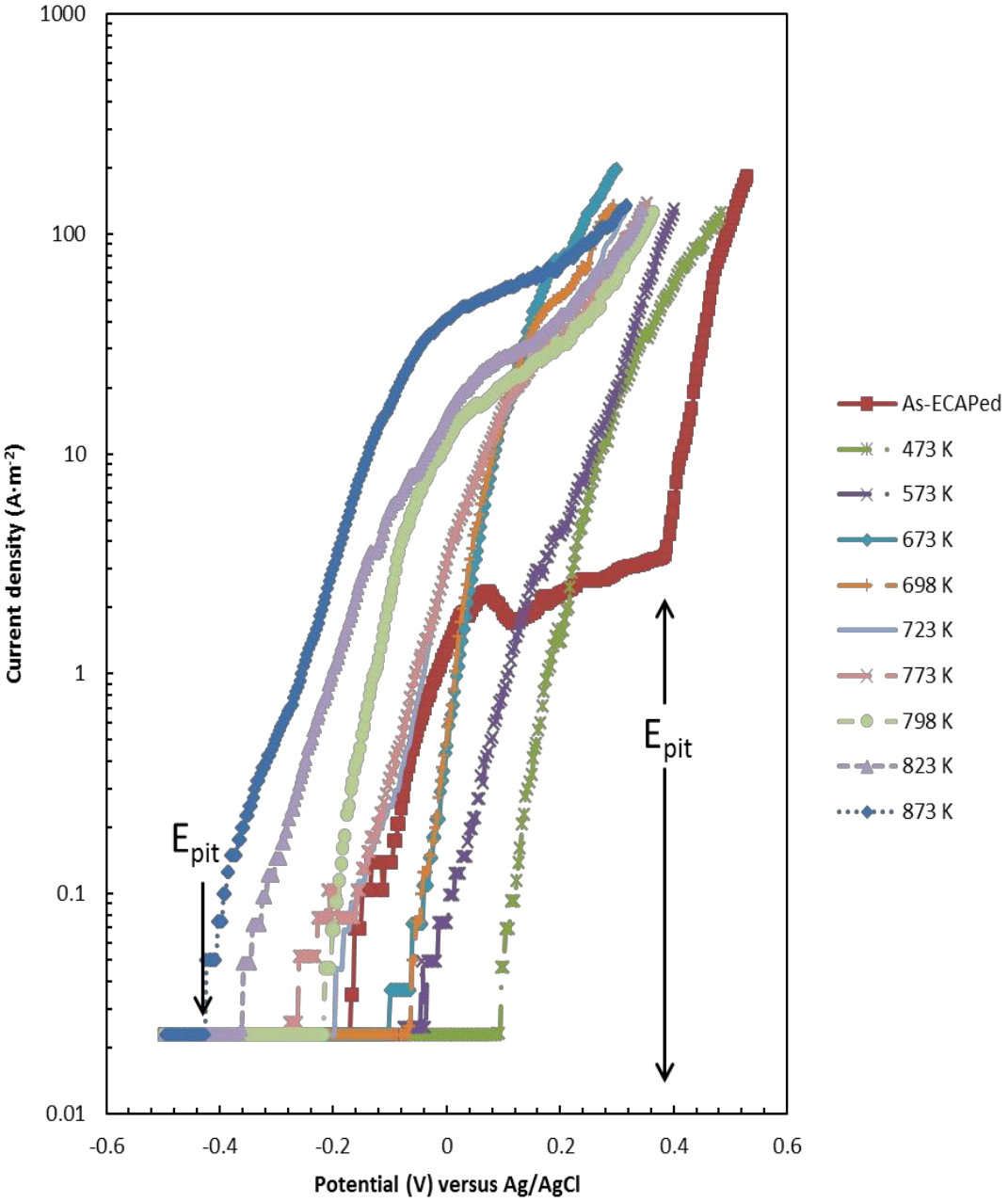

Figure 7.10. Dynamic anodic polarization curves in 1000 mol·m^{-3} NaCl solution

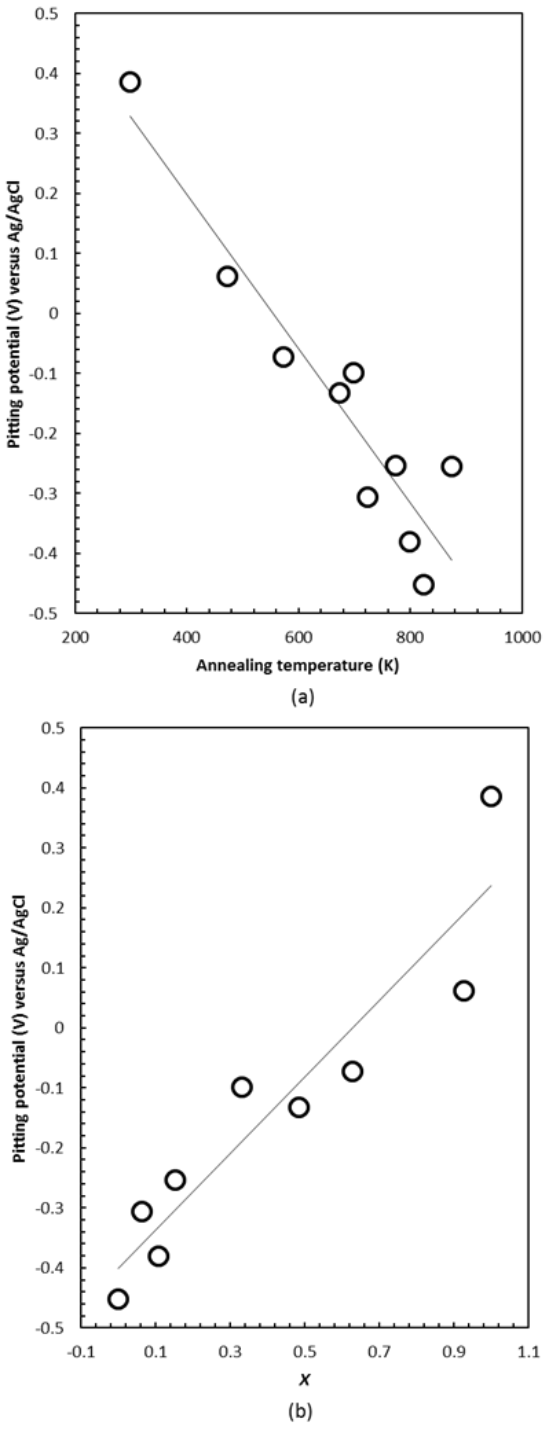

Figure 7.11. Relation between, (a) the pitting potential, E_p and annealing temperature and (b) X parameter

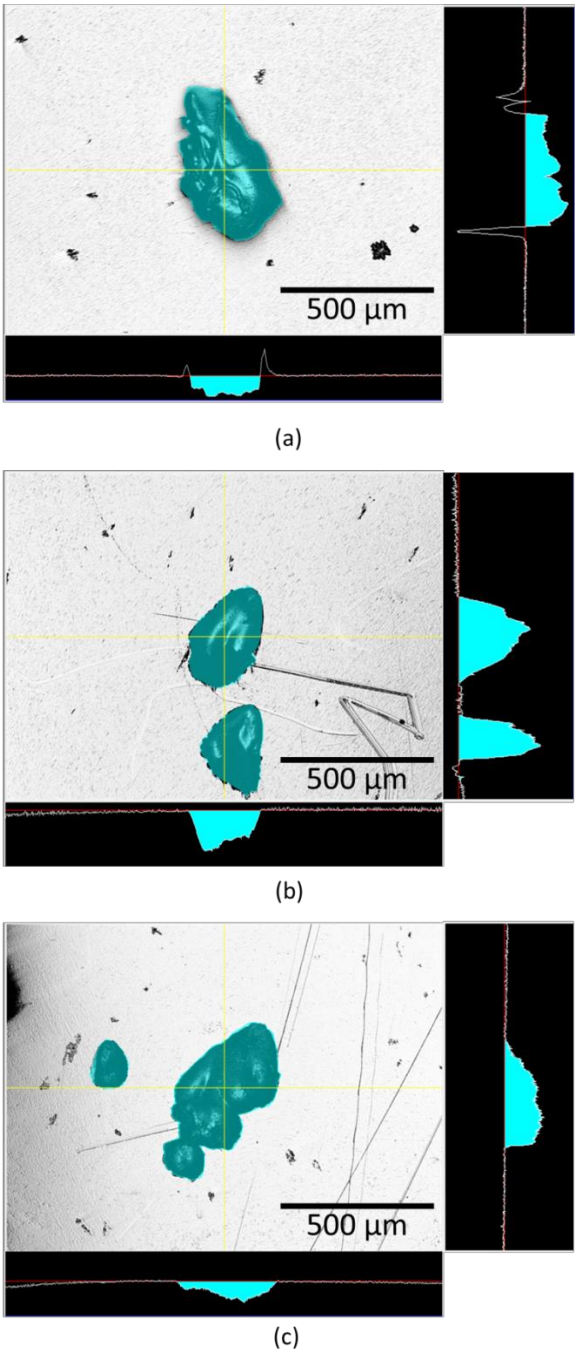

Figure 7.12. Laser microscope showing pitting corrosion of (a) as-ECAPed, (b) annealead at 573 K, (c) 773 K.

local chemical environment is substantially more aggressive than the bulk environment **[48]**. This explains why very high flow rates over a stainless steel surface tend to reduce pitting corrosion; the high flow rate prevents the concentration of corrosive species in the pit **[48]**.

The chemical composition of the alloy plays a major role in affecting the pitting potential. In stainless steels, chromium is the main alloying elements required to improve the pitting resistance. Increasing chromium content enhanced the stability of the passive film against pitting attack. The pitting potential was correspondingly found to increase dramatically as the chromium content has increased above the critical 13% needed to create stainless steel **[49]**.

The effect of grain size on pitting potential can be seen in **Figure 7.13**. This electrochemical testing exhibited low rates of corrosion or some level of passivity corrosion rated decreased with grain size reduction. This occurrence is coherent with pure grain refinement being principally confined to controlling the rate of anodic reactions and having little role in altering the rate at which cathodic reactions can be sustained [50].

This study was often reported that resistance to corrosion of stainless steel was enhanced by UFG formation by SPD **[26,35,36]**. This is often explained by the higher diffusion of Cr enhanced by high density of grain boundaries **[51-53]**. The higher diffusion of Cr is considered that the passive film form by selective dissolution of Fe atoms into the solution and resultant enrichment of Cr at the surface **[54,55]**. When pitting started to form, Cr concentration decreased locally, but this area would be supplied by enhanced Cr diffusion in UFG structures. If one can apply this idea to the present results, linear relation of X and Ep versus Ag/AgCl can be interpreted by the faster diffusion Cr along the stored dislocations inside the grains or/and non-equilibrium grain boundaries **[56,57]**. Indeed, the result has been shown that the grain boundary diffusivities in nanostructured metals processed by means of SPD in the temperature range of 398–448 K are 4–5 orders of magnitude higher relative to the same materials in a coarse-grained state **[56]**. Namely, early reduction of Ep versus Ag/AgCl by the

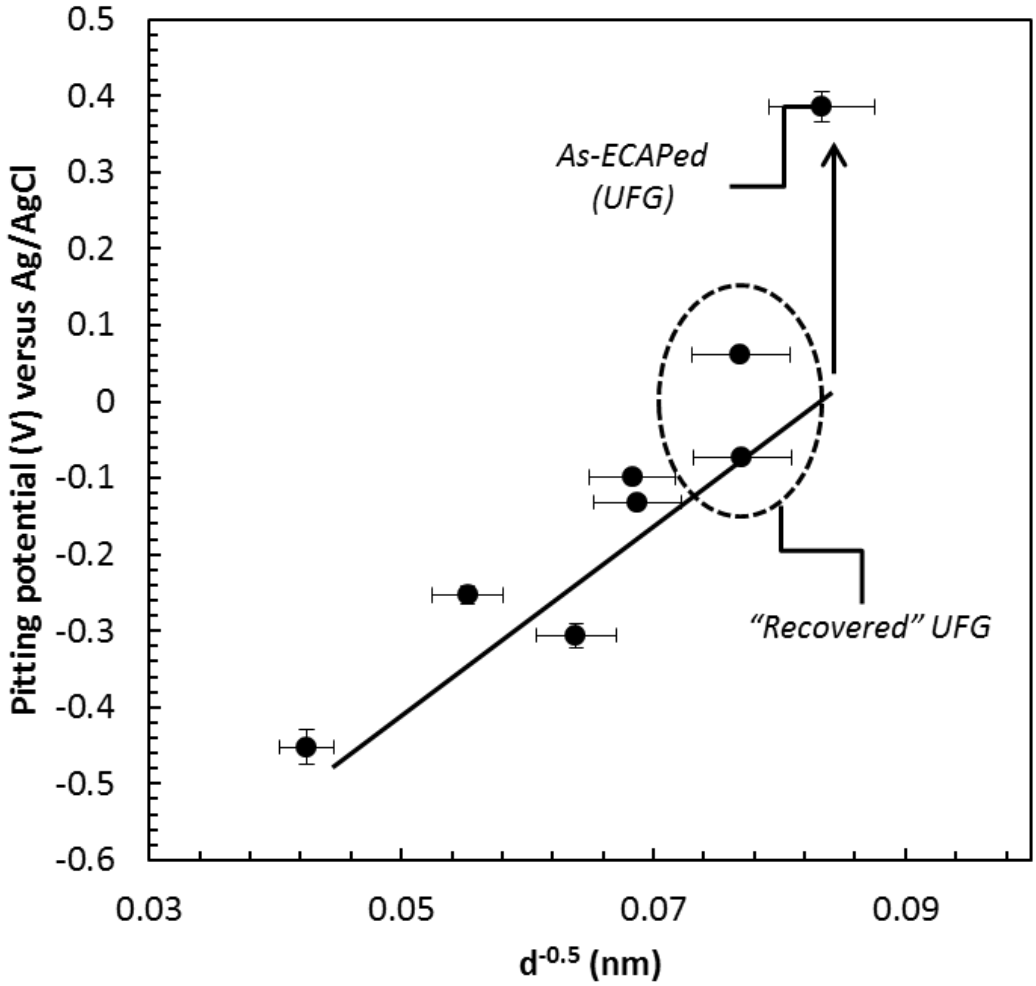

Figure 7.13. Relationship between pitting potential (V) vs Ag/AgCl and micro hardness.

annealing can be caused by diminish of dislocations or transformation from non-equilibrium to equilibrium grain boundaries. It was suggested that dislocation arrangements during the strain hardening stages could better explain this trend according to electrochemical approaches **[58]**.

7.5. Conclusion

Effect of post-ECAP annealing on the pitting corrosion of UFG low-C, N Fe-20%Cr steels fabricated by ECAP was studied. It was found that softening occurred by the typical three-stage change comprising of recovery with constant hardness, and subsequent recrystallization accompanying significant softening, and the final grain growth with constant hardness. Pitting potential was nobler in UFG state and more sensitive to annealing temperature than hardness. Namely, pitting potential started to decrease monotonously at lower temperature than the hardness which reflected grains size change. The early reduction of the pitting potential in the recovery process is attributed to less stabilized passivation caused by the rearrangement and annihilation of dislocations inside grains and in non-equilibrium grain boundaries. This result is concluded that nobler potentials of UFG states are realized by not only grain size reduction but also defective deformation-induced UFG.

Reference

[1] Valiev, R. Z., Islamgaliev, R. K., & Alexandrov, I. V. (2000). Bulk nanostructured materials from severe plastic deformation. Progress in materials science, 45(2), 103-189.

[2] Koch, C. C. (2003). Optimization of strength and ductility in nanocrystalline and ultrafine grained metals. Scripta Materialia, 49(7), 657-662.

[3] Langdon, T. G. (2007). The principles of grain refinement in equal-channel angular pressing. Materials Science and Engineering: A, 462(1), 3-11.

[4] Langdon, T. G. (2013). Twenty-five years of ultrafine-grained materials: achieving

exceptional properties through grain refinement. Acta Materialia, 61(19), 7035-7059.

[5] Zhu, Y. T., & Lowe, T. C. (2000). Observations and issues on mechanisms of grain refinement during ECAP process. Materials Science and Engineering: A, 291(1), 46-53.

[6] Rofagha, R., Langer, R., El-Sherik, A. M., Erb, U., Palumbo, G., & Aust, K. T. (1991). The corrosion behaviour of nanocrystalline nickel. Scripta metallurgica et materialia, 25(12), 2867-2872.

[7] Kim, S. H., Aust, K. T., Erb, U., Gonzalez, F., & Palumbo, G. (2003). A comparison of the corrosion behaviour of polycrystalline and nanocrystalline cobalt. Scripta Materialia, 48(9), 1379-1384.

[8] Kim, S. H., Erb, U., Aust, K. T., Gonzalez, F., & Palumbo, G. (2004). The corrosion behavior of nanocrystalline electrodeposits. Plating and surface finishing, 91(5), 68-70.

[9] Hasegawa, M., & Osawa, M. (1984). Corrosion behavior of ultrafine grained austenitic stainless steel. Corrosion, 40(7), 371-374.

[10] Miyamoto, H., Harada, K., Mimaki, T., Vinogradov, A., & Hashimoto, S. (2008). Corrosion of ultra-fine grained copper fabricated by equal-channel angular pressing. Corrosion Science, 50(5), 1215-1220.

[11] Balusamy, T., Kumar, S., & Sankara Narayanan, T. S. N. (2010). Effect of surface nanocrystallization on the corrosion behaviour of AISI 409 stainless steel. Corrosion Science, 52(11), 3826-3834.

[12] Hamu, G. B., Eliezer, D., & Wagner, L. (2009). The relation between severe plastic deformation microstructure and corrosion behavior of AZ31 magnesium alloy. Journal of alloys and compounds, 468(1), 222-229.

[13] Birbilis, N., Ralston, K. D., Virtanen, S., Fraser, H. L., & Davies, C. H. J. (2010). Grain character influences on corrosion of ECAPed pure magnesium. Corrosion Engineering, Science and Technology, 45(3), 224-230.

[14] Xu, X. X., Nie, F. L., Zhang, J. X., Zheng, W., Zheng, Y. F., Hu, C., & Yang, G. (2010). Corrosion and ion release behavior of ultra-fine grained bulk pure copper fabricated by ECAP in Hanks solution as potential biomaterial for contraception.

Materials Letters, 64(4), 524-527.

[15] Orlov, D., Ralston, K. D., Birbilis, N., & Estrin, Y. (2011). Enhanced corrosion resistance of Mg alloy ZK60 after processing by integrated extrusion and equal channel angular pressing. Acta Materialia, 59(15), 6176-6186.

[16] Jiang, J., Ma, A., Song, D., Yang, D., Shi, J., Wang, K., ... & Chen, J. (2012). Anticorrosion behavior of ultrafine-grained Al-26 wt% Si alloy fabricated by ECAP. Journal of Materials Science, 47(22), 7744-7750.

[17] Zheng, Z. J., Gao, Y., Gui, Y., & Zhu, M. (2012). Corrosion behaviour of nanocrystalline 304 stainless steel prepared by equal channel angular pressing. Corrosion Science, 54, 60-67.

[18] Deng, W., Lin, P., Li, Q., & Mo, G. (2013). Ultrafine-grained copper produced by machining and its unusual electrochemical corrosion resistance in acidic chloride pickling solutions. Corrosion Science, 74, 44-49.

[19] Vrátná, J., Hadzima, B., Bukovina, M., & Janeček, M. (2013). Room temperature corrosion properties of AZ31 magnesium alloy processed by extrusion and equal channel angular pressing. Journal of Materials Science, 48(13), 4510-4516.

[20] Brunner, J. G., Birbilis, N., Ralston, K. D., & Virtanen, S. (2012). Impact of ultrafine-grained microstructure on the corrosion of aluminium alloy AA2024. Corrosion Science, 57, 209-214.

[21] Gopala Krishna, K., Sivaprasad, K., Sankara Narayanan, T. S. N., & Hari Kumar, K. C. (2012). Localized corrosion of an ultrafine grained Al–4Zn–2Mg alloy produced by cryorolling. Corrosion Science, 60, 82-89.

[22] Krawczynska, A. T., Gloc, M., & Lublinska, K. (2013). Intergranular corrosion resistance of nanostructured austenitic stainless steel. Journal of Materials Science, 48(13), 4517-4523.

[23] Sikora, E., Wei, X. J., & Shaw, B. A. (2004). Corrosion behavior of nanocrystalline bulk Al-Mg-based alloys. Corrosion, 60(4), 387-398.

[24] Chung, M. K., Choi, Y. S., Kim, J. G., Kim, Y. M., & Lee, J. C. (2004). Effect of the number of ECAP pass time on the electrochemical properties of 1050 Al alloys. Materials Science and Engineering: A, 366(2), 282-291.

[25] Hadzima, B., Janeček, M., Estrin, Y., & Kim, H. S. (2007). Microstructure and

corrosion properties of ultrafine-grained interstitial free steel. Materials Science and Engineering: A, 462(1), 243-247.

[26] Pisarek, M., Keedzierzawski, P., Janik-Czachor, M., & Kurzydlowski, K. J. (2008). Effect of Hydrostatic Extrusion on the Corrosion Resistance of Type 316 Stainless Steel. Corrosion, 64(2), 131-137.

[27] Hellmig, R. J., Janecek, M., Hadzima, B., Gendelman, O. V., Shapiro, M., Molodova, X., ... & Estrin, Y. (2008). A portrait of copper processed by equal channel angular pressing. Materials transactions, 49(1), 31-37.

[28] Hockauf, M., Meyer, L. W., Nickel, D., Alisch, G., Lampke, T., Wielage, B., & Krüger, L. (2008). Mechanical properties and corrosion behaviour of ultrafine-grained AA6082 produced by equal-channel angular pressing. Journal of Materials Science, 43(23-24), 7409-7417.

[29] Akiyama, E., Zhang, Z., Watanabe, Y., & Tsuzaki, K. (2009). Effects of severe plastic deformation on the corrosion behavior of aluminum alloys. Journal of Solid State Electrochemistry, 13(2), 277-282

[30] Brunner, J. G., May, J., Höppel, H. W., Göken, M., & Virtanen, S. (2010). Localized corrosion of ultrafine-grained Al–Mg model alloys. Electrochimica Acta, 55(6), 1966-1970.

[31] Korchef, A., & Kahoul, A. (2013). Corrosion Behavior of Commercial Aluminum Alloy Processed by Equal Channel Angular Pressing. International Journal of Corrosion, 2013.

[32] Yu, B., Woo, P., & Erb, U. (2007). Corrosion behaviour of nanocrystalline copper foil in sodium hydroxide solution. Scripta materialia, 56(5), 353-356.

[33] Zeiger, W., Schneider, M., Scharnweber, D., & Worch, H. (1995). Corrosion behaviour of a nanocrystalline FeA18 alloy. Nanostructured Materials, 6(5), 1013-1016.

[34] Afshari, V., & Dehghanian, C. (2009). Effects of grain size on the electrochemical corrosion behaviour of electrodeposited nanocrystalline Fe coatings in alkaline solution. Corrosion Science, 51(8), 1844-1849.

[35] Raman, R. S., Gupta, R. K., & Koch, C. C. (2010). Resistance of nanocrystalline vis-à-vis microcrystalline Fe–Cr alloys to environmental degradation and

challenges to their synthesis. Philosophical magazine, 90(23), 3233-3260.

[36] Mahesh, B. V., Raman, R. S., & Koch, C. C. (2012). Bimodal grain size distribution: an effective approach for improving the mechanical and corrosion properties of Fe–Cr–Ni alloys. Journal of Materials Science, 47(22), 7735-7743.

[37] McCafferty, E. (2010). Introduction to corrosion science. Springer.

[38] Čížek, J., Procházka, I., Cieslar, M., Kužel, R., Kuriplach, J., Chmelík, F., ... & Islamgaliev, R. K. (2002). Thermal stability of ultrafine grained copper. Physical Review B, 65(9), 094106.

[39] Gertsman, V. Y., & Birringer, R. (1994). On the room-temperature grain growth in nanocrystalline copper. Scripta metallurgica et materialia, 30(5), 577-581.

[40] Komura, S., Horita, Z., Nemoto, M., & Langdon, T. G. (1999). Influence of stacking fault energy on microstructural development in equal-channel angular pressing. Journal of Materials Research, 14(10), 4044-4050.

[41] Molodova, X., Gottstein, G., Winning, M., & Hellmig, R. J. (2007). Thermal stability of ECAP processed pure copper. Materials Science and Engineering: A, 460, 204-213.

[42] Neishi, K., Horita, Z., & Langdon, T. G. (2002). Grain refinement of pure nickel using equal-channel angular pressing. Materials Science and Engineering: A, 325(1), 54-58.

[43] Sun, C., Yang, Y., Liu, Y., Hartwig, K. T., Wang, H., Maloy, S. A., ... & Zhang, X. (2012). Thermal stability of ultrafine grained Fe–Cr–Ni alloy. Materials Science and Engineering: A, 542, 64-70.

[44] Humphreys, F. J. (1997). A unified theory of recovery, recrystallization and grain growth, based on the stability and growth of cellular microstructures—I. The basic model. Acta Materialia, 45(10), 4231-4240.

[45] Gertsman, V. Y., Birringer, R., Valiev, R. Z., & Gleiter, H. (1994). On the structure and strength of ultrafine-grained copper produced by severe plastic deformation. Scripta metallurgica et materialia, 30(2), 229-234.

[46] Islamgaliev, R. K., Chmelik, F., & Kuzel, R. (1997). Thermal stability of submicron grained copper and nickel. Materials Science and Engineering: A, 237(1), 43-51.

[47] Moelle, C. H., & Fecht, H. J. (1995). Thermal stability of nanocrystalline iron prepared by mechanical attrition. Nanostructured Materials, 6(1), 421-424.

[48] Davis, J. R. (Ed.). (1994). Stainless steels. ASM international.

[49] Horvath, J., & Uhlig, H. H. (1968). Critical Potentials for Pitting Corrosion of Ni, Cr‐Ni, Cr‐Fe, and Related Stainless Steels. Journal of the Electrochemical society, 115(8), 791-795.

[50] Ralston, K. D., Birbilis, N., & Davies, C. H. J. (2010). Revealing the relationship between grain size and corrosion rate of metals. Scripta Materialia, 63(12), 1201-1204.

[51] Gupta, R. K., Raman, R. S., & Koch, C. C. (2012). Electrochemical characteristics of nano and microcrystalline Fe–Cr alloys. Journal of Materials Science, 47(16), 6118-6124.

[52] Andrievski, R. A. (2003). Review Stability of nanostructured materials. Journal of materials science, 38(7), 1367-1375.

[53] Koch, C. C. (2007). Structural nanocrystalline materials: an overview. Journal of Materials Science, 42(5), 1403-1414.

[54] Qian, S., Newman, R. C., Cottis, R. A., & Sieradzki, K. (1990). Validation of a Percolation Model for Passivation of Fe‐Cr Alloys: Two‐Dimensional Computer Simulations. Journal of The Electrochemical Society, 137(2), 435-439.

[55] Newman, R. C., Meng, F. T., & Sieradzki, K. (1988). Validation of a percolation model for passivation of Fe・Cr alloys: I current efficiency in the incompletely passivated state. Corrosion science, 28(5), 523-527.

[56] Kolobov, Y. R., Grabovetskaya, G. P., Ivanov, M. B., Zhilyaev, A. P., & Valiev, R. Z. (2001). Grain boundary diffusion characteristics of nanostructured nickel. Scripta materialia, 44(6), 873-878.

[57] Würschum, R., Herth, S., & Brossmann, U. (2003). Diffusion in nanocrystalline metals and alloys—a status report. Advanced Engineering Materials, 5(5), 365-372.

[58] Gutman, E. M. (1994). Mechanochemistry of solid surfaces (p. 322). Singapore: World scientific.

Chapter 8. Corrosion fatigue properties of UFG low C, N Fe-20%Cr steel by ECAP

8.1. Introduction

Equal-channel angular pressing (ECAP) is a technique using simple shear to produce bulk metallic materials with submicrocrystalline and high mechanical properties **[1,2]**. A very large plastic deformation leads to formation of inhomogeneous structures resulting in different of corrosion properties such as corrosion fatigue and stress-corrosion cracking (SCC) **[3-6]**.

SCC is a cracking that occurred by synchronized behavior of a corrosion and tensile stress, as shown in **Figure 8.1.a**. This cracking excludes a reduced corrosion which fails by rapid fracture. SCC is related three parameters, such as **[7]**: (1) vulnerable material, (2) environment and (3) tensile stress. On the other hand, corrosion fatigue is a fatigue test which carried out in corrosive environment, as shown in **Figure 8.1.b**. The corrosive environment is a significant role in the fatigue limit.

Fatigue corrosion is considered to be the main research topic of degradation metal mechanism in corrosive environment. The fatigue life is limited due to pit formation on the metal surface which is causing the crack initiation from pitting corrosion, as shown in **Figure 8.2**.

Characterization of corrosion fatigue of materials with the ultra-fine grain (UFG) size is importance to be observed. The corrosion behavior of ECAP material has reported in limited intention. The rate of dissolution of the UFG is higher in comparison with coarse grained material, as discussed in Chapter 7 **[8,9]**. The corrosive damage makes ECAP material attractive for practical applications in corrosive environment. The behavior of ECAP materials immersed into corrosive environment under stress has not been investigated yet.

Two mechanisms for crack propagation have been well recognized for stainless steel, as shown in **Figure 8.3**. One is slip step dissolution mode. In this model, slip step formed by active dislocation at a crack tip is dissolution anodic reaction, so that crack tip advance to further distance. The other is stress adsorption mechanism. In ideally brittle fracture, the work to form crack, W, become 2γ-γ. where γ_s is surface energy and

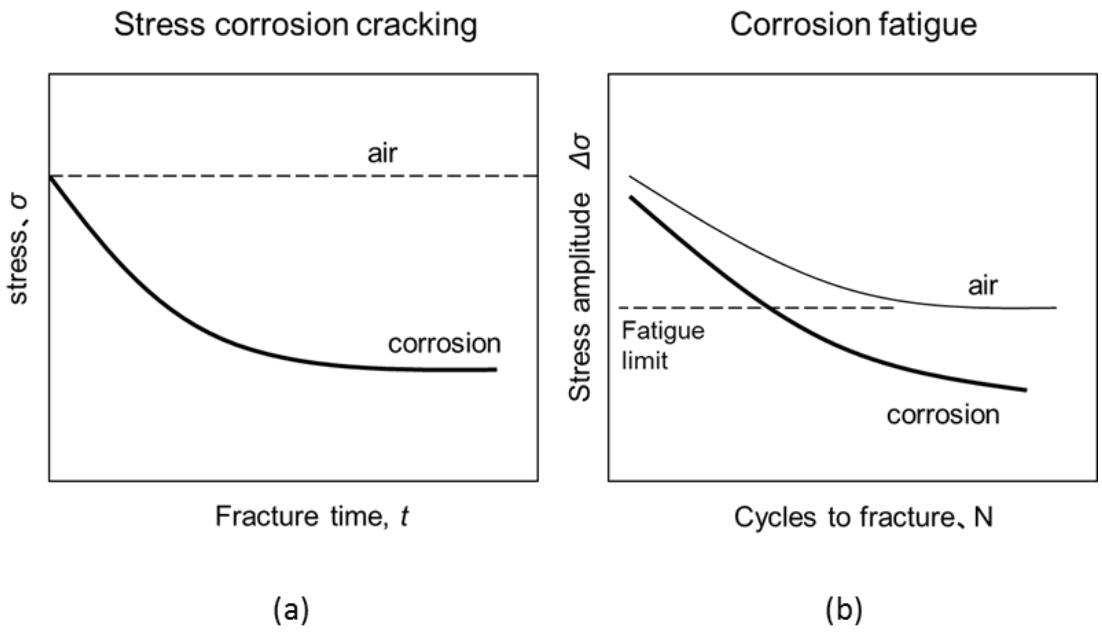

Figure 8.1. Schematic of result on SCC and corrosion fatigue.

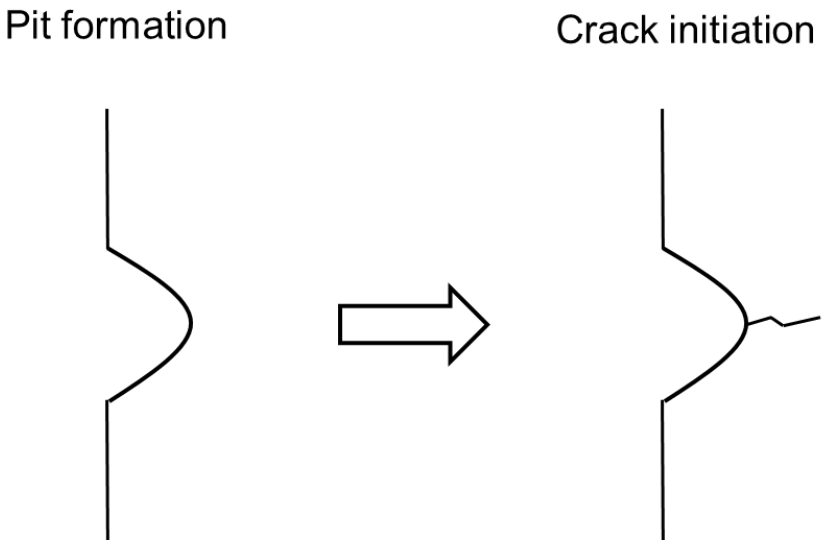

Figure 8.2. Schematic of pit formation and crack initiation.

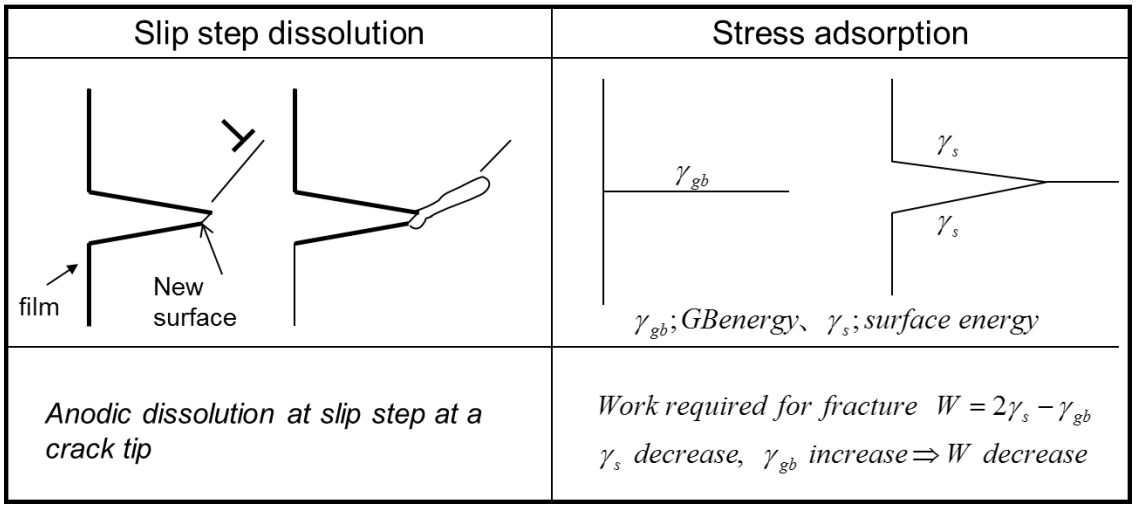

Figure 8.3. Mechanism of corrosion fatigue crack propagation.

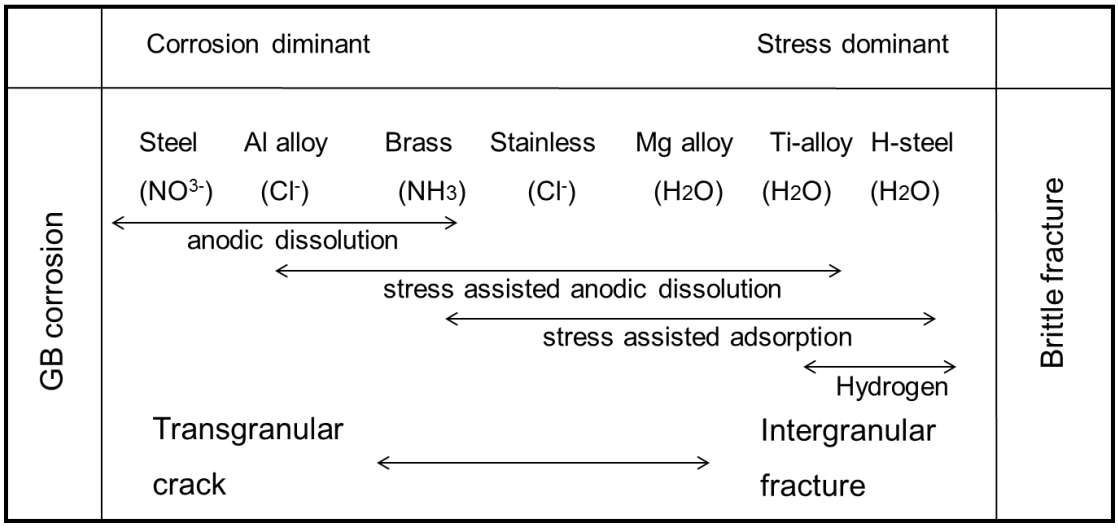

Figure 8.4. SCC and corrosion fatigue mechanism.

γ_{gb} is grain boundary energy. In this model, surface energy is reduced chemisorption so that the W is reduced. If $2\gamma_s = \gamma gb$, $W = 0$. It means that crack can form at essentially no stress. In either model, grain boundary energy γ_{gb} can influence the crack advance. If γ_{gb} become higher, anodic dissolution can be enhanced in the former model, thus crack advance is facilitated. In the latter model, the increased γ_{gb} can also reduce the work, W.

Both the corrosion and stress can affect the rate of crack advance in SCC and corrosion fatigue. However, degree of the effect of the two different among the materials-corrosion systems shows the various materials-environment system and degree of contribution of corrosion/stress, as shown in **Figure 8.4**. In carbon steel in NO_3 system, crack advance is dominated by mostly corrosion (right hand side) while it is dominated by stress in high strength steel in H_2O system. In former case, fracture mode seems to intergranular corrison while it seems brittle fracture in the latter case. In stainless steel in Cl^- system, contribution by corrosion and stress is comparable, and materials parameters may determine the fracture mode as follow.

In ductile material-corrosion system, there may be three schema of crack propagation as shown in **Figure 8.5**. On is transgranular crack propagation by slip-step dissolution in relatively larger grain size. Stress intensity factor to advance a crack is given $\Delta K_{sl} = \frac{a}{\sqrt{d}}$, thus it become higher with an decreasing grain size. In the other extreme case with smaller grain size, there may be two kinds of crack path, as shown in **Figure 8.5**. In corrosive environment where chemical reaction at grain boundary (GB) is active, so that crack tends to take GB path.

When grain size is reduced under submicron size, dislocation activity is suppressed. Thus mechanism tends to change from transgranular ductile fracture by slip-step dissolution to intergranular or transgranular brittle fracture, as shown in **Figure 8.5**. If one suppose the intergranular fracture (right upper), stress intensity to require crack advance $\Delta Kgb = \sqrt{(2\gamma_s - \gamma_{gb})E}$. In this case, the reduction of GB energy γ_{gb} leads to higher ΔKgb. Namely, it is expected that resistance to crack propagation can be enhanced by change from non-equilibrium to equilibrium grain boundary, as shown in **Figure 8.6**. However, pitting potential, Ep become lower by changing to equilibrium

grain boundary, as discussed in Chapter 7. Therefore, overall resistance to corrosion fatigue, is determined by the balance between Ep and *ΔKgb* after short time annealing.

In ductile materials under cyclic stress in corrosive environment, crack path change from transgranular to intergnranular mannter with a tends to propagate transgranularly since ΔK_{sl} is lower than ΔK_{gb} and ΔK_s. When grain boundary energy becomes lower, K_{gb} becomes higher. Thus, critical grain size where the transition from transgranular to intergranular moves to a smaller grain size and resistance to crack propagation is enhanced as shown in **Figure 8.6**.

8.2. Experimental procedure

The material used in this experiment had a chemical composition of low CN Fe-20%Cr alloy with Cr 19.97, C 0.0020, N 0.0015 and Fe balance (in mass percent). This material was machined with dimensions of 8 mm × 8 mm × 120 mm for ECAP pressing. ECAP was carried out using a split die with two channels intersecting at an inner angle of 90° and an outer angle of 0° at 423 K. The samples were lubricated with high temperature fluorine lubricating grease and pressed for four passes via route Bc. Annealing process was carried out at 773 K for one hour. A TEM (JEM 2100F) was used to examine the microstructures. Thin foils for TEM were polished using abrasive papers to about 100 μm thick and then thinned by a twin-jet polishing Tenupol 5 facility using a solution of 40% acetic acid, 30% phosphoric acid, 20% nitric acid and 10% distilled water. Mechanical and electrochemical properties were measured by micro hardness and pitting corrosion. The micro hardness experiments were performed on a Vickers hardness testing machine at room temperature. Corrosion fatigue testing was carried out at ambient temperature in a flat polarization cell, using platinum counter electrodes and SCE reference electrodes to measure the corrosion current and corrosion potential. The corrosion fatigue characteristic was obtained in neutral solutions 1 M NaCl, under stress amplitude of 200MPa. Corrosion fatigue sample and testing machine arrangement can be seen in **Figure 8.7** and **8.8**.

8.3. Results and Discussion

The micro hardness ECAPed and post-ECAP annealing is shown in **Figure 8.9**.

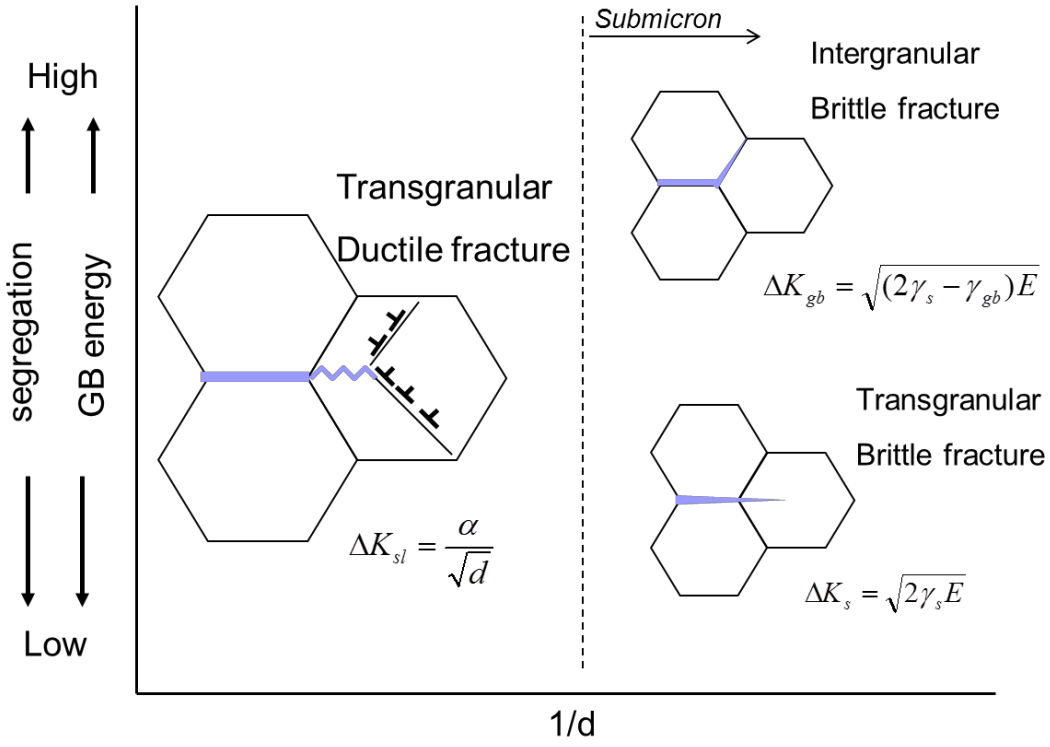

Figure 8.5. Crack propagation mode under cyclic stress.

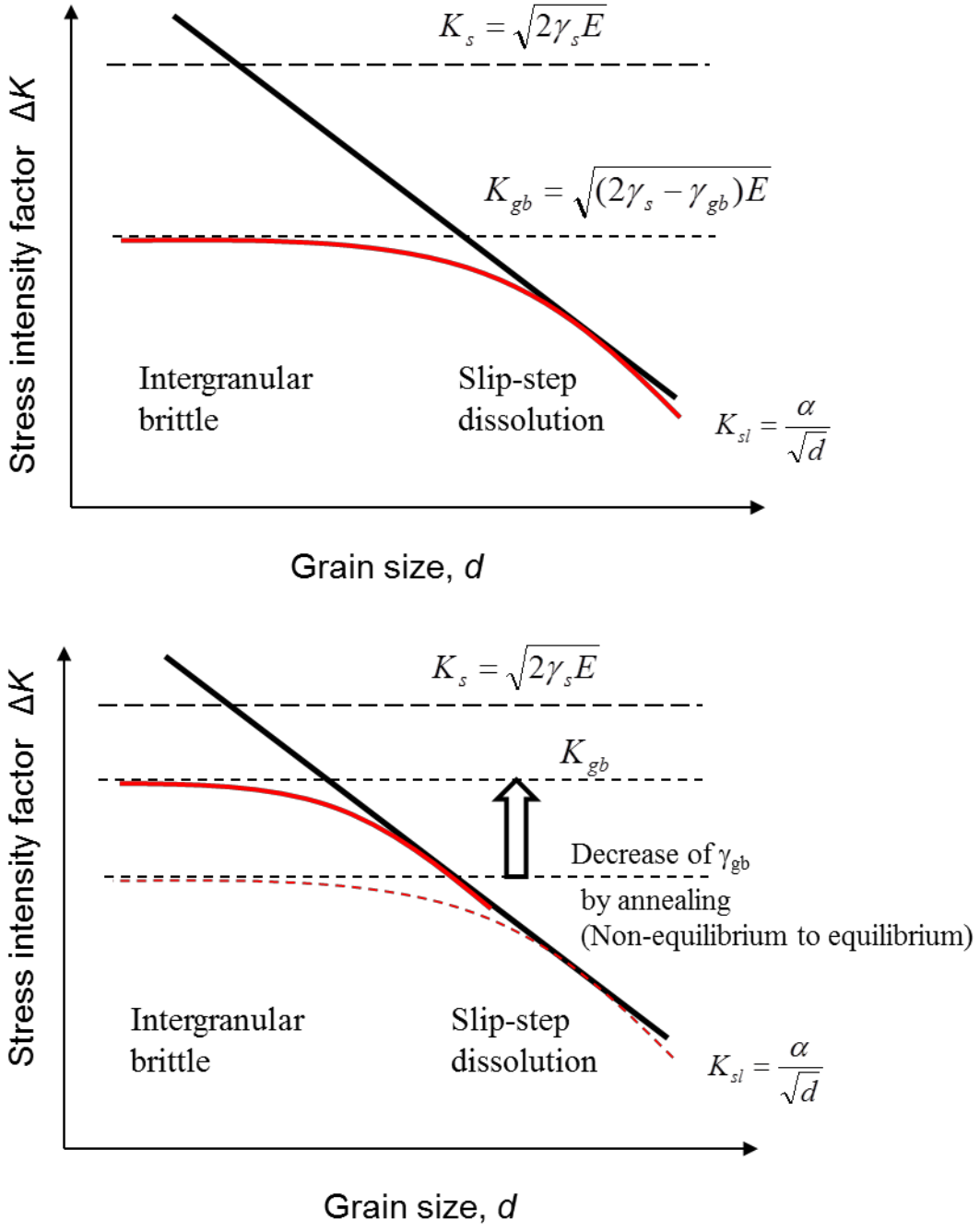

Figure 8.6. Schematic of critical grain size where the transition from transgranular to intergranular manner.

The micro hardness of ECAPed shows higher than post-ECAP annealing due to result from the slightly recrystallization accompanying with softening, as shown in **Figure 8.9**.

The microstructure of TEM was also observed on ECAP and after post-ECAP annealing at 773K for one hour, as shown in **Figure 8.10**. Under annealing temperature of 773 K, due to the recrystallization stage, there was a little difference in microstructure from the four passes ECAP. The microstructure of ECAPed sample exhibited a dark contrast and smaller grain size compared to that of the post-ECAP annealing. The dark contrast indicates that the dislocation was kept inside the UFG structure. The light contrast appeared at the TEM micrograph of the post-ECAP annealing due to the releasing of dislocation in grains.

Figure 8.11 shows XRD after ECAP and the post-ECAP annealing. In as-ECAP state, significant line broadening can be observed, and this line broadening is a result of non-equilibrium grain boundaries having a high density of extrinsic defects in their structure and resultant long range elastic stresses **[8,9]**.

Dislocation density and crystallite size can be identified by X-Ray broadening analysis. The crystallite size increased with annealing process. On the other hand, dislocation density decreased with the annealing process. It can be seen in **Figure 8.12**.

Grain boundary misorientation maps on ECAP and after post-ECAP annealing are represented in **Figure 8.13**. HAGB fraction on ECAPed microstructure are predominant with little fraction of LAGB. Because of low orientation resolution, boundaries with misorientation smaller than 2° was omitted. Homogeneous microstructure evolution with small equiaxed grains and high HAGB fraction was exhibited on post-ECAP annealing sample until 698 K. However, grain size increased gradually until the annealing temperature of 1373 K, but HAGB fraction almost remained constant. OIM of on the effect of corrosion fatigue of the ECAP sample are observed in rolling direction, as shown in **Figure 8.13**. It is apparent that grains are finely subdivided in the first pressing but in spite of that the former material has a larger grain size before the ECAP. Furthermore, arrays of planar and extended grain boundaries are developed parallel to the macroscopic shear plane of ECAP.

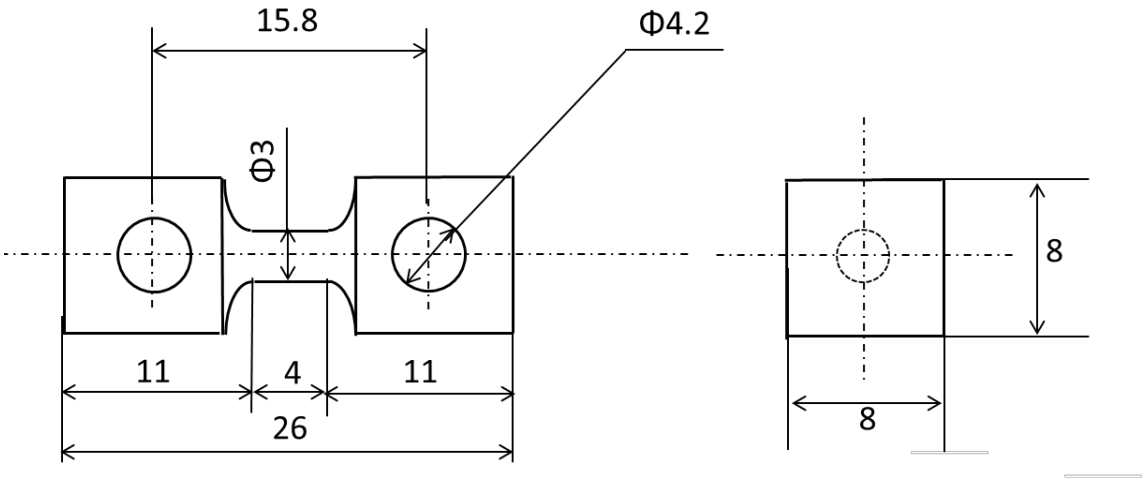

Figure 8.7. Schema of corrosion fatigue sample.

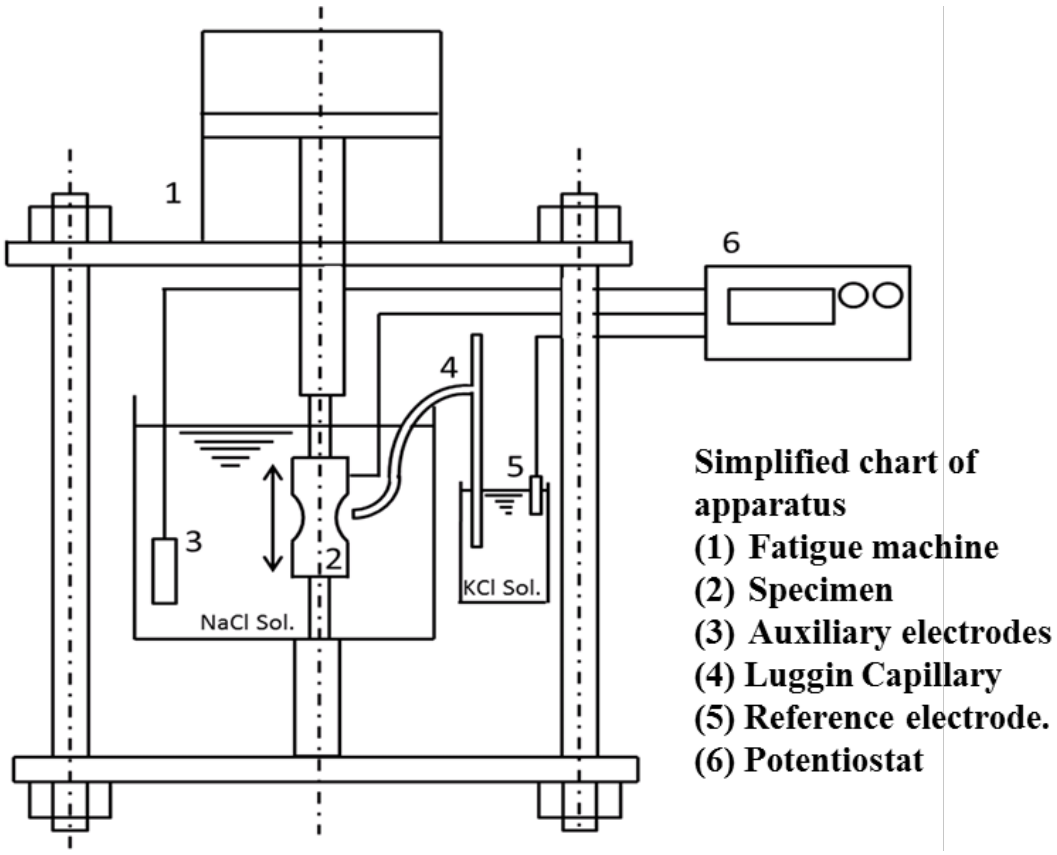

Figure 8.8. Schema of corrosion fatigue testing machine.

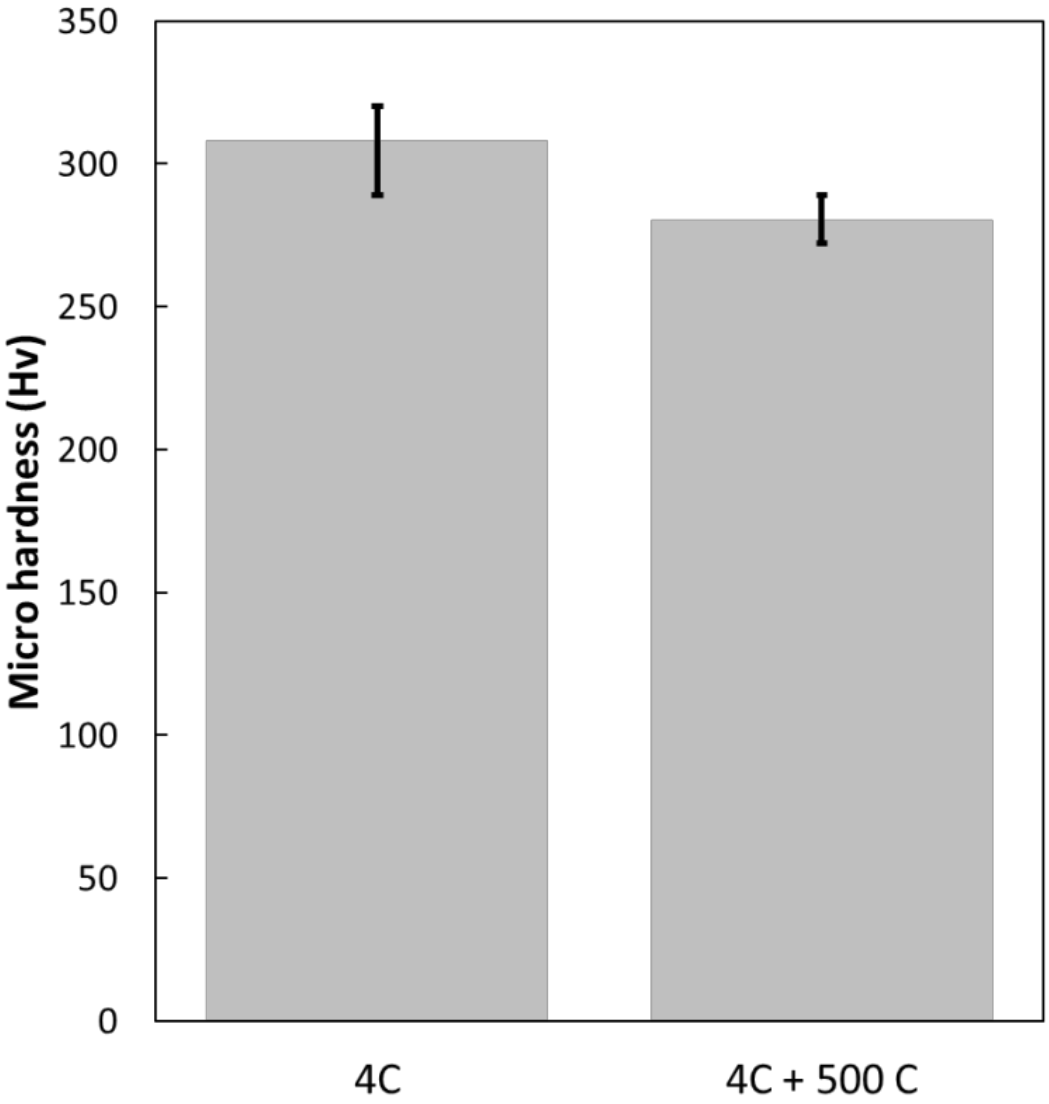

Figure 8.9. Micro hardness of ECAPed and post-ECAP annealed sample.

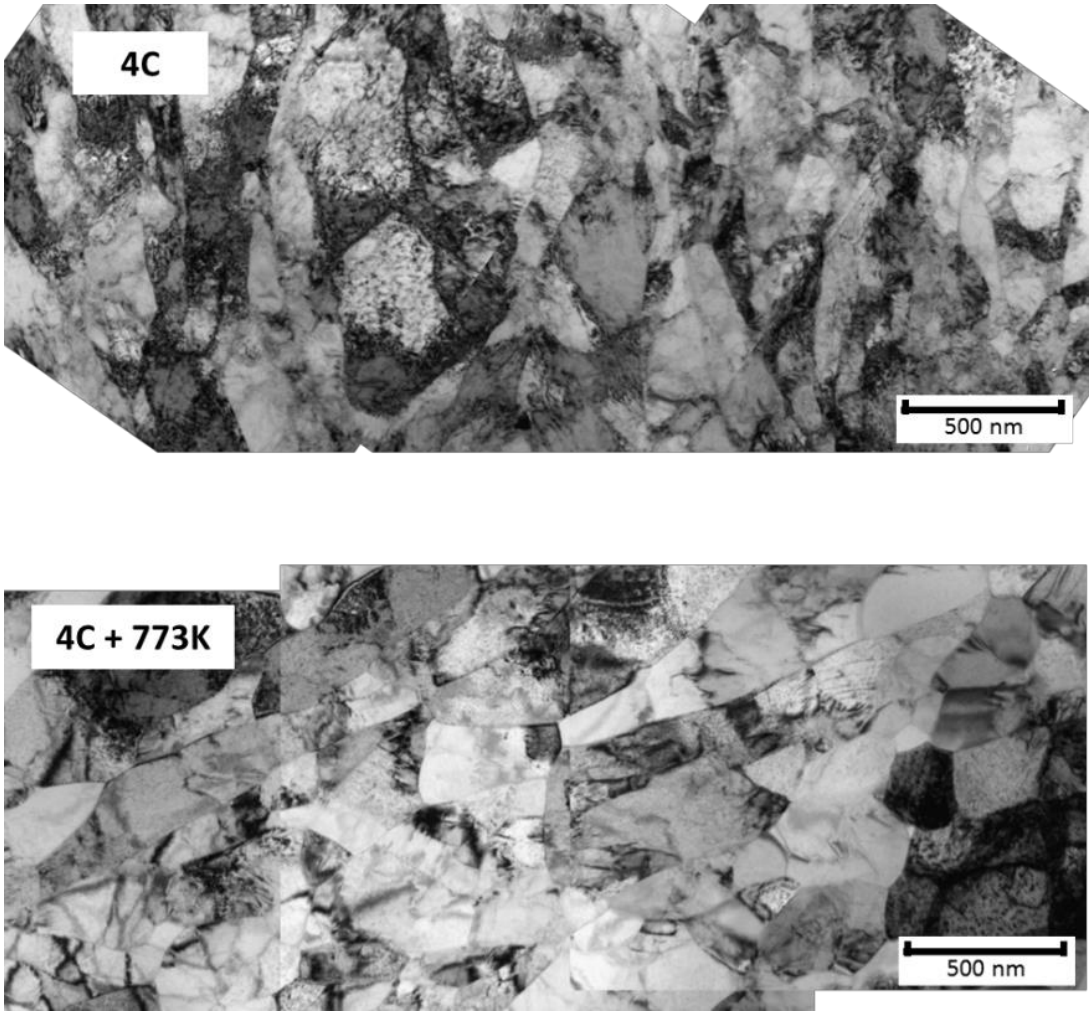

Figure 8.10. TEM micrograph of ECAPed and post-ECAP annealed sample. Observed from transverse direction.

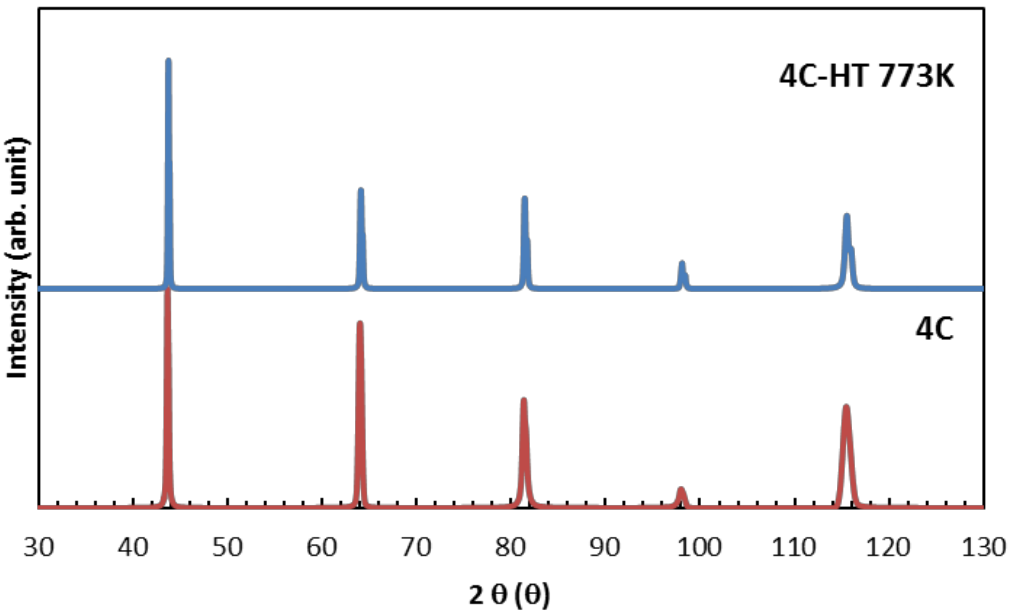

Figure 8.11. XRD of as ECAPed and post-ECAP annealed.

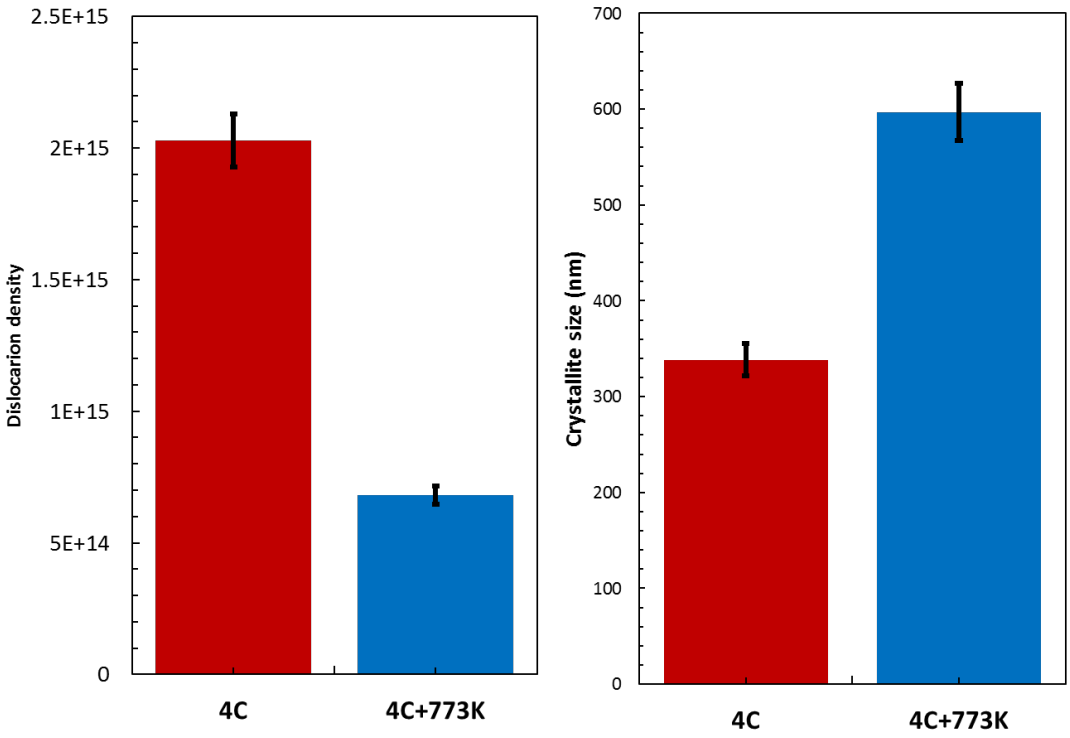

Figure 8.12. Dislocation density and crystallite size of as ECAPed and post-ECAP annealed.

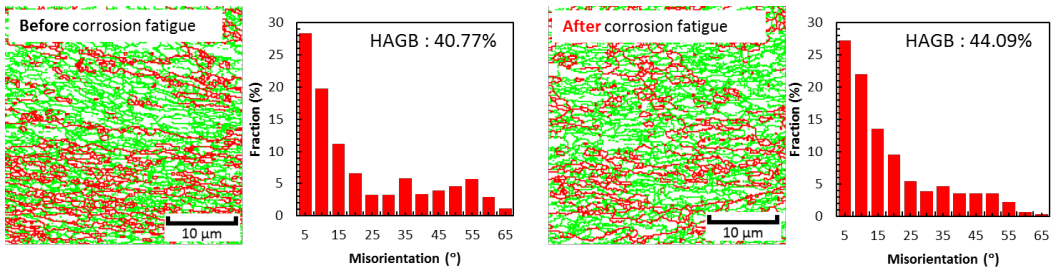

(a)

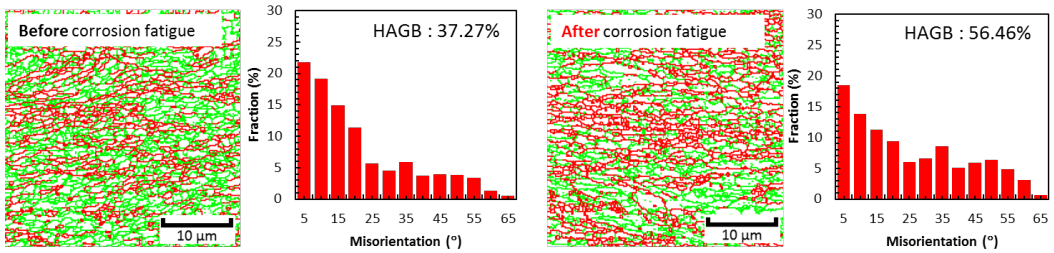

(b)

Figure 8.13. EBSD analysis of before and after corrosion fatigue (a) as-ECAPed sample and (b) post-ECAP annealed sample. Observed from transverse direction

Stress strain curves of as ECAPed and post ECAP annealed sample can be seen in **Figure 8.14**. Work hardening is observed after ECAP, although the ductility is limited, as is commonly observed in SPD metals. Four passes, the tensile strength increases while the elongation drastically compare to post-ECAP annealed sample. This implies that the improvement in strength accompanies with the loss of the ductility in the ECAPed sample. After the annealing process, the tensile strength of the samples extruded four passes decreases, while the elongation increases. In general, the ductility of the ECAPed samples can be improved by annealing process at the sacrifice of a little decrease of tensile strength.

Figure 8.14 exhibited post necking elongation at Fe-Cr alloys post-ECAP annealed sample. Post necking elongation can be affected from the grain structure which is equiaxed. The post necking elongation of post-ECAP annealed sample was larger than as-ECAP sample. HAGB can affect post necking elongation of equiaxed grain sample.

Figure 8.15.a shows the SEM micrograph of the fracture surface on as ECAPed and post-ECAP annealed sample after tensile testing. The observation with high magnification on as ECAPed and post-ECAP annealed sample had been done to understand dimple appearance on the fracture surface. Dimple appearance of post-ECAPed annealed was distributed homogeneously, as shown in **Figure 8.15.b**. From the observation above, it can be explained that post-ECAP annealed sample has good elongation with ductile fracture appearance. But as-ECAPed sample, fracture mode is transformed from ductile to brittle. It can be confirmed with the decreasing elongation of ECAP-processed sample.

It was often reported that resistance to pitting corrosion resistance of stainless steel was enhanced by UFG formation by SPD **[10-12]**. This is often explained by the higher diffusion of Cr enhanced by high density of grain boundaries **[13-15]**. It is considered that the passive film form by selective dissolution of Fe atoms into the solution and resultant condensation of Cr at the surface **[16,17]**. Pitting corrosion resistance of as ECAPed and post-ECAP annealed sample can be seen in **Figure 8.16**. When pitting started to form, Cr concentration decreased locally, but it would be supplied by enhanced Cr diffusion in UFG structures **[18,19]**. Indeed, it has been shown

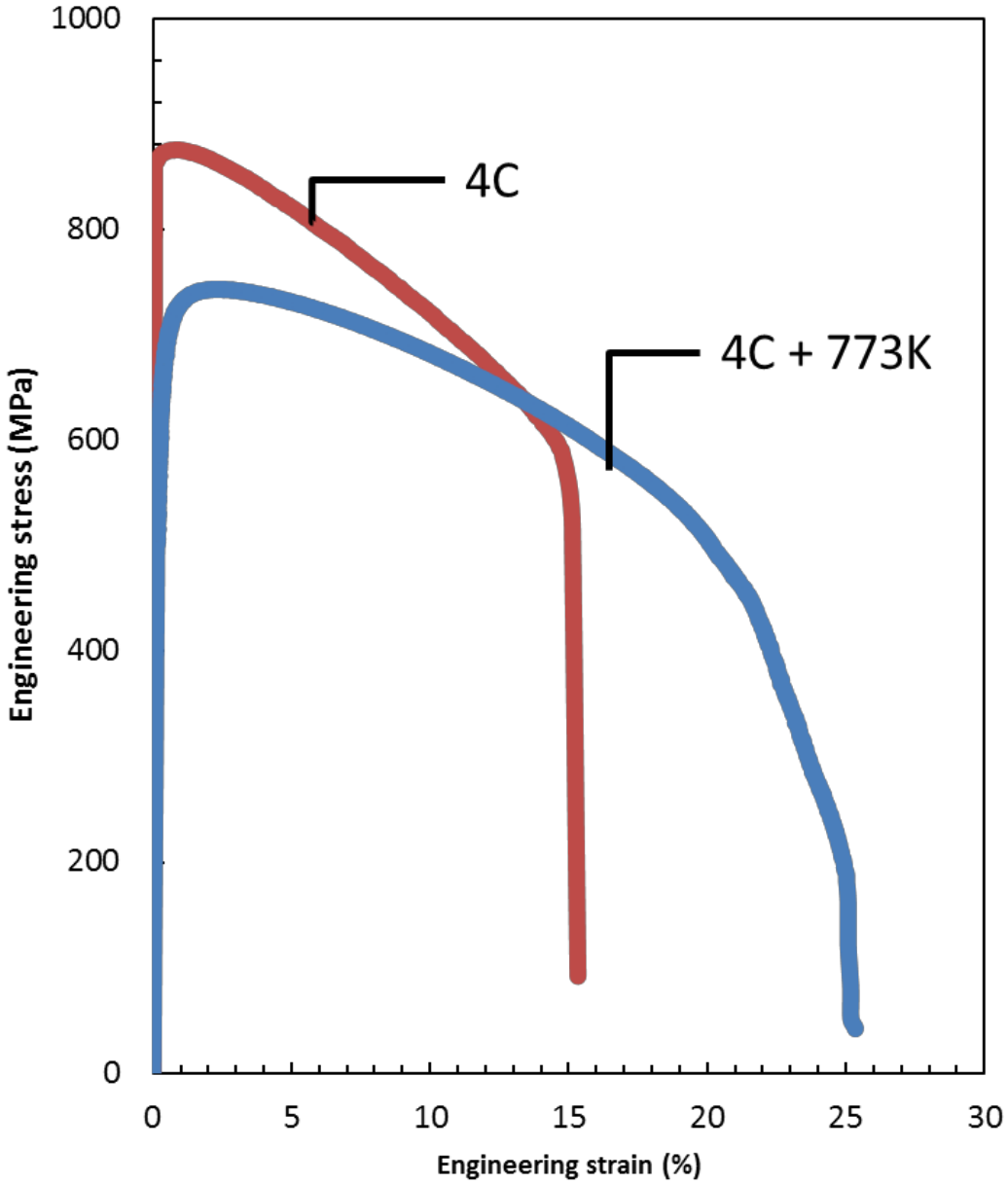

Figure 8.14. Stress and strain curve of as-ECAPed and post-ECAP annealed sample.

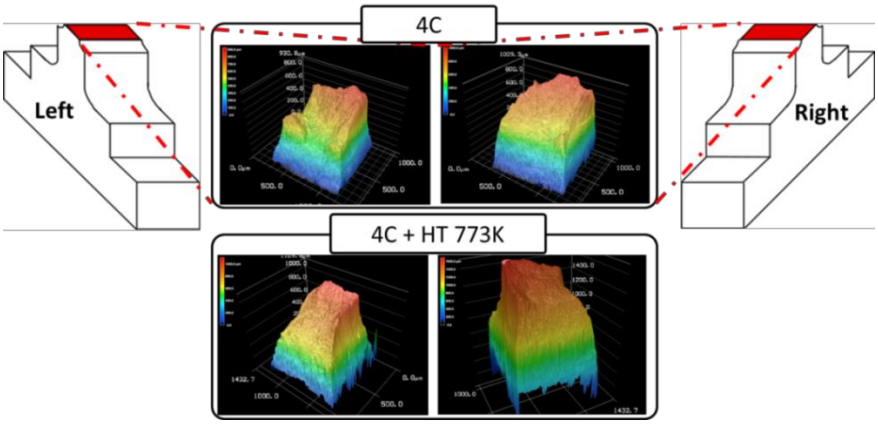

(a)

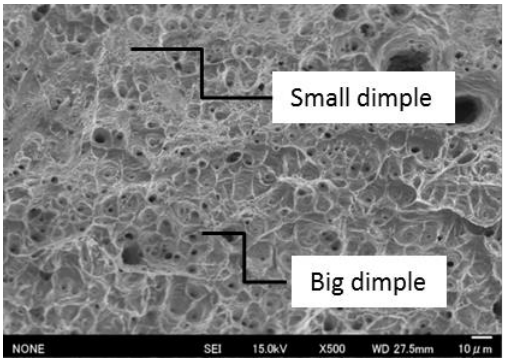

(b)

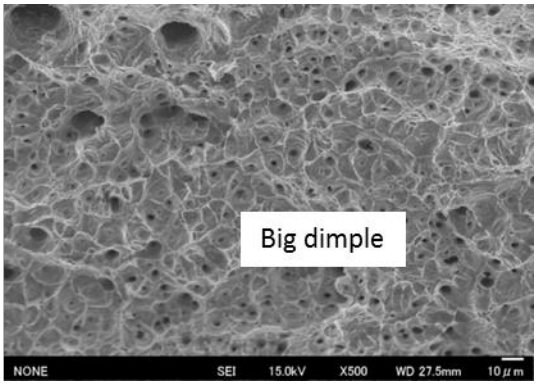

(c)

Figure 8.15. (a) Laser microscope observation of as-ECAPed and post-ECAP annealed sample, and Dimple appearance of (b) as-ECAPed and (c)post-ECAP annealed sample.

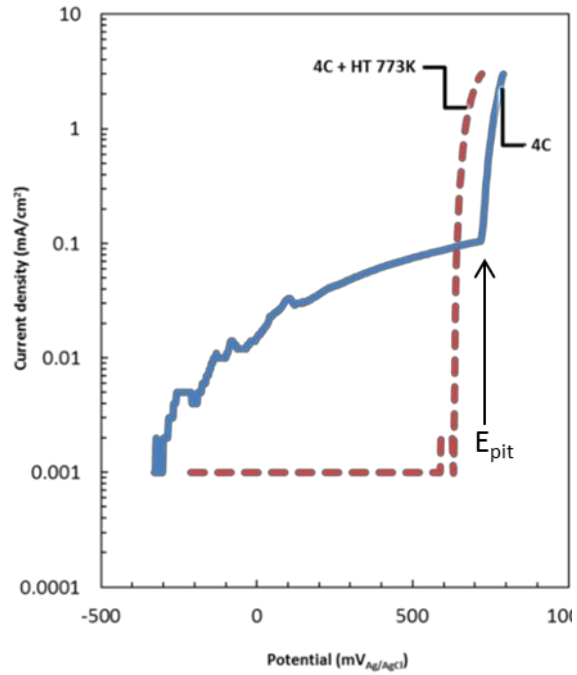

(a)

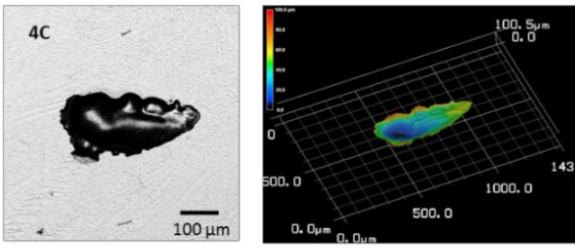

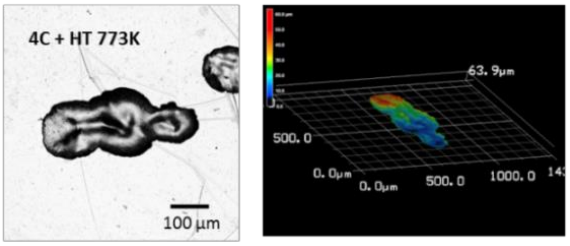

(b)

Figure 8.16. (a) Pitting corrosion resistance and (b) pitting appearance, of as-ECAPed and post-ECAP annealed sample.

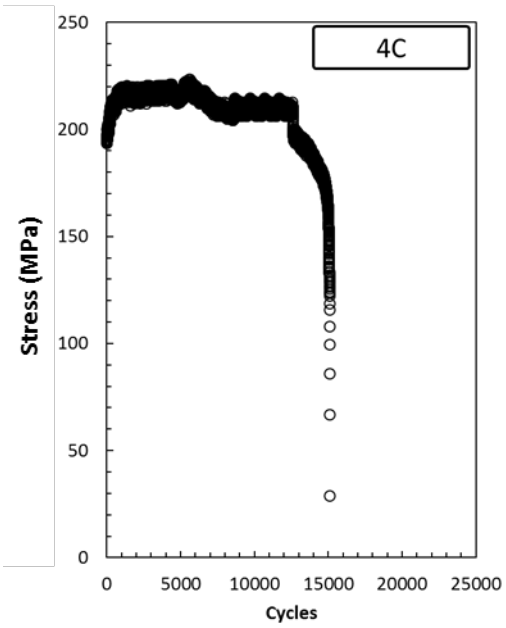

(a)

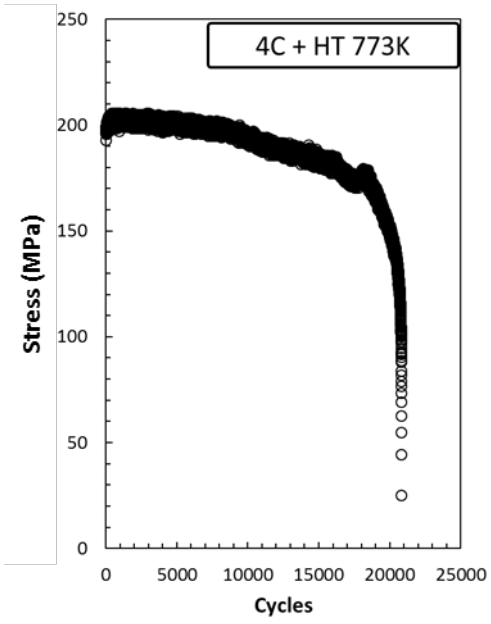

(b)

Figure 8.17. Cyclic deformation of (a) as-ECAPed and (b) post-ECAP annealed sample.

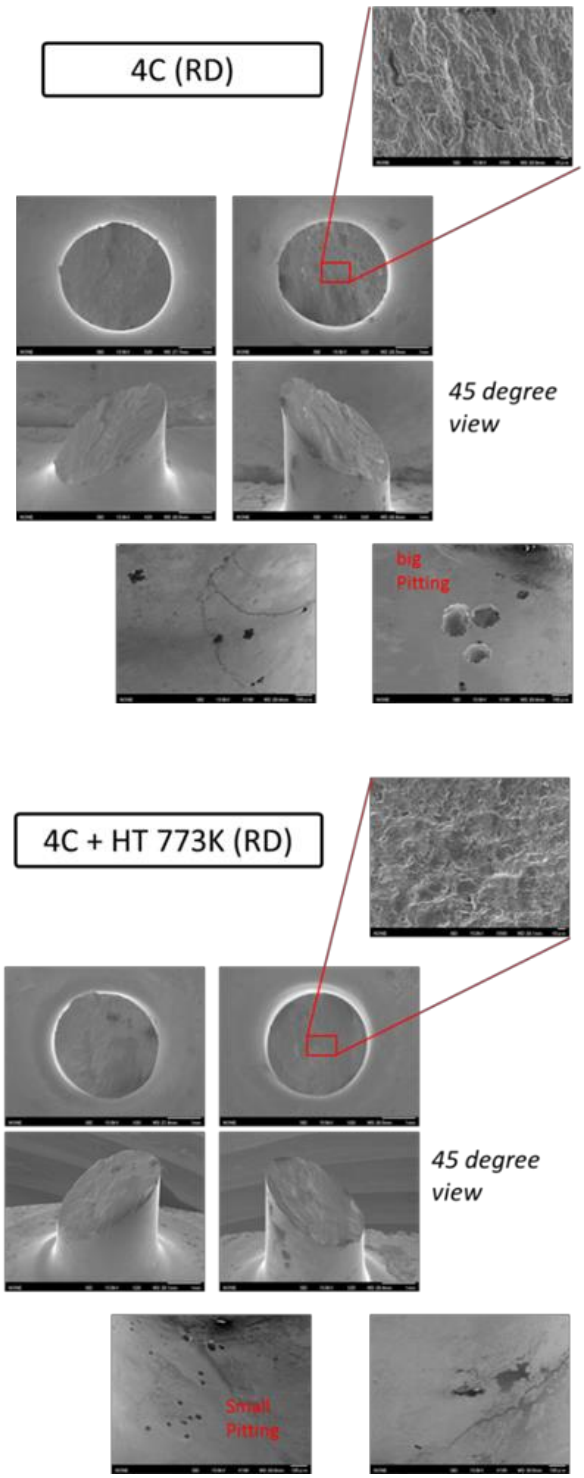

Figure 8.18. Fracture surface appearance on fatigue test of as-ECAPed and post-ECAP annealed sample.

that the grain boundary diffusivities in nanostructured metals processed by means of SPD in the temperature range of 398–448 K are 4–5 orders of magnitude higher relative to the same materials in a coarse-grained state **[18]**. Namely, early reduction of E_{pit} versus Ag/AgCl by the annealing can be caused by diminish of dislocations or transformation from non-equilibrium to equilibrium grain boundaries.

Corrosion fatigue test on ECAPed and post-ECAP annealed sample was clarified that crack initiation started from corrosion pits and propagated. Cyclic deformation of as ECAPed and post-ECAP annealed sample can be seen in **Figure 8.17**. Crack initiation and propagation on corrosion fatigue can be observed clearly. Crack propagation was occurred at the corrosion fatigue crack tip. This crack propagation is characteristics in corrosion fatigue process. It can be concluded that corrosion fatigue life of iron chromium alloy is managed by initiation and growth of corrosion pits.

After corrosion fatigue tests, the sample was observed by electron microscope, as shown in **Figure 8.18**. Corrosion pits can be seen on the surface of sample. Fracture happened after connected of many micro cracks. **Figure 8.18** shows Fatigue fracture image by SEM of iron chromium alloy manufactured by ECAP and post-ECAP annealing. Fatigue appearance can be seen less pronounced and micro cracks.

8.4. Conclusion

Corrosion fatigue crack initiation process of UFG iron chromium alloy was briefly reviewed on experimental results. The corrosion fatigue crack initiation and crack propagation process of iron chromium alloy can be characterized by corrosion pits and intergranular fracture, respectively. The most of the corrosion fatigue life of iron chromium alloy is spend by fatigue crack initiation.

References

[1] Segal, V. M. (1995). Materials processing by simple shear. Materials Science and Engineering: A, 197(2), 157-164.

[2] Abdulov, R. Z., Valiev, R. Z., & Krasilnikov, N. A. (1990). Formation of submicrometre-grained structure in magnesium alloy due to high plastic strains. Journal of Materials Science Letters, 9(12), 1445-1447..

[3] Antunes, R. A., & de Oliveira, M. C. L. (2012). Corrosion fatigue of biomedical metallic alloys: mechanisms and mitigation. Acta biomaterialia, 8(3), 937-962.

[4] Rubitschek, F., Niendorf, T., Karaman, I., & Maier, H. J. (2012). Corrosion fatigue behavior of a biocompatible ultrafine-grained niobium alloy in simulated body fluid. Journal of the mechanical behavior of biomedical materials, 5(1), 181-192.

[5] Yamasaki, T., Miyamoto, H., Mimaki, T., Vinogradov, A., & Hashimoto, S. (2001). Stress corrosion cracking susceptibility of ultra-fine grain copper produced by equal-channel angular pressing. Materials Science and Engineering: A, 318(1), 122-128.

[6] Kumar, S. R., Gudimetla, K., Venkatachalam, P., & Ravisankar, B. (2010). Stress corrosion cracking of Al7075 alloy processed by equal channel angular pressing. Int. J. Eng. Sci. Technol, 2, 53-61.

[7] M. Pisarek, P. Kedzierzawski, M. Janik-Czachor, K.J. Kurzydlowski, (2008). Effect of hydrostatic extrusion on the corrosion resistance of type316 stainless steel, Corrosion, 64, 131-137.

[8] Vinogradov, A., Mimaki, T., Hashimoto, S., & Valiev, R. (1999). On the corrosion behaviour of ultra-fine grain copper. Scripta Materialia, 41(3), 319-326.

[9] Vinogradov, A., Mimaki, T., Hashimoto, S., & Valiev, R. (1999, July). On Corrosion of Ultra-Fine Grained Copper Produced by Equi-Channel Angular Pressing. In Materials Science Forum (Vol. 312, pp. 641-646).

[10] R.K. Islamgaliev, F. Chmelik, R. Kuzel, Thermal stability of submicron grained copper and nickel, Mater. Sci. Eng. A, 237 (1997) 43-51.

[11] R.K.S. Raman, R.K. Gupta, C.C. Koch, (2010). Resistance of nanocrystalline vis-a-vis microcrytalline Fe-Cr alloys to environmental degradation and challenge to their synthesis, Philos. Mag., 90, 3233-3260.

[12] B.V. Mahesh, R.K. Singh Raman, C.C. Koch, (2012). Bimodal grain size distribution: an effective approach for improving the mechanical and corrosion properties of Fe-Cr-Ni alloys, J. Mater. Sci., 47, 7735-7743.

[13] R. Gupta, R.K. Singh Raman, C.C. Koch, (2012). Electrochemical characteristics of nano and microcrystalline Fe–Cr alloys, J. Mater. Sci., 47, 6118-6124.

[14] A. Andrievski, (2003). Review Stability of nanostructued materials, J. Mater. Sci.,

38, 1367-1375.

[15] C. Koch, (2007). Structural nanocrystalline materials: an overview, J. Mater. Sci., 42, 1403-1414.

[16] S. Qian, R.C. Newman, R.A. Cottis, (1990). Validation of a percolation model for passivation of Fe-Cr alloys: Two-dimensional computer simulation, J. Electrochem. Soc., 137, 435-439.

[17] K. Sieradzki, R.C. Newman, (1979). A percolation model for passivation in stainless steels, J. Electrochem. Soc., 133, 1979-1980.

[18] Y.R. Kolobov, G.P. Grabovetskaya, M.B. Ivanov, A.P. Zhilyaev, R.Z. Valiev, (2001). Grain boundary diffusion characteristics of nanostructured nickel, Scr. Mater., 44, 873-878.

[19] R. Würschum, S. Herth, U. Brossmann, (2003). Diffusion in Nanocrystalline Metals and Alloys—A Status Report, Adv. Eng. Mater., 5, 365-372.

Chapter 9. Conclusions and contributions to original knowledge

The microstructural evolution, mechanical and electrochemical properties of low C,N Fe-20%Cr subjected to SPD by ECAP and subsequent isothermal annealing has been investigated.

9.1. Conclusion of chapters 2-8

In Chapter 2, the microstructural evolution of Fe-Cr alloys and pure copper processed by ECAP for up to three passes was quantitatively analyzed by EBSD focusing on the initial stage of UFG formation. The deformation microstructure after one pass consists of deformation-induced extended subgrain boundaries typical to the geometrically necessary boundaries. The density of the boundaries is higher in Fe-Cr alloys than pure copper. With increasing ECAP passes, the fraction of HAB and mean misorientation angle increase, and HAB spacing decreases. This phenomenon is noticeable in Fe-Cr steels, and can be explained in terms of slip behavior intrinsic to BCC structure.

In Chapter 3, the microstructural evolution of extremely this alloy processed by ECAP from one to eight passes via routes A, Bc, and C were quantitatively analyzed by focusing on the degree of their anisotropy. The degree of anisotropy of microstructures was different among the three deformation routes. They were generally isotropic in route Bc, namely the grains were equiaxial, and the hardness was comparable in the three orthogonal planes.

In Chapter 4, the effect of the annealing behavior on a UFG this alloy by ECAP was studied focusing on the residual dislocation-related strain on early stage of grain growth. The softening of a material occurred in the typical three stages, comprised of recovery with constant hardness, and subsequent significant softening accompanying homogeneous grain-growth, and the final slow grain growth with little change of hardness. The extended recovery stage was confirmed by XRD prior to the appreciable grain-growth. The microstructure of the recovery stage shows homogeneous coarsened grain with grain appearance comparable with the ECAP processed structure.

In Chapter 5, ECAP processed and post-ECAP processed was comparable in

term microstructural evolution and tensile properties. With the increasing number of passes, the average grain size was gradually refined and the minimum average grain size is about 100 nm when the sample was extruded after eight passes at room temperature. The micro hardness and the tensile strength increase with the number of passes, while the corresponding elongation decreases. The annealing at 773K for 1 h can increase the average grain size to 200 nm at eight passes ECAPed sample and improve the ductility of the ECAPed samples at the sacrifice of a little decrease in tensile strength.

In Chapter 6, fatigue properties of ECAP processed and post-ECAP processed was analyzed in term of microstructural evolution and LCF behavior. The microstructure after four ECAP pass is homogeneous with several amounts of HAGB fraction, as is commonly observed in BCC metals at this equivalent strain. The ECAPed sample via routes A and Bc exhibited comparable. Cyclic softening is common for most cold worked and ECAPed sample. The cyclic softening is associated with dislocation density in fatigue of ECAPed sample in general. LCF behavior of iron chromium steel after ECAP for up to four passes shows that the deformation microstructure remained fine and stable after cyclic deformation.

In Chapter 7, effect of post-ECAP annealing on the pitting corrosion of UFG iron chromium alloy fabricated by ECAP was studied. The hardness was found that softening occurred by the typical three-stage change comprising of recovery with constant hardness, and subsequent recrystallization accompanying significant softening, and the final grain growth with constant hardness. Pitting potential was more nobles in UFG state and more sensitive to annealing temperature. Namely, pitting potential started to decrease monotonously at lower temperature than the hardness which reflected grains size change. The early reduction of the pitting potential in the recovery process is attributed to less stabilized passivation caused by the rearrangement and annihilation of dislocations inside grains and in non-equilibrium grain boundaries. This result is concluded that nobler potentials of UFG states are realized by not only grain size reduction but also defective deformation-induced UFG.

In Chapter 8, corrosion fatigue crack initiation process of UFG iron chromium alloy was briefly reviewed on experimental results. The corrosion fatigue crack initiation and crack propagation process of iron chromium alloy can be characterized by

corrosion pits and intergranular fracture, respectively. The most of the corrosion fatigue life of iron chromium alloy is spend by fatigue crack initiation.

9.2. Contributions to original knowledge of chapters 2-8

This thesis contributions to original knowledge are :

- In Chapter 2, this is the first study that the effects of microstructural evolution on the mechanical properties of an UFG low C, N Fe-20%Cr alloy and pure copper by ECAP. The microstructural parameters quantified by EBSD are connected to the mechanical properties. This influence was associated to fraction LAGBs and HAGB.
- In Chapter 3, this is the first study that the effect of deformation route ECAP on mechanical and electrochemical properties. The degree of anisotropy of microstructures was investigated in different planes among the three deformation routes
- In Chapter 4, This is the first study that details the annealing behavior of UFG low C,N Fe-20%Cr by ECAP. The softening of a material occurred in the typical three stages, comprised of recovery with constant hardness, and subsequent significant softening accompanying homogeneous grain-growth, and the final slow grain growth with little change of hardness.
- In Chapter 5, This is the first comparison study between ECAP processed and post-ECAP annealed of UFG iron chromium alloy in term of microstructural evolution and tensile properties.
- In Chapter 6, this is the first study that effect of deformation route ECAP of UFG iron chromium alloy. Fatigue behavior of iron chromium steel after ECAP for up to four passes shows that the deformation microstructure remained fine and stable after cyclic deformation.
- In Chapter 7, this is the first study about the effect of strain energy and grain size on corrosion resistance of UFG low C,N Fe-20%Cr alloy. The degradation of corrosion resistance in the early stage of annealing is attributed to stability change of passivation by recovery of dislocations structures inside grains and in non-equilibrium grain boundaries.

- In Chapter 8, this is first study that effect of annealing behavior on UFG structure of iron chromium alloy by ECAP in term of corrosion fatigue crack initiation and propagation.